Biochemical analysis of HDAC6-mediated Influenza A virus uncoating and its targeting by small artificial proteins

Inauguraldissertation

zur

Erlangung der Würde eines Doktors der Philosophie

vorgelegt der

Philosophisch-Naturwissenschaftlichen Fakultät

der Universität Basel

von

Longlong Wang

von China

Basel, 2021

Genehmigt von der Philosophisch-Naturwissenschaftlichen Fakultät auf Antrag von:

Prof. Dr. Patrick Matthias

Prof. Dr. Anne Spang

Basel, den 2. März 2021

Prof. Dr. Marcel Mayor, Dekan

Abstract

HDAC6 is a member of the histone deacetylases (HDACs) family and has a unique structure, with tandem catalytic domains and a conserved ubiquitin (Ub)-binding zinc finger (ZnF) domain. While the deacetylase activity is important for cell motility, stress response, cancer progression, among others, HDAC6 function also depends on its ZnF domain which engages Ub in many cases. For example, it is important for the formation of cellular granules, such as aggresome and stress granules. In particular, the aggresome/HDAC6 pathway can be hijacked by exogenous pathogens, like influenza A virus (IAV), to facilitate the infection: the HDAC6 ZnF domain is indispensable for virion uncoating, but the molecular details are still missing.

The goal of this thesis has been (i) to gain additional details about the cellular components recruited by the HDAC6 ZnF domain and involved in the viral uncoating and (ii) to use small artificial proteins to interfere with this recruitment.

Analysis by immunoprecipitations and biochemical assays allowed me to show that the recruitment of Ub by the HDAC6 ZnF is essential to allow the formation of a complex involving components of the actomyosin system, in particular myosin 10 and actin. Unanchored Ub chains form a bridge between HDAC6 and myosin 10. This also has an impact on the recruitment of another motor system, dynein: recruitment of dynein by HDAC6 is increased when Ub cannot be recruited. These biochemical data were combined with mathematical analysis of the system by our colleagues at D-BSSE, to model the uncoating of IAV. This allowed developing a tug-of-war model of uncoating which realistically depicts the biological observations. Besides, results from clinical samples could be obtained; in particular, two IAV strains, H1N1 and H3N2, show a different dependency on the HDAC6/aggresome pathway. We could show that this relates to their M1 matrix protein having different affinities (H1N1 > H3N2) for interaction with HDAC6. This information could also be integrated into the model and allowed to further refine it (Arctibasova*, Wang* et al., submitted).

Above we demonstrated the importance of HDAC6 ZnF-Ub interaction during IAV infection, we decided to target this protein-protein interaction, as it might be valuable therapeutically. To achieve this, we screened out multiple DARPins (**D**esigned **A**nkyrin **R**epeat **P**rote**ins**) which bind specifically to HDAC6 ZnF. One of the DARPins, F10, could be shown to efficiently block the HDAC6-Ub interaction by *in vitro* pull-down and split-GFP assays in cells. X-ray crystallographic data (with a resolution of 2.55 Å) showed that F10 occupies the pocket where Ub engages. We established cell lines for expression and conditional degradation of DARpin F10; this allowed us to show that IAV infection is greatly inhibited by F10 expression. Investigation of IAV M1 protein release by microscopy convinced us that the uncoating step is interrupted. Furthermore, we showed that another RNA virus, ZIKA, is also impaired by DARPin F10. Other cellular pathways, like aggresome and stress granule formation,

are inhibited as well (Wang et al., submitted). Considering that stress granule and aggresome are both potentially pathological granules in neurodegenerative diseases (e.g. Amyotrophic lateral sclerosis and Parkinson diseases), we have shown that the HDAC6 ZnF domain is a targetable site for drug discovery, with potential for patients who are suffering from severe virus infection or as neurodegenerative diseases.

Table of Contents

Introduction

1, Post-translation-modifications, Acetylation & HDACs

1) Post-translation-modifications

After the first isolation of DNA, which was named "nuclein" initially by a Swiss Physician -- Friedrich Miescher in 1869, scientists have shown that DNA carries the secret of life: It determines protein sequence, which further decides its structure and function. The process from DNA to RNA to protein is called "central dogma" (Crick, 1970) (Figure 1), and the last step from RNA to protein is "translation".

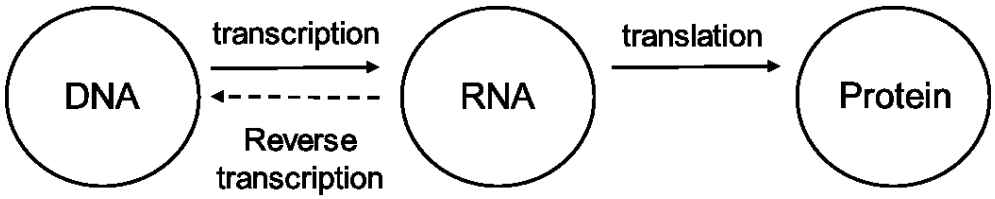

Figure 1, the central dogma of biology.

However, to fulfill a protein's function, we still need to put "decorations" on certain amino acids, and this is termed as **P**ost **T**ranslation **M**odifications (PTM). It refers to a covalent link of a small chemical group, e.g. phosphate and acetyl group, or proteins/peptides (such as in ubiquitination and SUMOylation), to amino acid side chains or at protein's C- or N- termini. The most frequent modification is Phosphorylation (the attachment of a phosphate group) (Khoury et al., 2011). It occurs mostly on amino acid serine (Ser), threonine (Thr), tyrosine (Tyr), and several others. The protein that transfers the phosphate to its substrate is called "kinase". One of the most studied kinases is Mitogen-activated protein kinase (MAPK). In eukaryotes, phosphorylation regulates multiple cellular pathways including proliferation, gene expression, differentiation, mitosis, cell survival, and apoptosis (Gray Pearson, 2001). Besides the modification which mediates protein function, there is one modification involving in protein degradation, named "ubiquitination". To prevent the accumulation of misfolded proteins, the cell is evolved with a **P**rotein **Q**uality **C**ontrol (PQC) system to degrade ubiquitinated targets (Chen et al., 2011). When the cell is under stress conditions, which are induced by exogenous stimulus (e. g. heat-shock), chemicals (e.g. MG132 & Arsenite), or pathogens (like virus or bacteria), the cellular PQC will be disturbed, leading to the accumulation of misfolded protein. Those aggregates could be very toxic in neurons, if they are not eliminated immediately and keep existing (Sweeney et al., 2017). Therefore, to get rid of misfolded proteins, the E3 ubiquitin (Ub) ligase, which forms a functional complex with E1 and E2, deposits Ub to the substrate lysine (K) residue. The linkage between substrate and Ub is classified by lysine's position on Ub, like K48 and K63. In general, K48-linked ubiquitination is responsible for the protein clearance, on the other hand, K63 linkage is involved in other pathways, such as signal transduction and protein recruitment (Behrends and Harper, 2011).

2) Acetylation

Acetylation, the second most frequent PTM (Khoury et al., 2011), refers to the reaction of adding an acetyl functional group to residues, mainly lysine (K). In the nucleus, this reaction happens commonly on histone proteins. The acetylation state of histones regulates the gene expression, for instance, acetylated H3K4 is always serving as an active expression marker. There are pieces of evidence to explain the causality between histone acetylation and gene activation. For example, the recruitment of certain complex through acetylated histone regulates gene expression. BRD4, short for bromodomain (which recognizes acetylated lysine residue) containing protein 4, could recruit the Mediator co-activator complex which is necessary for many genes transcription after binding to acetylated histone (Houzelstein et al., 2002; Jiang et al., 1998). Meanwhile, the deacetylation of H4 lysine 16 is important for the spreading of heterochromatin components, which leads to the gene silence in the related region, whereas acetylation of H4K16 serves as a barrier for the spreading (Shahbazian and Grunstein, 2007).

Besides histone acetylation, non-histone acetylation is getting increasingly important in recent years. For instance, since the deacetylation of tumor suppressor p53 leads to tumor development (Brooks and Gu, 2011), it is appealing to use small molecule, like Nutlin-3, to keep p53 from de-acetylation (Lyubomir T. Vassilev, 2004). Next, the acetylation of cytoplasmic protein regulates the cytoskeleton system. Microtubules, a tubular polymer, comprises two major tubulin types, α-tubulin, and β-tubulin, in eukaryotes. α-Tubulin is acetylated at lysine 40 by the cytoplasmic acetyltransferase TAT1 (Akella et al., 2010). It has been reported that the deletion of TAT1 increases the chance of stress-induced microtubule breakage, indicating that acetylation increases the mechanical resilience of microtubules to ensure the persistence of long-lived microtubules (Xu et al., 2017) (Figure 2a). Acetylation also regulates the actin network. Cortactin, a substrate of histone deacetylase 6 (HDAC6), will be hyper-acetylated if HDAC6 is deactivated, leading to its disassociation from actin filaments (Schnoor et al., 2018), further resulting in the disruption of actin polymerization as well as ciliary disassembly (Zhang et al., 2007) (Ran et al., 2015) (Figure 2b).

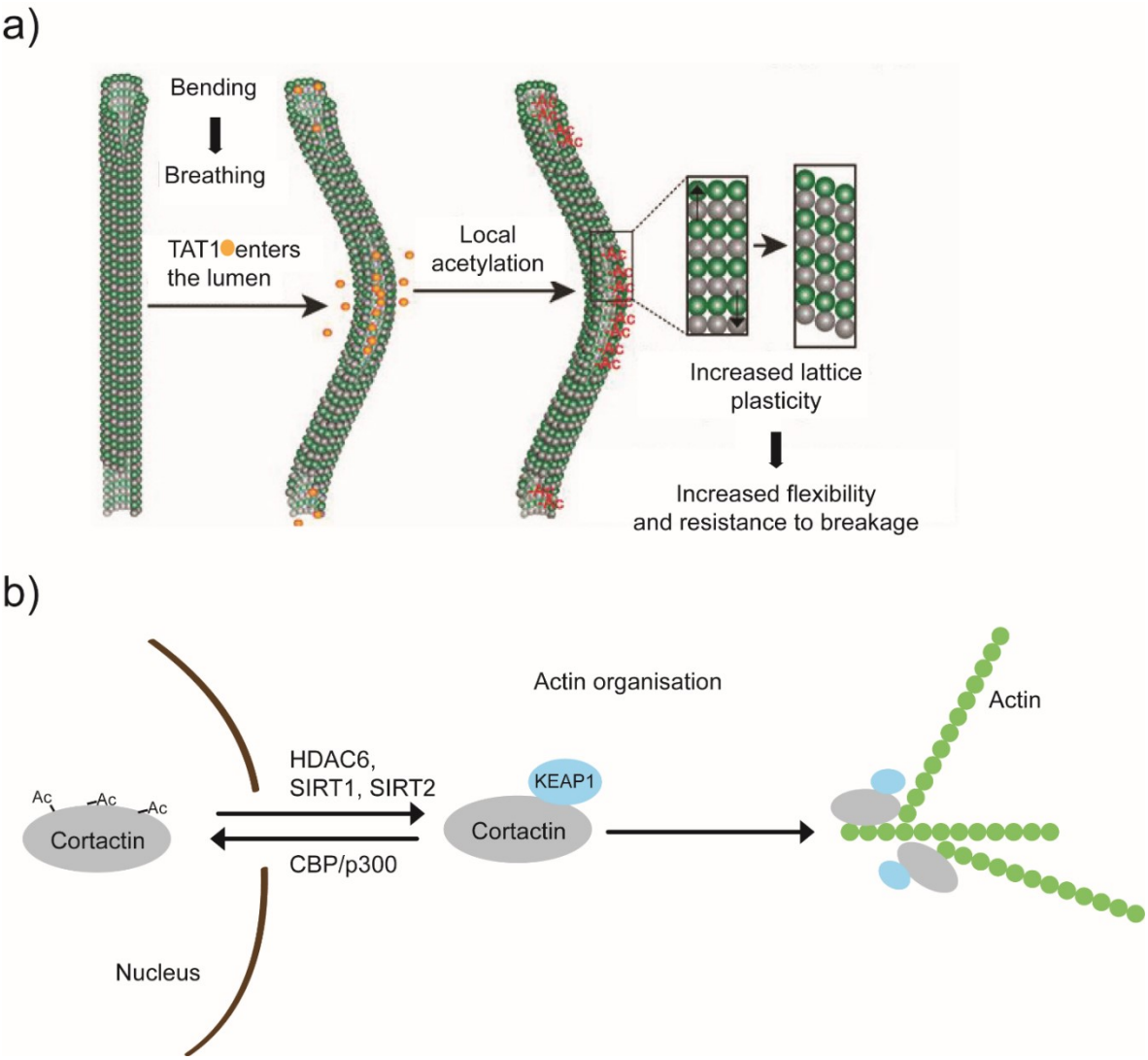

Figure 2, two examples of non-histone acetylation/deacetylation

a) α- Tubulin of the microtubule is acetylated and deacetylated at Lys40 by α- tubulin N- acetyltransferase 1 (TAT1) and histone deacetylase 6 (HDAC6), respectively. The acetylation can increase the microtubule's resistance to the shearing force and mechanical damages. Figure is taken from (Xu et al., 2017). b) Cortactin is acetylated at multiple residues in the nucleus by CREB-binding protein (CBP) and deacetylated by sirtuin 1 (SIRT1), SIRT2, and HDAC6. Deacetylated cortactin binds to KEAP1 and promotes cytoskeleton reorganization. The figure as well as the description are modified from ref (Narita et al., 2019).

3) Deacetylation and HDACs

As mentioned in Figure 2b, deacetylation is necessary for modulating cortactin interaction with KEAP1 which controls actin filaments re-organization. The enzyme to remove the acetyl group from lysine residue in both histone and non-histone protein is called deacetylase, or histone deacetylase (HDACs). In humans, there are 18 HDAC enzymes that use either zinc- or NAD+-dependent mechanisms to

deacetylate acetyl-lysine substrates (Seto and Yoshida, 2014). They are divided into 4 classes based on the sequence similarity: Class I, IIa/b, III, and IV (Figure 3). Class I contains HDAC1, HDAC2, HDAC3, and HDAC8. They are reported to mainly exist in the nucleus and ubiquitously expressed in different species. Acetylated histone is their main substrates. Class II is further classified into IIa and IIb subfamilies, and HDAC4, HDAC5, HDAC6, HDAC7, HDAC9, and HDAC10 are their members. A major difference between Class I and Class II is their subcellular distributions. Most members of Class II exhibit at least some existence in the cytosol, while HDAC6 is mainly a cytosolic protein (Seidel et al., 2015). Different from other HDACs, the substrates of HDAC6 are non-histone proteins, such as tubulin and cortactin. Moreover, unlike other HDACs that have one catalytic domain, HDAC6 has a second catalytic domain on its N-termini (Figure 3). The tandem catalytic domains share a great sequence similarity (~90%). It is still not clear whether they have different substrates or any preference for the substrate selection. HDAC10 also preserves two catalytic domains, and its only homology is HDAC6, therefore these two are sorted to the Class IIb. Unfortunately, the detail of HDAC10 currently is unclear. The following class III is a group of NAD-dependent deacetylases, named "Sirtuins". They are highly conserved from bacteria to humans and require NAD for their enzymatic activity (Nakagawa and Guarente, 2011). Same as other HDACs, it deacetylates histone, as well as some cytosolic protein. For instance, Sirt2 can deacetylate α-tubulin as HDAC6 does (North. et al., 2003), and its abnormal overexpression is associated with the aging of the central nervous system (CNS) (Maxwell et al., 2011). Last but not the least, HDAC11 is the only member of class IV deacetylase.

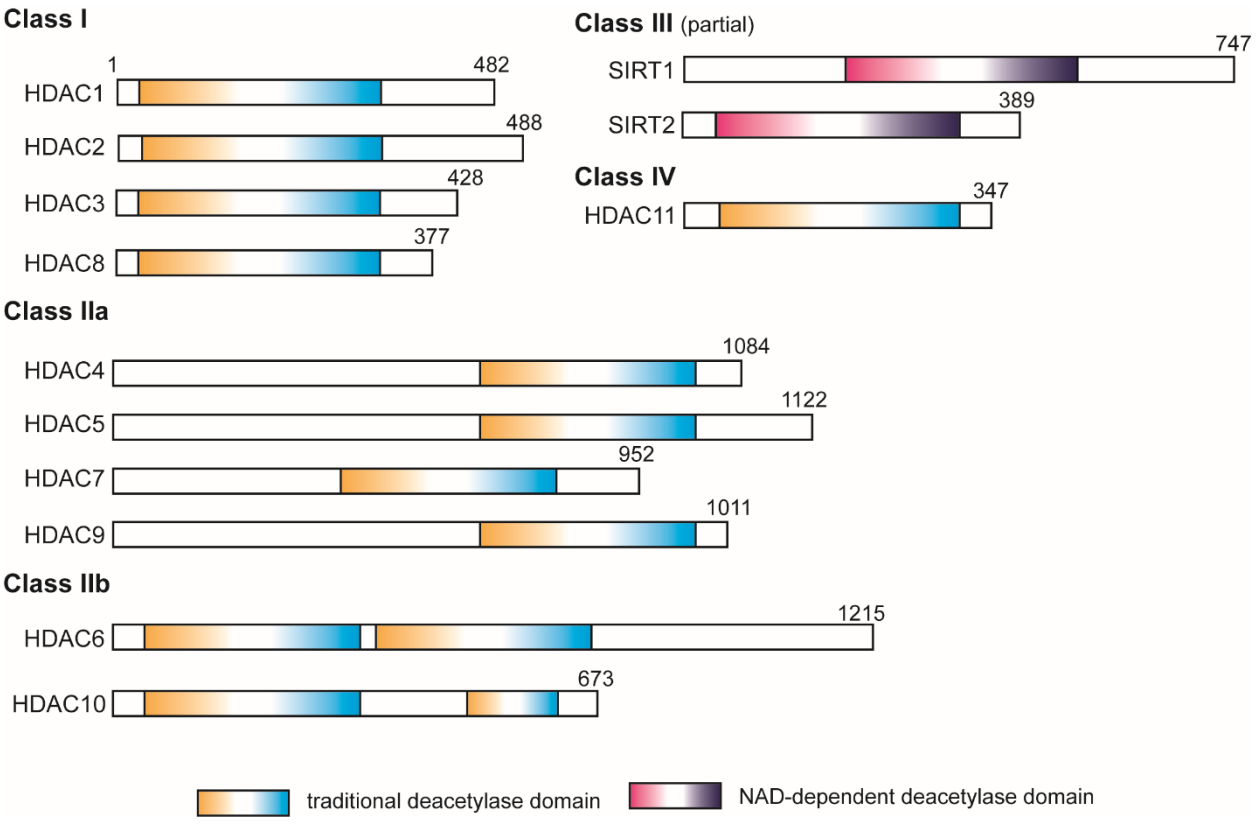

Figure 3, the secondary structure of 4 classes human HDACs and Sirtuins (partial)

The total amino acids are indicated at the right end of each protein, and the 2 different types of deacetylase domains are shown in different colors. Figure is adapted from Ref. (Seto and Yoshida, 2014).

4) HDAC6

My thesis will focus on HDAC6. Firstly, it has a tandem catalytic domain at its N-termini (Figure 4a). The active site of Catalytic Domain (CD) 1 and CD2 are highly conserved, which are featured by the typical narrow hydrophobic channels (Figure 4b and 4c) (Miyake et al., 2016). Even though both domains can remove the acetyl group from a single acetyl-lysine substrate *in vitro*, they show different deacetylase kinetics. The K_m is 31 μM, 59 μM and 44 μM for CD1, CD2, and CD1+2 (proteins covered both CD1 and CD2), respectively (Miyake et al., 2016). However, for the real substrate – α-tubulin, we find that after incubating mutated HDAC6 proteins (which had different mutations on either CD1 or CD2) with HDAC6 KO MEF cell lysate in which α-tubulin is fully acetylated, point mutations on CD1 do not result in compromised deacetylase activity of HDAC6 CD1+2 protein, while in contrast, mutations on CD2 do (Miyake et al., 2016). These indicate that for small substrates (e.g. acetyl-lysine) CD1 and CD2 are both functional, but merely CD2 is responsible for α-tubulin deacetylation. A deeper study on the other 13 artificial substrates shows that CD2 exhibits a broad substrate specificity, whereas CD1 is highly specific for substrates bearing C-terminal acetyl-lysine residues (Hai and Christianson, 2016). Additionally, HDAC6 prefers α/β-tubulin dimer as the substrate to microtubules (Miyake et al., 2016; Skultetyova et al., 2017). Nevertheless, we have confirmed that *in vitro* reconstituted microtubule can be deacetylated by purified HDAC6 catalytic domains, but how HDAC6 accesses the internal acetyl (the acetyl is located inside of microtubule lumen) is unknown. Since several new HDAC6 inhibitors are now under development for severe clinical diseases (Cosenza and Pozzi, 2018; Jiang et al., 2019; Li et al., 2018b), more studies about its deacetylase activity, including the substrate preference between CD1 and CD2, are foreseeable. Another important finding is that the region between CD1 and CD2 (from amino acid 436 to 484, figure 4a) is responsible for HDAC6/Dynein interaction (Banerjee et al., 2014a; Kawaguchi et al., 2003). It may not connect with HDAC6 deacetylase activity but is critical for HDAC6 another role in cells, and this role is the main topic of my thesis. Besides, for human HDAC6, there is another domain, called SE14 (Bertos et al., 2004), in the region between CD2 and ZnF. Very few studies are on this part, and it is only present in humans, regarded as a cytoplasmic anchoring motif.

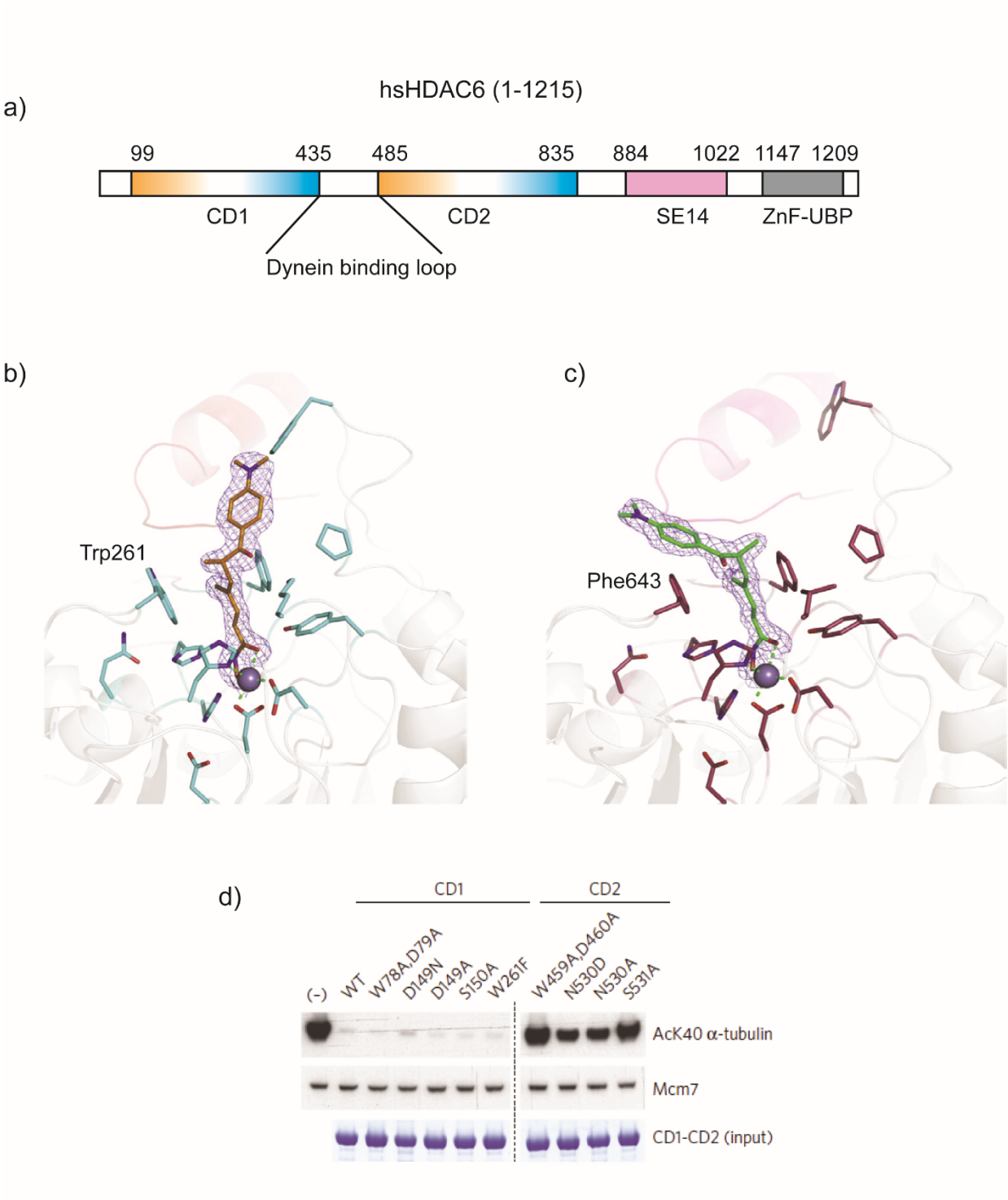

Figure 4, HDAC6 secondary structure in detail and CD1/CD2 difference (data is taken from our publication. Ref (Miyake et al., 2016))

a) Each domain is indicated below the corresponding region. b) & c) show the 3D structure of the enzymatic active site for HDAC6 CD1 and CD2 respectively. The major difference in structure is that Trp261 in CD1 is replaced by Phe643 in CD2. d) represents the experiment between different point mutated HDAC6 CD1-CD2 protein and HDAC6 KO MEF cell lysate. The point mutations can affect the indicated (top) catalytic domain's deacetylase activity. It shows all the five CD1^{mutated}-CD2 proteins still deacetylate the hyper-acetylated α-tubulin. While 4

CD1-CD2^{mutated} proteins lose their deacetylase activity. Taken together, it shows that CD2, not CD1, accounts for α-tubulin deacetylation.

Compare to its N-termini catalytic domain, the HDAC6 C-terminal ZnF domain is much less studied. In 2001, it was first identified as an Ub binding motif (Seigneurin-Berny et al., 2001), and the x-ray structure together with Ub C-termini peptide was solved in 2012 (Ouyang et al., 2012) (Figure 5a). Through its interaction with Ub, HDAC6 is associated with the transport of ubiquitinated aggregates formed by misfolded proteins, as a result of inhibition of the proteasome pathway. The aggregates will grow to a stress response related to cellular granule, called aggresome (Figure 5b). It is a big and unique granule in the cell, surrounded by an intermediate stress filament – vimentin formed cage (Johnston et al., 1998b). Under normal conditions, misfolded proteins will be ubiquitinated by the E3 ligase, and degraded by the proteasome. However, if proteasomal degradation is blocked or overloaded, the aggresome pathway will be activated. Here, misfolded proteins will be recognized by an HDAC6/Dynein complex through the Ub-ZnF domain interaction, then transported along the microtubules to **M**icro**t**ubule **O**rganizing **C**enter (MTOC), forming an aggresome. Finally, the aggresome will be cleared by autophagosome to recycle the material (Figure 5c). Not limited to the aggresome pathway, HDAC6 is also involved in the stress granule (SG) pathway, virus infection, and neurodegenerative diseases. More detail about the HDAC6 ZnF role in different cellular pathways will be explained in the following parts.

The validated HDAC6 substrates and interacting proteins (colored by sky blue) are listed in Table 1. The responsible domain has been indicated. Collectively, catalytic domains are for substrate deacetylation while the protein-protein interaction function is mainly assigned to ZnF domain.

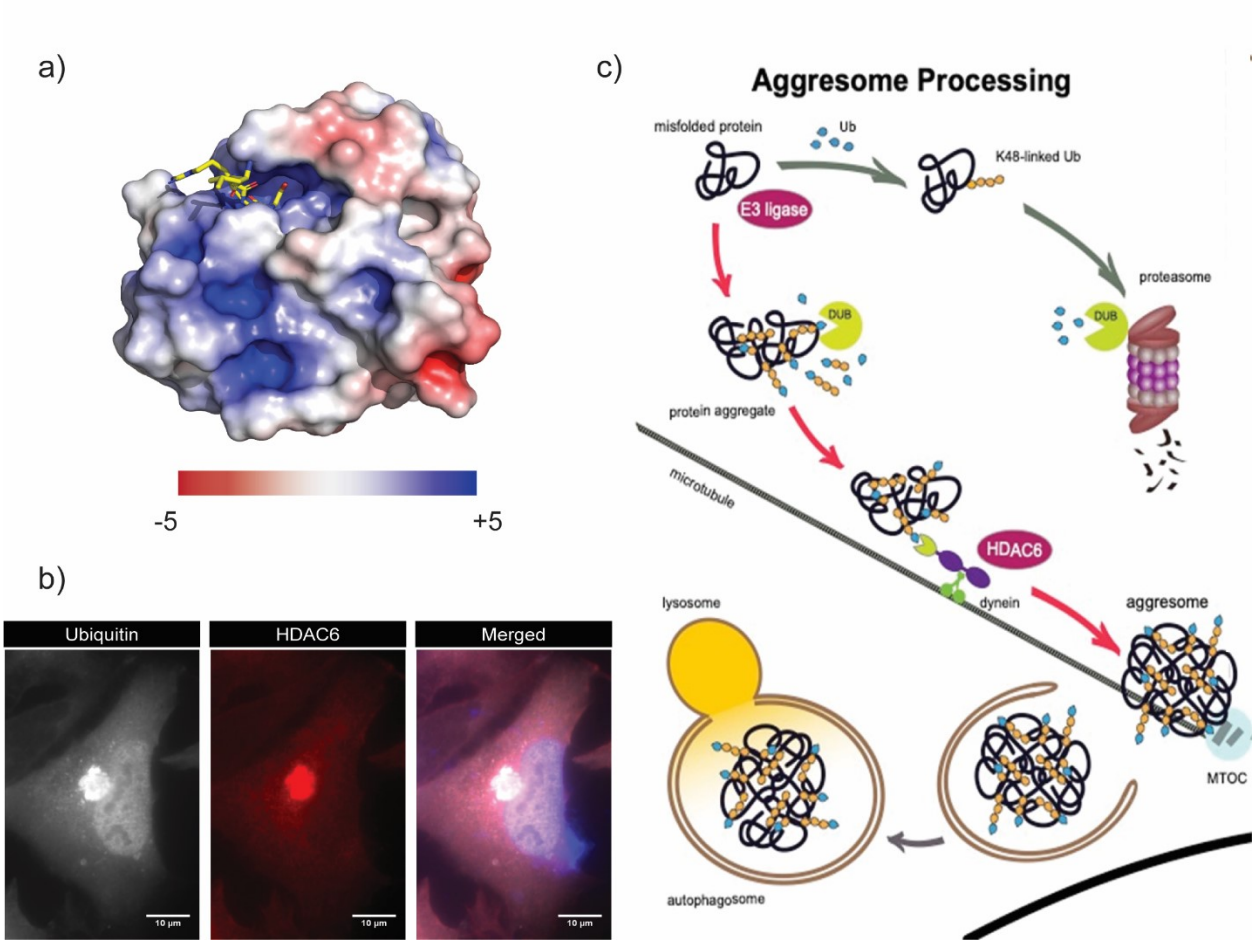

Figure 5, HDAC6 ZnF structure with Ub peptide and Scheme of Aggresome Pathway

a) The overall structure of the HDAC6 ZnF-Ub complex. The Ub C-terminal is shown as the yellow stick, and ZnF is plotted by the electrostatic surface (-5 KT/e to +5KT/e). The structure is modified from PDB: 3GV4. b) Aggresome induced by Carfilzomib (2 μM, 18 hrs) in A549 cells. Aggresome is indicated by Ub and HDAC6 signals. Both are markers for aggresome. Scale bar represents 10 μm. c) The scheme of Aggresome Pathway (Figure is taken from our collaborator Dr. Yohei Yamauchi, University of Bristol).

Protein substrate	**protein function affected by acetylation/deacetylation**	**Potential therapeutic target diseases**	**HDAC6 domain involved**
α-tubulin (Zhang et al., 2003b)	Tubulin deacetylation (Lys40); Regulation of immune synapse the formation, cell migration, and chemotaxis	Antigen presentation deficiencies; Tumor cell metastasis (cancer); Neurodegenerative disorders (Parkinson's disease, spin bulbar muscular atrophy, CMT disease)	CD1 or CD2
Cortactin (Zhang et al., 2007)	Cortactin deacetylation (nine Lys residues);	Biological disorders involved in actin-based cell migration	CD1+CD2

	Regulation of cellular migration and F-actin binding		
HSP90 (Bali et al., 2005)	HSP90 deacetylation (Lys294); Misfolded protein degradation and clearance; Regulation of gene transcription activation	Neurodegenerative disorders; Tumor cell (cancer)	CD1+CD2
Tat (Huo et al., 2011)	Tat deacetylation (Lys28); Suppression of Tat-mediated transactivation of the HIV	HIV	CD2
Ku70 (Subramanian et al., 2011)	Ku70 deacetylation (Lys539/542); Suppression of apoptosis	ND	CD1 or CD2
β-catenin (Gao et al., 2010)	β-catenin deacetylation (Lys49); Epidermal growth factor-induced β-catenin nuclear localization	Tumor cell (cancer)	CD1 or CD2
RIG-I (Choi et al., 2016)	RIG-I Deacetylation; Virus related Innate immunity	RNA virus infection	CD1 or CD2
Peroxiredoxins (Parmigiani et al., 2008)	Prx deacetylation (PrxI Lys 197, PrxII Lys196); Redox regulation	Neurodegenerative disorders Tumor cell (cancer)	CD1 or CD2
Survivin (Riolo et al., 2012)	Survivin deacetylation (Lys129); Anti-apoptotic function	Tumor cell (cancer)	CD2
DDX3X (Saito et al., 2019a)	N–terminal Intrinsically disordered region (IDR) deacetylation; Stress granule maturation	Neurodegenerative disorders	CD2
Ub (Crystallization) (Ouyang et al., 2012)	Proteasome pathway Aggresome Pathway Stress granule Pathway	Cancer/Neurodegenerative disorders /…	ZnF
Dynein (Co-IP) (Kawaguchi et al., 2003)	Misfolded protein transport Influenza A virus infection	Flu/Neurodegenerative disorders	DBM
P62 (Co-IP) (Yan et al., 2013)	Aggresome formation	Neurodegenerative disorders	CD2
Myosin 10 (Co-IP) (Banerjee et al., 2014a)	Aggresome formation Influenza A virus infection	Flu/Neurodegenerative disorders	ZnF (verified in result part)
P97/VCP(Co-IP) (Seigneurin-Berny et al., 2001)	Proteasome pathway	ND	ZnF

Table 1, HDAC6 substrates & interacting proteins

From α-tubulin to DDX3X, they are substrates for HDAC6, while from Ub to VCP (colored cells), they are HDAC6 interacting proteins. The method to validate the binding is indicated right after the protein name. As shown, except Ub, which has a solid *in vitro* binding data (crystallization), others are obtained from co-immunoprecipitation from cell lysate. They may directly interact with HDAC6, or indirectly through some intermediate proteins. Table is updated from (Li et al., 2013). ND: not determined.

5) HDAC6 and cytoskeleton

HDAC6 is regarded as a microtubule regulator as α-tubulin is the earliest identified HDAC6 substrate. However, the result of tubulin acetylation and de-acetylation remains obscure. Until now, a few pieces of evidence imply the de-acetylation of tubulin mainly affects 1) microtubules' physical properties and 2) its binding partner. It has been shown that HDAC6 mediated microtubules deacetylation is essential to increase cellular stiffness (a parameter connected to cell invasion) in oncogene expressing cells(Rathje et al., 2014). Likewise, GRK2, G protein-coupled receptor kinase 2, is an HDAC6 stimulator, which recruits and phosphorylates HDAC6 (1~837), leading to the deacetylation of microtubules, enhancing cell motility and adhesion (Lafarga et al., 2012). Meanwhile, as shown in Figure 2a, acetylated microtubules are long-lived and stable, and resist mechanical stress (Xu et al., 2017). In addition to the direct influence on microtubules, their acetylation state modulates interactions with microtubules binding proteins. Inhibition of HDAC6 induces the transport of JIP1 (**J**NK-**i**nteracting **p**rotein 1) by kinesin-1 (a microtubule interacting protein) to neurites and its accumulation in neurite-tips (Reed et al., 2006). Independently of HDAC6 enzymatic activity on microtubules, HDAC6 is reported to interact with microtubules associated motor protein, dynein, through the previously described loop region (436-484, Figure 4a) between the two catalytic domains. However, it is still not clear about which part of dynein is responsible for the interaction with HDAC6. Therefore, we cannot exclude the possibility that HDAC6 actually interacts with other dynein binding proteins and further recruits dynein.

Unlike tubulin, actin is not a substrate of HDAC6. The impact of HDAC6 on actin filaments is via other proteins. As mentioned in Figure 2b, HDAC6 deacetylates cortactin, re-organizing filament formation. Despite of the direct deacetylation, an interesting finding shows that inhibition of HDAC6 by its specific inhibitor-tubastatin A, upregulated myosin 10 (Myh10) expression, resulting in increasing actin dynamics, which facilitated ciliogenesis (Rao et al., 2014). Besides, expressing HDAC6 ZnF domain in neuro2a cells shows increased actin extensions as compared to control. Denser actin cytoskeleton and more neuritic extensions are observed by overexpression (Balmik et al., 2019). The detail of how

HDAC6 ZnF domain is participating in the actin dynamic is not clear. Considering that ZnF domain is non-enzymatic, the answer may lie in its interaction with Myh10 (shown in Result Part II). Finally, HDAC6 regulates intermediate filaments. Expression of oncogenes such as simian virus 40 large T antigen, c-Myc, and cyclin E lead to an upregulation of HDAC6, followed by a structural collapse of vimentin filament network (Rathje et al., 2014). All the above indicate that HDAC6 is actively participating in the cellular cytoskeleton regulation.

2, HDAC6-Ub interaction in cellular granules formation

1) HDAC6 interacts with C-terminal free Ub

From the structure (Figure 5a), it presents that Ub C-terminal end, -R-L-R-G-G inserts into ZnF pocket, indicating that Ub, either mono Ub or Ub chain, with a free C-terminal can be recruited by HDAC6 ZnF domain. Notably, given that the C-terminal of Ub is fused to lysine residue during the ubiquitination process, ubiquitinated proteins cannot be recognized by HDAC6 due to the ubiquitination process, which needs the help from 3 major enzymes/complexes: (1) E1, Ub-activating enzymes, (2) E2, Ub-conjugating enzymes and (3) E3, Ub ligases. The first step, called “activation”, is E1 captures a free Ub with energy from ATP hydrolysis. Then E1 transfers Ub to E2, a process named “conjugation”. Finally, the E2-Ub complex will bind to a substrate-specific E3 complex, and later Ub will be “ligated” to the substrate (Figure 6a). The result of this sequential cascade is to paste Ub to lysine residues on the protein substrate via an isopeptide bond (Figure 6b) (or to cysteine residues through a thioester bond, serine and threonine residues through an ester bond, or the amino group of the protein's N-terminus via a peptide bond (Komander and Rape, 2012)).

The category of ubiquitination is divided according to the length of Ub. 1) Monoubiquitination, meaning only one Ub is fused to the substrate. 2) Polyubiquitination. The substrate will be ubiquitinated at lysine residue with multiple Ubs. The final product is named after the conjugated lysine residue’s position, like K48/K63-linked Ub chains (Figure 6c). In all cases, the Ub C terminal will be fused to a lysine residue on the substrate (Figure 6c), hence, the ubiquitinated protein cannot be recognized by HDAC6 ZnF anymore. To generate the free C-terminal, the deubiquitinase (DUB) (Figure 6a) is needed. It functions on the isopeptide bond to cleave Ub from the conjugated lysine, creating the C-terminal free Ub chain or mono-Ub. A study on aggresome formation pathway has shown that ataxin-3, an aggregate-associated deubiquitinase, creates unanchored C-terminal free K48 linked Ub chains from the poly-ubiquitinated/misfolded proteins, then recruiting HDAC6 ZnF to the aggregate and helping the formation of aggresome (Ouyang et al., 2012). And for the following aggresome clearance phase, another DUB, Poh1, cleaves the ubiquitinated protein and releases free K64 linked Ub chains, which is captured by HDAC6, facilitating the clearance of aggresome (Hao et al., 2013; Nanduri et al., 2015).

Considering that DUBs cleave C-terminal free Ub from the ubiquitinated substrate, it is intriguing that HDAC6 can transport the ubiquitinated aggregates by interacting with an isolated Ub chain, which is no longer conjugated to the target, to MTOC site? Unfortunately, the answer is not clear. More efforts are needed.

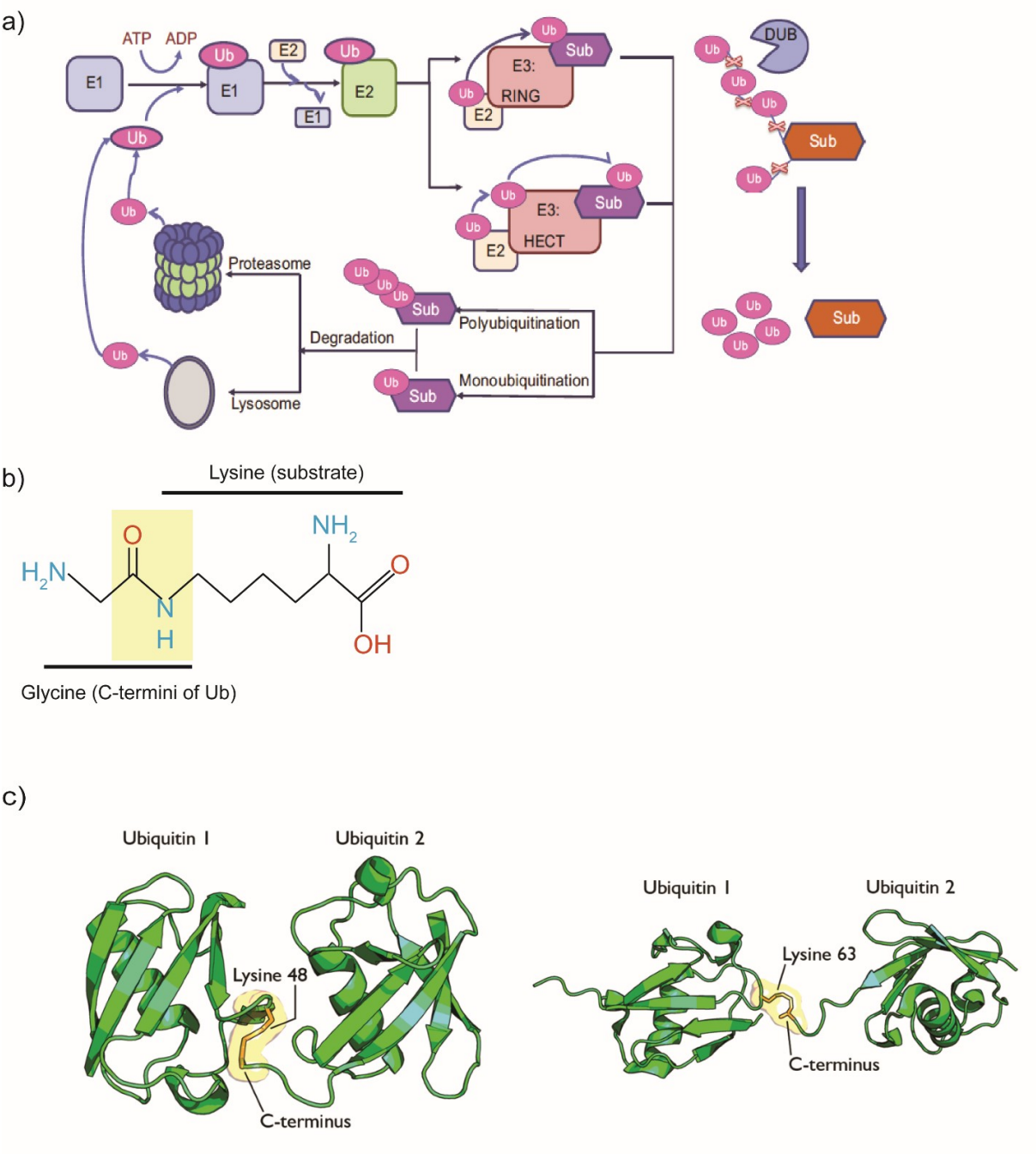

Figure 6, ubiquitination and the C-terminal of Ub

a) Protein ubiquitination and deubiquitination. E1 starts the ubiquitination with ATP, then passes Ub to E2. E2 forms complex with E3 ligase. Finally, E3 catalyzes Ub conjugating to the substrate. Ubiquitination is divided into mono-ubiquitination and poly-ubiquitination. They are all degraded by lysosome or proteasome, respectively. On the right, it shows deubiquitinase (DUB) removes Ub from the substrate, generating the mono Ub or Ub chains

with free C-termini. Figure & legends are modified from (Cai et al., 2018); b) the isopeptide bond (highlighted yellow) formed between the Ub C-terminal glycine residue and substrate's lysine residue. As shown, the C-termini of Ub is occupied; c) the structure of two typical Ub linkage: K48 (left) and K63 (Right) linked di-Ub chains. As we see, both C-terminus are anchored to the previous Ub and not feasible for HDAC6 ZnF domain. The structures are drawn based on PDB: 1AAR (K48) and PDB: 2JF5 (K63).

2) Aggresome and HDAC6

The aggresome, as shown above, is a proteasome-impairment induced cellular aggregate (Figure 5b & c). It is filled with ubiquitinated misfolded proteins and appears at MTOC site. Traditionally, aggresome formation is recognized as a cytoprotective response serving to sequester potentially toxic misfolded proteins and facilitate their clearance by autophagy (Olzmann et al., 2008). However, if the abnormal accumulation of pathological proteins, like Tau and TDP-43, occur at neurons, aggresome formation may be associated with multiple neurodegenerative diseases (Guthrie and Kraemer, 2011).

Considering that the brief introduction to the formation and clearance of aggresome in the previous chapter, the following will focus on individual protein or complex (Table 2), explaining their relations with HDAC6 and aggresome. The aggresome life cycle is divided into 3 phases: 1) the ubiquitination of certain proteins. This step needs the E3 ligase, for example, Parkin, a RING-type E3 ligase. It mediates multiple forms of ubiquitination, including mono-ubiquitination (Hampe et al., 2006) and K48-/K63-linked polyubiquitination (Lim et al., 2006). One of its substrates is synphilin-1, a protein known to form aggresome when co-expressed with α-synuclein (Tanaka et al., 2004). Another known substrate is TDP-43, a hallmark in **A**myotrophic **L**ateral **S**clerosis (ALS). Through the ubiquitination by Parkin, the TDP-43/Parkin complex can be recruited by HDAC6 and translocated to aggresome (Hebron et al., 2013). Misfolded and ubiquitinated DJ1 (or "Parkinson disease protein 7) protein is similarly relocated to aggresome (Olzmann et al., 2007).

The following step is 2) the recognition and transport by HDAC6/Dynein complex. As mentioned, for the ubiquitinated protein recognized by HDAC6 ZnF domain, DUBs are essential to generate C-terminal free mono Ub or Ub chains. The two discussed examples are ataxin-3 and Poh1. After the loading of cargos (ubiquitinated protein aggregates), Dynein will transport them alongside microtubules through its interaction with HDAC6 loop region (436-484) (Figure 4a). A remaining question here is whether HDAC6 catalytic domains affect the transport by deacetylating α-tubulin or other substrates. Next, protein aggregates are enriched at MTOC site forming aggresome, and the autophagy pathway is activated to degrade aggresome, then 3) clearance. In detail, HDAC6 deacetylates cortactin which is activated and mediates the recruitment and assembly of F-actin network around aggresome. Finally, with the help of motor protein myosin, autophagosome will be relocated to the aggresome site and starts digesting the aggregates. During the clearance, HDAC6 activity on cortactin is switched on due to the

recruitment of Ub, while in contrast, the activity is switched off by p62/SQSTM1 knock-down (Yan et al., 2013).

In conclusion, HDAC6 is at the crossroad of regulating aggresome: Interfering interaction between Ub and ZnF or dynein and Loop region (436-484) stands a chance to inhibit aggresome formation, while inhibiting HDAC6 enzymatic activity will impair aggresome clearance. Evidence shows that aggresome (or aggresome-like structures) is related to pathological aggregates. For example, a pathological mutation for Huntington's disease on huntingtin (Htt) exon 1 protein results in the formation of aggresome-like perinuclear inclusions (Waelter et al., 2001), and meanwhile neurodegenerative aggresome which contains α-Synuclein, Parkin, and Htt leads to the formation of the death-inducing signal complex of Hip-1, Hippi, and caspase-8 (Zhao et al., 2017), therefore regulating aggresome formation through HDAC6 is capable of interfering the progress of certain diseases, especially neurodegenerative diseases.

Protein	**Function**	**Wild-type protein localized to pathological inclusion bodies**	**Mutations associated with disease**
HDAC6	Deacetylase, adaptor protein	Lewy bodies	Unknown
Parkin	E3 Ub-protein ligase	Lewy bodies	Parkinson's disease
Ataxin-3	Deubiquitinating enzyme	SCA type-1 and 2 DRPLA intranuclear inclusions	SCA type-3
Dynein Motor complex	Retrograde microtubule motor	Unknown	Motor neuron degeneration
F-actin/Myosin	Actomyosin motor	Unknown	Neuron synaptic disorder

Table 2, Some proteins/complexes and their relation to aggresome (Table is modified based on: (Olzmann et al., 2008))

(SCA, spinocerebellar ataxia; DRPLA, dentatorubral-pallidoluysian atrophy)

3) Different roles of K48 and K63 linked Ub chains in aggresome pathway

Although two DUBs, ataxin-3 and Poh1, both generate free Ub chains acting as the docking site for HDAC6, the outcome is different. K48 linked ub-chains are from ataxin-3, while K63 linked ub chains

result from Poh1 action. Current data indicate that the interaction between K48 Ub chains and HDAC6 promotes aggresome formation. Considering K48 linked ubiquitination is a marker for proteasome degradation, the hypothesis is that under proteasome inhibition, HDAC6 binds to the accumulated K48 Ub-chains, further carrying the ubiquitinated aggregates through amyloid interaction between different Ub "fibers", and moves together as a fibrillary aggregate alongside microtubule to the aggresome forming site. On the other side, K63 Ub chains, which are not associated with proteasome degradation but involved in other processes like endocytic trafficking and DNA repair, accelerate aggresome clearance by autophagy. As mentioned, binding to K63 ub chains will upregulate HDAC6 enzymatic activity, resulting in the deacetylation of Cortactin, which helps the re-organization of F-actin and myosin 10 (actomyosin) network around the aggresome. Downregulation of myosin 10 by siRNA delayed aggresome clearance dramatically (Hao et al., 2013; Nanduri et al., 2015). The actomyosin network is the prerequisite for recruiting autophagosome to aggresome.

However, K48 linked ubiquitination is not merely for aggresome formation and proteasome degradation, neither K63 is for aggresome clearance. There is a report that Parkin-mediated K63 ubiquitination contributes to the relocation of misfolded DJ1 protein to aggresome (Olzmann et al., 2007). Meanwhile, another study shows that K63 linked ubiquitination serves as a seed of K63/K48 branched Ub chains and associates with proteasome degradation, which has overthrown the traditional conception that K63 is not proteasome related (Ohtake et al., 2018). Whatever, it is not only intriguing that the interaction between HDAC6 and different linkage Ub chains will have distinct outcomes, but also challenging for researchers to figure out a general rule for HDAC6 ZnF domain's impact on aggresome.

4) Stress Granule and HDAC6

Stress granules (SGs) are cytosolic aggregates of messenger ribonucleoproteins (mRNP) and RNAs, and appear when translation initiation is inhibited either by drugs or by stress responses (Anderson and Kedersha, 2009). The typical chemicals or conditions to induce SGs include heat shock, MG132 (proteasome inhibitor, mainly used to induce aggresome), sodium arsenite (SA, oxidative stress) (Figure 7a), thapsigargin (Thaps, endoplasmic reticulum stress), sorbitol, and UV light (Aulas et al., 2017). The proteomic analysis shows that ca. 20% of the SG contents are varied in a stress- and cell type-dependent way (Markmiller et al., 2018). And in our study, we choose the SG whose formation is mediated by HDAC6 under sodium arsenite treatment in human alveolar basal epithelial cell A549 to investigate.

Unlike aggresome, which has an obvious intermediate filament -vimentin formed boundary and is stable before the autophagosome digestion, SG is considered as a dynamic and membraneless structure, exhibiting liquid-like behavior, with a rapid exchange rate of its components. It will disassemble into mRNPs rapidly when the outside stimuli are removed. But it does not mean SG is an unshaped granule.

Super-resolution microscopy shows that SG contains internal substructures (Jain et al., 2016; Souquere et al., 2009). It has a condensed core in the center and a dynamic shell to surround the core (Figure 7b). How these structures are formed is still under investigation.

In detail, SG formation is always a consequence of the stress-induced phosphorylation of eukaryotic translation initiation factor -- eIF2α. Normally, eIF2 is a heterodimer complex composed of eIF2α, eIF2β, and eIF2γ, and its function is to recruit tRNA and GTP to the 40S ribosomal subunit. After displacing GDP with GTP under eIF2B's help, eIF2 is assembled into the 43S preinitiation complex, and then starts the translation (Kimball., 1999). Phosphorylation on the subunit eIF2α residue Ser 51, which is catalyzed by four kinases, PERK (PKR-like ER kinase), PKR (protein kinase double-stranded RNA-dependent), GCN2 (general control non-derepressible-2), and HRI (heme-regulated inhibitor) (Donnelly et al., 2013), will increase eIF2's affinity to eIF2B, stop the replacement of GDP, leading to an inactive state of eIF2 because of lack of GTP, therefore blocking the translation (Figure 7c). Although phosphorylation of eIF2α is common in many stress responses, yet it will change in a stress-specific manner (Aulas et al., 2017).

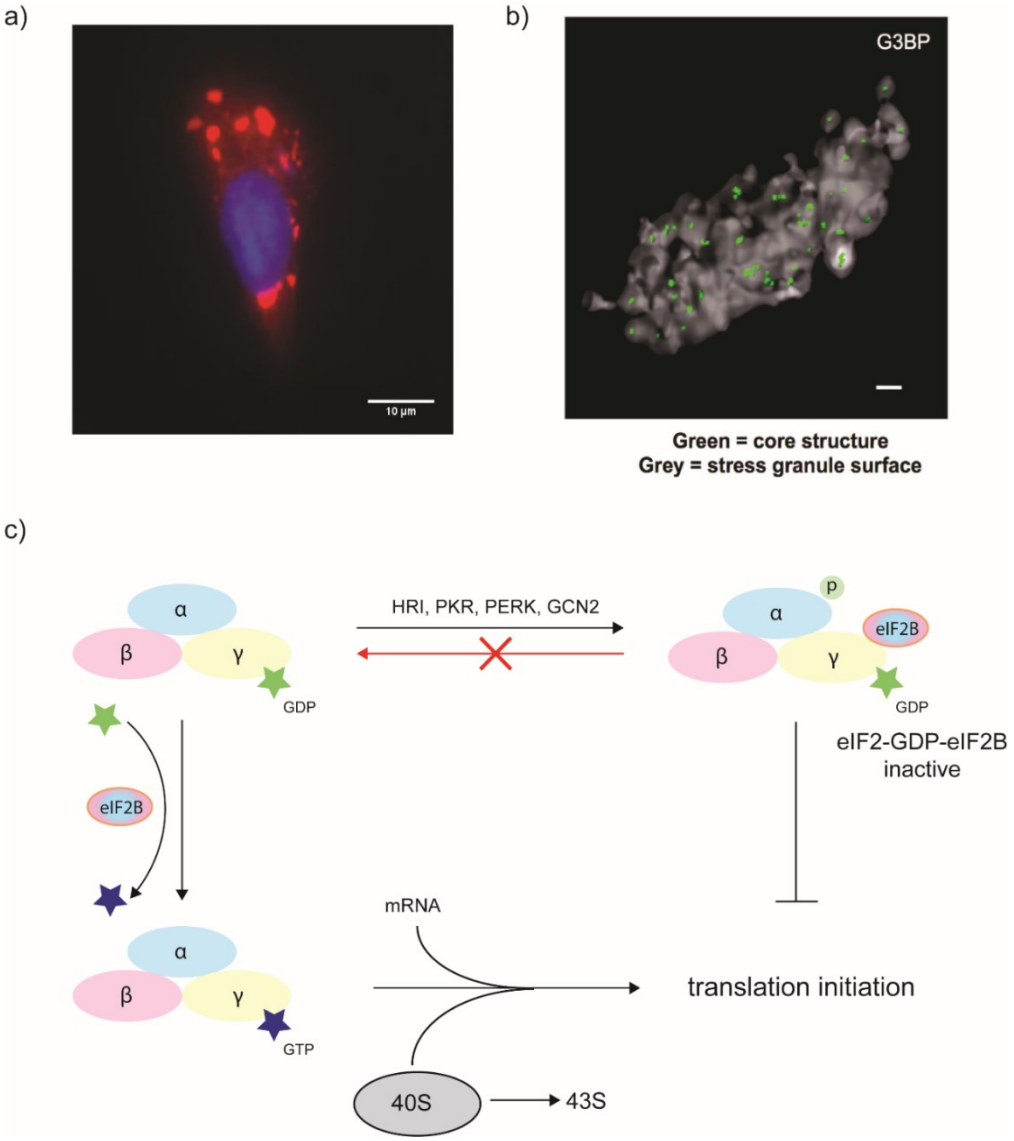

Figure 7, SG structure & the mechanism for eIF2α induced translation stalling.

a) Oxidative stress-induced G3BP1 positive SG (Red) under a wide-field microscope. G3BP1, the hallmark of SG, is colored as red. The picture is taken by 40x objective. DAPI is colored as blue. b) 3D STORM (Stochastic Optical Reconstruction Microscopy) image of an SG in vivo, showing the immune-fluorescence for GFP-G3BP. Gray surface represents surface of an SG. Cores are shown in green. Scale bar, 500 nm. Picture is from (Jain et al., 2016). c) The mechanism for the translation stalling by eIF2α phosphorylation. As shown, the phosphorylated eIF2α cannot disassociate from eIF2B, and GDP cannot be replaced by GTP, leading to the failure of translational initiation. Picture is drawn based on Ref. (Valiente-Echeverría et al., 2012)

The parsimonious model for SG formation could be divided into 2 steps: nucleation and maturation. The nucleation occurs wherein the formation of oligomeric assemblies of untranslated mRNPs (e.g. inactive eIF2 complex), and it could be at P bodies (**p**rocessing body, responsible for multiple RNA

decay) (Buchan et al., 2008). Two different models of nucleation have been proposed (Figure 8): 1) the core-first model & 2) LLPS (Liquid-liquid Phase Separation) -first model (Protter and Parker, 2016). In the core first model, the repressed mRNPs will aggregate together due to multiple stable interactions. While in the LLPS-first model, the aggregation of mRNPs is driven by the hydrophobic force, forming a membraneless oily droplet structure in aqueous cytosol, acting as the primary core for SG. Later, the solid aggregates or LLPS-droplet grows with the joining of additional mRNPs to form small SGs. Herein, the difference for the two nucleated models is that for the core first model, it experiences an additional transition from a solid aggregate to a liquid-like small SG, and very likely this is also a result of LLPS. Finally, in both models, the small SGs will merge together and form a stable core-shell structured SG in a microtubule dependent way.

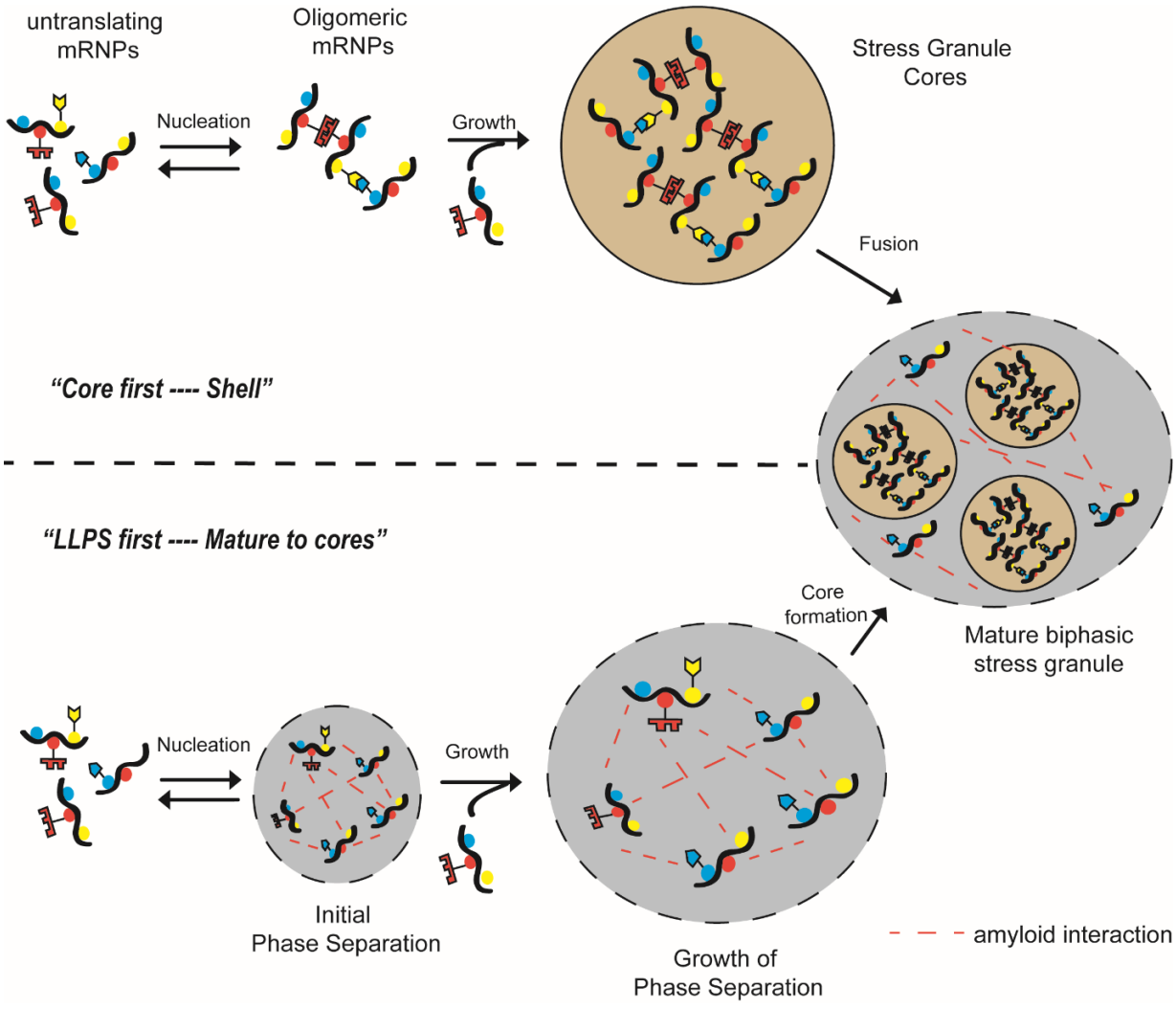

Figure 8, two different models for SG formation

Both models show two phases for SG formation: nucleation & maturation (or growth). In the Core first model, specific mRNPs aggregate together due to some tight interactions, like the specific interaction between protein-protein, forming the condensed cores. Later the cores are fused with other SG components, a process driven by LLPS or/and cytoskeleton transporting, leading to the mature of a biphasic SG. While in the LLPS first model,

mRNPs are associated together due to hydrophobic forces, forming an Oil-Like droplet by LLPS. Addition of more mRNPs will increase the droplet size. And inside the droplet, the SG core will be generated. Figure is modified from Ref. (Protter and Parker, 2016)

Although SG contents vary a lot in a stress-specific and cell-specific manner, several proteins, including HDAC6, are identified as the hallmark. For example, G3BP1 (Ras GTPase-activating protein-binding protein 1), a DNA unwinding enzyme that acts on DNA/DNA, DNA/RNA, or RNA/RNA duplexes, is important for SG formation under oxidative stress (e.g sodium arsenite-induced) (Solomon et al., 2007), while in yeast, Gtr1, Rps1b, and Hgh1 promote SG formation during glucose starvation (Yang et al., 2014). Our group was the first to show that HDAC6 is a critical component of SG and co-localized with G3BP1 (Kwon et al., 2007). Deletion or inhibition of HDAC6 downregulates SG formation. How HDAC6 participates in SG formation is not clear. In 2018, we found that HDAC6 regulated SG maturation step through its catalytic activity (Saito et al., 2019a). An ATP-dependent RNA helicase DDX3X is identified as a novel substrate of HDAC6, and coincidently, it is reported as a core component of SG in oxidative stress (Markmiller et al., 2018; Valentin-Vega et al., 2016). Multiple lysine residues at DDX3X N-terminal IDR region (**i**ntrinsically **d**isordered **r**egion, which refers to an unstructured fragment within a well-structured protein) can be deacetylated by HDAC6. After deacetylation, the interactome of DDX3X differs from the acetylated state. Deacetylation changes DDX3X IDR region's physical properties and enhances its interaction with other protein IDRs. And the interaction between different IDRs leads to LLPS of SGs (Lin et al., 2015). *In vitro* experiment showed that in comparison to acetylated DDX3X, deacetylated DDX3X is more favorable for oily droplet formation. And *in vivo*, the acetylation dead mutant of DDX3X promotes SG formation. Intrudingly, by analyzing the SG number (reflecting the nucleation) and the volume (referring to the maturation), it was found that upregulating DDX3X acetylation by HDAC6 specific inhibitors reduced the size of SGs (maturation) in the cytosol but not their number (nucleation). Therefore, we concluded that the activity of HDAC6 deacetylase domain modulates SG maturation phase by controlling the turnover of RNP's IDR acetylation state, which is associated with LLPS (Figure 9). A remaining question is whether HDAC6 ZnF domain is also involved in SG pathway. In the Result section, I will show that ZnF impacts the nucleation, but not the maturation. These data reveal the diverse role of HDAC6 in SG pathway.

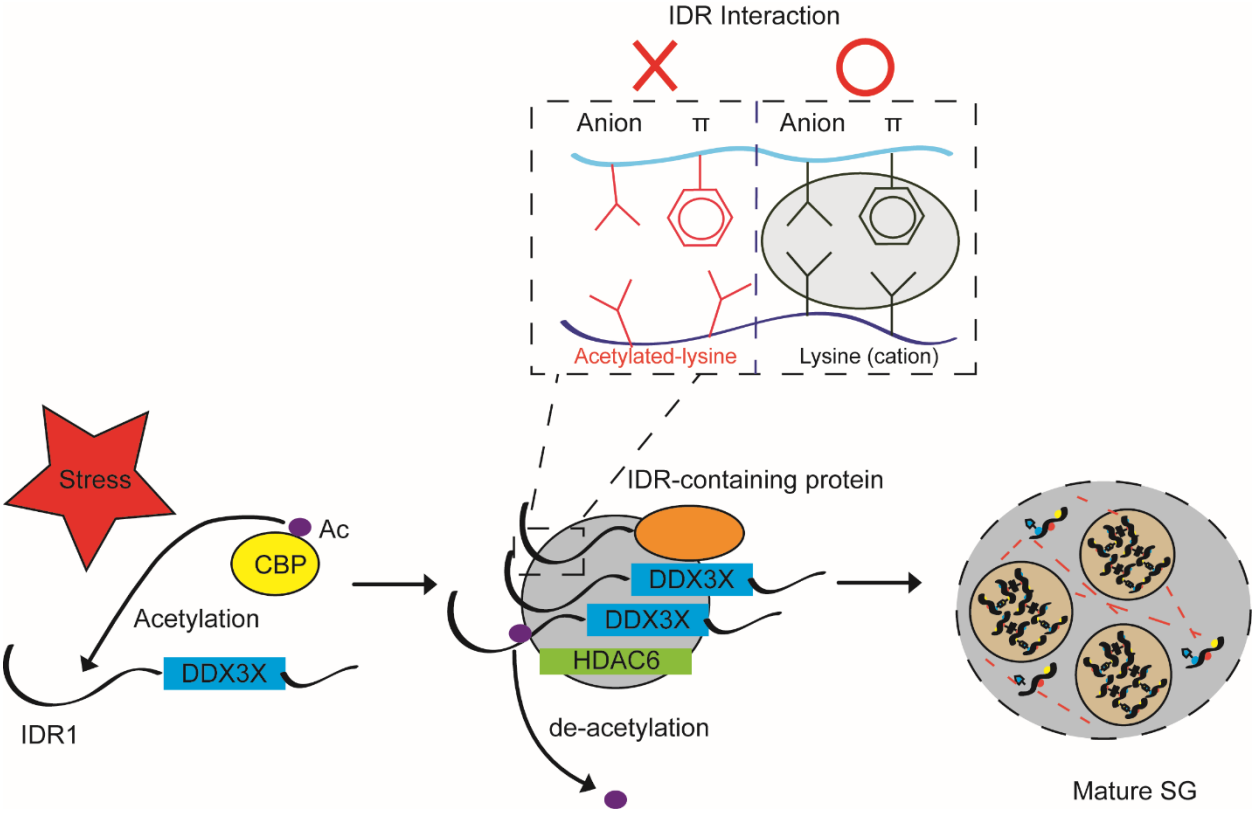

Figure 9, HDAC6 affects the SG maturation by deacetylated DDX3X's IDR

Under stress conditions, IDR of DDX3X will be firstly acetylated by CBP (**C**REB-**b**inding **p**rotein). This may help the nucleation of SG. In the protein aggregates, HDAC6 deacetylates IDR, enhancing the IDR-IDR interaction by changing the electrostatic of lysine residue. This promotes the LLPS-linked maturation of SG. Figure is taken from (Saito et al., 2019a)

Similar to aggresome, SGs are disease-related granules that have been involved in viral infection, neurodegenerative disease, and cancer therapy. During viral infection, different viruses have different relations with SG. Hepatitis C virus (HCV) hijacks SG components to suppress SG formation (Ariumi et al., 2011). And Poliovirus also inhibits SG formation via a different mechanism in which the viral 3C protease cleaves the SG core component G3BP1 (White et al., 2007). IAV inhibits SG by using its NS1 protein to blocks eIF2α phosphorylation (Khaperskyy et al., 2012). In contrast, Respiratory syncytial virus (RSV) induces SG formation to facilitate viral replication (Lindquist et al., 2010). Next, SGs have been proposed to play a pro-tumor role in cancer. In colorectal cancer, traditional therapy with Bortezomib induces SG formation, which enhances tumor cell resistance to drug-induced apoptosis (Fournier et al., 2010). While in breast cancer, SG-associated protein, G3BP2, initiates breast tumors directly (Gupta et al., 2017). Neurodegenerative disease is also closely connected to SG. Although the relationship between pathological inclusions that contain SG markers and actual functional SGs has yet to be rigorously tested, it is believed that SG, as a dynamic granule, will turn

into a stable inclusion body under persistent stress, and some pathological proteins, for example, TDP-43, will be enriched in this stable granule. The aggregated TDP-43 then is phosphorylated at serine residues 409 and 410, which is the hallmark observed in ALS and frontotemporal dementia (FTD) diseases (Reviewed in (Wolozin and Ivanov, 2019)). Therefore, inhibition of SG formation is hypothesized to be a benefit for multiple diseases to improve patient's behavior.

3, HDAC6 & Diseases

In past decades, HDAC6 has been targeted by pharmaceutical companies. Categories of HDAC6 specific inhibitors have been developed, e.g. Tubacin, Tubastatin among others, and they have been applied in basic research for years. Extended application in the clinic has been explored with newly synthesized inhibitors, like Ricolinostat (ACY-1215), which has shown the potential to accelerate multiple myeloma cell death by co-administration with carfilzomib (proteasome inhibitor) in clinical trials (Mishima et al., 2015). The possible mechanism for HDAC6 interfering with tumor progression is that HDAC6 promotes tumor formation and oncogenic transformation (Lee et al., 2008). After deleting HDAC6, MEF cells are more resistant to oncogenic Ras and ErbB2-dependent transformation. Another application of ACY-1215 is in breast cancer. Data *in vitro* and *in vivo* show that inflammatory breast cancer (IBC) is sensitive to HDAC6 inhibition. The mechanism is not clear, but an interesting observation is in IBC cells, HDAC6 activity is significantly higher than non-IBC cells (Putcha et al., 2015).

Unlike the cases of targeting HDAC6 catalytic domain by small molecule to interfere with cancers, clinical studies on HDAC6 ZnF domain imply a deep relation to neurodegenerative diseases. For example, its ability to be coupled with misfolded protein leads to the co-localization of HDAC6 and α-synuclein in Lewy body, a typical aggregate (termed as abnormal aggresome) identified in the Parkinson's dementia patients brain (Kawaguchi et al., 2003) (Figure 10). However, due to the limited understanding of different neurodegenerative diseases, HDAC6 seems to have various roles in different diseases. In Alzheimer's disease (AD), HDAC6 is over-expressed. Its protein level is increased by 52% in AD cortex and by 91% in AD hippocampus comparing with young normal brains (Simoes-Pires et al., 2013). Over-expressed HDAC6 interacts with Tau through its ZnF domain. This interaction inhibits HDAC6 deacetylase activity, further leading to the hyper-acetylation of microtubule and phosphorylation of Tau. Importantly, phosphorylation of Tau is a hallmark for Alzheimer. If a chemical or small peptide can be developed to target HDAC6-tau interaction, it might be able to improve the Alzheimer patient's behavior. In opposite, HDAC6 turns out to be protective in Parkinson disease (PD). It helps the aggregation of α-synuclein protein in cytosol through ZnF-Ub binding and further the clearance of those aggregates by autophagy pathway. Knock-down or inhibition of HDAC6 leads to the abnormal accumulation of α-synuclein in nucleus, result in increased cell death (Simoes-Pires et al.,

2013; Su et al., 2011). Therefore, we should be very careful about interfering with the aggregation of α-synuclein by targeting HDAC6 ZnF domain. Currently, none of the chemicals which target α-synuclein have survived from the clinical test (Dehay et al., 2015). Besides, HDAC6 is also implicated in other neurodegenerative diseases, including Frontotemporal lobar degeneration (FTLD) and Huntington disease (HD). Meanwhile, by interfering with the ZnF-Ub interaction, we can inhibit the formation of the NLRP3 inflammasome, which plays important role in immune surveillance of infections and danger by activating caspase-1, leading to cytokine maturation and pyroptosis (Magupalli et al., 2020). The causality between HDAC6 and these diseases is currently under investigation, but what we can be confident about is by targeting HDAC6 ZnF, it is possible to manipulate several severe aging-related neurodegenerative diseases.

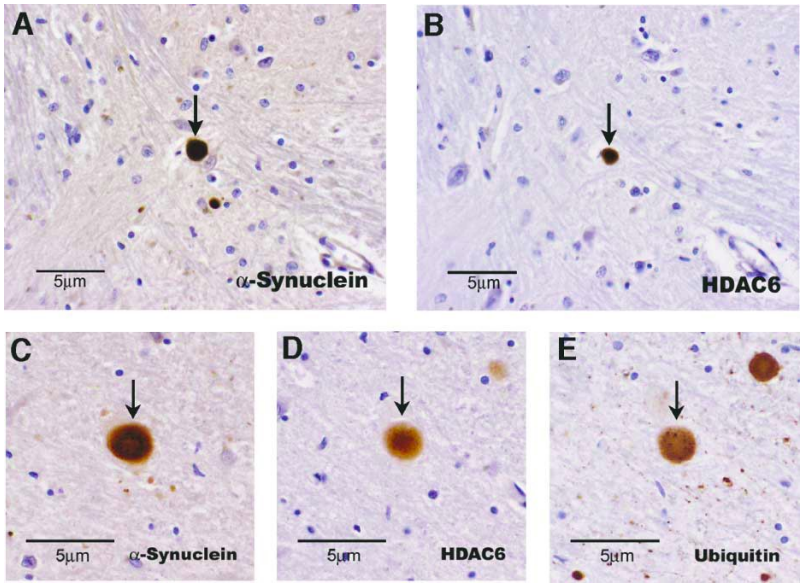

Figure 10, HDAC6 is enriched in the Lewy bodies of Parkinson Disease (figure is taken from (Kawaguchi et al., 2003).

Series of adjacent sections of neocortical Lewy bodies in Parkinson's disease brain (A and B, arrows) and brainstem Lewy bodies in brain sections from patients suffering from dementia with Lewy bodies (C–E, arrows) are immune-stained with antibodies for HDAC6, Ub protein conjugates, and α-synuclein as indicated.

4, HDAC6 & virus

Not limited to cancer and neurodegenerative diseases, HDAC6 is involved in viral infection as well. Our group has shown that by in MEF cells lacking HDAC6, we can downregulate influenza A virus (IAV) infection (Banerjee et al., 2014a). However, the conclusion that HDAC6 is only pro-viral would be arbitrary. A similar HDAC6-dilemma shown in neurodegenerative diseases exists likewise here. The

first observed virus that is regulated by HDAC6 is the efficient human immunodeficiency virus (HIV)-1. The binding of HIV-1 protein, gp-120, to CD4+ permissive cells inhibited HDAC6, leading to the hyper-acetylation of the microtubule. Rescue with overexpression of HDAC6 strongly inhibited HIV-1 infection (Valenzuela-Fernandez et al., 2005). More studies on HIV-1 showed that Tubacin, a specific HDAC6 inhibitor, will increase the susceptibility of uninfected CD4+ cells (Lucera et al., 2014). Similarly, the Rho GTPase-mediated up-regulation of microtubule acetylation was observed in Influenza A virus (IAV) infected epithelial cells (Husain and Harrod, 2011). Meanwhile, a recent publication argued that HDAC6 binds to and deacetylates IAV viral protein – PA, thereby promoting its degradation, and restricting IAV replication (Chen et al., 2019). Inhibiting HDAC6 catalytic domain seems pro-virus action, that is, HDAC6 catalytic domain counteracts viral infection (Figure 11). However, exceptions have been reported as well. For example, during hepatitis C virus (HCV) infection, if HDAC6 catalytic domain is inhibited with another specific inhibitor – tubastatin A (Tub A), the viral RNA concentration was reduced in a hepatocyte cell line. The proliferation of HCV is suppressed due to the acetylation of microtubules (Kozlov et al., 2014). Despite these exceptions, the HDAC6 catalytic domains appear to be generally anti-viral. And the mechanism is mainly based on its regulation on microtubule acetylation, further affecting viral post-entry steps, like trafficking or replication (Husain and Cheung, 2014). Another pathway of the catalytic domain regulating viral infection is through RIG-I, short for **R**etinoic acid **I**nducible **G**ene-**I**. It is a pathogen receptor that initiates innate immune responses against many RNA virus infections by controlling the type-1 interferon (IFN1) response. Inhibition of HDAC6 resulted in the deactivated state of RIG-I, which is acetylated and unable to recognize viral RNA, leading to the shut-down of the innate immune response and in turns favors viral infection (Choi et al., 2016; Liu et al., 2016). Inhibiting HDAC6 catalytic domain has already been used in clinical to promote the Oncolytic viral (OV) therapy, which utilizes genetically engineered tumor-targeting viruses, in glioma (Nakashima et al., 2015), enhancing the therapeutic virus replication as well as the translocation to the nucleus.

Similar to the study on HDAC6 in other fields, the mainstream of the HDAC6-virus field focus on its deacetylase activity. Limited investigations deal with the relation between HDAC6 ZnF domain and virus. Together with collaborators, we showed that a single mutation on ZnF domain, which displaces Ub from ZnF, reduces IAV infection by interrupting virus uncoating step (Banerjee et al., 2014a). The data indicate that the interaction between ZnF and Ub plays a pro-viral role (Figure 11). With immunoprecipitation, we propose that both dynein/microtubule and myosin/actin-mediated cytoskeleton systems are involved in IAV uncoating, but the molecular cascade and network organization are not clear.

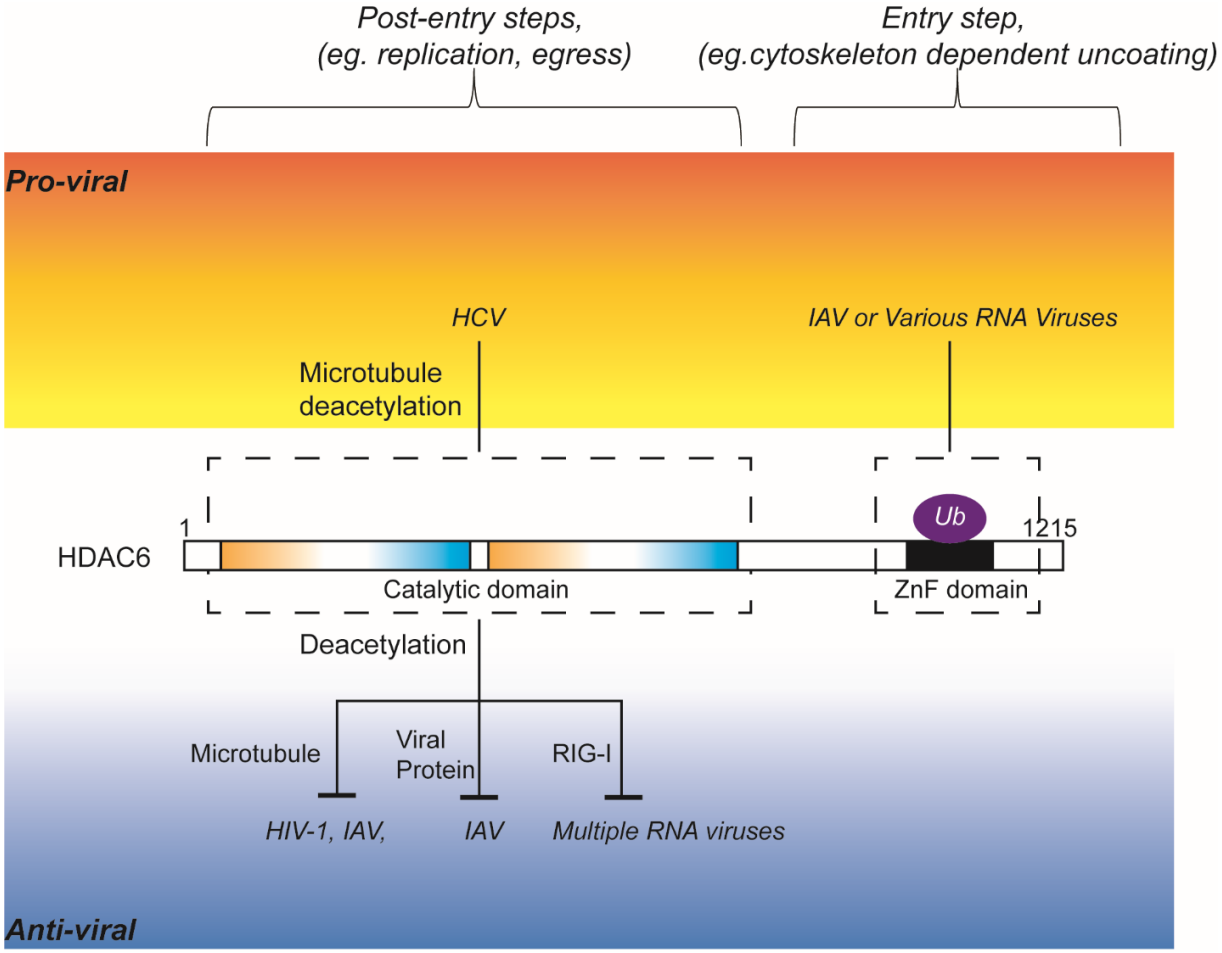

Figure 11, diverse roles of HDAC6 in viral infection

Taken together, we know HDAC6 is deeply involved in viral infection, with both anti-viral and pro-viral character (Figure 11). For instance, in IAV case, the two structured motifs, catalytic domain and ZnF domain, play opposite roles at different stages during the IAV life cycle. In the following part, I will focus on Influenza A virus.

1) Influenza A Virus (IAV) structure

IAV is a single strand, negative sense and segmented RNA virus. The sub-strains are named after the viral protein – hemagglutinin (H) and neuraminidase (N). H varies from 1 to 18, and N goes up to 11 (Tong et al., 2013). All the strains can be isolated from wild birds, and occasionally, the virus can be transmitted to a human, causing the avian flu. In 1918, the influenza pandemic led to 50 to 100 million deaths. The culprit was later identified as the strain H1N1.

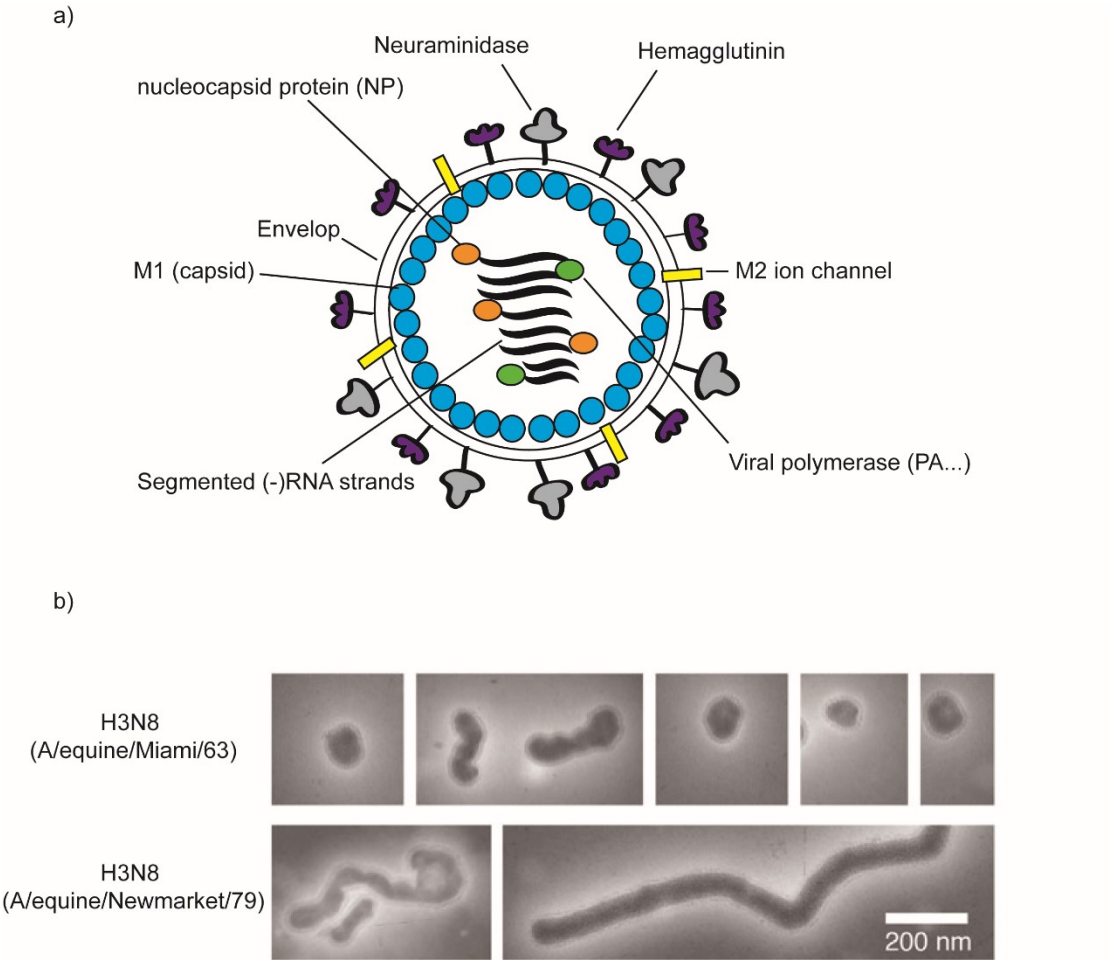

Figure 12, structure and shape of Influenza A virus

a) Scheme showing the organization of a typical IAV (H1N1). b) Example of the negative stained transmission electron microscopy (TEM) pictures for two different IAV H3N8 strains. Miami/63 is a non-filamentous virion, in contrast Nkt/79 exists as filaments. Figure is taken from Ref. (Elton et al., 2013)

Many IAV strains virions are spherical (Figure 12b top). Nevertheless, some exist in filamentous form as well, which is suggested to facilitate the spread of viruses *in vivo* (Badham and Rossman, 2016) (Figure 12b bottom). As a sphere, the diameter is around 100 nm, and the filamentous form extends to 300 nm in length. In nature, besides IAV, other viruses, like Ebola and many plant viruses (TMV …), can also adopt a filamentous form.

The influenza virion is an enveloped particle, protected by a lipid bilayer structure that is derived from the host plasma membrane (Figure 12a). At the surface of envelope, there are glycoprotein spikes of the hemagglutinin and neuraminidase. These two are recognized and processed by host cells as antigen.

The inner side of the lipid membrane consists of Matrix protein 1 (M1). It forms the shell, or capsid of virion, interacting with both the outside envelop and inside viral genome via NP (Hilsch et al., 2014). Another matrix protein, M2, is a pH-regulated proton ion channel which traverses the envelope. Low pH activates the M2 channel, leading to the weakening of electrostatic interactions between M1 and viral ribonucleoprotein complex, which consists of viral RNA segments together with the nucleoprotein (NP) and heterotrimeric RNA-dependent RNA polymerase (PB1, PB2, and PA). The basic structure above varies depending on the strain. For example, influenza B virus has four envelope proteins: HA, NA, NB, and BM2. influenza C virus has only one major surface glycoprotein - the hemagglutinin-esterase-fusion (HEF) protein, which corresponds functionally to the HA and NA of influenza A and B viruses, and one minor envelope protein - CM2 (Bouvier. and Palese., 2008).

2) IAV life cycle

The life cycle of IAV can be divided into 5 steps: 1) the entry to the host cell, including endocytosis, fusion and uncoating; 2) transport of vRNP into the host nucleus; 3) genome replication/transcription and translation; 4) vRNP transport from nucleus to cytoplasm; 5) viral particle assembly and budding (Watanabe et al., 2010) (Figure 13). The viral hemagglutinin (HA) is critical for starting the entry. It is recognized by the host receptor (mainly glycoprotein) through an α2,6-linkage (Matrosovich. et al., 2000). Following the receptor binding, the viral particle enters the cell by endocytosis and relocates to endosome later. The endosome, a membrane-bound cellular organelle, is a part of the endocytic recycling compartment (Vale-Costa and Amorim, 2016). It is classified into early endosome (EE) and late endosome (LE) in terms of time. The major difference between EE and LE is the pH. EE has an internal pH=6.5, while the LE is 5.5 (Hu et al., 2015). Many DNA and RNA viruses need to be trafficked from EE to LE, like Dengue. Due to the acidic environment, viral envelope is fused with the endosome membrane, then M2 ion channel is activated. The proton influx acidifies the interior of viral particle, leading to the disassociation of M1 and vRNP complex (Matsuoka et al., 2013). Later the M1 protein shell is disassembled by host proteins, so that the virus can release its vRNP components to the cytoplasm. This is called uncoating step. The relocation of vRNP to the nucleus is dependent on an active transporting machinery – the nuclear pore complex (NPC). Inside nucleus, viral genome replication and transcription are mainly dependent on viral proteins – PB1, PB2 and NP, while host cell translation machinery is responsible for the translation. Several host translation factors, for instance, eIF4A and eIF4E interacting with viral mRNA to produce viral protein (G.Katze et al., 1984). Newly synthesized vRNP together with matrix protein M1 and other envelop proteins are transported from nuclear to cytoplasm, further to the assembly/budding site that is closed to plasma membrane. During the transportation and budding, cytoskeleton system is believed to be involved. Interaction between

M1/NP and actin has been identified (RT et al., 1997). However, how the microtubule and its acetylation affect the virial protein transportation is not clear.

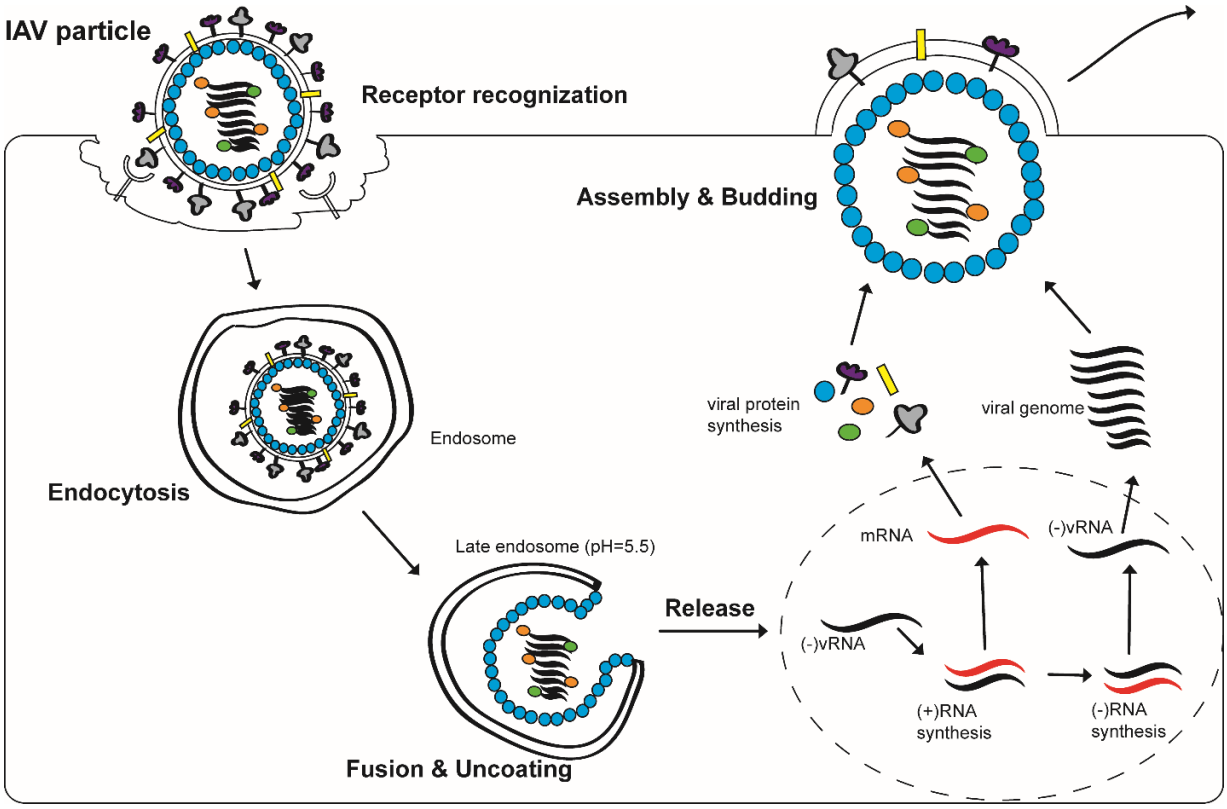

Figure 13, the life cycle of IAV

The IAV virion is recognized and processed (e.g. Endsome related uncoating) by host cells, meanwhile the virus takes advantage of the host machinery (e.g. Translation complex) to accomplish its amplification, resulting a geometric yield of the newly generated virus.

In the following parts, I discuss the early stage of IAV life cycle, especially the uncoating step, which is determined by both multiple host cellular components and viral proteins. Among them, HDAC6 is a newly confirmed but critical regulator.

3) IAV uncoating and HDAC6

As presented in the paper (Banerjee et al., 2014a), we found that after deleting HDAC6 or mutating its ZnF domain in MEF cells, IAV M1 protein is restricted in the virial particle and no longer diffused in cytosol (Figure 14a and 14c), meaning the uncoating step is blocked. And the explanation is connected to HDAC6 ZnF-Ub interaction: First, by imaging Ub with a specific antibody, which is against

ubiquitin's C-termini free peptide specifically, we learned that the interior of virus is filled with C-termini free Ub (Figure 14b). After the fusion and acidification in late endosome, virion opens its capsid and exposed the interior Ub, which recruits HDAC6. Collecting the IAV-infected cells at an early time-point when uncoating takes place (2.5 hrs post-infection), we identified the interactions between HDAC6 and viral & motor proteins, including M1, myosin 10 and dynein by Co-immunoprecipitation (CoIP) (Figure 14 d&e).

Considering that knock-down of myosin 10 and dynein by siRNA also downregulates IAV uncoating ratio, we proposed a model that during the uncoating step, HDAC6, together with viral protein like M1 and motor proteins (myosin 10 and dynein), form two complexes: viral protein/HDAC6/myosin 10 and viral protein/HDAC6/dynein. Myosin 10 moves on actin network which is less organized and extends in randomized directions, while dynein walks on microtubules that extend from MTOC site to plasma membrane. Due to these two filaments (actin and microtubule), viral particle will be torn apart, or "uncoated" and release the viral genome. Here, we found that 1) HDAC6's interaction with C-terminal free Ub, 2) HDAC6's association with dynein/microtubule and 3) Ub enrichment in particles (in aggresome they are ubiquitinated misfolded-protein aggregates, while in IAV, virion itself is an Ub-containing particle) are shared by aggresome pathway and IAV uncoating step. Therefore, we

hypothesize that during IAV infection, the virion will hijack the host cellular aggresome pathway to complete its uncoating process (Figure 15).

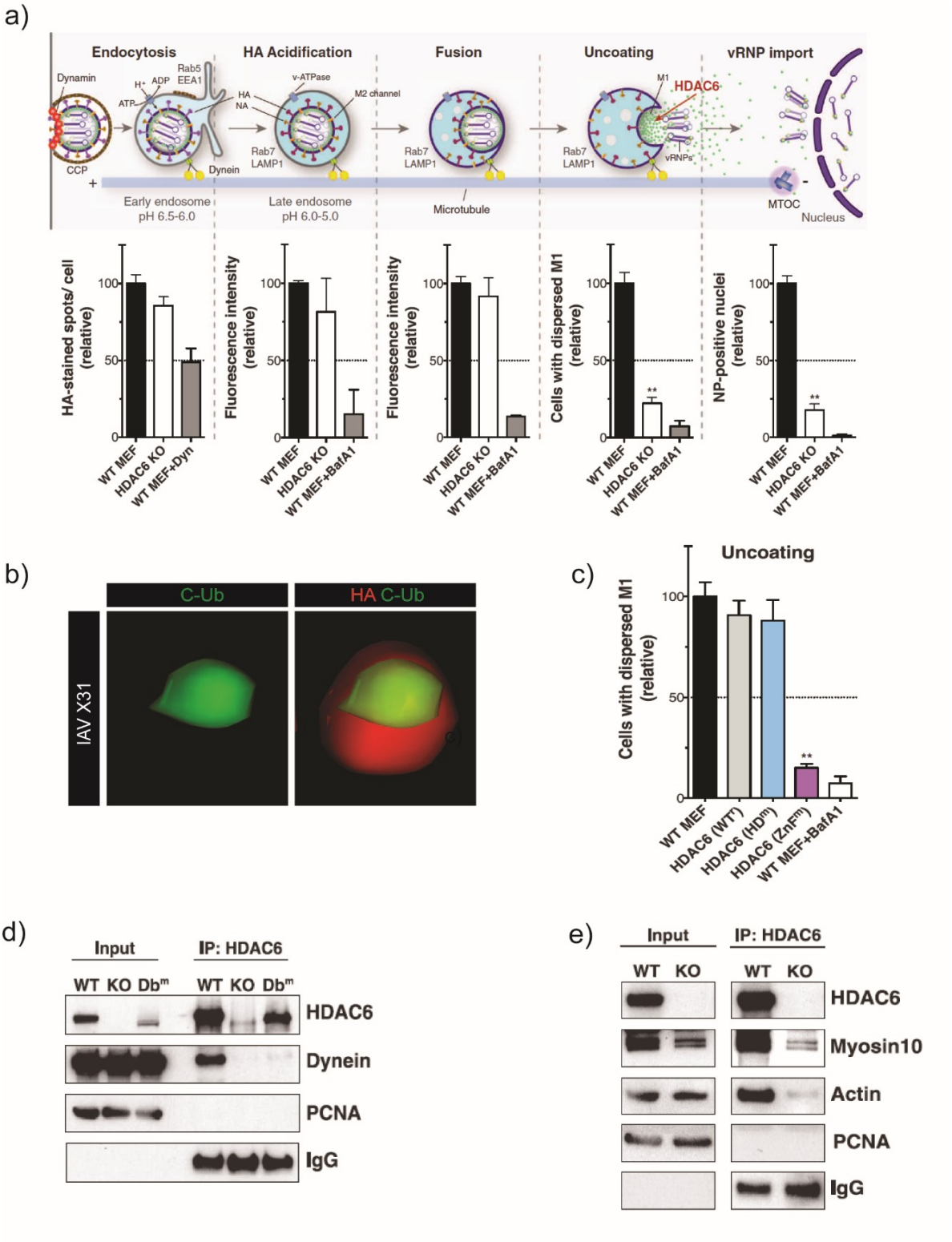

Figure 14, HDAC6 ZnF is responsible for IAV uncoating & HDAC6 interacts with motor proteins (figures are taken from (Banerjee et al., 2014a)

a) HDAC6 KO leads to a reduced infecting ratio at uncoating step; b) IAV particle is filled with C-termini free Ub (C-Ub, green); c) single mutation on HDAC6 ZnF domain (W1182A), which cannot bind to Ub, dramatically downregulates viral uncoating, assessed by M1 signal in the cytosol; d) & e) show that HDAC6 Co-IP with motor protein dynein and myosin 10 during IAV infection, respectively.

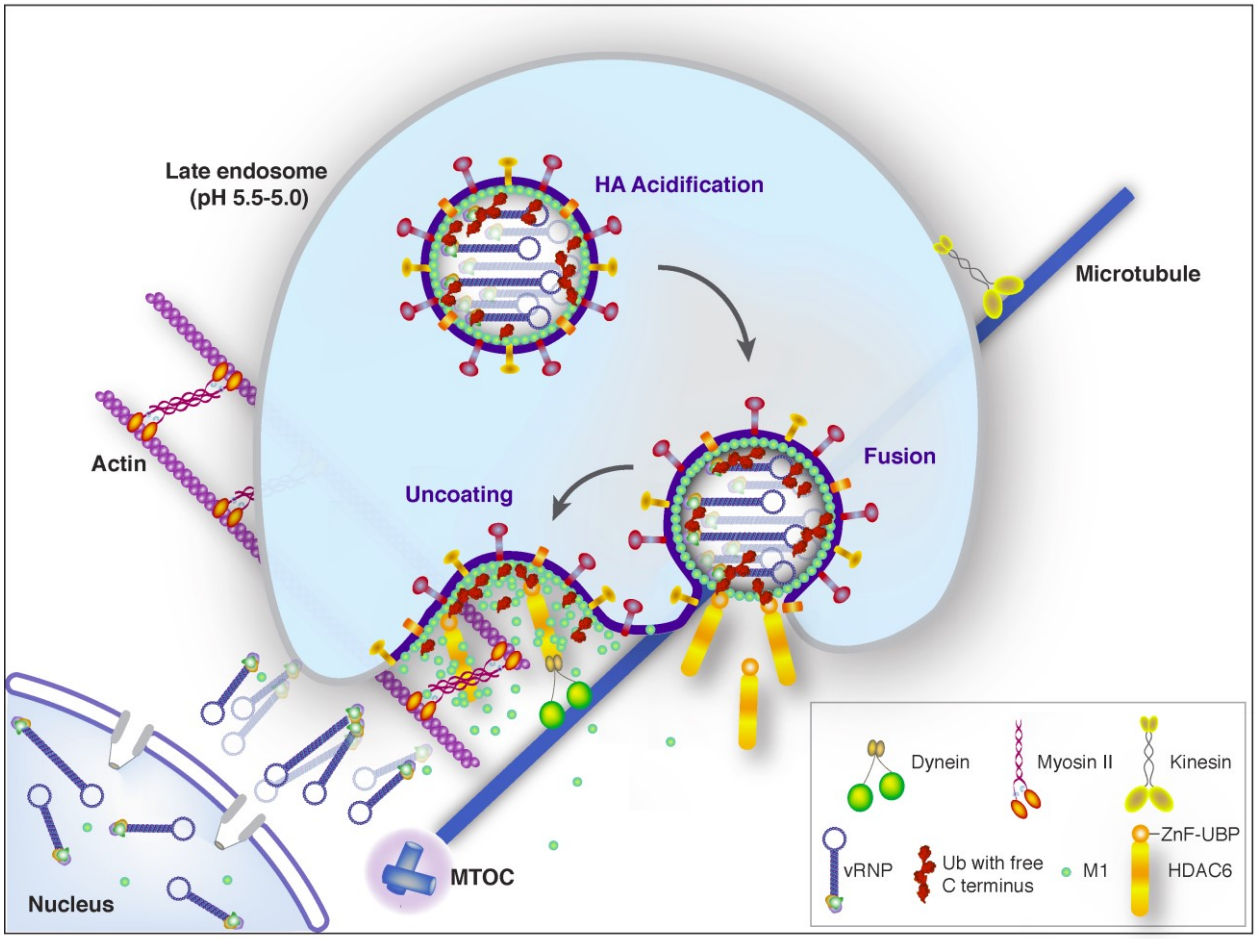

Figure 15, IAV uses aggresome machinery for uncoating

The model indicates that after processing by late endosome, IAV particle exposes its internal c-termini free Ub together with other viral proteins like M1 and NP. Through their interaction with HDAC6, the virion will be transported by two different cytoskeleton systems: dynein/microtubule and myosin 10/actin. The movement on these two filaments generates the breaking force for uncoating viral particle, releasing viral genome further to host cell nucleus.

Interactions between HDAC6 and motor proteins support this model, but more detail is required. Although the HDAC6 linker region between two catalytic domain (mentioned above) is the dynein binding site (Kawaguchi et al., 2003), still we have remained questions to answer that which domain is responsible for binding to Myosin 10 and how the two different cytoskeleton systems cooperate.

4) Similarity between aggresome and virus

To validate our proposed model (Figure 15), we explored the interaction between each component in a virus-infection mimic condition -- inducing aggresome formation in cells. The concept that aggresome formation is similar to virus infection has been proposed for years. The first evidence was from African Swine Fever Virus (ASFV). Colin Heath and his colleagues show that viral factories or viral inclusions, which are formed at MTOC site for viral replication and assembly, are surrounded by an aggresome marker, vimentin (Figure 16a). In addition, the chaperone HSP70, which is enriched at aggresomes and helps remodel misfolded proteins, is co-localized with ASFV structural protein p34 (Heath et al., 2001). Similar data have been obtained from Herpes simplex virus (HSV), an enveloped DNA virus. After infection, at MTOC site, an aggresome-like structure forms, enriched with viral tegument proteins and newly synthesized nucleocapsid proteins, and positive for aggresome markers HSP40 and HSP70 as well (Nozawa et al., 2004). Human Papilloma Virus (HPV), a Papillomavirus with double-strand DNA, is also assembled into an aggresome-like structure. HPV protein E1^E4 is co-localized with HDAC6 and HSP40 at aggresome site (Kajitani et al., 2013) (Figure 16b), so does the Bombyx mori nucleopolyhedrovirus (BmNPV) (Guo et al., 2015).

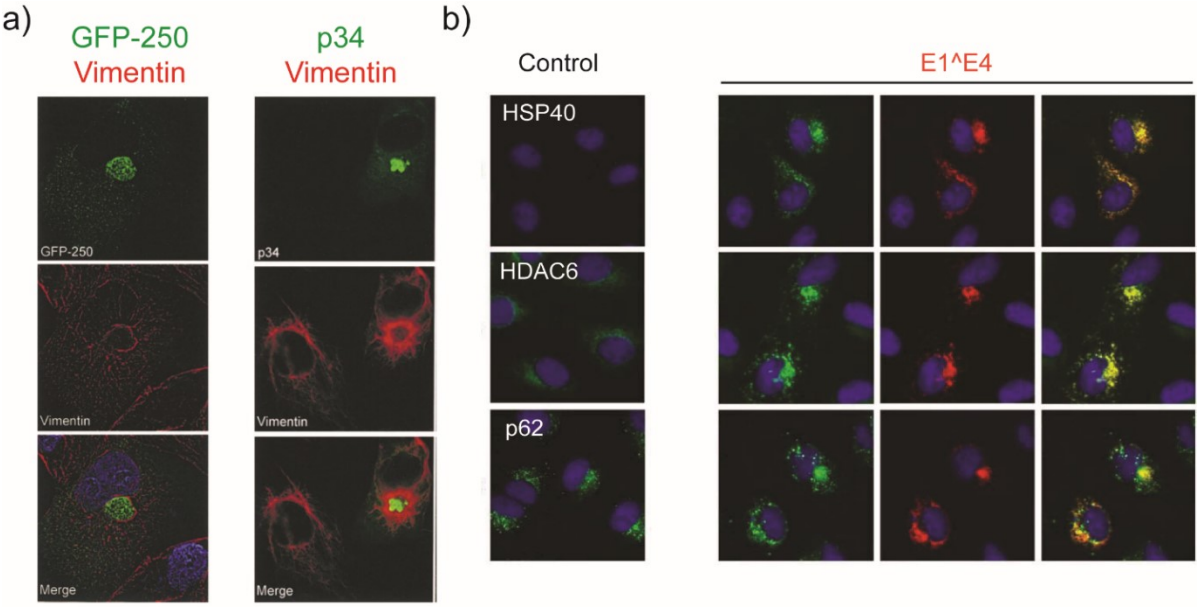

Figure 16, virus infection leads to aggresome-like structure formation

Two viruses, a) ASFV and b) HPV18 (indicated by viral protein E1^E4, red), both co-localize with aggresome components – GFP-250, vimentin and HDAC6 as well as other aggresome components at the perinuclear site. Figures were taken from (Heath et al., 2001) and (Kajitani et al., 2013) respectively. GFP-250 is an exogenous protein accumulated at aggresome. p34 and p62 are viral protein for ASFV and HPV18 respectively. HDAC6 and HSP40 in b) are colored green.

The above evidence shows that several viruses form at the MTOC assembly structures, called viral inclusion or viral factories that have similarities with the aggresome and are enriched with aggresome markers such as. HDAC6, Vimentin and HSPs. The mechanism underneath is not clear though. We suggest that infected viral particle is recognized as protein aggregates by host cell due to their similarity in morphology and components. Many viruses particles have a similar size (60-100 nm) as protein aggregates (Wileman, 2007). In addition, IAV particles are filled with C-termini free Ub, and this is observed in protein aggregates as well. As discussed, the generation of C-termini free Ub chains in aggresome pathway is due to DUBs like ataxin-3 and Poh1. In the case of Adenovirus, knock-down or inhibition of USP7, a K48 specific deubiquitinase, downregulates infection (Ching et al., 2013). Next, formation of aggresome-like viral inclusions needs the entire microtubules system, including dynein (Araujo et al., 2005; Arnaud et al., 2007). In plant, by fusing GFP to viral protein MP17 from Tobacco mosaic virus MP30 (TMV MP30), researchers found that after destroying microtubule with colchicine, the aggresome like structure is not formed. Interestingly, in this study, they also observed that actin filaments are involved in viral protein MP17's relocation (Vogel et al., 2007). Last but not least, HDAC6 enzymatic activity, which is dispensable for aggresome formation, is not needed for the ASFV viral factory formation as well. After deleting protein BAG3 (a chaperone for HSP70) and inhibit HDAC6 catalytic activity by Tubacin, individually or spontaneously, viral factory formation was not disturbed (Munoz-Moreno et al., 2015). Since the same machinery is shared in both pathways, it is reasonable to use aggresome inducing conditions as an alternative for viral infection to study the viral uncoating (Figure 17). However, it is clear that this assumption cannot be applied for all the viruses. We currently limited its application in IAV infection, and the aim is merely to figure out the HDAC6 related interaction that are shared with both pathway.

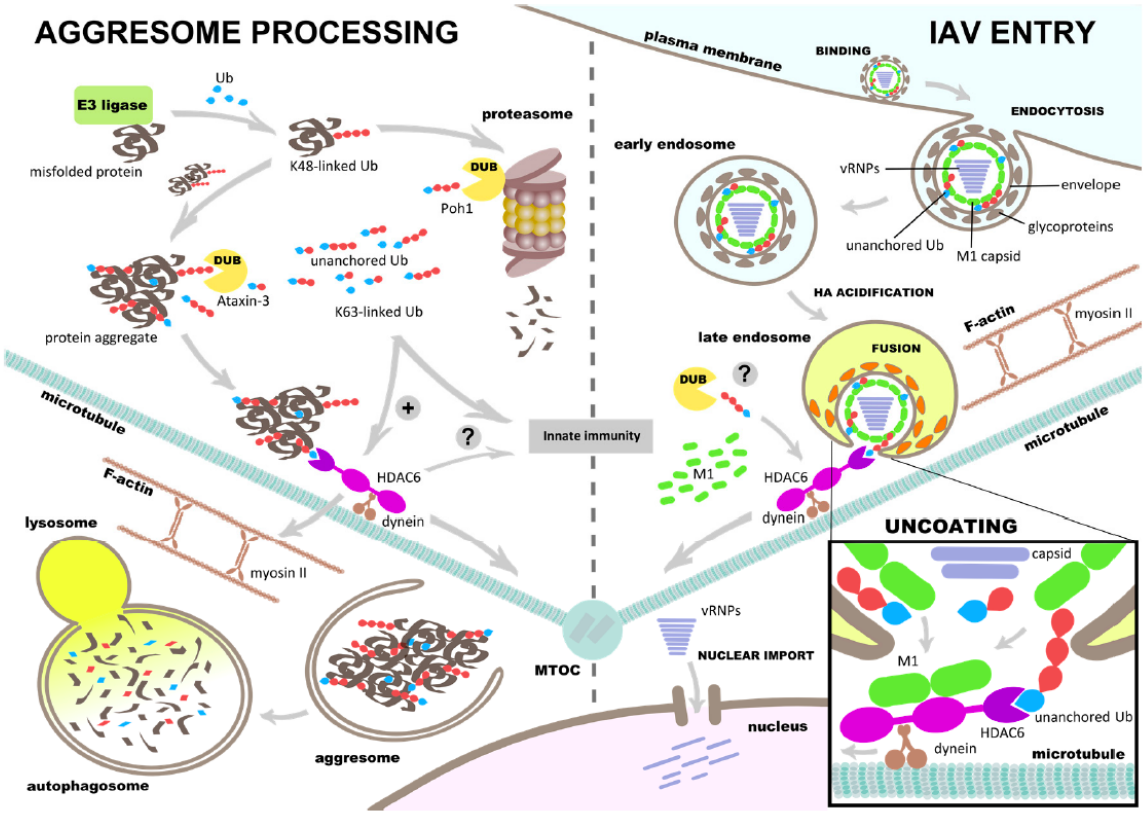

Figure 17, similarities between aggresome processing pathway & IAV entry (Figure was taken from (Rudnicka and Yamauchi, 2016))

Comparing IAV entry steps (right) to aggresome processing pathway (left), we find that they share a lot of proteins/complexes: 1) they both need unanchored Ub which is the product of specific DUBs; 2) they are transported by HDAC6/dynein/microtubule system; 3) F-actin and myosin 10 are involved in certain steps (need more investigation); 4) they are both relocated to the MTOC site. Therefore, we can use the aggresome processing pathway to mimic the IAV infection, at least the entry steps, studying the IAV uncoating machinery.

5, Targeting HDAC6 ZnF-Ub interaction

1) Targeting Protein-protein interactions (PPIs)

As the ZnF-Ub interaction is critical in both aggresome formation and IAV uncoating pathways, we would like to target this interaction with either chemicals or synthetic proteins. However, it has been a difficult and challenging task in past decades to target protein-protein interactions (PPIs). The main difficulties are: (1) large PPI interface areas, (2) lack of deep pockets, (3) the presence of noncontiguous binding sites, and (4) a general lack of natural ligands (Ivanov et al., 2013). Although there are promising natural products (NPs) acting on PPI such as rapamycin for mTOR, it is still rare and unexpected for most proteins. Therefore, researchers have developed several synthetic approaches to screen out the small molecules, peptides or proteins which act as modulator on PPIs. Approaches to

generate these bio-functional materials can be categorized into: Phenotypic screens, Target-based screens, Structure-based design, Fragment-based design and Protein Domain Mimics (Modell et al., 2016). The most popular one is the target-based screen, which refers to the use of a chemical library and screen out a modulator against the target of interest in a high-throughput way. It is simple but efficient. For example, Nutlins, which are small-molecule ligands of Mdm2 and potent inhibitors for p53–Mdm2 interaction, is discovered from a target-based high-throughput screen (Azzarito et al., 2013; Modell et al., 2016).

Recent studies from Canada have identified several small molecules against HDAC6 ZnF, aiming to interrupt Ub recruiting (Ferreira de Freitas et al., 2018; Harding et al., 2017). The crystal structures show that compound 31 fits into the Ub binding pocket (Figure 18a) (PDB: 3GV4), and it is capable of displacing Ub C-terminal peptide (–R-L-R-G-G) from ZnF *in vitro*. Unfortunately, it does not tell whether compound 31 functions properly *in vivo*, meanwhile, its ability to replace the entire Ub is not verified. Last, the off-target effect is not clear. To solve all these problematic issues, we decide to choose the Designed Ankyrin Repeats Proteins (DARPins) as the tool to interfere with ZnF-Ub interaction.

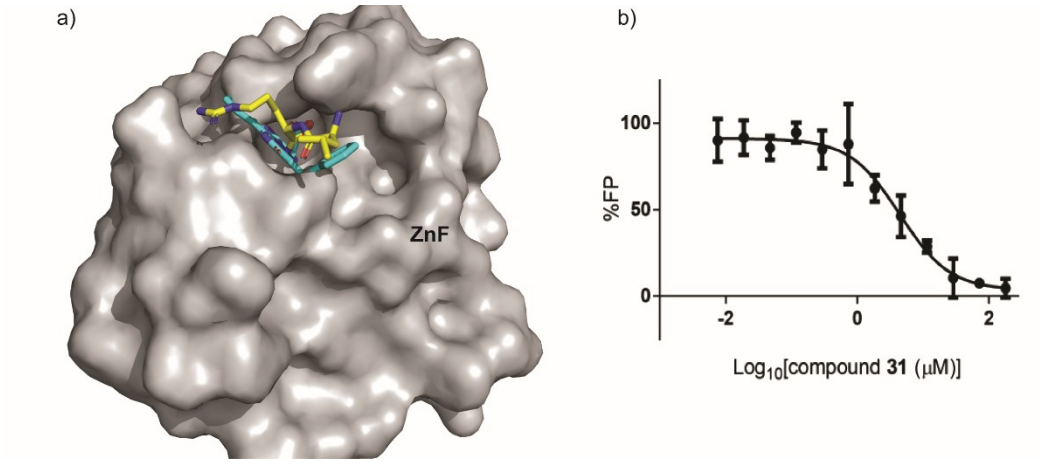

Figure 18, Compound 31 (colored cyan) from (Ferreira de Freitas et al., 2018) a) binds to the same pocket as Ub C-termini (colored yellow) do. HDAC6 ZnF (gray) is plotted by the surface. PDB: 3GV4 and PDB: 5WBN are aligned and overlapped. Both ZnF are plotted by its surface. b) FP (**F**luorescence **P**olarization) competition assay is done by using an increasing concentration of compound 31, a FITC-labeled RLRGG peptide (50 nM) and full-length HDAC6 (1 μM).

2) DARPin

DARPin (Designed Ankyrin Repeats Protein), which is derived from natural Ankyrin proteins (Figure 19a) (a family to attach integral membrane proteins to cytoskeletal elements like spectrin-actin) (Vann and Anthony, 2001), can recognize its target with high specificity and affinity that equals or superiors to the antibody (Plückthun, 2015). It consists of 4~6 ankyrin repeats, defined as a 33 amino acids motif

containing two following anti-parallel α-Helix separated by a β loop (Figure 19b). Among them, the variable residues on the Loop region (Figure 19b and 19c) form the interacting surface against the target, while α-Helix builds the consensus framework that is conserved and responsible for protein folding. After avoiding the residues Cys (to eliminate disulfide formation), Pro, and Gly (as some of the residues are located in a helix) in randomized residues on loop region, a huge DARPin designing library will be generated (Virnekäs et al., 1994). In terms of the screen method, the size of library can be estimated up to 10^{12} in ribosome display (Figure 19d) and 10^{10} in phage display (to select binders against targets on the surface of whole cells) (Siva et al., 2008). Using ribosome display, screened DARPins can bind targets with a disassociation constant (Kd) in pM range (Binz et al., 2004). Due to the rational design, DARPin has a smaller size (14~18 kDa) than antibody so that it can be rapidly purified from *E.Coli* system as monomer, avoiding aggregation. In contrast, the application of antibody is always limited by its size as well as the producing method and yield. Besides the high affinity, DARPin can be a conformation-sensitive binder. A typical example is from extracellular signal-regulated kinase (ERK). Researchers develop two DARPins against normal ERK as well as the phosphorylated ERK (p-ERK). Crystal structures show that these two DARPins bind to the same area of ERK, but because of conformation change in adjacent areas after phosphorylation, they have different binding surface, and no cross-reaction (Kummer et al., 2012).

Thanks to all the benefits, DARPin has great values in biomedical research. DARPin against p-ERK has been developed into a solvatochromic merocyanine dye to monitor ERK activation in living cells (Kummer et al., 2013). In clinical, an anti-VEGF DARPin (MP0112) has been applied in a Phase I/II, open-label, multicenter, and dose-escalation trial with diabetic macular edema (DME) patients (Campochiaro et al., 2013). Pharma Company (Molecular Partners ®) now has several DARPins in clinical trials, showing a very promising future for the antibody-liked protein drug.

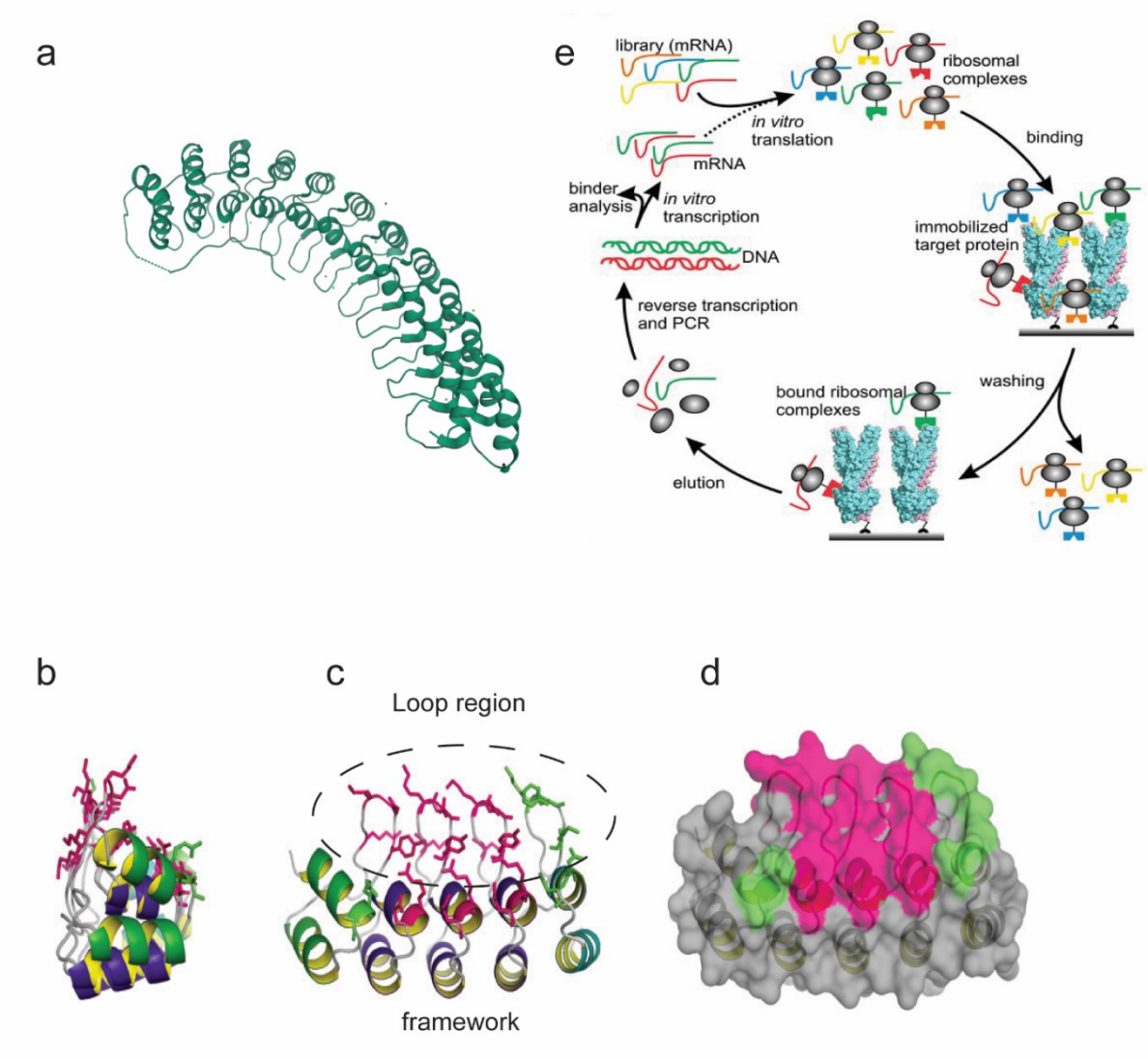

Figure 19, the structure of a typical DARPin and the ribosome display screen for DARPin

a) Structure of human Anykrin-R (PDB:1N11) with 12 ANK repeats; b) The side view of DARPin structure, and c) is the front view after a 90° turn from b). The residues on loop region shown as sticks indicate the randomized amino acids. Magenta refers to the internal ankryin repeats, while green shows N- and C-terminal repeat. d) DARPin surface. Figure b) to d) are taken from (Plückthun, 2015). e) The scheme for ribosome display to screen a binder/DARPin. Figure is taken from (Seeger et al., 2012).

3) Inducible expression system, degron and dTAG

Gain- or loss-function of a protein helps to understand its function in cells. Multiple methods are now applied to transiently or stably express or delete the protein of interest (POI). For example, to establish a stable cell line, retrovirus/lentivirus delivers either the DNA of POI for expressing the exogenous protein or siRNA/shRNA sequence for inhibiting endogenous protein expression to the genome. With the development of the crisper-cas9 technique, it is now possible to manipulate the POI transcription

by editing the genome in situ. For transient expression, transfecting a plasmid containing DNA of POI with a proper promoter will achieve an over-expression in 1~3 days. And transfecting efficiency varies according to cell line. HEK293T is easily transfected, while MEF cells are quite difficult. However, if we want to control the level of POI precisely, instead of transient expression, an inducible expression system should be introduced.

The most popular inducible expression system is Tetracycline Controlled Operator System. It is classified into 2 configurations: Tet-On, meaning adding tetracycline or doxycycline (a derivative of tetracycline) will turn on the transcription of POI; on opposite, Tet-off turns off the transcription. Both configurations depend on the Tn10-specified tetracycline-resistance operon from *E.coli*. Interplays between Tet-Operator (TetO), Tet-Repressor (TetR), and doxycycline (Dox) decide whether the downstream gene's transcription is on or off (Figure 20). With Tet-On/Off, we can easily modulate the expression of POI. However, it has some drawbacks: firstly, the "leaky" expression is severe. In Tet-On configuration, a background expression of POI is always observed; secondly, the switch is not real-time. It needs 2~3 days to change protein level after Dox addition. And due to this time lag, it is difficult to apply Tet system in a transient biological event, like virus uncoating, which only happens in 3 hours post-infection. A much faster and more real-time inducible system is needed.

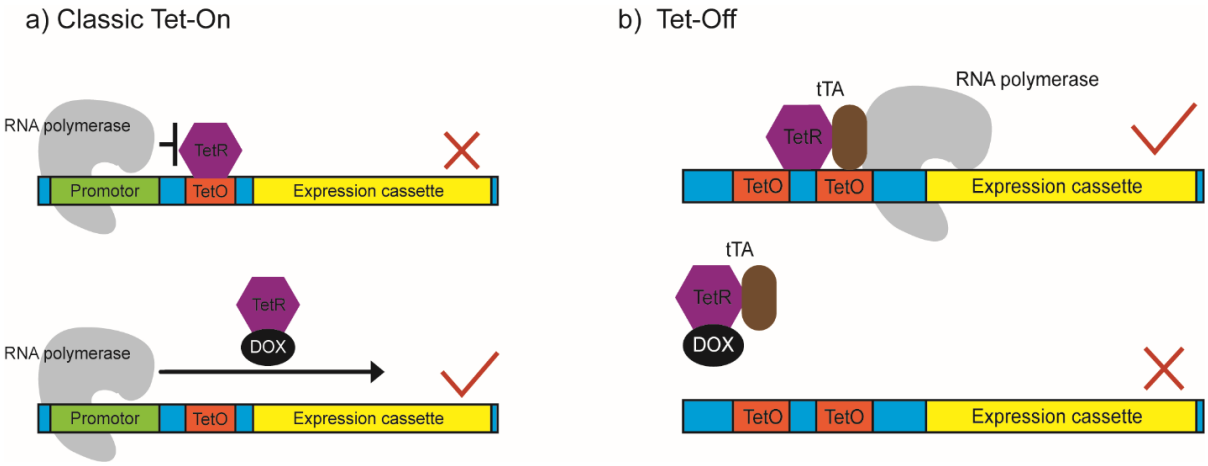

Figure 20, Schematic representations of two typical tetracycline-controled operator systems.

The traditional Tet-on a) needs an insertion of TetO sequence between the promotor and gene of POI. Due to the interaction between TetO and TetR, transcription machinery is stalled by TetR and cannot move to the downstream gene. Addition of Dox leads to the binding of Dox-TetR and later disassociation of TetR from TetO. This allows the transcription of POI. While in Tet-Off b), the TetR is firstly fused to the C-terminal domain of VP16 (**v**irion **p**rotein 16), an essential transcriptional activating domain from HSV (herpes simplex virus). The fused protein is called tetracycline-controlled transactivator (tTA). Thanks to the interaction between TetO (upstream of POI) and TetR, tTA will consistently function on the downstream gene, which encodes the POI, producing mRNA without Dox. In this case, adding Dox will displace tTA from TetO, resulting in the shut-down of transcription. *tTA: a fused protein from TetR and transcription activator(TA)*

To overcome the time lag, it is better to target protein directly. Thanks to the protein quality control system, it is possible to use the endogenous degradation pathway to control the protein level. Thus, the concept of degron, referring to the domain or tag that induces the instability of its fused protein has been put forward. In the majority, the degradation of chimeric protein is controlled by ligands. According to the pairing of degron and ligand, the conditional degrading systems can be divided as following (Figure 21):

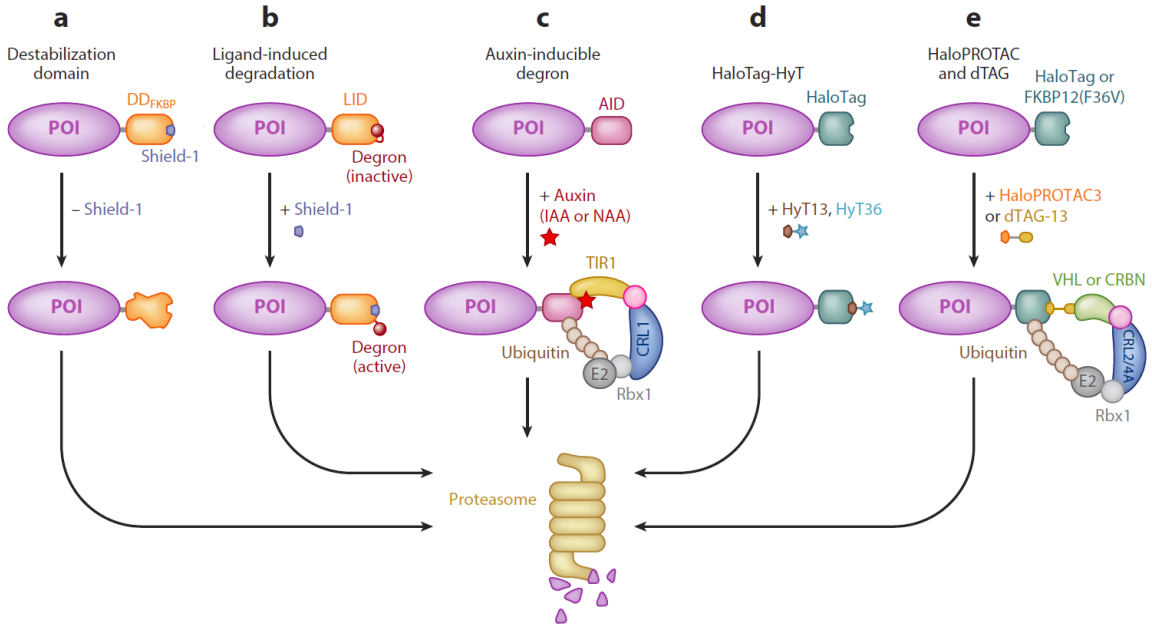

Figure 21, ligands-controlled degradation system.

a) A FKBP12 (FK506 binding protein) based destabilizing domain (DD) (Banaszynski et al., 2006) is fused to protein of interest (POI). The fusion protein is unstable and then degraded in few hours due to the DD domain, while adding ligand Shield-1, a derivative of rapamycin, stabilized POI. b) A different FKBP12 variant is called ligand-induced degradation domain (LID). Binding of Shield-1 leads to the conformational change, and the internal 19-aa degron peptide will be exposed, leading to the degradation of POI. c) In plant a unique degradation pathway is controlled by Auxin family plant hormones. An auxin binding domain or protein, like *Arabidopsis* IAA17, is an auxin-induced degradation degron (AID). Addition of auxin recruits E3 ligase complex (TIR1-CRL1) and results in the POI degradation. d) Halo-tag is a versatile tag that can be used for protein purification and imaging. It binds to a bifunctional molecule, like HyT13 or HyT36. However, the binding will change Halo-tag conformation, exposing its hydrophobic moiety, which mimics the partially denatured state of protein, thus engaging the cellular quality control machinery to induce proteasomal degradation (Neklesa et al., 2011). e) Besides, the HaloTag forms a covalent association with chemical HaloPROTAC3, which recruits the fusion protein to CRL2–VHL E3 Ub ligase for rapid ubiquitylation. Similarly, $FKBP12^{F36V}$ binds to chemical dTAG-13,

which brings the fusion protein to CRL4A–CRBN E3 Ub ligase. Figure and figure legends are adopted from (Natsume and Kanemaki, 2017)

Among these systems, dTAG (degradation tag) systems are firstly described in the research against the transcriptional coactivator BRD4, a protein critical for cancer cell growth and survival (Winter et al., 2015). A chemical, dBET1, bridges BET domains (in BRD2, 3&4) to an E3 Ub ligase (cereblon, CRBN), resulting in the ubiquitination of BET proteins and degradation. Application of E3-binding heterobifunctional chemicals has now been extended to FKBP12, ERRα, RIPK2 (Bondeson et al., 2015) and BRD9 (Remillard et al., 2017). Among them, an engineered variant - $FKBP12^{F36V}$ which is previously described by Ariad Pharmaceuticals is developed. It possesses a cavity (or 'hole') for the selective recognition by a 'bumped' synthetic $FKBP12^{F36V}$-directed ligand AP1867. Meanwhile, the structure of E3 Ub ligase CUL4–RBX1–DDB1–CRBN (known as $CRL4^{CRBN}$) shows a thalidomide binding pocket (Fischer et al., 2014), therefore a chemical –dTAG 13, which is derived from AP1867 and thalidomide, is bifunctional to bridge $FKBP12^{F36V}$ and $CRL4^{CRBN}$. Fusing $FKBP12^{F36V}$ to the POI leads to its ubiquitination and further degradation by the proteasome (Figure 22a). Experiments confirmed that $FKBP12^{F36V}$ fused HDAC1, Ezh2, MYC, $KRAS^{G12V}$ can be degraded under a low dosage (500 nM) dTAG-13 addition in 1~4 hours (Figure 22b). Thanks to the short response time, the dTAG-$FKBP^{F36V}$ system can adjust protein amount in nearly real-time.

a)

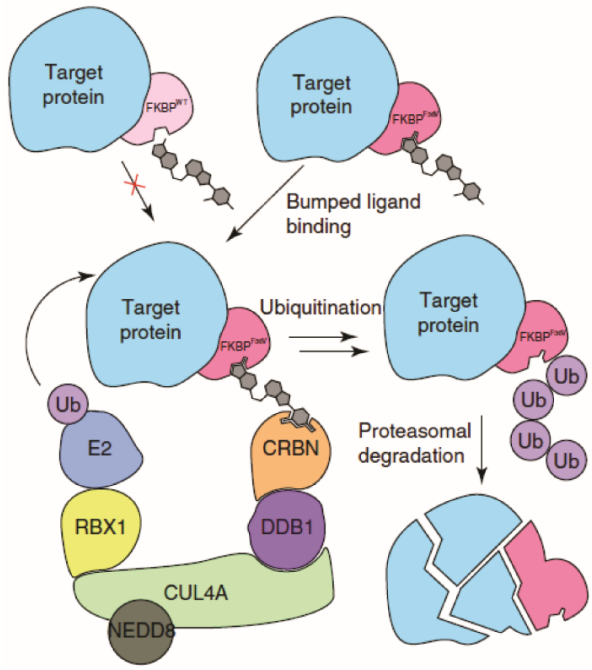

b)

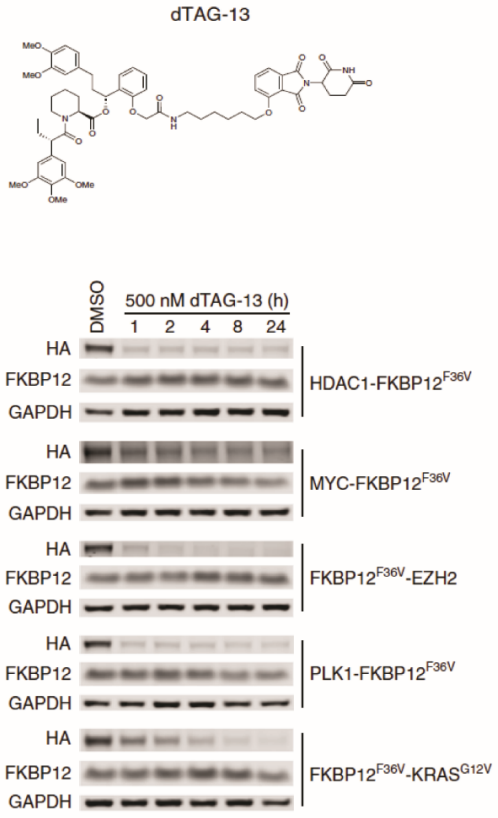

Figure 22, scheme for dTAG system and its potency and efficacy

a) Adding of dTAG-13 (Gray colored chemical) leads to the $FKBP^{F36V}$, not WT FKBP fused target protein degradation with the help of CRBN-CUL4A E3 ligase complex. b) Upper panel is the chemical structure of dTAG-13. And in the lower part, it shows that treatment with 500 nM dTAG-13 can efficiently degrade different fused proteins in less than 8 hours. Figures are taken from (Nabet et al., 2018).

6, Aim & Progress of the project

1) Structural insights into HDAC tubulin deacetylation and its selective inhibition

Our lab has focused on HDAC6 for years. To understand the detail of its deacetylation on tubulin, we decided to solve its structure by crystallography. We obtained the structures of a) zebra fish HDAC6 tandem catalytic domain with HDAC6-specific inhibitor nexturastat A, and b) single catalytic domain with the (R) and (S) enantiomers of trichostatin A (TSA) (pan-HDACs inhibitor). Herein, we understood the organization of the tandem domain, as well as the inter-domain linker. We also identified important active sites differences in both catalytic domains and revealed the binding mode of HDAC6 selective inhibitors. Next, by replacing the corresponding region in between HDAC6 and HDAC8, a uniquely positioned α-helix was first identified to be critical for tubulin deacetylation. Surprisingly, although we showed that HDAC6 could deacetylate microtubule *in vitro*, it prefers α/β-tubulin dimers.

2) A quantitative model for HDAC6-mediated virus uncoating predicts Influenza A Virus (IAV) infectivity

Although we already acknowledged that 1) HDAC6 regulates IAV uncoating steps together with Ub, motor protein/complex (Myosin 10, Dynein) and 2) the interaction between ZnF domain and Ub is essential, we were not aware that how the interaction between HDAC6 and Myosin 10/Dynein is arranged. Therefore, we investigated those interactions under aggresome inducing condition (mimicking IAV early entry steps) with HDAC6 ZnF mutant (W1116A) cell line, finding that losing interaction with Ub leads to the disassociation of HDAC6-Myosin 10 complex, but reversely enhance HDAC6-Dynein interaction. After combining the experimental data and computational analysis, we quantitatively elucidated mechanisms of influenza A virus (IAV) uncoating *in vivo* with a biophysical modeling (collaborated with Jörg Stelling from D-BSSE, ETH). Interestingly, integrating the data that viral protein M1 from H1N1 & H3N2 binds to HDAC6 differently helped the model successfully predicting that IAV strain H1N1 is more dependent on HDAC6 than H3N2. And this result was consistent with the observation from the lab.

3) Targeting the HDAC6 zinc finger domain impacts virus infection and cellular stress pathways

Protein-protein interaction (PPI) has gained increasing importance as a target for drug discovery. Therefore, we would like to identify a biological tool to block the HDAC6 ZnF – Ub interaction, which is necessary for both IAV uncoating and cellular granule (e.g. aggresome, SG…) formation. Considering several small molecules (Ferreira de Freitas et al., 2018; Harding et al., 2017) have been developed to target HDAC6 ZnF, we chose DARPin to block ZnF-Ub interaction. Among all the provided HDAC6 ZnF interacting DARPins, we identified one DARPin – F10 that blocks Ub recruitment both *in vitro* and *in vivo*. A 2.55 Å X-ray structure illustrated that F10 binds to the same pocket as Ub does. Due to the high affinity, F10 displaces Ub from HDAC6 efficiently. After generating a dTAG-induced degradation F10 cell line, we found that F10 not only inhibits cellular granules, aggresome and SG formation but also down-regulates IAV infection by interrupting the uncoating process as expected. Furthermore, F10 inhibits another RNA virus, ZIKA infection. All the data strongly promote HDAC6 ZnF as a new targetable drug discovery site for both pathological granules and virus infection.

Results

Part I

Structural insights into HDAC6 tubulin deacetylation and its selective inhibition

(I contributed to Table 1 and Figure 3, as well as to the supplementary figures 4, 9, 13, 17 which are available online.)

ARTICLE
PUBLISHED ONLINE: 25 JULY 2016 | DOI: 10.1038/NCHEMBIO.2140
nature chemical biology

Structural insights into HDAC6 tubulin deacetylation and its selective inhibition

Yasuyuki Miyake[1,4], Jeremy J Keusch[1,4], Longlong Wang[1], Makoto Saito[1], Daniel Hess[1], Xiaoning Wang[2], Bruce J Melancon[2], Paul Helquist[2], Heinz Gut[1] & Patrick Matthias[1,3]*

We report crystal structures of zebrafish histone deacetylase 6 (HDAC6) catalytic domains in tandem or as single domains in complex with the (*R*) and (*S*) enantiomers of trichostatin A (TSA) or with the HDAC6-specific inhibitor nexturastat A. The tandem domains formed, together with the inter-domain linker, an ellipsoid-shaped complex with pseudo-twofold symmetry. We identified important active site differences between both catalytic domains and revealed the binding mode of HDAC6 selective inhibitors. HDAC inhibition assays with (*R*)- and (*S*)-TSA showed that (*R*)-TSA was a broad-range inhibitor, whereas (*S*)-TSA had moderate selectivity for HDAC6. We identified a uniquely positioned α-helix and a flexible tryptophan residue in the loop joining α-helices H20 to H21 as critical for deacetylation of the physiologic substrate tubulin. Using single-molecule measurements and biochemical assays we demonstrated that HDAC6 catalytic domain 2 deacetylated α-tubulin lysine 40 in the lumen of microtubules, but that its preferred substrate was unpolymerized tubulin.

Acetylation on lysine residues of histone and other proteins has been recognized as a major post-translational modification that affects multiple aspects of protein function. Protein acetylation levels are regulated by the balance of enzymes with opposing activities: histone acetyltransferases (HATs) and HDACs[1]. HDAC6 is the major deacetylase for tubulin, and it also deacetylates proteins such as HSP90 and cortactin, among others[2–4]. It is mostly cytoplasmic with unique characteristics that set it apart from other deacetylases: tandem catalytic domains with the capacity to deacetylate tubulin and the presence of a zinc finger domain with homology to ubiquitin-specific proteases (ZnF-UBP), which binds unanchored ubiquitin. HDAC6 is a central modulator of stress responses and autophagic clearance, essential for the formation of aggresomes or stress granules[5–7]. It also has an important role for regulatory T cells[8], influenza virus infection[9] and in pathological conditions such as cancer, inflammation and neurodegeneration[10,11].

Microtubules (MTs) are assembled from α- and β-tubulin heterodimers to form dynamic cytoplasmic filaments, involved in multiple cellular functions comprising cell cycle, cell shape, cellular motility and intracellular transport of cargos such as vesicles or viruses[12]. MTs are heavily decorated by post-translational modifications including acetylation, glutamylation, tyrosination or phosphorylation, which have been proposed to regulate their properties, stability and functions[13,14]. α-TAT is the only acetyltransferase targeting Lys40, a residue located in a flexible loop of α-tubulin in the luminal side of MTs[15,16]. α-TAT prefers MTs over α/β-tubulin heterodimers for the efficient acetylation of α-tubulin Lys40 (refs. 17,18), and stochastic acetylation of MTs by α-TAT had been recently demonstrated[19]. Deacetylation of tubulin is promoted by HDAC6 (refs. 2,20) and by the NAD-dependent class III deacetylase SIRT2 (ref. 21). HDAC6 and SIRT2 interact and may function together[21,22]. However, alteration of HDAC6 levels is sufficient to increase tubulin acetylation, and fibroblasts lacking HDAC6 have fully acetylated tubulin[23]. HDAC6 also interacts with plus-end tip-binding proteins such as EB1 or Arp1 (ref. 24), indicating that it might deacetylate the end of microtubules. It is not firmly established which is the preferred substrate of HDAC6, α/β-tubulin dimers or polymeric MTs[2,25]. It has recently been reported that interaction between HDAC6 and tubulin is direct[26] but also that septins facilitate interaction between HDAC6 and acetylated α-tubulin[27].

HDACs comprise 11 family members and are considered promising targets in a number of pathologies, with cancer being the most advanced indication[28]. In most cases however, the critical HDAC(s) have not been conclusively identified, and the four inhibitors (vorinostat, romidepsin, belinostat and panobinostat) approved for cancer treatment until now all target multiple HDACs[29]. HDAC6 is currently evaluated as a potential therapeutic target in particular in multiple myeloma. HDAC6-selective inhibitors have been developed and clinical trials are underway with a recent HDAC6-selective inhibitor, ricolinostat (ACY-1215)[30].

We solved the crystal structure of both catalytic domains of HDAC6, which together with the inter-domain linker form an ellipsoid-shaped complex with pseudo-twofold symmetry. We structurally and functionally defined features that are critical for HDAC6 to deacetylate its physiologic substrate tubulin, and we showed that HDAC6 prefers tubulin dimers as substrate but that it can stochastically deacetylate MTs. We also determined the crystal structures of individual catalytic domains bound to either enantiomer of TSA or to the HDAC6-specific inhibitor nexturastat A (NextA), and found that (*S*)-TSA had moderate selectivity for HDAC6.

RESULTS

Organization of the HDAC6 tandem catalytic domains

To understand how HDAC6 deacetylates tubulin and other substrates we characterized this multidomain protein by X-ray crystallography. As we did not obtain crystals with the mouse protein, we used the zebrafish ortholog, which efficiently deacetylates tubulin from various sources (**Supplementary Results**, **Supplementary Fig. 1**). To facilitate the comparison between zebrafish and other species, we aligned sequences of HDAC6 proteins (**Supplementary Fig. 2**). We first used proteins containing the tandem catalytic domains to characterize their activity in an HDAC assay using Fluor de Lys as

[1]Friedrich Miescher Institute for Biomedical Research (FMI), Basel, Switzerland. [2]Department of Chemistry & Biochemistry, University of Notre Dame, Notre Dame, Indiana, USA. [3]Faculty of Sciences, University of Basel, Basel, Switzerland. [4]These authors contributed equally to this work.
*e-mail: patrick.matthias@fmi.ch

substrate. We compared wild-type catalytic domains 1 and 2 (CD1-CD2) to proteins with an inactivating substitution in either catalytic domain ($CD1_{H193A}$-CD2 or CD1-$CD2_{H574A}$) or in both domains ($CD1_{H193A}$-$CD2_{H574A}$)[20,31,32]. SDS-PAGE and size-exclusion chromatography with multi-angle light scattering analysis showed that the proteins used were highly pure and homogeneous (**Supplementary Fig. 3a,b**). Whereas the wild-type CD1-CD2 fusion was highly active, substitution of the first catalytic site ($CD1_{H193A}$-CD2) had almost no impact. In contrast, substitution of the second site (CD1-$CD2_{H574A}$) strongly impaired the protein but without fully inactivating it, and the doubly substituted variant ($CD1_{H193A}$-$CD2_{H574A}$) was fully inactive (**Supplementary Fig. 3c**). This indicates that the first catalytic domain of zebrafish HDAC6 has a weak but measurable enzymatic activity (see below). When tested in our assay, the full-length human HDAC6 protein showed weaker activity (**Supplementary Fig. 3c**).

We then determined structures of the tandem catalytic domains in complex with NextA (CD1-CD2, residues 25–831, 2.9 Å, interdomain linker present; and residues 40–831, 2.0 Å, interdomain linker cleaved), CD1 in complex with TSA (CD1-TSA, residues 40–418, 1.5 Å), CD2-TSA (residues 441–831, 1.6 Å), as well as of the ZnF-UBP domain (residues 974–1081, 1.9 Å; highly similar to the human ortholog[33]; **Fig. 1a** and **Supplementary Fig. 4**). Data collection and refinement statistics are summarized in **Supplementary Table 1**. In the CD1-CD2 crystal structure both CD1 and CD2 adopted a classical arginase-deacetylase fold[34,35] and had a conserved deacetylase active site ~50 Å apart. The two domains were closely attached to each other (**Fig. 1b** and **Supplementary Fig. 5**). The large domain-domain interface was formed by helices H13, H14, H15 and H18 of CD1, and H32, H33 and H34 of CD2; by loops connecting helices H17 and H18 of CD1, and H36 and H37 of CD2; as well as by the linker (418–442) connecting the two domains and by the C-terminal part of CD2 (794–806). This resulted in a large buried surface area of ~2,100 Å^2 on each domain upon formation of the complex. CD1 and CD2 were structurally very similar (r.m.s. deviation = 1.0 Å, 354 C_α atoms, 45% sequence identity), and the same structural elements were engaged in the domain-domain interface, resulting in a pseudo-twofold axis running along the interface perpendicular to the α-helices on both sides (**Fig. 1b** and **Supplementary Fig. 5**).

We next determined structures of individual CD1 and CD2 domains in complex with the pan-HDAC inhibitor TSA. The isolated CD1 domain contained (*R*)-TSA in its catalytic center (**Fig. 1c**), and we obtained the structure of CD2-TSA as we were trying to crystallize the tandem domains with TSA: during crystallization, proteolysis repeatedly took place and liberated the individual domains, yielding crystals of CD2 with (*S*)-TSA bound (**Fig. 1d**). Backbones of CD1 and CD2 were highly similar also in single domain structures (r.m.s. deviation = 0.77 Å). Superposition of other HDAC structures revealed variations in the N-terminal and C-terminal part of the HDAC6 catalytic domains (**Supplementary Fig. 6**). A notable feature is the presence of a uniquely positioned 10-residue α-helix, referred to as H6 in CD1 and H25 in CD2, found in each catalytic domain near the active sites, as well as a unique loop at the N terminal part of each catalytic domain: H1-H2 in CD1 and H20-H21 in CD2, containing Trp78 and Asp79 (CD1) and Trp459 and Asp460 (CD2) (**Fig. 1c,d** and **Supplementary Fig. 2**).

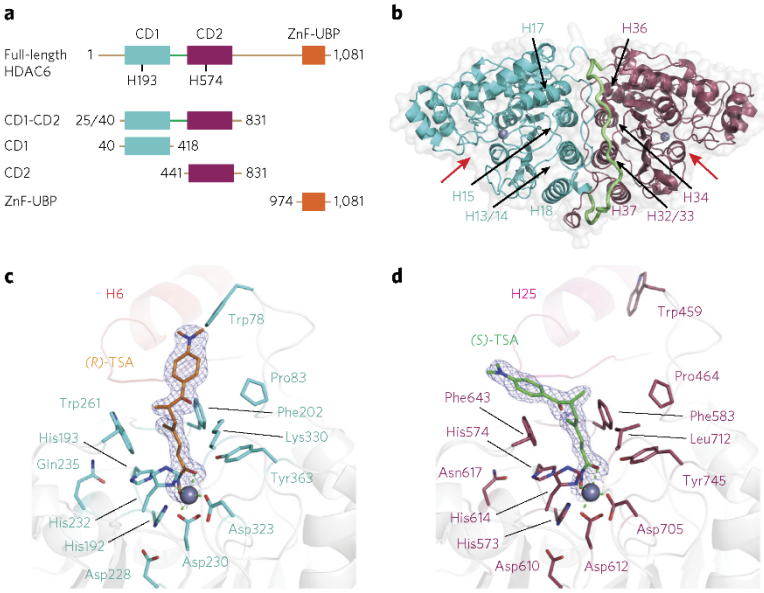

Figure 1 | Overall structure of HDAC6 catalytic domains. (**a**) HDAC6 domain architecture and constructs used for structural studies. This color scheme is used throughout all figures. Amino acid boundaries of all constructs are indicated; for CD1-CD2, two alternative proteins were made starting at position 25 or at position 40. (**b**) Cartoon representation of the CD1-CD2 crystal structure, with CD1 and CD2 in cyan and dark red, respectively, and the interdomain linker in green. Metal ions are shown as gray spheres and red arrows point to the substrate binding clefts. Helices engaged in the CD1-CD2 interface are labeled. (**c**,**d**) Magnified view into inhibitor binding sites of CD1-(*R*)-TSA (**c**) and CD2-(*S*)-TSA (**d**) structures. Residues interacting with TSA or involved in catalysis are drawn as sticks in cyan (CD1) and dark red (CD2); catalytic domain backbones are shown as light gray cartoons with helices H6 and H25 in light red and pink. (*R*)- and (*S*)-TSA are shown as orange (CD1) and green (CD2) sticks with sigma-A-weighted $2mF_o - DF_c$ composite omit electron density maps displayed as blue mesh (1 σ). Zinc ions are shown as gray spheres, and polar interactions involved in Zn^{2+} binding are represented as green dashed lines.

CD1 and CD2 catalytic pockets, and TSA binding

Both HDAC6 CD1 and CD2 active sites were highly conserved and featured the typical narrow hydrophobic channel formed by residues Pro83, Gly201, Phe202 and Trp261 in CD1, and Pro464, Gly582, Phe583, Phe643 and Leu712 in CD2 (**Fig. 1c,d**). The Zn^{2+} ion was coordinated by Asp230, His232 and Asp323 in CD1, and Asp612, His614 and Asp705 in CD2. In CD1, the two charge relay systems consisted of the His192-Asp228 and His193-Gln235 dyads, with the latter normally being a His-Asn pair. In contrast, CD2 had the classical dyad arrangement with His573-Asp610 and His574-Asn617. Lastly, Tyr residues located next to the catalytic zinc ion and thought to stabilize the reaction intermediate, as in class I enzymes[35], were conserved in CD1 (Tyr363) and CD2 (Tyr745). A noteworthy difference present in all HDAC6 sequences when comparing CD1 and CD2 is the use of the bulkier Trp261 in CD1, instead of the usual phenylalanine (Phe643 in CD2), to form one wall of the hydrophobic acetylated lysine binding channel (**Supplementary Figs. 2** and **7**).

(*R*)- and (*S*)-TSA binding to CD1 and CD2 were highly similar for the hydroxamate moiety that complexes the corresponding Zn^{2+} ion in a bidentate fashion using its carbonyl and hydroxyl oxygens (**Fig. 1c,d**). The unsaturated aliphatic TSA linkers were nearly planar and sandwiched between the aromatic side chains of Phe202

Table 1 | Inhibitory profile of (*R*)-TSA and (*S*)-TSA against zebrafish and human HDAC6 as well as against human HDAC1–11

Isoform	(*R*)-TSA IC_{50} (nM)	(*S*)-TSA IC_{50} (nM)
Zebrafish HDAC6 (CD1-CD2)	5.45 ± 0.62	9.88 ± 1.01
Human HDAC6	4.67 ± 0.06	11.1 ± 0.62
Human HDAC1	5.76 ± 1.05	206.30 ± 15.84
Human HDAC2	17.81 ± 1.08	612.65 ± 116.60
Human HDAC3	8.09 ± 0.28	320.80 ± 27.01
Human HDAC4	9,613 ± 2,329.21	6,341 ± 627.91
Human HDAC5	4,385 ± 1,248.75	6,325 ± 117.38
Human HDAC7	3,499.50 ± 123.74	1,823.50 ± 6.36
Human HDAC8	410.50 ± 43.27	312.20 ± 3.96
Human HDAC9	8,861 ± 60.10	4,824 ± 228.40
Human HDAC10	29.19 ± 0.06	403.35 ± 10.25
Human HDAC11	3,642.50 ± 683.77	2,684.00 ± 398.81

IC_{50} is the mean of two experiments ± s.d. obtained from curve fitting of 10-point enzyme assays with threefold serial dilution. HDAC6 assays started at 2 μM inhibitor; HDAC4, HDAC5 and HDAC9 assays started at 450 μM inhibitor; HDAC1, HDAC2, HDAC3, HDAC7, HDAC8, HDAC10 and HDAC11 assays started at 50 μM inhibitor. Values were extracted from fitting dose-response curves to the data points using GraphPad software.

and Trp261 in CD1, and Phe583 and Phe643 in CD2. Whereas the carbonyl group of the hydroxamate was almost coplanar with the unsaturated aliphatic chain, the best fit to the electron density was achieved by kinking the hydroxylamine toward the zinc ion by ~30°, somewhat resembling the TSA conformation in the HDAC7-TSA complex structure[36] (Protein Data Bank: 3C10). The TSA dimethylamino-phenyl CAP group used the first part of a CD1 groove formed by H6 and loop H1-H2 for hydrophobic interaction with Trp78 and Phe202 side chains. Owing to crystallization of the (*S*) enantiomer in CD2, we did not see such an orientation of the CAP group, and it instead interacted with the Phe643 side chain. The side chains of Trp78 in CD1 and of the corresponding Trp459 in CD2 assumed different conformations in their respective grooves when engaged in ligand binding (CD1) or it was free (CD2), thus pointing to a role in substrate recognition (see below). We present additional differences between CD1 and CD2 and their possible role in substrate recognition in **Supplementary Figure 7**.

(*S*)-TSA vs. (*R*)-TSA inhibition of HDAC6 and other HDACs

It had previously been reported that the unnatural (*S*) enantiomer of TSA is biologically inactive[37] and does not inhibit partially purified HDACs from mouse cells[38]; subsequently most studies have used the natural form, (*R*)-TSA. Our observation that HDAC6 CD2 was bound by (*S*)-TSA in our crystal structure was intriguing, and we set out to characterize the activity of (*S*)-TSA vs. (*R*)-TSA on zebrafish and human HDAC6, as well as on all other human HDACs. With pure preparations of the two enantiomers[39] (**Supplementary Fig. 8**), we found that (*R*)-TSA and (*S*)-TSA inhibited zebrafish and human HDAC6 similarly (half-maximal inhibitory concentration (IC_{50}) for zebrafish was 5.45 nM (*R*-TSA) and 9.88 nM (*S*-TSA), and for human, 4.67 nM (*R*-TSA) and 11.1 nM (*S*-TSA)). In contrast, when we tested other human HDACs, we observed differences between (*R*)-TSA and (*S*)-TSA: class I HDACs HDAC1–3 and class II HDAC10 were all strongly inhibited by (*R*)-TSA but only weakly by (*S*)-TSA, whereas other HDACs, including HDAC6, were inhibited about equally or with only small differences (**Table 1**). Thus, although (*R*)-TSA is a pan-HDAC inhibitor, (*S*)-TSA, the unnatural enantiomer, had *in vitro* moderate selectivity for HDAC6 (~20-fold lower IC_{50} compared to the next closest isoform, HDAC1).

To test whether (*S*)-TSA also has activity *in vivo*, we treated mouse embryonic fibroblasts (MEFs) with (*R*)-TSA or (*S*)-TSA, or with the HDAC6-specific inhibitor NextA. After treatment with inhibitor, we prepared protein lysates and monitored acetylation of tubulin or histone H3 by immunoblotting (**Supplementary Fig. 9**). (*S*)-TSA was active *in vivo*, although weaker than the (*R*) enantiomer. However, acetylation of tubulin increased slightly more rapidly than that of histone H3, indicating a moderate selectivity for HDAC6. As expected, NextA, which *in vitro* has very high selectivity for HDAC6 (600-fold over HDAC1 and >1,000-fold over HDAC2; ref. 40), affected acetylation of tubulin without appreciably impacting histone H3 acetylation.

Conservation of active site and surrounding residues

We wondered whether active site differences between CD1 and CD2 are conserved through evolution, and used ConSurf[41] to build a multiple-sequence alignment to map site-specific conservation scores onto the CD1-CD2 surface (**Supplementary Fig. 10a,b** and **Supplementary Dataset 1**). This analysis indicated that the CD2 active site and substrate recognition region were under more evolutionary pressure for conservation than the CD1 site and may point to different functions for the two domains, with a more important role for CD2 (see below).

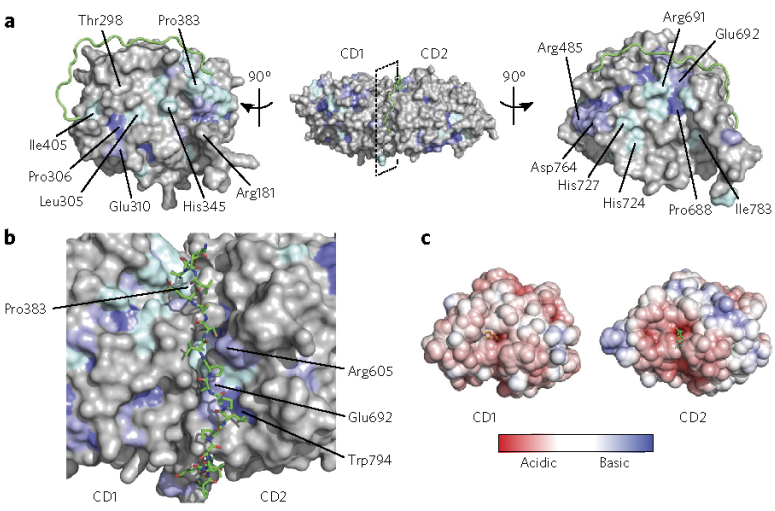

Figure 2 | Conservation analysis of CD1 vs. CD2. (**a**) Site-specific conservation scores computed by ConSurf (http://consurf.tau.ac.il/) from 150 HDAC6 sequences mapped onto the HDAC6 surface. Consurf color grades 9 (dark blue), 8 (light blue) and 7 (cyan) highlight the degree of residue conservation from high to medium. The surface representation of the CD1-CD2 crystal structure is shown in the center. The linker connecting CD1 and CD2 is shown in green as a coil. On the left and right, CD1 and CD2 domains are rotated by 90° around a vertical axis to display the interdomain interface. (**b**) Detailed view on the linker connecting CD1 and CD2, and its interaction with conserved residues on both domains. (**c**) Mapping of the electrostatic surface potential from −8 *kT/e* (red) to +8 *kT/e* (blue) onto the CD1 and CD2 domains (APBS implemented in PyMOL). The domains have been reoriented to show the TSA-bound catalytic sites from the top. Here the linker is included in the surface representation of CD1.

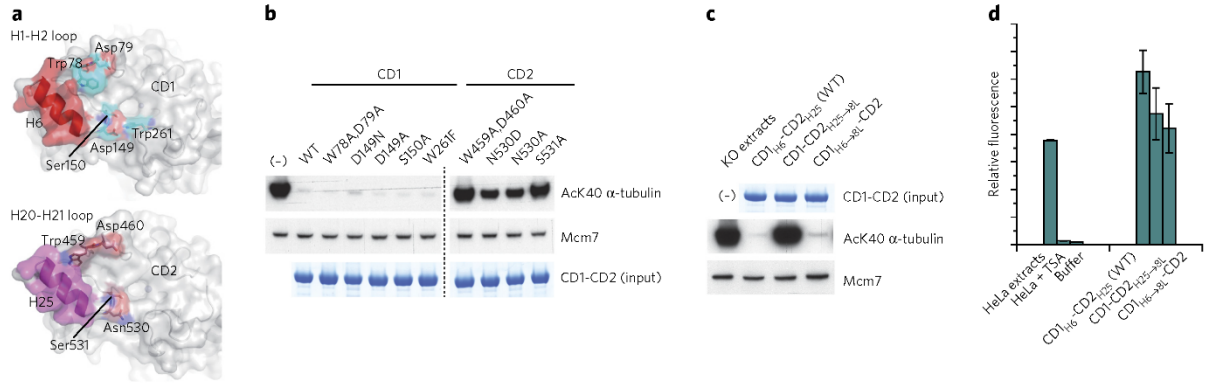

Figure 3 | Structural and molecular determinants for tubulin deacetylation. (**a**) Surface representation of CD1 and CD2 with α-helices H6 and H25, and tested amino acids indicated. (**b**) Immunoblot analysis of variant proteins in extracts from *Hdac6* knockout MEFs tested using an antibody against α-tubulin acetylated at Lys40 (AcK40), or Mcm7 to control for equal extract amount and loading. Gel at the bottom shows equal amounts of the different proteins used (full gel images are available in **Supplementary Fig. 11**). (−) denotes *Hdac6* knockout MEFs extract only (without addition of any protein). WT, wild-type CD1-CD2 sequence. (**c**) Immunoblot analysis of HDAC6 α-helix (H6 and H25) to HDAC8 loop swap changes in CD2 ($CD1_{H6\rightarrow 8L}$-CD2, $CD1\text{-}CD2_{H25\rightarrow 8L}$), were tested with HDAC6 knockout (KO) extracts as in **b** and compared to the wild-type CD1-CD2 fusion, $CD1_{H6}\text{-}CD2_{H25}$ (WT). The top gel shows equal amounts of the different proteins used (full gel images are available in **Supplementary Fig. 12**). (**d**) Enzymatic activity of purified HDAC6 proteins with the indicated changes as in **c**, tested for activity with a Fluor de Lys HDAC assay kit. HeLa extract with or without TSA addition was used as a control. Shown are mean values of three independent experiments with s.d.

Conservation of domain-domain interface

We used the above information to examine in more detail the CD1-CD2 interface (**Fig. 2a**). Several patches of conserved residues took part in the interface, and a large area was composed of less conserved residues. Important hydrophobic binding energy was provided by CD1 residues Pro306, Pro383, Leu305 and Ile405, and on the CD2 side Pro688, Ile783 and the Arg691 guanidinium group contributed the most. A key interaction was formed by the side chain stacking of His345 and His727, located at the same structural position in CD1 and CD2, with the pseudo-twofold axis running through the imidazole stacking pair. Neither the linker connecting CD1 and CD2 (418–442), nor loops H17-H18 in CD1 and H36-H37 in CD2, all of which contribute to the interface, are highly conserved (**Supplementary Fig. 2**). Nevertheless, a closer look at the linker and its interaction with CD1 and CD2 revealed that it interacted with conserved residues on both domains (for example, Pro383 on CD1; Arg605, Glu692 and Trp794 on CD2) and provided a seal between them (**Fig. 2b**).

Structural features critical for tubulin deacetylation

Because HDAC6 is a major tubulin deacetylase, it is important to understand which features endow it with the capacity to deacetylate this substrate. Calculation of the electrostatic surface potentials around each catalytic pocket highlights the mixed hydrophobic and polar character and the differences between CD1 and CD2 (**Fig. 2c**). This observation suggests the potential for differential substrate recognition by these two domains (**Fig. 3**). We hypothesized that the H1-H2 and H20-H21 loops that contain Trp78 and Asp79 in CD1, or Trp459 and Asp460 in CD2, are flexible and contribute to substrate recognition. In addition, we focused on several highly conserved amino acids, which are also around, but not in, the catalytic pocket, in particular Ser150 in CD1 and Ser531 in CD2, which correspond to Asp101 in the H6-H7 loop of HDAC8. This residue is critical for substrate or inhibitor binding by HDAC8 (ref. 42). We analyzed activities of alanine substitutions (loss of function) or conserved amino acid substitutions (gain of function) variants *in vitro* (**Fig. 3a**,**b**). To determine the activity of the mutants against the physiologic substrate α-tubulin, we incubated purified HDAC6 proteins with extracts from *Hdac6* knockout MEFs, in which α-tubulin is fully acetylated[23], and measured the resulting level of α-tubulin K40 acetylation by immunoblotting. We also assayed the enzymatic potential of the variants on the small substrate Fluor de Lys. The different point mutations in the sequence encoding CD1 did not result in compromised deacetylation activity on α-tubulin. In contrast, several point mutants in sequences encoding CD2 (the W459A,D460A double-substitution variant, or variants with single substitutions N530A, N530D or S531A) were all strongly impaired for α-tubulin deacetylation (**Fig. 3b** and **Supplementary Figs. 11** and **12**). However, when we tested these variants on the Fluor de Lys substrate, their activity was almost intact (**Supplementary Fig. 13**), suggesting that these residues are involved in substrate recognition, but not in the catalytic process.

Importance of H6 and H25 and of tandem catalytic domains

We considered that the unique H6 and H25 α-helices (**Supplementary Fig. 6**) might be critical for substrate specificity. Hence, we substituted them in CD1 or CD2 with the H6-H7 loop from HDAC8 (**Supplementary Fig. 14**). Replacement of CD2 H25 by loop H6-H7 of HDAC8 ($CD1\text{-}CD2_{H25\rightarrow 8L}$) dramatically impaired the activity on α-tubulin (**Fig. 3c**), whereas substitution of CD1 H6 had almost no detrimental effect ($CD1_{H6\rightarrow 8L}$-CD2). These proteins were similarly active when tested on Fluor de Lys substrate (**Fig. 3d**), indicating that the catalytic potential of HDAC6 was not impaired, but rather the capacity to use tubulin as a substrate was impaired. This was further demonstrated by *in vivo* experiments in which we stably reintroduced the same variant zebrafish proteins into *Hdac6* knockout MEFs and monitored tubulin acetylation by immunoblotting. The results of these experiments were identical to the *in vitro* results, and confirmed the critical role of CD2 H25 (**Supplementary Fig. 15**).

We next interrogated the overall contribution of each catalytic domain for tubulin deacetylation, using the same assay as above. Inactivating CD1 ($CD1_{H193A}$-CD2) had no impact, whereas inactivating CD2 ($CD1\text{-}CD2_{H574A}$) abolished tubulin deacetylation (**Supplementary Fig. 16a**). Furthermore, isolated CD2 deacetylated α-tubulin, but isolated CD1 did not; however, the isolated CD2 was about tenfold less active than CD1-CD2, as for human[31]. Moreover, adding increasing amounts of CD1 to a reaction containing a

fixed amount of CD2 did not influence tubulin deacetylation (**Supplementary Fig. 16b**), suggesting that under these conditions CD1 cannot enhance, or inhibit, CD2 activity. When tested on a Fluor de Lys substrate, isolated CD1 showed weak but measurable activity and also enhanced the activity of CD2 when the two domains were linked (**Supplementary Fig. 17a,b**). The activity of zebrafish CD1 largely depends on F202, which in other species is a tyrosine (**Supplementary Fig. 2**); conversion of F202 into a tyrosine ($CD1_{F202Y}$) strongly impaired activity (**Supplementary Fig. 17c**). The fact that zebrafish CD1 had no activity on α-tubulin but was catalytically active on Fluor de Lys suggested that it may recognize other substrates.

Stochastic deacetylation of microtubules by HDAC6

We next examined how HDAC6 deacetylates tubulin or MTs (for their preparation, see Online Methods and **Supplementary Fig. 18a–c**). We first tested whether HDAC6 can act on MTs from the ends, or whether like α-TAT it diffuses in MTs and deacetylates them stochastically. We reacted MTs with the HDAC6 tandem catalytic domains using varying enzyme amounts or for various durations; then we fixed them and analyzed by fluorescence microscopy. Addition of the HDAC6 catalytic domains led to deacetylation of the MTs over their entire length, in a dose-dependent and stochastic manner (**Fig. 4a,b**). We observed no preferential reaction toward the ends of MTs, even at the shortest incubation duration (**Fig. 4c**). Thus, *in vitro*, the α-tubulin Lys40 in the lumen of MTs was accessible for deacetylation by HDAC6. Next, we compared the capacity of HDAC6 to deacetylate tubulin dimers or taxol-stabilized MTs; for this, we incubated HDAC6 tandem catalytic domains with radiolabeled acetylated tubulin or MTs and used the TCA-precipitable radioactivity to determine HDAC6 activity. Deacetylation was ~2.5× more effective on tubulin heterodimers than on MTs (**Fig. 4d**), and we obtained the same results with a different experimental setup (**Supplementary Fig. 19**).

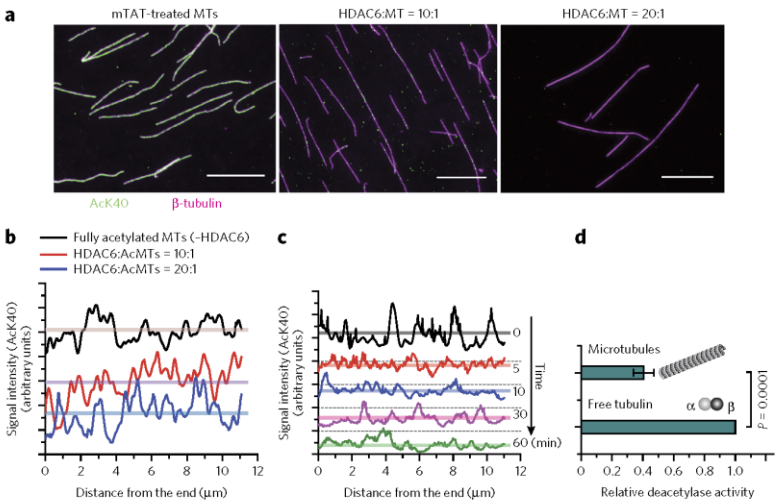

Figure 4 | HDAC6 prefered tubulin dimers, but deacetylated MTs stochastically. (**a**) Microscopy analysis of fully acetylated MTs (mTAT-treated; left) and with HDAC6 added at indicated ratios to monitor deacetylation (middle and right). Scale bars, 10 μm. Magenta staining identifies β-tubulin (MTs), and green staining corresponds to AcK40 of α-tubulin. (**b**) Quantification of fluorescence relative to that of fully acetylated MTs in **a** for an average of 20 line scans of microtubule ends; all scanned MTs were longer than 10 μm and initial MTs had been fully acetylated by α-TAT. Fluorescence intensity of fully acetylated MTs is shown by the black line. Fluorescence intensity of MTs deacetylated by HDAC6 treatment is shown by red (HDAC6:AcMTs = 10:1) and blue (HDAC6:AcMTs = 20:1) lines, respectively. Horizontal lines show respective average fluorescence intensity. (**c**) Time course deacetylation experiment on MTs, with scans indicating AcK40 signal intensity along the MTs at indicated time points after HDAC6 addition. Dashed lines indicate *x* axis for each time point. Line scans from each time point are staggered vertically for clarity. (**d**) Deacetylation activity on MTs vs. free tubulin dimers. Shown are mean values of three independent experiments with s.d.; *P* value is based on a two-tailed Student's *t*-test. Deacetylation activity on free tubulin dimers was set to 1.

Structure of CD1-CD2 in complex with NextA

Although no crystal structure of HDAC6 was available, several HDAC6 selective inhibitors have been developed in recent years[40,43,44]. To gain structural insight into HDAC6 selective inhibition, we determined the structure of the HDAC6 tandem catalytic domains in complex with NextA, an inhibitor with high selectivity for HDAC6 (ref. 40). NextA features a classical hydroxamate zinc-binding group (ZBG) with a benzylic linker connected to a urea-based cap group consisting of a second benzyl and an n-butyl moiety (**Supplementary Fig. 20a**). NextA bound to CD1 and CD2 active sites with distinct characteristics when compared to our TSA structures, giving insight into selective inhibition (**Fig. 5a** and **Supplementary Fig. 20b–d**).

Human HDAC6 homology model and NextA selectivity

Using our zebrafish HDAC6 structures we computed CD1 and CD2 homology models of the human ortholog to understand selectivity of NextA for human HDAC6. Zebrafish CD1 has two critical positions His82 and Phe202, which are Phe105 and Tyr225 in the human protein (**Supplementary Fig. 21a**). As mentioned above, mutation of zebrafish Phe202 into tyrosine resulted in a strong reduction in activity (**Supplementary Fig. 17c**). Human CD2 in contrast had only two amino acid changes located at the periphery of the pharmacophore: zebrafish residues Asn530 and Asn645 are Asp567 and Met682 in the human protein, and all residues found to interact with (*S*)-TSA or NextA are fully conserved (**Supplementary Fig. 21b**). This indicates that the structure of zebrafish CD2 and the corresponding homology model of the human protein may be valid to understand selective NextA inhibition of HDAC6 over other HDAC isoforms.

Superposition of all HDAC isoform structures with zebrafish HDAC6 CD2 and the corresponding human homology model revealed important differences between isoform-specific pharmacophores influencing inhibitor selectivity (**Fig. 5a–c** and **Supplementary Fig. 21c**). Owing to the unique position of helix H25 and the conformation of the following loop, only HDAC6 had a large open basin ~14 Å wide. NextA selectivity for HDAC6 thus seems to come from (i) the isoform-specific shape and height of the rim between the wide HDAC6 basin and the acetylated lysine binding channel where the NextA benzyl cap group docked, and (ii) the bulkiness of residues occupying the basin in other isoforms. Owing to the rigid nature of NextA and the 90° angle between the linker and the urea-benzyl cap, these isoform-specific steric constraints will determine how far the short NextA benzylic linker can reach into the cavity and whether the ZBG can complex the Zn^{2+} ion favorably. Given these structural features, only HDAC6 provided sufficient space in this region to allow tight NextA binding,

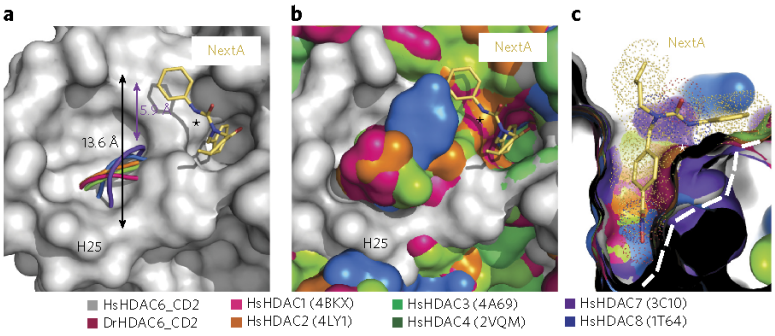

Figure 5 | HDAC6-specific inhibitor binding. (**a**–**c**) Superposition of HDAC isoforms with zebrafish (Dr) HDAC6 CD2 (dark red) and its human (Hs) homology model (gray) to highlight differences in the active site architecture. Human HDAC6 CD2 is shown in surface representation, and all other isoforms are cartoon models (**a**). NextA is shown as sticks in gold; arrows highlight the width of the basin adjacent to the acetylated lysine binding channel for HDAC6 (black) and HDAC7 (violet). HDAC6 helix H25 is labeled. The asterisk marks the rim under the NextA cap group which defines selective inhibitor access in different isoforms. In **b**, all HDAC structures are depicted in surface representation. Cross-section through the acetylated lysine binding channel under the NextA cap group (**c**). All HDAC structures are shown in surface mode. The white dashed line underlines the lowered rim of the channel for HDAC6–8, while all other isoforms have a much more elevated rim (asterisk) and therefore restricted access to the active site. Van der Waals radii for NextA atoms are shown as dots.

whereas other isoforms restricted binding either with bulky side chains occupying the basin or with an elevated rim hindering the ZBG from reaching the Zn^{2+} ion. Similarly, only HDAC6 provided the unique position of H25 and conformation of the following loop, which, together with residues located in loop H29-H30, seemed to provide superior binding energy for (*S*)-TSA, explaining selectivity over other HDAC isoforms (**Supplementary Fig. 21d**).

DISCUSSION

The crystal structure of the HDAC6 tandem catalytic domains revealed that the two domains interact over a large surface area, and that both catalytic sites point outside and are accessible to substrates. The interdomain linker, which varies in length between species, was at the outside of the complex and sealed the two catalytic domains. Previous mutagenesis studies had shown an important role of the linker for optimal activity of HDAC6 (ref. 32). Moreover the linker region is essential for interaction between human or mouse HDAC6 and dynein motor proteins[6,9]. Given the position of the linker observed in our structure, it is conceivable that it forms part of an interface interacting with dynein, possibly together with additional residues in the catalytic domains.

The structure of each domain in complex with inhibitors revealed features of the catalytic pockets. The binding of (*R*)-TSA and (*S*)-TSA to CD1 and CD2 was highly similar for the hydroxamate moiety, but crystal lattice constraints favored a packing of CD2 in complex with (*S*)-TSA where the CAP group orientation differed compared with (*R*)-TSA binding to CD1. Our observations did not indicate a preferential binding of (*S*)-TSA to CD2, but were intriguing, as early reports had suggested that this enantiomer is inactive[37,38]. We found that *in vitro* both pure (*S*)-TSA and (*R*)-TSA inhibited similarly HDAC6. In contrast, when tested on all human HDACs, the two forms showed distinct inhibitory profiles, and (*S*)-TSA appeared to be a HDAC6-selective inhibitor, with ~20-fold selectivity for that isoform. This observation may open up avenues for the generation of new HDAC6-specific inhibitors. Furthermore, in MEF cells (*S*)-TSA was active, albeit less than (*R*)-TSA, and also showed moderate selectivity. The reduced activity of (*S*)-TSA on the main class I HDACs may explain why it had initially been considered to be biologically inactive[37,38].

Mutational analysis revealed that helix H25 and the loop H20-H21 in CD2 were critical for deacetylation of Lys40 on α-tubulin, but not for the small substrate Fluor de Lys; together with Asn530 and Ser531 they form the recognition platform for the α-tubulin loop encompassing Lys40.

Early studies showed that deacetylation of MTs correlates with their depolymerization *in vivo*[45] and in *C. elegans* mutation of the acetyltransferase MEC-17 (the homolog of α-TAT) affects MTs integrity[46,47]. In cultured cells and mouse organs tubulin acetylation is usually low due to the action of HDAC6 and possibly SIRT2 (refs. 20,21,23). Ablation of HDAC6 in mice or cells leads to an almost complete acetylation of α-tubulin, indicating that the balance between HDAC6 and α-TAT is critical to maintain physiological levels of this modification. Recently molecular and structural studies described how α-TAT acetylates MTs, in preference over tubulin; thereby, the α-TAT enzyme enters the lumen of MTs and acetylates them stochastically[19]. When HDAC6 is tested in similar assays it can also deacetylate Lys40 in the lumen of MTs, but the preferred substrate is unpolymerized tubulin, as also observed in ref. 26.

Although zebrafish HDAC6 showed some differences compared to the human enzyme (for example, the activity of CD1 on Fluor de Lys substrate) our overall analysis indicated that it is a valid model to describe the human enzyme. Our structure of CD1-CD2 in complex with the HDAC6-specific inhibitor NextA and homology modeling of the human CD2 domain help to understand selective inhibition of HDAC6. The unique position of H25 and the conformation of the following loop provided selectivity for NextA, (*S*)-TSA and likely also other HDAC6-specific inhibitors. The results presented here will be useful to better understand the biology of HDAC6 and to accelerate drug development.

Received 4 December 2015; accepted 22 June 2016;
published online 25 July 2016

METHODS

Methods and any associated references are available in the online version of the paper.

Accession codes. Atomic coordinates and structure factors have been deposited in the Protein Data Bank under accession codes 5G0G (CD1-TSA), 5G0H (CD2-TSA), 5G0I (CD1-CD2 NextA, cleaved linker), 5G0J (CD1-CD2 NextA, linker intact) and 5G0F (ZnF-UBP).

References

1. Yang, X.J. & Seto, E. The Rpd3/Hda1 family of lysine deacetylases: from bacteria and yeast to mice and men. *Nat. Rev. Mol. Cell Biol.* **9**, 206–218 (2008).
2. Hubbert, C. *et al.* HDAC6 is a microtubule-associated deacetylase. *Nature* **417**, 455–458 (2002).
3. Kovacs, J.J. *et al.* HDAC6 regulates Hsp90 acetylation and chaperone-dependent activation of glucocorticoid receptor. *Mol. Cell* **18**, 601–607 (2005).
4. Zhang, X. *et al.* HDAC6 modulates cell motility by altering the acetylation level of cortactin. *Mol. Cell* **27**, 197–213 (2007).
5. Boyault, C. *et al.* HDAC6 controls major cell response pathways to cytotoxic accumulation of protein aggregates. *Genes Dev.* **21**, 2172–2181 (2007).

6. Kawaguchi, Y. *et al.* The deacetylase HDAC6 regulates aggresome formation and cell viability in response to misfolded protein stress. *Cell* **115**, 727–738 (2003).
7. Kwon, S., Zhang, Y. & Matthias, P. The deacetylase HDAC6 is a novel critical component of stress granules involved in the stress response. *Genes Dev.* **21**, 3381–3394 (2007).
8. de Zoeten, E.F. *et al.* Histone deacetylase 6 and heat shock protein 90 control the functions of Foxp3(+) T-regulatory cells. *Mol. Cell. Biol.* **31**, 2066–2078 (2011).
9. Banerjee, I. *et al.* Influenza A virus uses the aggresome processing machinery for host cell entry. *Science* **346**, 473–477 (2014).
10. Aldana-Masangkay, G.I. & Sakamoto, K.M. The role of HDAC6 in cancer. *J. Biomed. Biotechnol.* **2011**, 875824 (2011).
11. Seidel, C., Schnekenburger, M., Dicato, M. & Diederich, M. Histone deacetylase 6 in health and disease. *Epigenomics* **7**, 103–118 (2015).
12. Lawson, J.L.D. & Carazo Salas, R.E. Microtubules: greater than the sum of the parts. *Biochem. Soc. Trans.* **41**, 1736–1744 (2013).
13. Janke, C. & Bulinski, J.C. Post-translational regulation of the microtubule cytoskeleton: mechanisms and functions. *Nat. Rev. Mol. Cell Biol.* **12**, 773–786 (2011).
14. Yu, I., Garnham, C.P. & Roll-Mecak, A. Writing and Reading the Tubulin Code. *J. Biol. Chem.* **290**, 17163–17172 (2015).
15. Nogales, E., Whittaker, M., Milligan, R.A. & Downing, K.H. High-resolution model of the microtubule. *Cell* **96**, 79–88 (1999).
16. Soppina, V., Herbstman, J.F., Skiniotis, G. & Verhey, K.J. Luminal localization of α-tubulin K40 acetylation by cryo-EM analysis of fab-labeled microtubules. *PLoS One* **7**, e48204 (2012).
17. Kormendi, V., Szyk, A., Piszczek, G. & Roll-Mecak, A. Crystal structures of tubulin acetyltransferase reveal a conserved catalytic core and the plasticity of the essential N terminus. *J. Biol. Chem.* **287**, 41569–41575 (2012).
18. Shida, T., Cueva, J.G., Xu, Z., Goodman, M.B. & Nachury, M.V. The major alpha-tubulin K40 acetyltransferase alphaTAT1 promotes rapid ciliogenesis and efficient mechanosensation. *Proc. Natl. Acad. Sci. USA* **107**, 21517–21522 (2010).
19. Szyk, A. *et al.* Molecular basis for age-dependent microtubule acetylation by tubulin acetyltransferase. *Cell* **157**, 1405–1415 (2014).
20. Zhang, Y. *et al.* HDAC-6 interacts with and deacetylates tubulin and microtubules in vivo. *EMBO J.* **22**, 1168–1179 (2003).
21. North, B.J., Marshall, B.L., Borra, M.T., Denu, J.M. & Verdin, E. The human Sir2 ortholog, SIRT2, is an NAD+-dependent tubulin deacetylase. *Mol. Cell* **11**, 437–444 (2003).
22. Nahhas, F., Dryden, S.C., Abrams, J. & Tainsky, M.A. Mutations in SIRT2 deacetylase which regulate enzymatic activity but not its interaction with HDAC6 and tubulin. *Mol. Cell. Biochem.* **303**, 221–230 (2007).
23. Zhang, Y. *et al.* Mice lacking histone deacetylase 6 have hyperacetylated tubulin but are viable and develop normally. *Mol. Cell. Biol.* **28**, 1688–1701 (2008).
24. Zilberman, Y. *et al.* Regulation of microtubule dynamics by inhibition of the tubulin deacetylase HDAC6. *J. Cell Sci.* **122**, 3531–3541 (2009).
25. Matsuyama, A. *et al.* In vivo destabilization of dynamic microtubules by HDAC6-mediated deacetylation. *EMBO J.* **21**, 6820–6831 (2002).
26. Zhao, Z., Xu, H. & Gong, W. Histone deacetylase 6 (HDAC6) is an independent deacetylase for alpha-tubulin. *Protein Pept. Lett.* **17**, 555–558 (2010).
27. Ageta-Ishihara, N. *et al.* Septins promote dendrite and axon development by negatively regulating microtubule stability via HDAC6-mediated deacetylation. *Nat. Commun.* **4**, 2532 (2013).
28. Falkenberg, K.J. & Johnstone, R.W. Histone deacetylases and their inhibitors in cancer, neurological diseases and immune disorders. *Nat. Rev. Drug Discov.* **13**, 673–691 (2014).
29. Schölz, C. *et al.* Acetylation site specificities of lysine deacetylase inhibitors in human cells. *Nat. Biotechnol.* **33**, 415–423 (2015).
30. Santo, L. *et al.* Preclinical activity, pharmacodynamic, and pharmacokinetic properties of a selective HDAC6 inhibitor, ACY-1215, in combination with bortezomib in multiple myeloma. *Blood* **119**, 2579–2589 (2012).
31. Zou, H., Wu, Y., Navre, M. & Sang, B.C. Characterization of the two catalytic domains in histone deacetylase 6. *Biochem. Biophys. Res. Commun.* **341**, 45–50 (2006).
32. Zhang, Y., Gilquin, B., Khochbin, S. & Matthias, P. Two catalytic domains are required for protein deacetylation. *J. Biol. Chem.* **281**, 2401–2404 (2006).
33. Ouyang, H. *et al.* Protein aggregates are recruited to aggresome by histone deacetylase 6 via unanchored ubiquitin C termini. *J. Biol. Chem.* **287**, 2317–2327 (2012).
34. Finnin, M.S. *et al.* Structures of a histone deacetylase homologue bound to the TSA and SAHA inhibitors. *Nature* **401**, 188–193 (1999).
35. Lombardi, P.M., Cole, K.E., Dowling, D.P. & Christianson, D.W. Structure, mechanism, and inhibition of histone deacetylases and related metalloenzymes. *Curr. Opin. Struct. Biol.* **21**, 735–743 (2011).
36. Schuetz, A. *et al.* Human HDAC7 harbors a class IIa histone deacetylase-specific zinc binding motif and cryptic deacetylase activity. *J. Biol. Chem.* **283**, 11355–11363 (2008).
37. Yoshida, M., Hoshikawa, Y., Koseki, K., Mori, K. & Beppu, T. Structural specificity for biological activity of trichostatin A, a specific inhibitor of mammalian cell cycle with potent differentiation-inducing activity in Friend leukemia cells. *J. Antibiot. (Tokyo)* **43**, 1101–1106 (1990).
38. Yoshida, M., Kijima, M., Akita, M. & Beppu, T. Potent and specific inhibition of mammalian histone deacetylase both in vivo and in vitro by trichostatin A. *J. Biol. Chem.* **265**, 17174–17179 (1990).
39. Cosner, C.C. *et al.* Evolution of Concise and Flexible Synthetic Strategies for Trichostatic Acid and the Potent Histone Deacetylase Inhibitor Trichostatin A. *Eur. J. Org. Chem.* 162–172 (2013).
40. Bergman, J.A. *et al.* Selective histone deacetylase 6 inhibitors bearing substituted urea linkers inhibit melanoma cell growth. *J. Med. Chem.* **55**, 9891–9899 (2012).
41. Ashkenazy, H., Erez, E., Martz, E., Pupko, T. & Ben-Tal, N. ConSurf 2010: calculating evolutionary conservation in sequence and structure of proteins and nucleic acids. *Nucleic Acids Res.* **38**, W529–W533 (2010).
42. Dowling, D.P., Gantt, S.L., Gattis, S.G., Fierke, C.A. & Christianson, D.W. Structural studies of human histone deacetylase 8 and its site-specific variants complexed with substrate and inhibitors. *Biochemistry* **47**, 13554–13563 (2008).
43. Butler, K.V. *et al.* Rational design and simple chemistry yield a superior, neuroprotective HDAC6 inhibitor, tubastatin A. *J. Am. Chem. Soc.* **132**, 10842–10846 (2010).
44. Silvestri, L., Ballante, F., Mai, A., Marshall, G.R. & Ragno, R. Histone deacetylase inhibitors: structure-based modeling and isoform-selectivity prediction. *J. Chem. Inf. Model.* **52**, 2215–2235 (2012).
45. Black, M.M., Baas, P.W. & Humphries, S. Dynamics of alpha-tubulin deacetylation in intact neurons. *J. Neurosci.* **9**, 358–368 (1989).
46. Cueva, J.G., Hsin, J., Huang, K.C. & Goodman, M.B. Posttranslational acetylation of α-tubulin constrains protofilament number in native microtubules. *Curr. Biol.* **22**, 1066–1074 (2012).
47. Topalidou, I. *et al.* Genetically separable functions of the MEC-17 tubulin acetyltransferase affect microtubule organization. *Curr. Biol.* **22**, 1057–1065 (2012).

Acknowledgments

We thank J. Spector and A. Roll-Mecak for sharing information about total internal reflection fluorescence microscopy experiments and discussions, S. Weiler and U. Schopf and U. Rass for helpful discussions, K. Verhey for a technical suggestion, L. Gelman for help with microscopy analysis, and D. Klein and J. Seebacher for mass spectrometry analysis to identify domain boundaries. Part of this work was performed at beamlines X10SA and X06DA of the Swiss Light Source. We thank G. Matthias, C. Cao and M. Regenass for helpful technical assistance, and O. Truee, R.G. Clerc and all the members of the Matthias laboratory for fruitful discussions. This work was supported by the Novartis Research Foundation and M.S. was also partly supported by a Fellowship from the Nakajima Foundation. Work performed at the University of Notre Dame is supported by the Ara Parseghian Medical Research Foundation, the National Institutes of Health (1R01NS092653), the Warren Family Center for Drug Discovery and Development and the Department of Chemistry and Biochemisry. X.W., B.J.M. and P.H. thank J. Zajicek and J. Pontius for NMR microscopy support and discussion.

Author contributions

Y.M., H.G. and P.M. designed experiments; Y.M. performed biochemical and microscopy experiments, Y.M., J.J.K., L.W. and M.S. prepared and purified proteins and performed assays; M.S. and L.W. performed cellular inhibitor assays; J.J.K. crystallized proteins; X.W., B.J.M. and P.H. synthesized and purified (*R*)- and (*S*)-TSA; H.G. and J.J.K. collected diffraction data and H.G. determined crystal structures; D.H. analyzed mass spectrometry data; Y.M., H.G. and P.M. wrote the manuscript; P.M. oversaw the work. All authors contributed to the final manuscript.

Competing financial interests

The authors declare no competing financial interests.

Additional information

Any supplementary information, chemical compound information and source data are available in the online version of the paper. Reprints and permissions information is available online at http://www.nature.com/reprints/index.html. Correspondence and requests for materials should be addressed to P.M.

ONLINE METHODS

Cloning of HDAC6 constructs. A full-length *Danio rerio* HDAC6 cDNA clone was made by synthesizing the first 495 base pairs (bp) of the coding region (GeneArt) and fusing it to the partial cDNA IMAGE clone 7051100 (Source BioScience) via In-Fusion cloning (ClonTech). The translated sequence corresponds to Uniprot F8W4B7. PCR products were cloned into pOPINF, which introduces sequence encoding an N-terminal 6×His tag and a 3C protease cleavage site before the sequence encoding HDAC6; in some cases, pOPINM vectors containing sequence encoding an N-terminal 6×His tag and a maltose binding protein (MBP) tag before the 3C protease cleavage site were used.

Expression and purification of HDAC6 proteins. HDAC6 CD1-CD2 (encompassing amino acid residues 25–831, or 40–831) and HDAC6 CD1 (40–418) were expressed in Sf9 insect cells using the FlashBAC baculovirus system. HDAC6 CD1-CD2 protein was extracted from a baculovirus-infected Sf9 cell pellet by thoroughly resuspending the cells in ice-cold nickel lysis buffer (50 mM Tris, pH 7.5, 200 mM NaCl, 20 mM imidazole, 5% glycerol, 2 mM TCEP, 0.2% Tween-20), freshly supplemented with Complete EDTA-free protease inhibitors (Roche) and Benzonase (Sigma). After 20 min on ice the lysate was centrifuged at 30,000*g* for 30 min at 4 °C. The clarified soluble lysate was incubated in batch mode with Ni-NTA IMAC agarose (Qiagen), and then transferred into a 10 ml Econo-Pac column (Bio-Rad) for washing with nickel wash buffer (50 mM Tris, pH 7.5, 200 mM NaCl, 20 mM imidazole, 5% glycerol, 2 mM TCEP). The target protein was eluted in nickel wash buffer containing 125 mM imidazole. The imidazole concentration in the eluate was adjusted to 20 mM. After an overnight digestion at 4 °C with His-tagged 3C protease, the cleaved HDAC6 was further purified over Ni-NTA agarose resin. The flow-through and wash fractions containing untagged HDAC6 were pooled, concentrated and separated using an AKTA Pure system (GE healthcare) with a HiLoad 16/600 Superdex 200 (GE Healthcare) gel filtration column equilibrated in 20 mM Tris, pH 7.5, 200 mM NaCl, 2 mM TCEP, 0.02% NaN_3. In some cases, a Sephacryl S-300 16/60 gelfiltration column (GE Healthcare) run on a DUO FLOW system (Bio-Rad) was used. Protein fractions were analyzed on a 4–12% Bis-Tris NuPAGE gel and pure fractions containing HDAC6 CD1-CD2 were pooled and concentrated to 11 mg/ml. Gels were stained with InstantBlue. HDAC6 CD1 protein was purified as described above for the HDAC6 CD1-CD2 protein, with the following modifications. Two gel-filtration steps were performed on S200 in 20 mM Tris, pH 7.5, 200 mM NaCl, 2 mM TCEP, 0.02% NaN_3. The first gel filtration run was after the initial Ni-NTA affinity step and the second gel filtration run was as a final polishing step. HDAC6 CD1 protein was concentrated to 10 mg/ml.

HDAC6 ZnF-UBP (974–1081) was expressed in *E. coli* BL21 (DE3) cells and induced with 0.5 mM IPTG at 20 °C for 20 h. *E. coli* BL21 (DE3) cells expressing HDAC6 ZnF-UBP were pelleted, resuspended in lysis buffer (50 mM Tris, pH7.5, 500 mM NaCl, 20 mM imidazole, 1 mM TCEP, 0.2% Tween-20) then rapidly frozen on dry-ice and stored at −80 °C. The frozen cell suspension was thawed at room temperature and supplemented with Complete EDTA-free protease inhibitors (Roche) and 3 U/ml Benzonase (Sigma), before passing through an Avestin EmulsiFlex-C3 cell disruptor. The clarified soluble lysate was incubated with Ni-NTA superflow resin (Qiagen) in batch mode and the bound protein was eluted in 50 mM Tris, pH 7.5, 500 mM NaCl, 500 mM imidazole. The protein was digested overnight with His-tagged 3C protease while dialyzing against 20 mM Tris, pH 7.5, 200 mM NaCl, 20 mM imidazole, 1 mM TCEP, 0.02% NaN_3 at 4 °C. The dialyzed protein was filtered through a 0.22 µm filter and then purified over Ni-NTA superflow resin. Untagged HDAC6 ZnF-UBP protein was collected in the flow-through fraction and concentrated before separating on a Superdex 75 HiLoad 16/60 (GE Healthcare) gel filtration column equilibrated in 20 mM Tris, pH 7.5, 200 mM NaCl, 2 mM TCEP and 0.02% NaN_3. Fractions corresponding to the pure HDAC6 ZnF-UBP protein were pooled and concentrated to 14 mg/ml.

Crystallization of HDAC6 proteins. Nanoliter crystallization experiments were performed with a Phoenix dispensing robot (Art Robbins) using the sitting-drop vapor diffusion method at 20 °C. Drops with HDAC6 CD1-CD2 (40-831) protein at 14 mg/ml and 1.3 mM Nexturastat A (NextA, BioVision), an HDAC6-specific inhibitor, crystallized after 5 d in 3.3 M sodium formate. The single crystals were harvested after 15 d and cryoprotected in 3.3 M sodium formate, 0.1 M Tris, pH 7.5, 17% glycerol, 2 mM NextA and 4% DMSO. These crystals contained CD1 joined to CD2 via its internal intact linker. Crystallization experiments using HDAC6 CD1-CD2 (25–831) protein at 11 mg/ml and 0.66 mM NextA, yielded thick plate crystals after 40 days in 23.2% PEG3350, 0.1 M KCl. These crystals contained CD1 associated with CD2 although the linker region was proteolytically cleaved. The crystals were cryoprotected in mother liquid containing 17% ethylene glycol, 0.6 mM NextA and 1.3% DMSO. HDAC6 CD1 at 10 mg/ml was incubated with 1 mM TSA (*R* form, Sigma), a pan-HDAC inhibitor. Crystals did not appear in the absence of HDAC inhibitor. Long thick plate crystals appeared after 2 d in 23.2% PEG 3350, 0.2 M $MgCl_2$, 0.1 M HEPES, pH 7.0 and Silver Bullet additive A7 (Hampton Research). The crystals were harvested after 3 weeks and cryoprotected in mother liquor containing 20% ethylene glycol, 4 mM TSA (*R* form, Sigma) and 4% DMSO. Crystals containing HDAC6 CD2 were formed from crystallization experiments set up with HDAC6 CD1-CD2 at 9 mg/ml with 0.5 mM TSA (racemic mixture, MBL) in 15% PEG 3350, 0.1 M KCl. Long thick plate crystals appeared after 13 days and were harvested two days later and cryoprotected in mother liquor containing 25% ethylene glycol and 0.5 mM TSA (racemic mixture, MBL) and 1.7% DMSO. Two crystals used for data collection were dissolved in H_2O and analyzed by SDS-PAGE and mass-spectrometry. Crystals contained only the CD2 domain likely resulting from slow proteolysis of the CD1-CD2 protein during crystallization. Crystallization experiments with HDAC6 ZnF-UBP at 14.4 mg/ml yielded many poor quality crystals soon after the trays were dispensed. By slowing down the nucleation process, the best crystals appeared after several months in 1 M Li_2SO_4, 5 mM $NiCl_2$, 0.1 M Tris, pH 8.5. Crystals were harvested and cryoprotected in 2 M Li_2SO_4.

Size-exclusion chromatography with multi-angle light scattering. Purified zebrafish HDAC6 proteins were concentrated to 1–5 mg/ml and filtered through a 0.1 µM Amicon filter before injection. In all, 38 µl of each protein was separated on a Superdex 200 10/300 GL gel-filtration column (GE Healthcare) equilibrated in 20 mM Tris, pH 7.5, 200 mM NaCl, 1 mM TCEP, 0.02% NaN_3 at a flow rate of 0.65 ml/min. Light scattering was recorded on an in-line miniDAWN TREOS three-angle light scattering detector (Wyatt Technology) and protein concentration detected with an in-line Optilab Trex refractive index detector. The weight-averaged molecular mass of material contained in chromatographic peaks was determined using ASTRA 6 software (Wyatt Technology).

Data collection and structure solution. X-ray data collection was carried out at the SLS PX-II/III beamlines in Villigen, Switzerland. CD1-TSA and CD2-TSA crystals belonged to space group $C222_1$ and $P2_1$, respectively, (one chain per a.u. in both cases) and diffracted to 1.50 (λ = 0.978 Å) and 1.60 Å (λ = 1.000 Å). CD1-CD2 (cleaved linker) in complex with NextA crystallized in space group C2 (two chains per a.u.) and crystals diffracted to 2.00 Å (λ = 1.000). CD1-CD2 crystals with intact interdomain linker and NextA diffracted to 2.88 Å (λ = 1.000) and belonged to space group $P3_221$ with one molecule per a.u. and a solvent content of ~79%. The ZnF-UBP domain crystallized in space group I23 with one molecule per a.u. and crystals diffracted to 1.9 Å resolution (λ = 1.000). Diffraction data for all projects was integrated and scaled using the XDS program package[48], except for the anisotropic $P3_221$ CD1-CD2 (NextA, intact linker) diffraction data which was processed with AutoPROC[49].

CD1-TSA and CD2-TSA structures were solved by the molecular replacement method with PHASER[50] using homology models of respective zebrafish (Dr)HDAC6 domains. Phases from molecular replacement solutions were calculated and used for automatic model building with BUCCANEER[51]. Structures were then manually completed and further improved by the crystallographic simulated annealing routine followed by individual B-factor refinement in PHENIX[52]. The CD1-TSA structure was finalized by alternating rounds of rebuilding in COOT[53] and refinement in PHENIX using individual anisotropic B-factor refinement as this lowered R_{free} by more than 1% compared to isotropic ADP treatment.

The CD2-TSA structure was finalized by several rounds of manual rebuilding in COOT and refinement in BUSTER[54] using TLS and individual isotropic B-factor methods. Structures of CD1-CD2 (cleaved linker) and CD1-CD2

(intact linker) in complex with NextA were solved by molecular replacement using high resolution CD1 and CD2 structures as search models. Both CD1-CD2 structures were finalized by alternating rounds of rebuilding in COOT and refinement in BUSTER with and without TLS refinement, respectively. Map sharpening implemented in COOT was used to enhance details for modeling the CD1-CD2 (intact linker) structure. The ZnF-UBP structure was solved by molecular replacement using PDB entry 3C5K as search model and the structure was completed by iterating rounds of manual rebuilding in COOT and refinement in BUSTER.

Metal ions were modeled considering crystallization conditions and peak heights in anomalous difference Fourier electron density maps. The metal ion bound to the CD1 active site in the CD1-CD2 NextA (intact linker) structure did not display any significant peak in the anomalous difference Fourier electron density map and metal ligand distances refined to values > 2.7 Å with notable rearrangement of metal position and ligand orientations owing to a crystal contact with the Lys57 side chain from a symmetry related molecule which is bound in the active site channel. Therefore, Zn^{2+} binding was very unlikely and a K^+ ion was modeled at this position instead which refined well at 100% occupancy (no $mF_o - DF_c$ electron density peak at ± 3 σ) matching B-factor values of the environment. Contrary, the active site in CD2 of this structure (complexed by NextA) displayed a large peak in the anomalous difference Fourier electron density map (14.9 σ) with much shorter metal ligand distances confirming binding of a Zn^{2+} ion.

Metal sites were validated using the CheckMyMetal server (http://csgid.org/csgid/metal_sites) and ligand restraints were generated with the Grade web server (http://grade.globalphasing.org). Final structures were validated using COOT. Ramachandran-plot statistics: CD1-TSA: allowed 99.3%, outliers 0.7%; CD2-TSA: allowed 99.4%, outliers 0.6%, CD1-CD2 NextA (cleaved linker): allowed 99.7%, outliers 0.3%; CD1-CD2 NextA (intact linker): allowed 99.1%, outliers 0.9%; ZnF-UBP: allowed 99.0%, outliers 1.0%. Structural images for figures were prepared with PyMOL[55].

Homology modeling of human HDAC6 CD1 and CD2 domains. HHPRED[56] was used to generate a large multiple sequence alignment of HDAC6 orthologous protein sequences. Aligned zebrafish and human HDAC6 sequences from this alignment were used as input to the modeler software[57] together with high-resolution HDAC6 CD1 or CD2 structures from zebrafish as templates. TSA inhibitors and Zn^{2+} ions were included in the modeling calculations, and treated as rigid bodies. 100 models for each domain were generated and the best model was chosen according to lowest values for the modeler objective function and quality of the Ramachandran plot.

Deacetylase assays with HDAC6 knockout MEFs extracts. Microtubule deacetylation activity was measured with *Hdac6* knockout cell[23] extracts followed by immunoblotting analysis. Extracts were prepared by lysing cells on ice for 30 min with CSK buffer (10 mM PIPES, pH6.8, 300 mM sucrose, 100 mM NaCl, 3 mM $MgCl_2$, 1 mM EGTA, 0.1% Triton X-100) containing Complete protease inhibitor cocktail (Roche). The soluble supernatant containing most of tubulin was collected by centrifugation for 5 min at 13,200 r.p.m. at 4 °C and protein concentration was measured by Bradford assay.

30 µg knockout extracts were mixed with different amounts of purified HDAC6 catalytic domains, and incubated for 1 h at 37 °C. The reaction was stopped by adding SDS sample buffer and proteins were loaded onto 4–12% NuPAGE gels (Invitrogen), transferred onto polyvinylidene fluoride (PVDF) membranes (Millipore) and detected with specific antibodies (anti-AcK40 (BML-SA452-0100, Enzo, 1:3,000) and Mcm7 (47DC141(Ab2360), Abcam, 1:3,000).

HDAC activity assays and IC_{50} determinations of (*R*)-TSA and (*S*)-TSA on HDAC1–11. Enzymatic characterization (Km determinations, **Supplementary Fig. 3C**) of zebrafish HDAC6 proteins (CD1-CD2; $CD1_{H193A}$-CD2; CD1-$CD2_{H574A}$; $CD1_{H193A}$- $CD2_{H574A}$) was done with 50 nM of purified protein and increasing amounts of Fluor de Lys substrate, using an HDAC assay kit from Enzo biochemicals and following the manufacturer's instructions. Human HDAC6 protein (HsHDAC6 FL) was obtained from Reaction Biology Corporation. The fluorescence intensity was detected with a Spectromax Gemini plate reader (Molecular Devices). Curve fitting was done using GraphPad (GraphPad Software). The values expressed are the average of duplicate independent trials ± s.d.

IC_{50} of (*R*)- and (*S*)-TSA on human HDACs as well as on zebrafish HDAC6 were determined by Reaction Biology Corporation. Fluorogenic peptide from p53 residues 379-382 (RHKK(Ac)AMC) was used for HDAC1, 2, 3, 6 and zebrafish HDAC6. Fluorogenic HDAC class IIa substrate (trifluoroacetyl Lysine) was used for HDAC4, 5, 7, 9, and 11. Fluorogenic peptide from p53 residues 379–382 (RHK(Ac)K(Ac)AMC) was used for HDAC8. The assay buffer contained Tris-HCL, pH 8.0, 127 mM NaCl, 2.7 mM KCl, 1 mM $MgCl_2$, 1 mg/mL BSA and 1% DMSO. Inhibitors were diluted in DMSO, preincubated with the enzyme for 10 min, after which substrate was added and the reaction allowed to proceed for 2 h at 30 °C. The reaction was terminated by addition of TSA and developer. Dose-response curves were generated by serial threefold dilution of compound to generate 10-dose plots; curve-fitting was done with GraphPad. IC_{50} values were derived from the plots and the values are expressed as the average of duplicate determinations ± s.d.

Cellular assays with (*R*)-TSA and (*S*)-TSA. MEFs were treated with the different inhibitors ((*R*)-TSA, (*S*)-TSA, TSA (Sigma) and NextA) for 12 h. The cells were washed with PBS and lysed in RIPA buffer (50 mM Tris–HCl, pH8.0, 500 mM sodium chloride, 1 mM EDTA, 1.0% NP-40, 0.5% sodium deoxycholate, 0.1% SDS and Complete EDTA-free protease inhibitors (Roche)). After removal of the insoluble fraction by centrifugation, 20-30 µg protein extract was boiled for 10 min in LDS sample buffer (Invitrogen), and separated on 4–12% NuPAGE gels (Invitrogen). Proteins were transferred onto PVDF membranes (Immobilon-P, Millipore), probed overnight with specific primary antibodies (α-tubulin: DM1A, Sigma T9026, 1:2,500), ((K(Ac)40)-alpha-tubulin: BML-SA452-0100, Enzo, 1:5,000), (histone H3: Abcam1791, 1:4,000), (acetyl-histone H3: Millipore 06-599, 1:4,000), followed by secondary antibodies in 5% non-fat dry milk in TBS blocking buffer. Detection was done with Amersham ECL western blotting reagent (GE Healthcare).

(*R*)- and (*S*)-TSA synthesis and purification. Racemic TSA was obtained via synthetic methods described in[58]. Racemic TSA was purified using a Waters XBridge Prep C18 5 µm OBD column (19 × 50 mm) and water/acetonitrile gradient (15–80% ACN in water, pH = 7; 18 min run, flow rate = 20 ml/min; racemic TSA RT = 8.0 min). With analytically pure racemic TSA in hand, a method was developed for the chiral separation. Racemic TSA was determined to be separable using a Daicel ChiralPAK AD-H 5 µm column (amylose tris(3,5-dimethylphenylcarbamate-coated 5 µm silica gel, 4.6 × 250 mm) and heptane/isopropanol gradient (10–60% IPA in heptane, no additives; 23 min run, flow rate = 3 ml/min). (*R*)-TSA eluted at RT = 15.81 min. (*S*)-TSA eluted at 14.41 min. These samples were collected and measured for their optical rotation. (*R*)-TSA $[a]^{20}_D$ = + 80.5 (*c* = 0.2, MeOH). (*S*)-TSA $[a]^{20}_D$ = −75.5 (*c* = 0.2, MeOH). ^{1}H NMR and LCMS data conform to previously reported structural data in ref. 39.

Cloning, expression and purification of mouse α-TAT. For expression of the α-TAT protein, a cDNA encoding mouse α-TAT (amino acids 1–197) was cloned into pOPINF vector via Gibson assembly (NEB) and expressed in Sf9 cells. Primers were constructed based on cDNA sequence (NP_001136216.1), mRNA was extracted from MEFs by using RNeasy mini kit (QIAGEN) as a template for cDNA. α-TAT was purified with the same procedures as described above for HDAC6 CD1. After first Ni-NTA IMAC agarose, His-tag was digested with 3C protease at 4 °C overnight. The cleaved α-TAT was further purified with second Ni-NTA agarose resin, then injected onto S200 gel filtration column (one step gel filtration). Purified α-TAT was assessed by *in vitro* acetylation assay with acetyl-CoA in the microtubules as previously described[17–19].

Tubulin and microtubule deacetylation assays. Microtubules were reconstituted with purified porcine brain tubulin or bovine brain tubulin (Cytoskeleton T238P or TL238, respectively). Microtubule reconstitution was done as described[59]; briefly, 10 mg/mL purified tubulin was polymerized with 2× Polymix (80 mM PIPES pH6.8, 1 mM EGTA, 1 mM $MgCl_2$, 2 mM GTP, 20% DMSO) for 40 min at 37 °C, then stabilized with pre-warmed BRB80-DT

doi:10.1038/nchembio.2140

(80 mM PIPES pH6.8, 1 mM EGTA, 1 mM $MgCl_2$, 5 mM DTT, 20 µM Taxol) buffer for 10 min. Taxol-stabilized microtubules were spun down 16,000*g* for 30 min at room temperature. Subsequently, polymerized microtubules were treated at 37 °C for 1 h with 5 µM mouse TAT (α-TAT) in the presence of ^{3}H-acetyl-CoA (0.1mCi/mL). Fully-acetylated microtubules were spun down at 16,000*g* for 30 min at room temperature, and washed with BRB80-DT buffer three times to remove α-tubulin α-TAT and unincorporated radioactivity of acetyl-CoA. Free tubulin dimers were generated from this material by cold treatment together with nocodazole: radiolabeled microtubules were spun down and dissolved in BRB80 buffer containing 5 mM DTT and 1 mM nocodazole. After incubation on ice for 1 h, residual MTs were spun down at maximum speed for 30 min. The supernatant was used as the free tubulin fraction. The absence of contamination with residual microtubules was checked by microscopy. For experiments with polymerized microtubules, MTs were stabilized with Taxol in BRB80-DT buffer. For the assays, different amounts of purified HDAC6 proteins were incubated at 37 °C for 1 h with equal amounts of radiolabeled acetylated microtubules or free tubulin. The reaction was stopped by adding 5% TCA, and the precipitated material was collected by a filter binding assay. The amount of precipitable ^{3}[H] tritium remaining in the tubulin or MTs was measured by liquid scintillation counting (Beckman). The level of tubulin deacetylase activity was determined by subtracting the counts obtained with HDAC6 treatment from those without HDAC6 treatment (i.e., input radioactivity).

Single molecule assay by immunofluorescence microscopy for microtubule deacetylation. Microtubules were reconstituted *in vitro* as mentioned above, and fully acetylated with 5 µM α-TAT and 250 µM acetyl-CoA, because tubulin from brain is not fully acetylated[60]. Deacetylation assays were performed with purified catalytic domains of zebrafish HDAC6 at 37 °C for different time point. Reactions were stopped by fixation with 1% glutaraldehyde, and dropped onto poly-Lys-coated coverslips for 10 min. Microtubules were stained with rabbit anti-AcK40 antibodies (BML-SA452-0100, Enzo, 1:400 dilution) and anti-beta tubulin antibodies (Sigma-Aldrich, 1:400 dilution), then detected by staining with Alexa-488 goat anti-rabbit (Lifetechnologies, 1:1,000 dilution) and Alexa-568 goat anti-mouse secondary antibodies (Lifetechnologies, 1:500 dilution). Microtubule images were captured with an Axioimager Z1 microscope (Zeiss) using a 100x objective lens. The acetylated microtubule signal intensity was traced and quantified by ImageJ (NIH).

48. Kabsch, W. Xds. *Acta Crystallogr. D Biol. Crystallogr.* **66**, 125–132 (2010).
49. Vonrhein, C. *et al.* Data processing and analysis with the autoPROC toolbox. *Acta Crystallogr. D. Biol. Crystallogr.* **67**, 293–302 (2011).
50. McCoy, A.J. *et al.* Phaser crystallographic software. *J. Appl. Crystallogr.* **40**, 658–674 (2007).
51. Cowtan, K. The Buccaneer software for automated model building. 1. Tracing protein chains. *Acta Crystallogr. D Biol. Crystallogr.* **62**, 1002–1011 (2006).
52. Afonine, P.V. *et al.* Towards automated crystallographic structure refinement with phenix.refine. *Acta Crystallogr. D Biol. Crystallogr.* **68**, 352–367 (2012).
53. Emsley, P., Lohkamp, B., Scott, W.G. & Cowtan, K. Features and development of Coot. *Acta Crystallogr. D Biol. Crystallogr.* **66**, 486–501 (2010).
54. Bricogne, G. *et al.* BUSTER version 2.11.4. (Global Phasing Ltd., Cambridge, UK, 2011).
55. Schrödinger, LLC. *The PyMOL Molecular Graphics System* Version 1.7.6 (2010).
56. Söding, J., Biegert, A. & Lupas, A.N. The HHpred interactive server for protein homology detection and structure prediction. *Nucleic Acids Res.* **33**, W244–W248 (2005).
57. Martí-Renom, M.A. *et al.* Comparative protein structure modeling of genes and genomes. *Annu. Rev. Biophys. Biomol. Struct.* **29**, 291–325 (2000).
58. Cosner, C.C. & Helquist, P. Concise, convergent syntheses of (±)-trichostatin A utilizing a Pd-catalyzed ketone enolate α-alkenylation reaction. *Org. Lett.* **13**, 3564–3567 (2011).
59. Ziółkowska, N.E. & Roll-Mecak, A. In vitro microtubule severing assays. *Methods Mol. Biol.* **1046**, 323–334 (2013).
60. Carbajal, A., Chesta, M.E., Bisig, C.G. & Arce, C.A. A novel method for purification of polymerizable tubulin with a high content of the acetylated isotype. *Biochem. J.* **449**, 643–648 (2013).

Part II

A quantitative model for HDAC6-mediated virus uncoating predicts Influenza A infectivity (submitted)

(I generated all the data in Figure 3, Figure 6C and Figure S2-1 to S2-3. In addition, I contributed intellectual input to decide the organization of the mathematical model presented in Figure 4A.)

A quantitative model for HDAC6-mediated virus uncoating predicts Influenza A infectivity

Alina Artcibasova[1,6], Longlong Wang[2,5,6], Stephanie Anchisi[3], Yohei Yamauchi[4], Mirco Schmolke[3], Patrick Matthias[2,5,*], Jörg Stelling[1,*]

1 Department of Biosystems Science and Engineering and SIB Swiss Institute of Bioinformatics, ETH Zurich, 4058 Basel, Switzerland.

2 Friedrich Miescher Institute for Biomedical Research (FMI), 4058 Basel, Switzerland.

3 Department of Microbiology and Molecular Medicine, University of Geneva, 1211 Geneva, Switzerland.

4 School of Cellular and Molecular Medicine, University of Bristol, BS8 1TD, Bristol, United Kingdom.

5 Faculty of Sciences, University of Basel, 4031 Basel, Switzerland.

6 Equal contributions.

* Correspondence: patrick.matthias@fmi.ch, joerg.stelling@bsse.ethz.ch.

Abstract

Capsid breakage (uncoating) is a critical step for virus infection of new host cells. In this dynamic, active and regulated process, host components, such as molecular motors, functionally interact with the virus. To get a mechanistic understanding, we combine experiments and computation to quantitatively elucidate mechanisms of influenza A virus (IAV) uncoating in vivo. Biophysical modeling demonstrates that interactions between capsid M1 proteins, host histone deacetylase 6 (HDAC6), and molecular motors can physically break the capsid in a tug-of-war mechanism. Biochemical analysis and biochemical-biophysical modelling identify the essential role of unanchored Ub chains in bridging HDAC6 and the actomyosin network in uncoating, and allow to robustly predict uncoating efficiency in vivo. Remarkably, the difference in infectivity between two clinical strains can be ascribed to a single amino acid variation in M1 that affects binding to HDAC6. Such mechanism-based mathematical models could help formulating novel strategies for broad-range antiviral treatment.

Keywords: virus uncoating, influenza, mathematical model, HDAC6, ubiquitin, cytoskeletal motors, aggresome.

Introduction

To infect a new host cell, eukaryotic viruses have to successfully complete a sequence of steps that starts with cell entry, often via endocytic pathways, to eventually deliver a functional viral genome at an appropriate intracellular location (depending on the type of virus). One critical step in this sequence is uncoating, the disassembly of the protective outer protein shell (capsid), which enables release of the DNA or RNA and associated proteins from the viral core. Uncoating has long been viewed as a passive process that is pre-programmed during viral assembly: while transiting through the host cell's different milieus during transport away from the membrane, a metastable viral core experiences triggers, such as acidification in late endosomes that successively weaken the capsid (Marsh and Helenius, 2006). Capsid breakage and genome release may also be aided by high internal pressure exerted by the confined, tightly packaged DNA or RNA (Brandariz-Nuñez et al., 2019), or by host receptors that destabilize the capsid (Zhao et al., 2019). Detailed mechanistic studies of uncoating are sparse because uncoating is a dynamic, transient phenomenon that is hard to measure experimentally in vivo and to replicate in vitro. For example, while increased internal pressure due to reverse transcription can uncoat human immunodeficiency virus 1 (HIV-1) in vitro (Rankovic et al., 2017), in vivo interactions of viral capsid and host proteins appear critical for the rate-limiting, initial breakage (Marquez et al., 2018; Rawle and Harrich, 2018). In vivo studies, including genetic and biochemical evidence, reveal uncoating – instead of being pre-programmed – as an active process relying on complex, dynamic interactions between viral and host factors, in which the host cell's cytoskeleton and its associated motor proteins play prominent roles (Greber and Flatt, 2019; Helenius, 2018; James and Jacques, 2018; Walsh and Naghavi, 2019).

However, the specific roles of the cytoskeleton and of molecular motors remain largely unclear. The prominent hypothesis states that these host components mediate the correct spatio-temporal positioning of the capsid for uncoating. For example, single-particle studies in live cells show that uncoating is spatially and temporally tightly controlled to release the viral genome in the perinuclear region for influenza A virus (IAV) (Qin et al., 2019) and in the cytoplasm for HIV-1 (Francis et al., 2016). In this context, the attachment of motor proteins with opposing directionalities to the capsid could be important for efficient virus transport, akin to the transport of intracellular organelles (Kural et al., 2005).

Motors attached to the viral protein capsid could also exert a more direct influence on uncoating by generating forces that mechanically break the capsid in a tug-of-war mechanism. Direct experimental evidence for a tug-of-war comes from adenovirus (AdV), which binds to the nuclear pore complex (NPC) as static 'hold' and indirectly to kinesin-1 motors, leading to disruption of both the viral capsid

and the NPC (Greber and Flatt, 2019; Strunze et al., 2011). The disassembly patterns also resemble those of mechanically stressed AdV particles in vitro leading to genome release (Ortega-Esteban et al., 2015; Ortega-Esteban et al., 2013). In addition, it has been hypothesized that different types of motors attached to the same virus particle could uncoat the capsid in a tug-of-war mechanism. For HIV-1, capsid CA proteins can bind to dynein and kinesin-1 molecular motors via cellular adaptor proteins (Carnes et al., 2018; Lukic et al., 2014; Malikov and Naghavi, 2017), but it is unknown if they attach to the same particle and if the motors exert sufficient forces (Malikov and Naghavi, 2017). Similarly, IAV exploits the host cell's aggresome pathway for uncoating, mediated by the recruitment of histone deacetylase 6 (HDAC6) and of molecular motors such as dynein and myosin 10 to the viral capsid (Banerjee et al., 2014). These findings are consistent with a tug-of-war mechanism of uncoating that involves different motor types walking on different filaments, but we do not know if such a mechanism exists and what the precise processes involved would be.

More generally, in part due to the difficulties of experimental measurements, there is no consistent understanding or quantitative description for any virus of how the various virus-host interactions integrate with the viral capsid mechanics to impact uncoating and ultimately infectivity. Here, we therefore combine experimental analysis with computational modeling to quantitatively elucidate the mechanisms of HDAC6-mediated uncoating of influenza A virus in vivo. Our biophysical model incorporates the viral capsid composed of M1 proteins, the host cytoskeleton, and molecular motors. It shows that a tug-of-war mechanism is physically possible with interacting motors, given their known characteristics. Biochemical analysis identifies an essential role for unanchored ubiquitin chains in bridging HDAC6 with the actomyosin network, and leads to a detailed biochemical- biophysical model that robustly predicts IAV uncoating efficiency in vivo, in unperturbed infection as well as across various perturbed conditions. Finally, we demonstrate that the infectivity difference between two clinical influenza strains (H1N1 and H3N2) depends on a single amino acid variation between their M1 proteins. This difference affects binding to HDAC6, HDAC6-dependent uncoating, and infectivity consistently between experiments and model predictions, further supporting our tug- of-war mechanism for influenza A uncoating.

Results

Molecular motor forces are sufficient to break the capsid

The mostly cytoplasmic deacetylase HDAC6 plays an important role in the management of misfolded proteins and the stress response: it is a critical component of the aggresome pathway (Kawaguchi et al., 2003) and it participates in the formation of SGs (Kwon et al., 2007; Saito et al., 2019). HDAC6 exerts its diverse biological functions by deacetylating various substrates such as tubulin, HSP90 or cortactin

(Hubbert et al., 2002; Kovacs et al., 2005; Zhang et al., 2007; Zhang et al., 2003), and also by binding to unanchored Ub chains via a conserved zinc finger domain (Hook et al., 2002; Seigneurin-Berny et al., 2001). During influenza A uncoating after membrane fusion in late endosomes, HDAC6 mediates physical connections between the virus and molecular motors such as dyneins and myosins (Figure 1A). To approach a mechanistic and quantitative understanding of HDAC6-mediated uncoating, we first asked whether it is physically plausible that molecular motors exert sufficient forces on the viral M1 capsid for its breakage. In a tug-of-war scenario, forces exerted by these motors could break the M1 capsid and release the viral ribonucleoprotein (RNP) complex (Figure 1A, B) (Banerjee et al., 2014).

To represent the underlying biophysics of a tug-of-war mechanism, we developed a mathematical model featuring the capsid at the stage when it is exposed via the fusion pore, interactions between the capsid and molecular motors, and interactions between motors and the host cell's cytoskeleton (Figure 2A). Specifically, we assume that M1 proteins (the masses) are arranged in a regular mesh approximately of the size of the fusion pore (Hilsch et al., 2014); they are connected to each other by elastic bonds (springs with Morse potentials; see Methods for details). We represent the cytoskeleton by a single, randomly directed microtubule and by a denser network of actin filaments with a randomly located nucleation point. Molecular motors can be connected (directly or indirectly, which we do not distinguish in this model) to the M1 proteins exposed to the cytoplasm and to the cytoskeleton, and thereby exert forces. Specifically, dynein motors can walk along the microtubule in a single direction, while myosin motors can walk along actin filaments in random directions. We compute the resulting forces through a tug-of-war model with experimentally determined motor characteristics (Gennerich et al., 2007; Muller et al., 2008; Norstrom et al., 2010), which we modified to represent dyneins, kinesins, and positive- and negative-direction myosins. Importantly, the model considers that the force exerted by each individual motor depends on all the other motors bound to the same cargo. If these combined motor forces lead to the distance between any two neighboring M1 nodes exceeding the diameter of the viral ribonucleoprotein (RNP) complex for a sufficient duration, we classify the capsid as broken (see Methods for details).

Model-predicted capsid breakage probabilities for varying numbers and combinations of myosin and dynein motors are shown in Figure 2B. As expected, dyneins alone (zero myosins scenario) were unable to pull the capsid apart because all dynein motors exert their force in the same direction, constrained by the orientation of the microtubule adjacent to the fusion pore. The model predicted that myosins alone (zero dyneins scenario) could exert sufficient forces in different directions to uncoat the viral capsid. In this scenario, we achieved maximum ~50% capsid breakage probability when 9 out of the inner 16 capsid nodes were occupied by myosins. However, with higher myosin occupancy, interference between myosin motors reduced this probability to approximately 30%. Surprisingly, our simulations predict that the tug-of-war between a single dynein motor and 5-7 myosin motors leads to 80-90%

probabilities of capsid breakage. Introducing more dyneins still allows high breakage, but requires a larger number of myosin motors.

To assess the robustness of these predictions, we analyzed the effects of the interaction strength between M1 proteins on capsid breakage probability. We varied the stiffness of the M1-M1 bond and the dissociation energy well depth for the Morse potential, which we originally inferred from indirect measurements and as approximations from other viruses (see Methods). Strengthening the M1-M1 bond led to lower breakage probabilities, and vice versa (Figure S1C). These changes, however, are primarily quantitative and do not affect the main conclusions: molecular motors, in realistic geometries and with realistic characteristics, can exert sufficient forces for virus uncoating, and the capsid breakage probability increases with the synergistic interaction of (few) dyneins and (primarily) myosins attached to the virus capsid.

Key interactions are HDAC6-Ub-Myosin

Next, we wished to biochemically provide further experimental evidence for refining the tug-of-war uncoating model. For this, we examined interactions between HDAC6 and cytoskeletal proteins that are components of the model, under stress conditions. We first used immunoprecipitation of endogenous HDAC6 and mass spectrometry to define the HDAC6 interactome of cells infected by IAV, or treated with MG132 or Cytochalasin D, two drugs that elicit a stress response and lead to formation of an aggresome (Johnston et al., 1998) or an aggresome-like structure (Lázaro-Diéguez et al., 2008). As control, a similar immunoprecipitation was performed with HDAC6 knockout cells. As shown in Figures S2-1, together with Figure 3A, under all three conditions the spectrum of HDAC6-interacting proteins is highly similar and comprises many cytoskeletal actomyosin-related proteins; in particular, myosin 10 was identified as a strong HDAC6 interactor. It might serve as the core component of a putative HDAC6 containing stress-related complex. Consistent with this, immunofluorescence microscopy analysis of cells treated with MG132 confirms that myosin 10, as well as actin are enriched together with HDAC6 at the aggresome (Figure 3B); confocal microscopy further showed that actin and myosin 10 closely surround the aggresome (Figure S2-2). As is evident from the intensity of the signal trace (see Figure S2-2B, C), the actin and myosin 10 signals are distributed around, but not in the HDAC6-enriched aggresome. Co-immunoprecipitation assays with extracts from cells treated with MG132 followed by immunoblotting demonstrated that induction of aggresome formation is required for complex formation between HDAC6, actin and myosin 10; in absence of treatment, actin and myosin fail to co-immunoprecipitate with HDAC6 (Figure 3C). When cells are treated with Cytochalasin D, which disrupts actin filaments but does not lead to formation of monomeric actin while promoting short filaments polymerization (Figure S2-2D) (Schliwa, 1982; Taylor et al., 2011), HDAC6 still efficiently recruits actin and myosin 10. In contrast, when Latrunculin A, which promotes formation of monomeric

actin is used (Figure S2-2D) (Taylor et al., 2011), recruitment is almost abolished (Figure 3D). This indicates that filamentous actin rather than monomeric actin associates with HDAC6 during the stress response.

Remarkably, when cells express an HDAC6 protein with a mutation in the zinc finger domain (ZnF mut; see Figure 1C for the domain organization of HDAC6) so that it no longer binds Ub (Ouyang et al., 2012), the recruitment of actin and myosin is abolished (Figure 3E). These results indicate that HDAC6 binding to unanchored Ub chains is critical to orchestrate the formation of a complex involving components of the actomyosin network such as actin and myosin 10. We next tested whether myosin 10 can assemble with Ub chains in vivo. We transfected a construct encompassing the C-terminal cargo-binding region (amino acids 1103-2007) of myosin 10 fused to GFP, or GFP as a control. Immunoprecipitation was done with an anti-GFP nanobody and presence of co-precipitated polyUb chains (with a MW > 50 kd) was detected by immunoblotting. As shown in Figure 3F, the C-terminal region of myosin 10 was able to robustly recruit Ub chains in MG132-treated cells. This is reminiscent of the observed interaction between myosin 6 and several kinds of Ub chains (He et al., 2016). Recruitment of myosin 10 by HDAC6 also takes place when the catalytic activity is inhibited by Tubacin (Figure S2-3A), indicating that it is not dependent on engagement with a substrate. Under proteasome inhibition, HDAC6 recruits polyubiquitin chains efficiently in cellular lysates; in vitro, the purified HDAC6 ZnF domain interacts equally well with K48- or K63-linked chains, consistent with interaction taking place via the Ub C-terminus (Figures S2-3B, C). In contrast, the purified myosin 10 C-terminal region only interacts appreciably with K48-linked Ub chains (Figure S2-3D). Together these data strongly indicate that high molecular weight K48 polyubiquitin chains bring together HDAC6 and myosin 10, via its C-terminal domain.

The interaction between HDAC6 and dynein has been previously reported (Banerjee et al., 2014) and we tested whether it would be affected by the HDAC6 ZnF mutation (Figure S2-3E). Indeed, loss of Ub binding slightly enhanced the interaction of HDAC6 with dynein, opposite to the interaction with myosin 10. This observation indicates that the dynein-HDAC6 interaction is modulated by Ub, even though it is the linker between the tandem catalytic domains of HDAC6 that interacts with dynein. Together, these biochemical results indicate that the interaction between HDAC6 and Ub chains is central to the recruitment of filamentous actin and molecular motors for viral capsid opening.

HDAC6 complex formation models predict capsid breakage robustly

Next, we aimed to integrate the biochemical interaction mechanisms with the mechanics of virus uncoating quantitatively, for example, to determine how many cellular motors per exposed capsid are

feasible in vivo, and how their actions will translate to virus uncoating (and eventually, infectivity). Because it was not possible to define all interaction mechanisms unambiguously with prior data and our own data, we formulated three reaction model schemes for HDAC6 complex formation that incorporate distinct mechanistic hypotheses (Figure 4A). We based one model variant termed 'Viral Ub' on the previously available uncoating data (Banerjee et al., 2014); it assumes competition between capsid-borne and cellular unanchored Ub chains (Ubs) for the zinc finger domain of HDAC6. The two model variants incorporating our new protein interaction results assume that cellular Ub chains either assist with binding of both myosin and dynein motors to HDAC6 (variant 'Symmetric'), or only with binding of myosin (variant 'Asymmetric').

To make the models consistent with prior in vivo data, we used published reaction rate parameters for influenza A (or averages and similar parameters where data was not available) as well as protein abundances in lung tissues from proteomicsDB (Schmidt et al., 2018). Even when we widely sampled the reaction rate parameters uniformly (with fixed protein concentrations), the 'Viral Ub' model failed to generate capsid breakage for any combination of reaction rate parameters. We then optimized unknown and imprecise reaction rate parameters for the other two models to achieve both myosin and dynein recruitment, and thereby maximize breakage, while keeping the reaction rate parameters close to literature values. This yielded reference parameter sets for each model variant. To represent the model uncertainty and to assess its effect on model predictions, we then sampled total protein concentrations normally around the means of previously reported values, and rate parameters log-normally close to their reference values (see Methods for details).

We used the reaction model to compute motor complex abundances for the 'Symmetric' and 'Asymmetric' model variants at steady state. Both variants can lead to motor complex configurations that are conducive to efficient virus uncoating (see Figure S3C, D), but the 'Asymmetric' variant leads to higher myosin and dynein binding (Figure 4B). Next, we used the mass-spring mechanical model to predict average capsid breakage probabilities from the motor configurations (see Methods). The 'Asymmetric' model variant showed a higher density of capsid breakage probabilities close to 100% for uniform sampling (Figure 4B), indicating efficient virus uncoating. We obtained qualitatively similar results with a different sampling strategy (Figure S3B). Thus, our models – which incorporate both known constraints and uncertainties – suggest that Ub chains are important for forming motor complexes and thereby for efficient capsid breakage.

To identify critical factors for efficient virus uncoating, we varied individual total protein concentrations and rate parameters (Figure 4C, D). Both model variants showed similar sensitivities in the examined ranges. The capsid breakage probability was not sensitive to changes of capsid protein M1 abundance (due to averaging by the number of virions). A decrease in tubulin concentrations led to a weak increase in capsid breakage. In contrast, we observed a peak close to the reference point for dynein, myosin, and

HDAC6 concentrations, suggesting an optimal abundance of these proteins for uncoating. For the 'Asymmetric' model, changes in Ub elicited a similar peak-like shape, while for the 'Symmetric' variant, we observed a plateau. This trend is reversed for the model variants' actin dependencies. For most of the on-rates, capsid breakage is largely insensitive to changes of reaction rate parameters. However, the 'Asymmetric' model is not sensitive to changes in kCH , but sensitive to low values of kUH . The reverse holds for the 'Symmetric' model. Dissociation constants did not affect capsid breakage at low values, then, sometimes, reached a small peak, and dropped dramatically. One notable difference between the models is that in the 'Asymmetric' ('Symmetric') case, KUH (KHM) peaks near the reference point, which can be explained by those two reaction rates controlling HDAC6-myosin binding, respectively. Overall, we conclude that our models that combine the biochemistry and mechanics of HDAC6-mediated uncoating can yield robust predictions of capsid breakage in vivo, based on the identified mechanism with asymmetric influence of Ub chains on motor binding.

The models predict in vivo responses to host pathway perturbations

To assess to what extent the model predictions match with independent experimental observations in vivo, namely previously published virus uncoating data (Banerjee et al., 2014), we first analyzed how uncoating efficiency is affected by perturbations in components of the host cell. We generated predictions with both model variants after introducing model perturbations that correspond to, or are at least similar to, the experimental perturbations (see Methods and Table S3). Specifically, most of the proposed perturbations are relatively straightforward to incorporate, by assuming a reduction of available reactants. For CiliobrevinD, we assume that immobile dyneins do not contribute to capsid breakage (technically it is possible that these fixed motors exert force by holding the capsid protein matrix in place). We represent protein domain mutations – HDAC6 ΔDMC MEF cell line and HDAC6 ZnFm (W1116A) MEF cell line – through increased dissociation constants between HDAC6 and dynein (KHD) or Ub (KUH), motivated by the model being sensitive to changes in these parameters (Figure 4C, D).

First, we focused on perturbations of the host cell's molecular motors. Experimental data on virus uncoating efficiency were obtained in acid bypass assays that mimic normal infection by lowering the extracellular pH and blocking the natural acidification in endosomes (Banerjee et al., 2014). For the examined perturbations, the predicted median uncoating efficiencies agree well with the experimental results (Figure 5A). The 'Symmetric' predictions were slightly closer to the experimental results.

For a wide variety of HDAC6 perturbations, including knockdowns and mutations of specific domains, the models' predictions aligned well with the experimental data (Figure 5B). Notably, predictions were consistent with data from bypass experiments as well as experiments that measured endosomal

uncoating in the normal virus infection pathway. Note, however, the difference in predicted viral capsid breakage probability in HDAC6 mutants or siRNA knockdown; the model only represents HDAC6-mediated uncoating, while in vivo there are likely additional pathways or mediators capable of assisting in the uncoating (Gschweitl et al., 2016; Huotari et al., 2012; Miyake et al., 2019; Su et al., 2013; Yángüez et al., 2018). The 'Symmetric' model captured siRNA perturbations better than the 'Asymmetric' variant, due to the former being less sensitive to reduction in HDAC6 (Figure 4C, D), but the 'Asymmetric' prediction for the ZnF mutant was closer to the experimental observation.

Finally, we compared model predictions with experimental data from perturbations of the host cell's cytoskeleton and from an endosomal drug screen (Banerjee et al., 2014) (Figure 5C). Both variants performed well, with one notable exception: the 'Asymmetric' variant did not capture the effect of nocadazole treatment, which is consistent with it being less sensitive to reduction in tubulin concentrations (Figure 4C, D). Interestingly, except for nocodazole treatment, the 'Asymmetric' variant performed better for endosomal perturbations (Figure 5C, drug screen). Overall, we conclude that the combined model predictions compare well against published experimental data. Even when model limitations make the predictions imprecise, the models at the very least predict the correct direction of the perturbation effect on the viral capsid breakage probability.

Infectivity in vivo and sensitivity to HDAC6 inhibition depend on M1

Viral dependence on HDAC6-assisted uncoating could rely on strain-specific features. To assess the generality of our initial findings for the H1N1 strain also, we compared the early replication efficacy of a panel of influenza A virus strains in wild type (WT) and HDAC6-deficient A549 lung epithelial cells (Figure S4A, B). Strikingly, a clinical H3N2 isolate from 2013 displayed low dependence on HDAC6 for early replication steps as determined by automated fluorescence microscopy for viral nucleoprotein (NP). Specifically, this H3N2 isolate did not rely on a functional ZnF domain of HDAC6 while a clinical H1N1 isolate (pH1N1) from 2010 did. Inactivating HDAC6 deacetylase activity by a mutation in CD2 affected neither of the isolates (Figure 6A). A likely immediate target of HDAC6 is the viral matrix protein M1. Sequence alignment of M1 from HDAC6- dependent (H1N1) and -independent (H3N2) viral strains (Table S4) revealed a single amino acid substitution (A218T in H3N2) previously associated with matrix shape (Elleman and Barclay, 2004). Reversion of the 2003 H3N2 virus (A/Wyoming/03/2003) M1 residue 218 to alanine by reverse genetics restored HDAC6 dependence to a similar extent to H1N1 virus (Figure 6B) and reduced particle length (Figure S4C, D). Importantly, efficient co-immunoprecipitation of purified C-terminal M1 proteins with HDAC6 depends on alanine at position 218 of M1 (Figure 6C-D). Specifically, these data suggest that the A218T mutation reduces binding of M1 to HDAC6 by approximately two- fold (Figure 6E).

To represent the effect of the amino acid substitution in the reaction models, we assumed that the M1 protein mutation affects the binding between the capsid and HDAC6, specifically the dissociation constant KCH. We generated reaction model predictions for the mutant by choosing a multiplication coefficient for both models, setting the desired level of capsid breakage in an individual perturbation experiment (Figure 4C, D) to the observed average level of M1 binding (Figure 6C; Table S4). These model predictions aligned well with the experimental results from in vitro M1 pull-down quantification and from in vivo automated fluorescence microscopy for both viral strains and their respective M1 mutants (Figure 6E). However, the models did not fully capture interactions between different perturbations. For example, the relative infectivity of the pandemic H1N1 (pH1N1) strain in the HDAC6 ko/ki ZnF mutant cells corresponds to reduction of the binding rate kUH between the HDAC6 ZnF domain and Ub, and the infectivity of the H3N2 strain in HDAC6 ko/ki WT cells to the increased dissociation rate KCH . Both cases lead to a reduction in capsid breakage. However, our NP fluorescence microscopy data for the H3N2 ko/ki ZnF mutant show a slight increase of viral entry compared to the ko/ki ZnF mutant (Figure 6E), in contrast to either of the models. In sum, these results suggest that the models represent key mechanisms of virus uncoating in vivo, despite focusing on only a few biochemical and mechanical interactions between virus and host components.

Discussion

A physically realistic tug-of-war model for IAV uncoating

Uncoating is arguably an enigmatic step of virus entry, with only few detailed studies available for a limited set of viruses (Helenius, 2018; Walsh and Naghavi, 2019). As a transient step, uncoating is hard to measure quantitatively; for example, only recently have dynamic measurements in cells with complete influenza A viruses become possible using monoclonal antibodies (Banerjee et al., 2014) or quantum dots (Qin et al., 2019). In addition, uncoating involves diverse (host and virus) components and interrelated (biophysical, biochemical, and cell biological) processes, making it difficult to integrate the relevant data and knowledge. These aspects may have contributed to limited conclusive evidence for a tug-of-war mechanism that has been proposed for several viruses (Banerjee et al., 2014; Lukic et al., 2014; Radtke et al., 2010; Strunze et al., 2011). However, the combination of biochemical analysis and mechanistic mathematical modeling described here for IAV uncoating demonstrates the feasibility of such integration, up to consistent predictions of differential infectivity of IAV strains with a single amino acid substitution in the M1 capsid protein.

Intriguingly, the model neither relies on exact knowledge of component concentrations and interaction parameters, nor on their direct estimation from experimental data except for M1 binding mutants, which

could prevent truly independent predictions. We represented uncertainties explicitly, allowing us to integrate in a consistent manner relatively precise knowledge such as molecular motor forces with much less certain aspects such as binding affinities to make the model physically realistic. Despite these uncertainties being reflected in model predictions, the qualitative and often quantitative agreement with the experimental data indicates substantial robustness to assumptions made in model construction. In general, we aimed to identify core mechanisms that suffice to explain the collected experimental observations on IAV uncoating using a minimal model. We assume, for example, singular bonds between M1s in the capsid, no influence of endosomal transport on the tug-of-war mechanisms, and maximal capsid breakage for reaction rate optimization. This minimal nature of the model also implies that pleiotropic effects of perturbations are not well captured. For example, discrepancies for nocadazole experiments may arise because the drug not only disrupts microtubule dynamics, but also affects cell metabolism and viral traffic (Naghavi et al., 2017).

Mechanisms of IAV uncoating

For a mechanistic interpretation, it is important that our model does not represent directional transport by multiple motors associated to a cargo (Hancock, 2014), but rather the generation of mechanical forces by the molecular motors. The high consistency between our model predictions and experimental data, however, argues against a mere positioning effect of the capsid inside the cell as a condition for uncoating, as hypothesized in early tug-of-war concepts (Lukic et al., 2014; Radtke et al., 2010). The recent discovery of two host proteins activated early in infection and facilitating IAV uncoating supports this notion. Epidermal growth factor receptor pathway substrate 8 (EPS8) possibly fulfills a function in uncoating by modulating actin dynamics (Larson et al., 2019). G protein-coupled receptor kinase 2 (GRK2) appears to act via non-canonical targets (Yángüez et al., 2018), and it is known to control cytoskeletal dynamics as well.

In more detail, a key element of our proposed mechanism is the Ub-mediated binding between HDAC6 and molecular motors. Future studies should identify the source and nature of the binding- mediating Ub chains. They could be provided by the virus (Banerjee et al., 2014), or by local or general host sources. Our models, however, suggest that viral Ub alone does not support efficient capsid breakage (Figure 4A, B). In addition, while our data suggest preferences for K48- linked Ub chains (Figure S2-3C, D), we cannot exclude functions of K63-linked or of mixed K48/63-linked chains as mediators for uncoating. With the current experimental data, we cannot conclusively select between the ‘Symmetric’ or ‘Asymmetric’ model variants. The ‘Symmetric’ variant is less predictive for most of the endosomal uncoating experiments (Figure 5) and the ‘Asymmetric’ variant seems more realistic because the HDAC6 ZnF mutant enhances HDAC6-dynein interaction and reduces HDAC6-myosin-10 interaction (Figures S2-3E, 3E). Discrepancies between models and experiments may arise due to involvement of

other factors, or other types of polyubiquitin in the HDAC6-dynein interaction that are not accounted for. These discrepancies may also indicate the areas where we lack an understanding of underlying mechanisms. The 'Symmetric' model variant assumes that binding of myosin and dynein both are conditional on Ub, in contrast to the 'Asymmetric' variant, where dynein binding is independent of Ub (Figure 4A). Experimental perturbations to Ub, myosin, and dynein recruitment, and their combinations, compared to corresponding model perturbations, could help identify the true pattern of Ub-dependent motor recruitment.

Our focus on minimal mechanisms also implies that strain-specific characteristics of HDAC6-dependent virus uncoating require further study. Using clinical IAV strains, we found that influenza H1N1 is more sensitive to the HDAC6/aggresome pathway than H3N2. To understand this behavior, we considered only direct effects of M1 sequence variations at position 218 on the HDAC6-M1 interaction. These variations also affect virion shape (Elleman and Barclay, 2004), which could result in altered capsid stability (Dadonaite et al., 2016): using transmission electron microscopy of infected MDCK cells we demonstrated increased length of Wy/03 WT virions as compared to the predominantly spherical shape of Wy/03 M1 T218A mutant particles (Figure S4B, C). Our previous results (Banerjee et al., 2014) were mostly based on studies with the X31 strain of IAV, which is referred to as an H3N2 virus. However, X31 is a hybrid virus between PR8 (H1N1) internal genes and glycoproteins from A/Aichi/2/68 (H3N2), and its M1 gene is PR8-derived (thus H1N1; (Banerjee et al., 2013)). Therefore, our new data are entirely consistent with our previous work. In addition, we cannot exclude an impact of residue 218 on M1-M1 dimerization strength; future studies could address this by atomic force microscopy measurements. In line with the above, however, we argue with Occam's razor: altered capsid stability or M1 dimerization strength do not seem essential to explain the observed differences in IAV infectivity.

Implications for other viruses and antiviral treatment

An intriguing open question is if, and to what extent the tug-of-war uncoating mechanism transfers to other viruses. Adenovirus uncoating may have the closest similarity, with the nuclear pore complex (NPC) acting as a static 'hold' that facilitates disruptive force generation by microtubule- associated kinesins (where the NPC-equivalent are dyneins for IAV) (Flatt and Butcher, 2019; Greber and Flatt, 2019). For HIV-1 the picture is more complex: while initial opening of the capsid is the rate-limiting step for uncoating (Marquez et al., 2018), it is unclear, if in vivo, a tug-of-war mechanism (Rawle and Harrich, 2018), pressure increase in the capsid due to reverse transcription (Rankovic et al., 2017) or a dedicated uncoating receptor akin to the case for enteroviruses (Zhao et al., 2019) initiate the breach. Intriguingly, the proposed uncoating receptor for HIV-1 is the β- karyopherin transportin-1 (TRN-1/TNPO1) (Fernandez et al., 2019), the same host protein that induces the debundling of IAV

ribonucleoproteins after capsid breakage (Miyake et al., 2019; Yamauchi, 2020). Differences between HIV-1 and IAV uncoating may simply result from, for example, transcription initiation of viral genes in the cytoplasm and nucleus, respectively. We argue that such parallels nevertheless warrant more detailed experimental in vivo probing of potential tug- of-war mechanisms in HIV-1 uncoating, preferably integrated with quantitative mechanistic modeling as shown here.

Finally, because host components are particularly attractive targets for novel antiviral treatment strategies, and because the HDAC6/aggresome pathway appears to be used by multiple viruses (manuscript in preparation), we see potential for antiviral treatment development by targeting HDAC6-mediated uncoating. Compared to recently proposed targets such as EPS8 (Larson et al., 2019) and GRK2 (Yángüez et al., 2018) such developments appear promising for two main reasons:(i) a clear mechanistic picture relating several identified host components to viral infectivity via uncoating, and (ii) a predictive model that allows one to account for differences between viral strains. In addition to an extended experimental analysis discussed above, refined mathematical models could, for example, include intracellular transport or structure-function relationships for capsid and individual proteins. The potential transfer of the proposed mechanisms and of the overall experimental-computational framework beyond influenza, in addition, could make such efforts worthwhile.

Acknowledgements

We thank L. Kaiser (Univ. Geneva) for discussions, L. Gelman and S. Bourke (FMI) for help with microscopy analysis, D. Hess, J. Seebacher and V. Iesmantavicius (FMI) for mass spectrometry analysis, E. Moreira (FMI) for help with viral infection for mass spectrometry, F. Silva and B. Maco (Univ. Geneva) for excellent technical support during analysis of the electron micrographs, and L. Widmer (ETH Zurich) for help with the mass-spring model. Financial support through the SystemsX.ch MRD project VirX 2014/264, evaluated by the Swiss National Science Foundation, is gratefully acknowledged. This work was supported by the Novartis Research Foundation.

Author contributions

Y.Y., M.S., P.M. and J.S. conceived the study. A.A. designed and implemented the mathematical models. L.W. performed the biochemical and cell biological experiments. S.A. performed the virology experiments. A.A., L.W., S.A., M.S., P.M. and J.S. analyzed the data. A.A. prepared figures. A.A., L.W., M.S., P.M. and J.S. wrote the manuscript. Y.Y. critically revised the manuscript. All authors approved the final manuscript.

Declaration of Interests

The authors declare no conflict of interest.

Figures

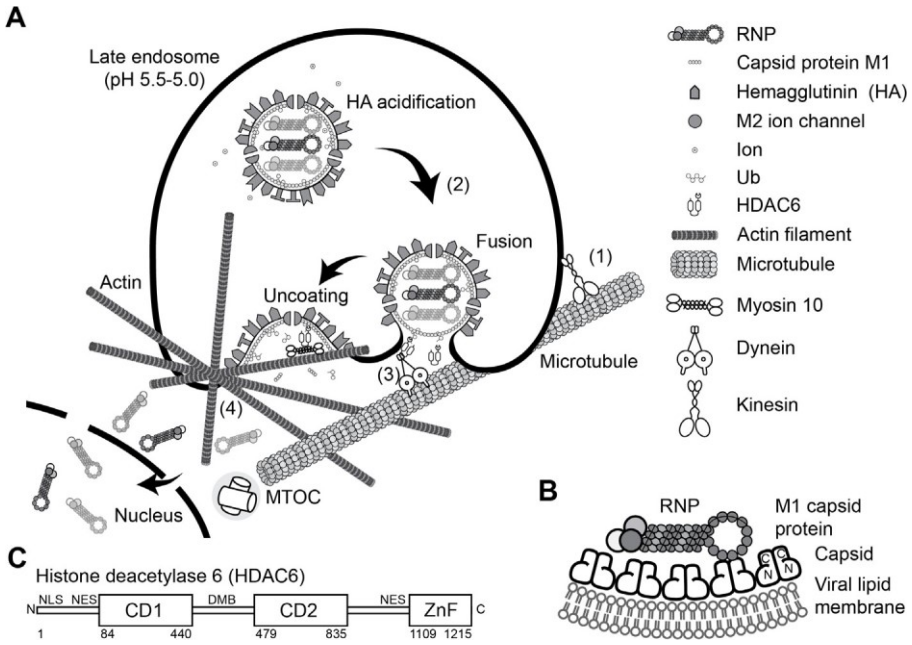

Figure 1: HDAC6 and its role in influenza uncoating.

(A) Schematic representation of the influenza A virus M1 capsid disassembly mechanism involving histone deacetylase 6 (HDAC6), adapted from (Banerjee et al., 2014). Influenza virions enter the host cell through receptor-mediated endocytosis. (1) An endosome with the viral particle is transported along microtubules by the molecular motors dynein and kinesin. (2) Endosomal acidification during transport towards the cell nucleus primes the viral core for uncoating via the influx of protons and potassium into the core through the viral M2 channel. At the critical pH, viral HA triggers fusion of the viral envelope with the endosomal membrane, forming a fusion pore and exposing the viral matrix protein M1 to the cytosol. (3) The virus mimics misfolded proteins by carrying unanchored Ub (Ub) chains. The current conceptual model assumes that HDAC6 binds these Ub chains and recruits molecular motors dynein and myosin-10 for the transport along microtubules towards the aggresome, a perinuclear assembly of misfolded proteins at the microtubule organizing center (MTOC). (4) Forces exerted by the motors break the viral capsid and thereby release viral genetic material.

(B) Schematic representation of the intact viral capsid. M1 oligomers in the capsid are broken down into dimers after acidification. The N-N oligomer dissociates in response to low pH, but the C-C dimer is maintained, holding the complex together as a dimer (Zhang et al., 2012).

(C) HDAC6 domain organization (Hai and Christianson, 2016; Miyake et al., 2019): NLS, nuclear localization signal; NES, nuclear export signal; DMB, dynein motor binding; ZnF, zinc-finger Ub-binding domain; CD1 and CD2, catalytic domains.

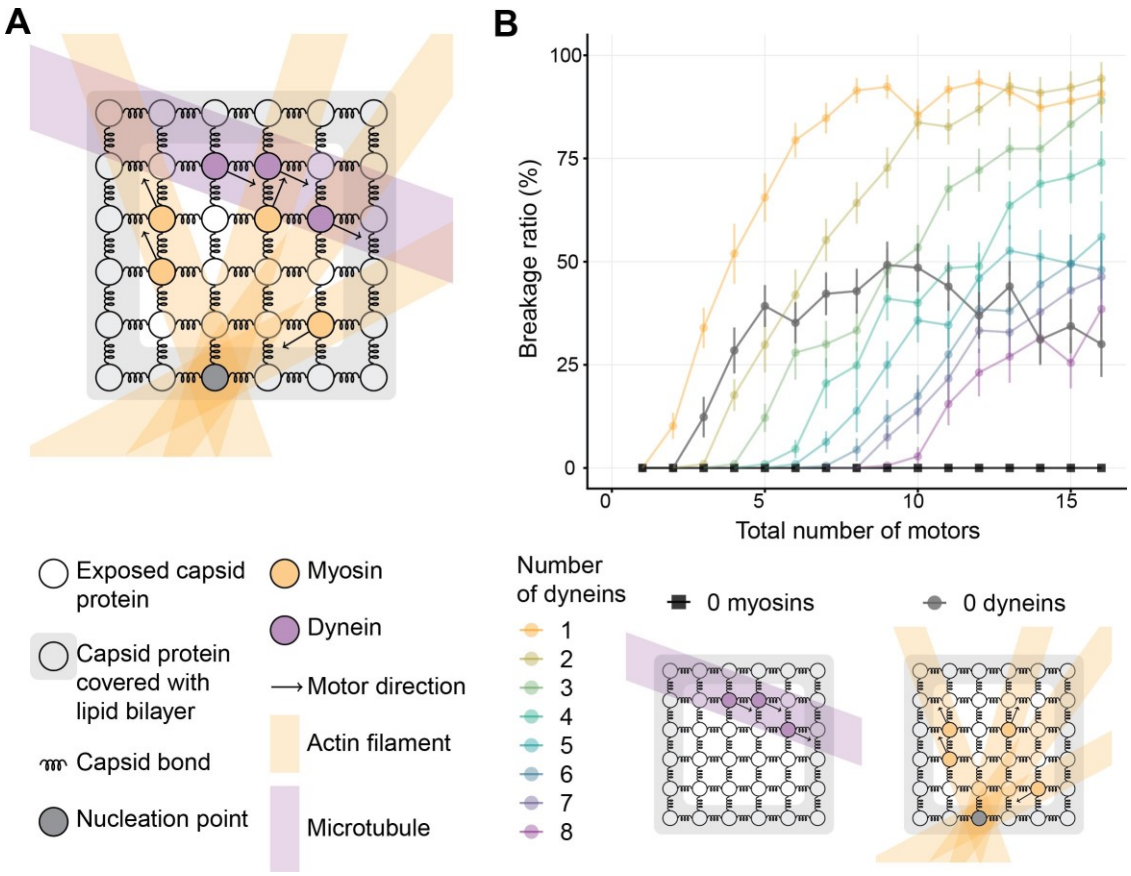

Figure 2: A mass-spring model for capsid-motor interactions predicts that motor forces suffice for efficient virus uncoating.

(A) Structure of the two-dimensional viral capsid model. Exposed M1 protein in the viral capsid is represented as a square grid with edges anchored in the lipid bilayer. One microtubule is randomly oriented relative to the capsid. Dynein and myosin motors are attached to the exposed capsid proteins. Dyneins are only able to move along the microtubule, while myosins can move in any direction along the dense actin filament network anchored at the fusion pore with the nucleation point (see Methods for details).

(B) Predicted capsid breakage probabilities for varying numbers of myosin and dynein motors, and combinations thereof, when they are attached to the capsid. Simulation results are presented as means and standard deviations for at least 100 random motor configurations. Insets illustrate geometries of selected configurations as in (A).

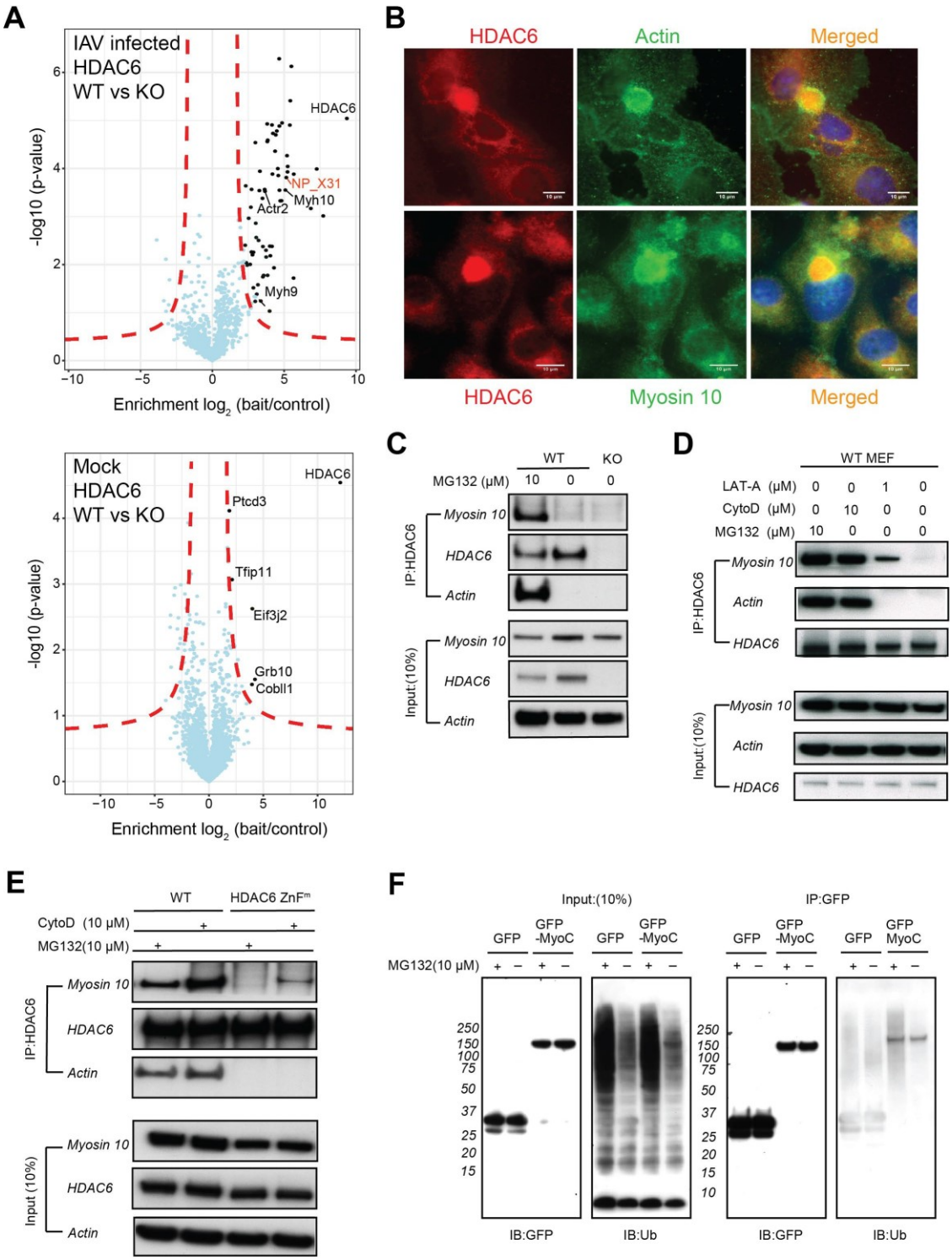

Figure 3: Formation of a complex between HDAC6, actin, myosin 10 and Ub.

(A) HDAC6 interactome under influenza A virus infection. HDAC6 was immunoprecipitated from HDAC6 wild type (WT) or knock-out (KO) MEF cells that had been infected with IAV (strain X31, upper panel) or mock-treated (lower panel). Interactors were analyzed by LC-MS/MS. The HDAC6 KO cells allowed to subtract non-specific interactors. Statistical analysis was done in Perseus (version 1.5.2.6) and potential interactors were

determined using Student's two-tailed t-test and visualized by a volcano plot. Red dashed lines denote a given false detection rate (FDR) and estimate of the volatility of the measurement ('fudge factor', s0) (0.01 and 2, respectively). The viral protein NP (red) indicates a successful infection. Myosin 10 (Myh10) is indicated.

(B) HDAC6, as well as Actin (top) and Myosin 10 (bottom) are enriched at the aggresome. A549 cells were treated to induce aggresome formation (5 μM MG132, 18 hrs) and immunofluorescence microscopy was used to visualize the localization of HDAC6 (red), Actin (green) or Myosin 10 (green). DAPI (blue) was used to visualize the nucleus. Scale bar = 10 μm.

(C) HDAC6 recruits actomyosin under conditions of aggresome formation. MEF cells (WT, wild type; KO, HDAC6 knock-out) were treated with MG132 (10 μM, 6hrs) to induce aggresome formation, or control-treated with the vehicle DMSO, and HDAC6 was immunoprecipitated from cell lysates. The presence of diverse proteins in the precipitate (IP) or in the input lysate was determined by immunoblotting with the indicated antibodies.

(D) HDAC6 interacts with filamentous actin. MEF cells were treated with Latrunculin A (LAT-A) or Cytochalasin D (CytoD), two drugs that lead to formation of an aggresome-like structure, or control- treated with DMSO, and actin/myosin recruitment was tested by immunoprecipitation of endogenous HDAC6 followed by immunoblotting with the indicated antibodies.

(E) Recruitment of actin and myosin 10 by HDAC6 requires binding to Ub. WT or HDAC6 ZnF mutant MEF cells were treated with CytoD or MG132 and used for HDAC6 immunoprecipitation assays followed by immunoblotting analysis.

(F) Myosin10 interacts with poly-Ub chains. GFP-tagged Myosin10 C-terminal (1103-2007) cargo binding region (GFP-MyoC) was expressed in A549 cells which were treated with MG132, as indicated. Lysates were prepared and GFP proteins were captured with GFP-trap beads; recruitment of Ub was detected by immunoblotting (IB). Left two panels, input; right two panels, GFP immunoprecipitation. A robust enrichment of poly-Ub chains is observed when MyoC is immunoprecipitated from MG132-treated cells.

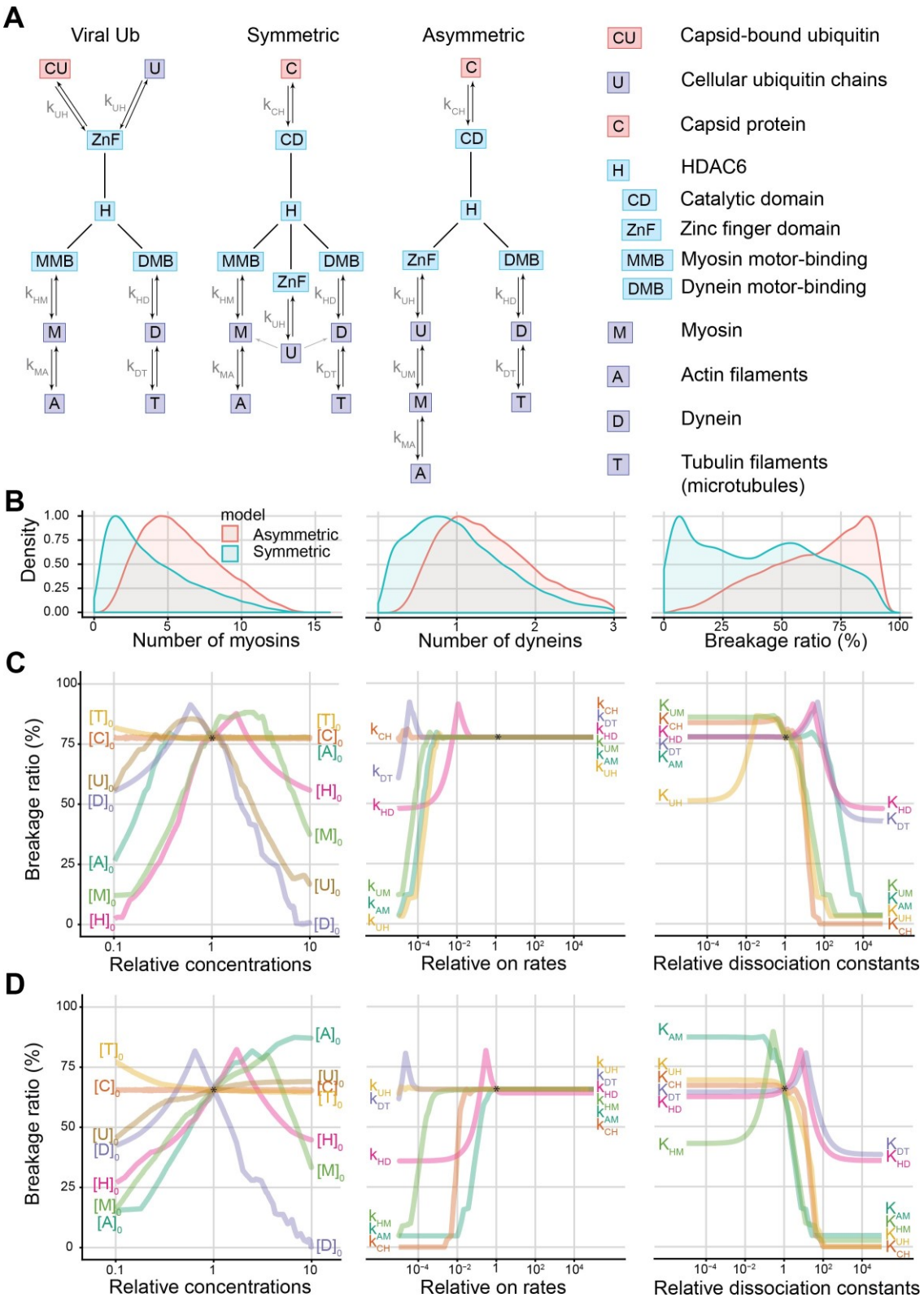

Figure 4: An in vivo reaction model elucidates biochemical interaction mechanisms involved in capsid breakage.

(A) Interaction schematics for the three reaction model variants. Nodes represent proteins or protein domains (linked by solid lines) and arrows denote biochemical reactions with their dissociation constants indicated next to the arrows. Node colors distinguish between viral proteins (red), HDAC6 (cyan), and other host proteins (purple).

(B) Density distributions of number of myosin motors (left), number of dynein motors (middle), and capsid breakage probabilities (right) for the 'Symmetric' and 'Asymmetric' reaction model variants. Initial concentrations and reaction rate constants were sampled uniformly around literature values and rate constant values were adjusted accordingly. The 'Asymmetric' model variant allows for relatively high amounts of myosins and dyneins, and total highest breakage probability (see Methods for details). All the densities were normalized by their peak for easier comparison.

(C), (D) Influence of varying individual initial protein abundances and reaction rate parameters on the capsid breakage probability for the 'Asymmetric' (C) and 'Symmetric' (D) model. All the varied parameters were normalized by the values corresponding to the reference conditions.

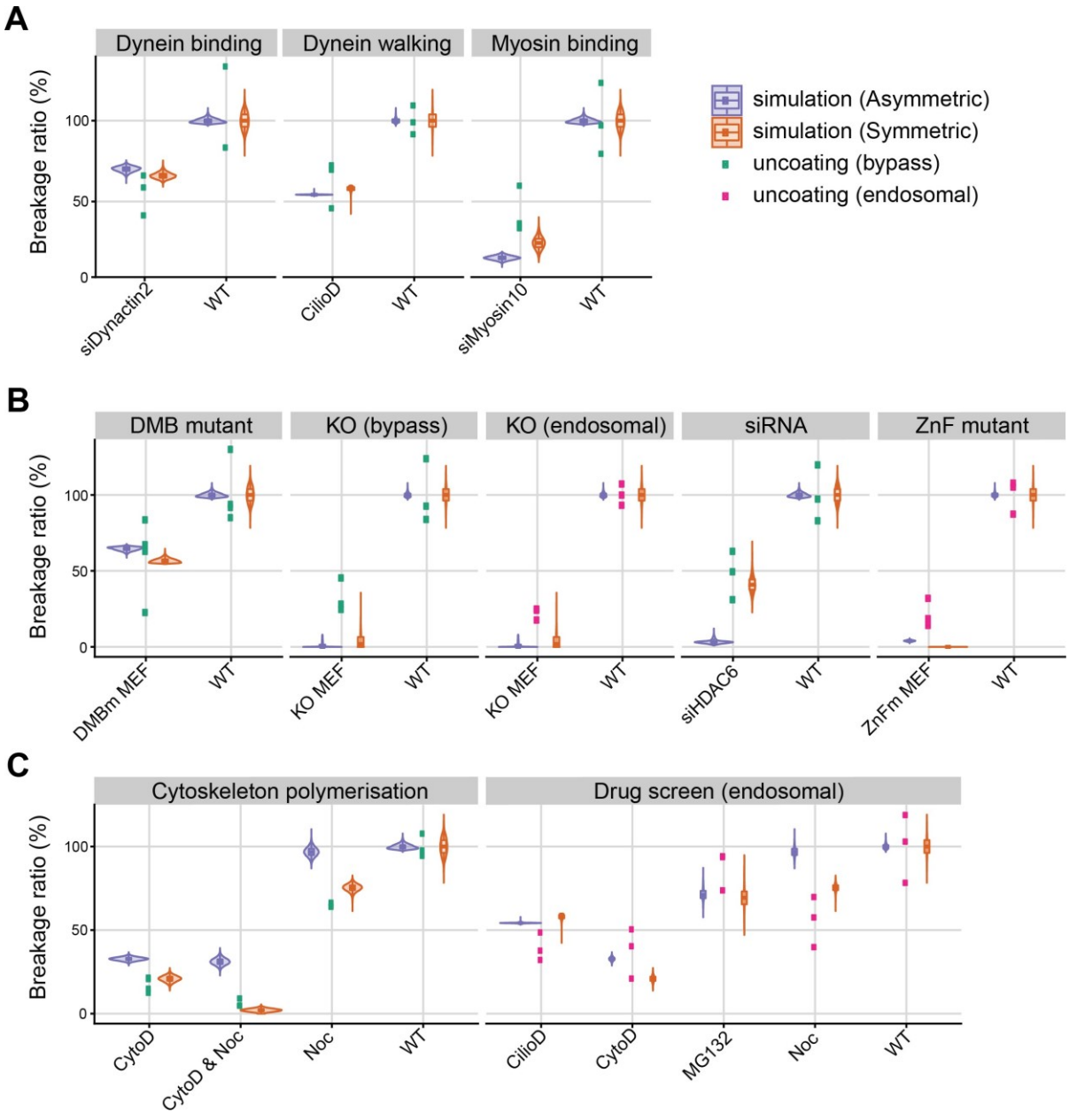

Figure 5: The model predicts in vivo uncoating efficiencies upon perturbations of the host cell.

(A) Perturbations of molecular motors. Grey labels indicate the type of perturbations, and axis labels the specific experimental conditions. Abbreviations: WT, wild type; siDynactin2, siRNA for Dynactin2; CilioD, Ciliobrevin D; siMyosin10, siRNA for myosin10.

(B) Perturbations of HDAC6. Abbreviations: DMBm, dynein motor binding mutant; KO, knock out; MEF, mouse embryonic fibroblasts; siHDAC6, siRNA for HDAC6; ZnFm, zinc finger mutant.

(C) Cytoskeletal perturbations and drug screen for inhibition of endosomal entry. Abbreviations: CytoD, Cytochalasin D; Noc, Nocodazole; CilioD, Ciliobrevin D. All data shown are bypass (emerald) and endosomal

(pink) experimental uncoating efficiencies and capsid breakage probabilities predicted by simulation of the 'Asymmetric' (purple) and 'Symmetric' (orange) reaction model with correspondingly perturbed initial conditions and rate parameters (see Methods for details). Experimental data are from (Banerjee et al., 2014). Functional categories of perturbations are indicated by top gray bars. All data are normalized with respect to the untreated WT.

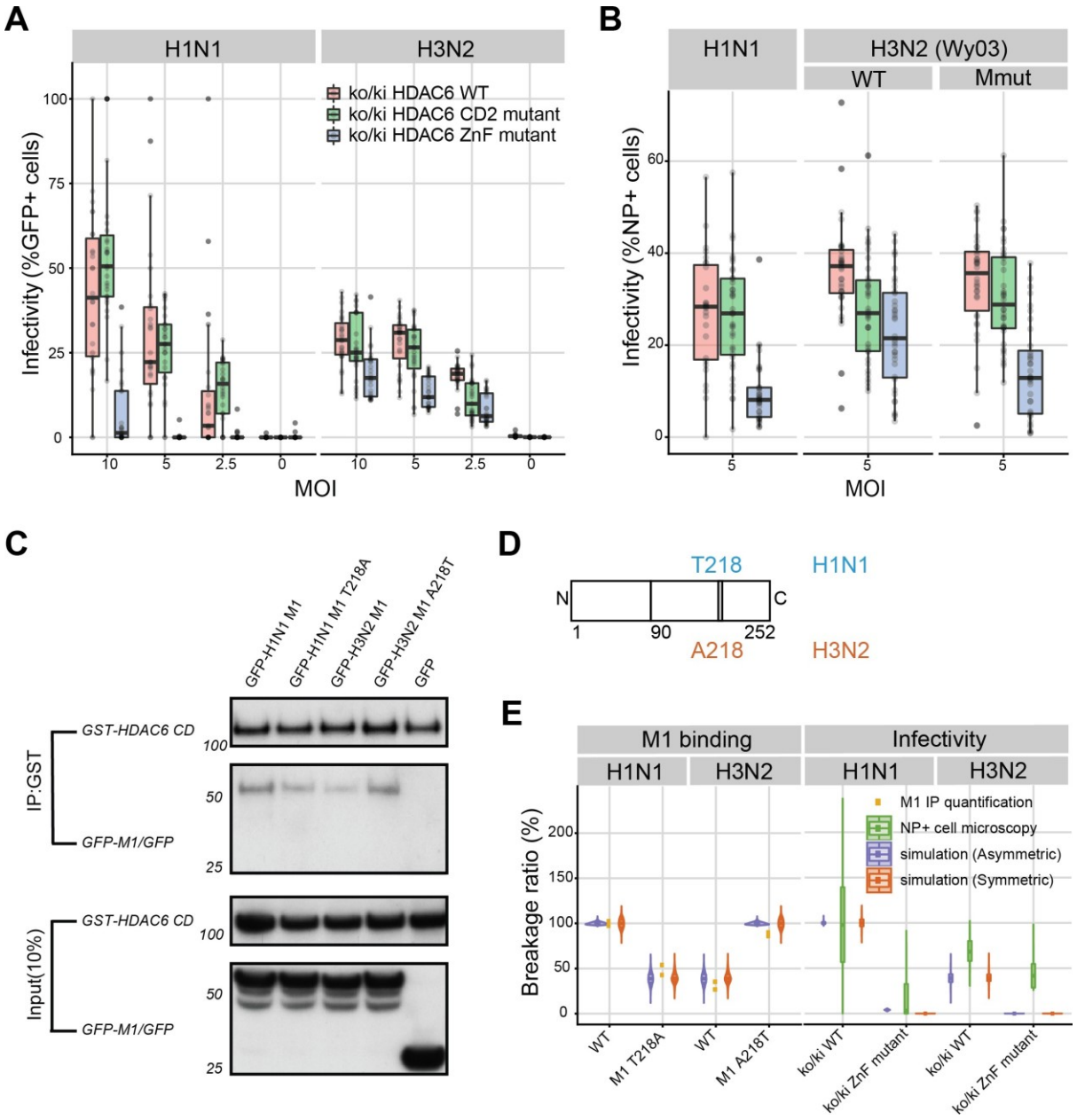

Figure 6: Strength of interaction between influenza M1 and HDAC6 determines dependency on aggresome pathway and infectivity.

(A) Influenza H1N1 shows stronger dependence on the HDAC6/aggresome pathway than H3N2. A549 cells expressing different HDAC6 versions (WT, CD2 mutant or ZnF mutant) were infected with pH1N1 or H3N2 virus at indicated multiplicity of infection (MOI) and cells were stained for viral NP.

(B) Substitution of A218T in M1 of Wy/03 (H3N2) by reverse genetics increases its dependence on HDAC6 for uncoating. A549 cells expressing WT, CD2 mutant or ZnF mutant HDAC6 were infected with 5 MOI of pH1N1, Wy/03 WT or Wy/03 M1 A218T (H3N2) and cells were stained for viral NP.

(C) Preferential interaction of viral H1N1 M1 protein with HDAC6 depends on residue T218. GFP- M1 fusion proteins (H1N1 WT or T218A, H3N2 WT or A218T) were transiently expressed in 293Tcells and lysates were incubated with purified GST-HDAC6 (amino acids 82-837, catalytic domains) protein. GST-Trap beads were used to capture HDAC6 and associated proteins. The presence of diverse proteins in the precipitate (IP) or in the input lysate was determined by immunoblotting with anti-GFP (M1) or anti-GST (HDAC6) antibodies.

(D) Schematic of H1N1 vs H3N2 M1, highlighting residue 218.

(E) Experimental M1 IP quantification data from (C, yellow) and NP+ cell microscopy from (B, green) viral activities for perturbations of viral protein M1 variant for H1N1 and H3N2 viruses, compared against capsid breakage probabilities predicted by simulation of the ‘Asymmetric’ (purple) and ‘Symmetric’ (orange) reaction model with correspondingly perturbed initial conditions and rate parameters (see Methods for details). Abbreviations: IP, immunoprecipitation; NP+, nucleoprotein positive; ko/ki, knock out/knock in; WT, wild type; ZnF, zinc fing

Supplemental figures

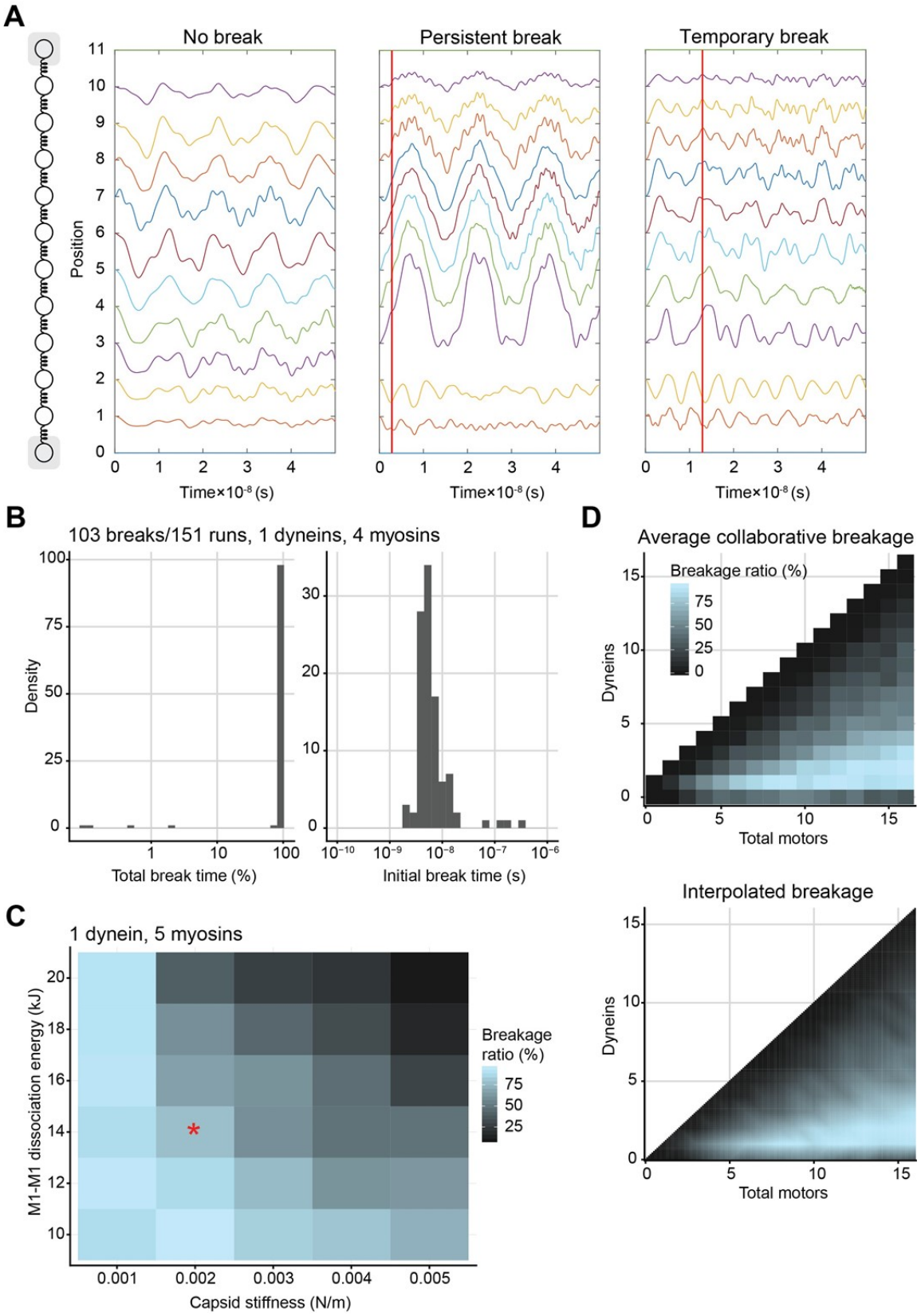

Figure S1: Mass-Spring Grid algorithm

(A) Non-break (left), persistent break (middle), and momentary break (right) scenarios for a one- dimensional protein mass-spring example (left scheme). Initial break times are indicated by vertical red lines. A break is considered to occur if the distance between any two adjacent nodes at any time exceeds two. A break is considered persistent if the system spends more than half of the simulation time points broken.

(B) The total break time (fraction of time points in which the system is broken) and initial break times for simulations where breakage occurred for a 4x4 grid with one dynein and four myosin motors. Most simulations that achieve a break have the initial break early on (~10-8 s, for a total 10-6 s simulation time).

(C) Higher stiffness and dissociation energy of the capsid protein M1-M1 bond lead to a lower capsid breakage probability. The red * symbol indicates stiffness and dissociation energy values reported in the literature, used for our simulations (see STAR Methods for details).

(D) Collaborative breakage by myosin and dynein motors (left) and the interpolated capsid breakage probability (right) that is used to estimate capsid breakage in the reaction model.

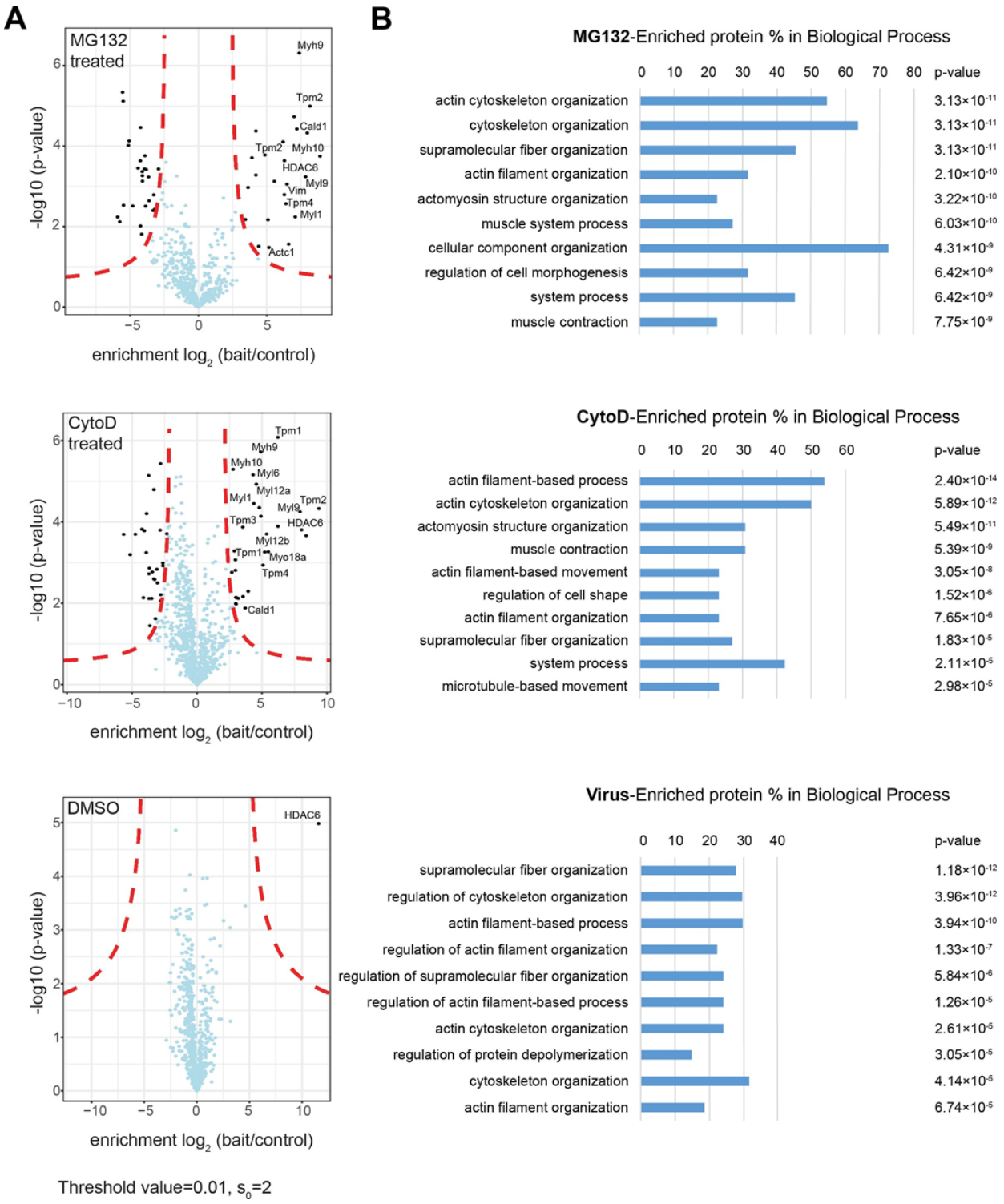

Figure S2-1: HDAC6 interactome under proteasome inhibition or actin network disruption in MEF cells

(A) Volcano plot from LC-MS analysis of the HDAC6 interactome under proteasome stress (MG132 treatment), actin stress (CytoD treatment) and control (DMSO) conditions. Following treatment of the cells, endogenous HDAC6 was immunoprecipitated with a polyclonal anti-HDAC6 antibody) and interacting proteins were analyzed by LC-MS/MS. Statistical analysis was done in MaxQuant (version: 1.5.3.8) (Tyanova et al., 2016) using biologically independent samples (n = 3); potential interactors were determined using Student's two-tailed t-test

and visualized by a volcano plot. Red dashed lines correspond to FDR = 0.01 and SO = 2. Identified interactors were annotated with Perseus (version 1.5.2.6). Each plot represents the comparison of the results obtained in WT vs HDAC6-deficient cells. Proteins at the right side of the plot and labeled are enriched.

(B) Pathway analysis of HDAC6 interacting proteins. Enriched proteins in each experiment in (A) were analyzed with STRING (Szklarczyk et al., 2019), and the biological processes involved were determined. From top to bottom, the false discovery rate is increasing (indicated in the right by P value). Actin cytoskeleton organization, actin filament organization and supramolecular fiber organization are enriched pathways in all three experimental conditions; in addition, actin-related processes are also frequently observed in the analysis.

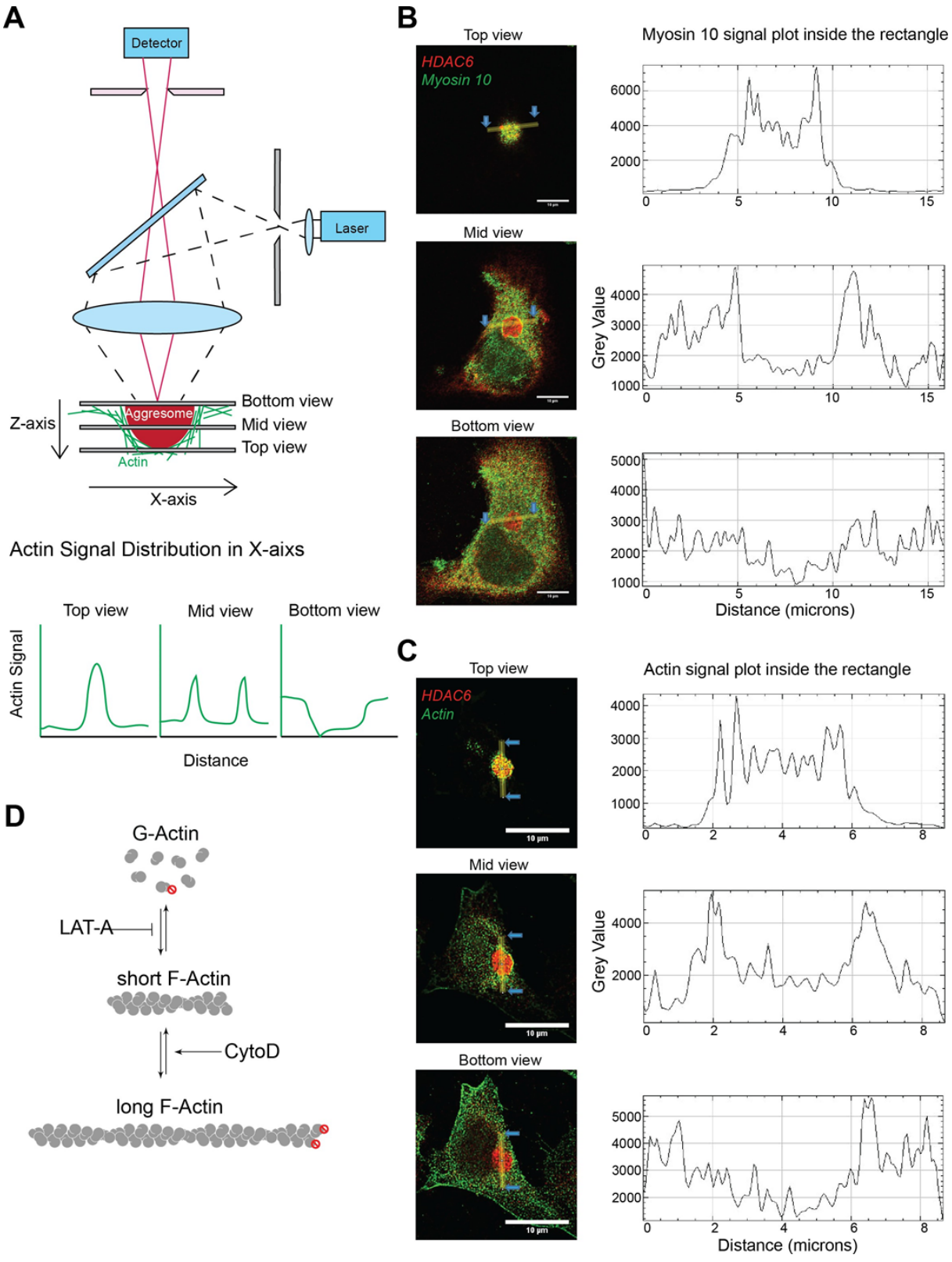

Figure S2-2: Myosin 10 and Actin form a cage around the HDAC6-enriched aggresome

(A) Scheme of the method to determine the actin or myosin 10 signal distribution around the aggresome by confocal microscopy.

(B) Myosin 10 is distributed around the aggresome. A549 cells were treated with MG132 and myosin 10 (green) was stained by an anti-myosin 10 antibody. The photographs show the myosin 10 signal across 3 planes, from top to bottom. Next to each picture a graph shows the corresponding signal intensity of a longitudinal cross-section across the aggresome (indicated in the picture by the line between 2 blue arrows, from left/top to right/bottom). Two signal peaks are visible at the rim of the aggresome, with much higher intensity than the signal in the cytosol or in the aggresome. This indicates an enrichment of myosin 10 around the aggresome.

(C) Actin is distributed around the aggresome. Actin was stained by an anti-actin antibody and analysis was done as in (B). Together with the widefield microscopy data in Figure 3B, this shows that both myosin 10 and actin form a cage around the aggresome.

(D) Schematic representation of actin polymerization inhibition by LAT-A and CytoD.

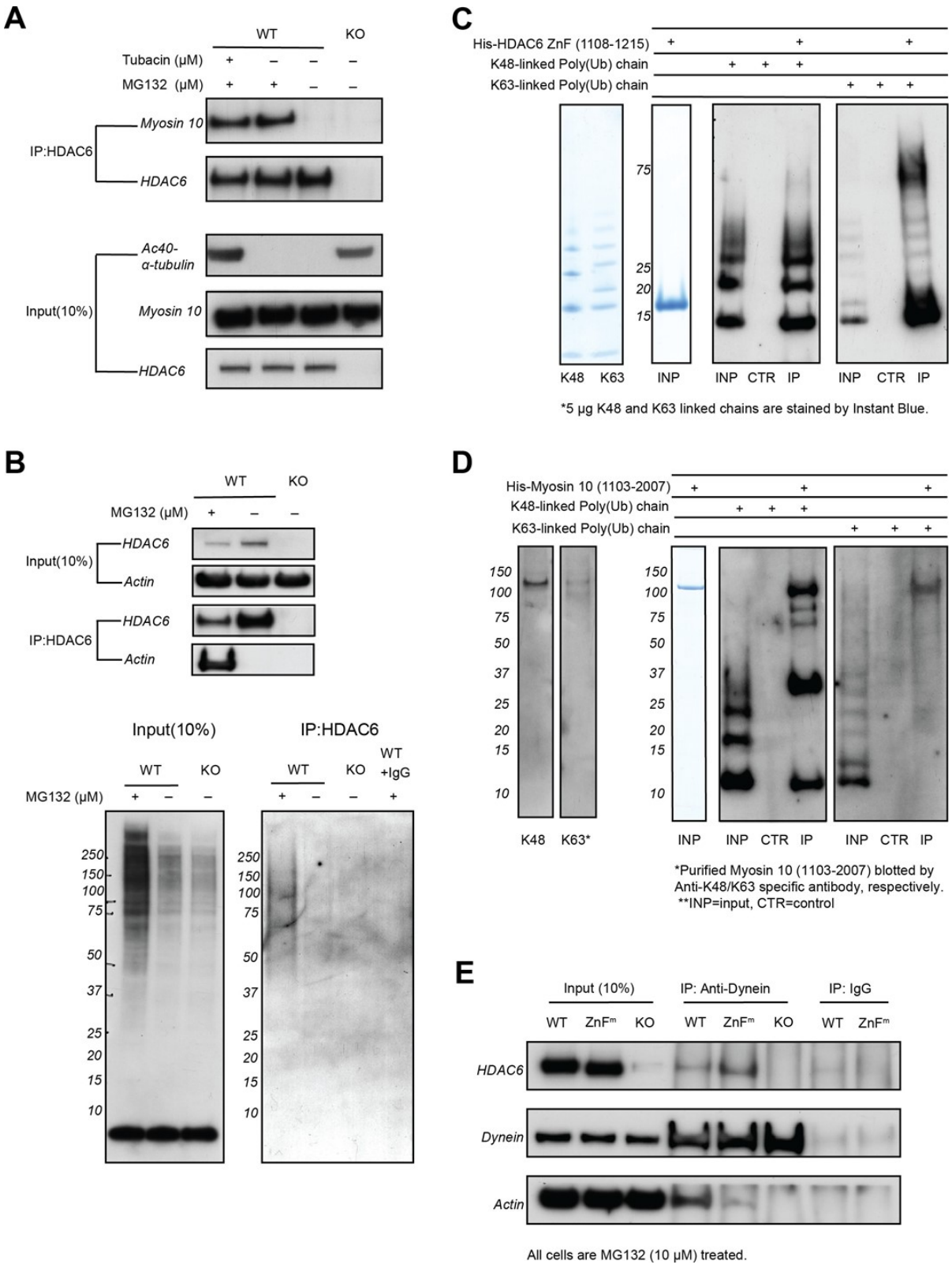

Figure S2-3: HDAC6 ZnF and myosin 10 C-terminal domain both interact with poly-Ub chains

(A) Inhibition of HDAC6 catalytic activity does not affect HDAC6-myosin 10 interaction under proteasome inhibition. Immunoprecipitation of endogenous HDAC6 can still capture myosin 10 from cell lysate in the presence of the HDAC6 inhibitor Tubacin.

(B) Immunoprecipitation of endogenous HDAC6 pulls down high molecular weight Ub (poly-Ub chains) from cell lysate under proteasome inhibition (MG132). Intriguingly, mono-Ub is not observed under these conditions.

(C) Purified HDAC6 ZnF domain interacts with both K48- and K63-linked poly-Ub chains. Purified His-ZnF domain was incubated together with K48- or K63-linked poly-Ub chains followed by pull- down of the ZnF domain and extensive wash. The Ub signal was detected by immunoblotting with specific anti-K48 or anti-K63 antibodies.

(D) Purified myosin 10 C-terminal region (1103-2007) interacts preferentially with K48-linked poly- Ub chains. Similar to (C), in vitro pull-down assay was done with purified His-myosin 10 (1103-2007) and K48- or K63-linked poly-Ub chains. The Ub signal was detected by immunoblotting by specific antibodies, as above. Note the ubiquitination (K48- and K63-linked) of purified myosin 10 (1103- 2007) during expression in insect cells. This explains why in the final IP panel Ub signals are visible around the myosin 10 (1103-2007) molecular weight.

(E) Increased interaction of HDAC6 ZnF mutant (W1116A) with dynein complex. MEF cells expressing WT or ZnF mutant HDAC6 were treated with MG132 (10 μM) and after lysate preparation, dynein was immunoprecipitated followed by immunoblotting. Note that the ZnF mutant, which frees HDAC6 from Ub/poly-Ub chain binding, helps HDAC6 interaction with the dynein motor complex, with a 50% increase in the pulled-down HDAC6 signal.

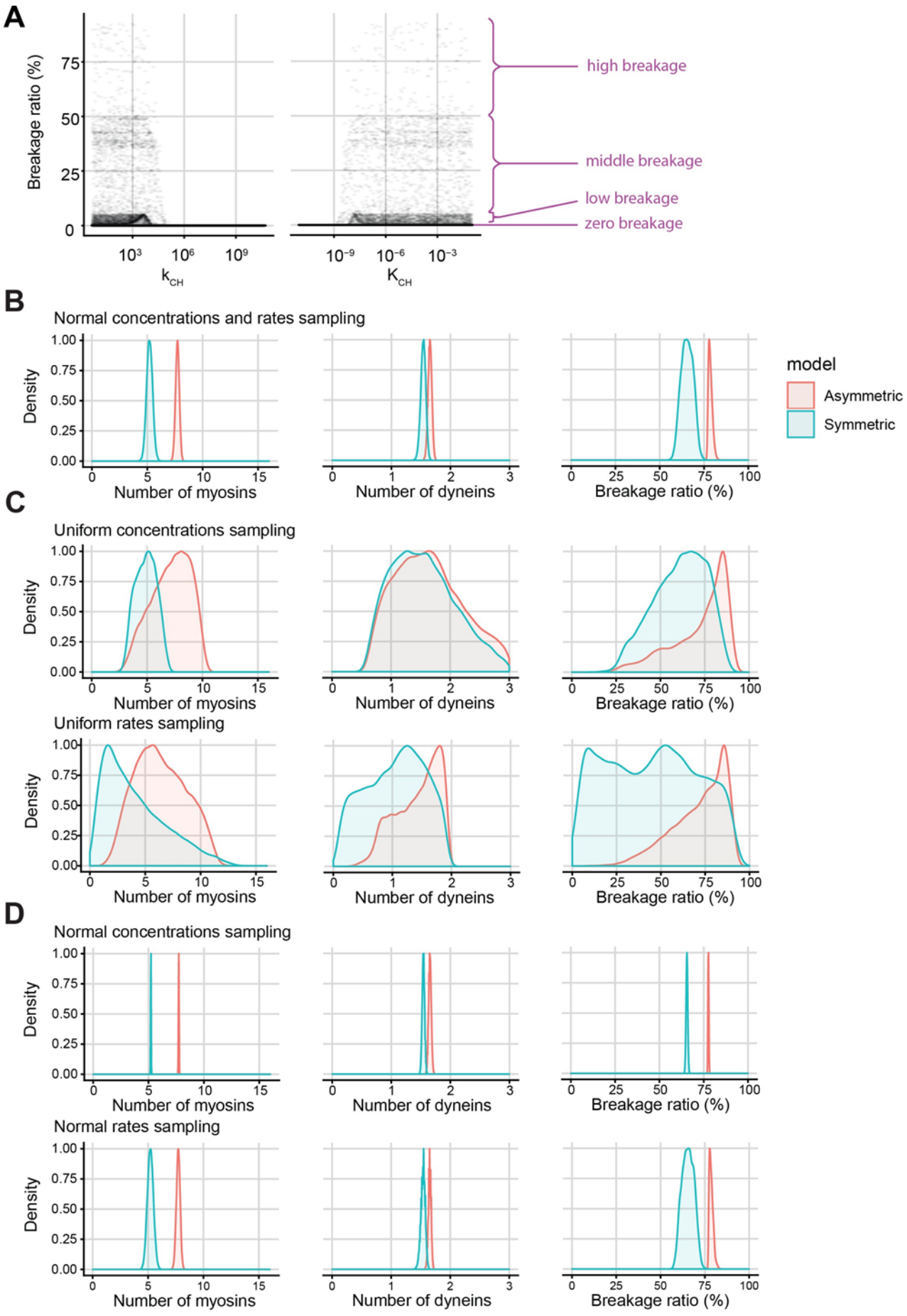
A
Breakage ratio (%)
75
50
25
0
high breakage
middle breakage
low breakage
zero breakage
10^3 10^6 10^9
k_{CH}
10^{-9} 10^{-6} 10^{-3}
K_{CH}
B
Normal concentrations and rates sampling
Density
1.00
0.75
0.50
0.25
0.00
Number of myosins
Number of dyneins
Breakage ratio (%)
model
Asymmetric
Symmetric
C
Uniform concentrations sampling
Uniform rates sampling
D
Normal concentrations sampling
Normal rates sampling

Figure S3: Reaction Model Analysis

(A) Breakage ratio modes observed after wide sampling around approximate values available in the literature. We optimized the reaction rates using the high breakage mode because it manages to efficiently recruit both myosin and dynein motors.

(B) Reaction models' density profiles for the numbers of myosin and dynein motors and for the estimated capsid breakage ratio for normally jointly sampled rates and concentrations.

(C) Density profiles as in (B) for uniformly separately sampled rates or concentrations.

(D) Density profiles as in (B) for normally separately sampled rates or concentrations. In (B)-(D) models are marked analogously to Figure 4.

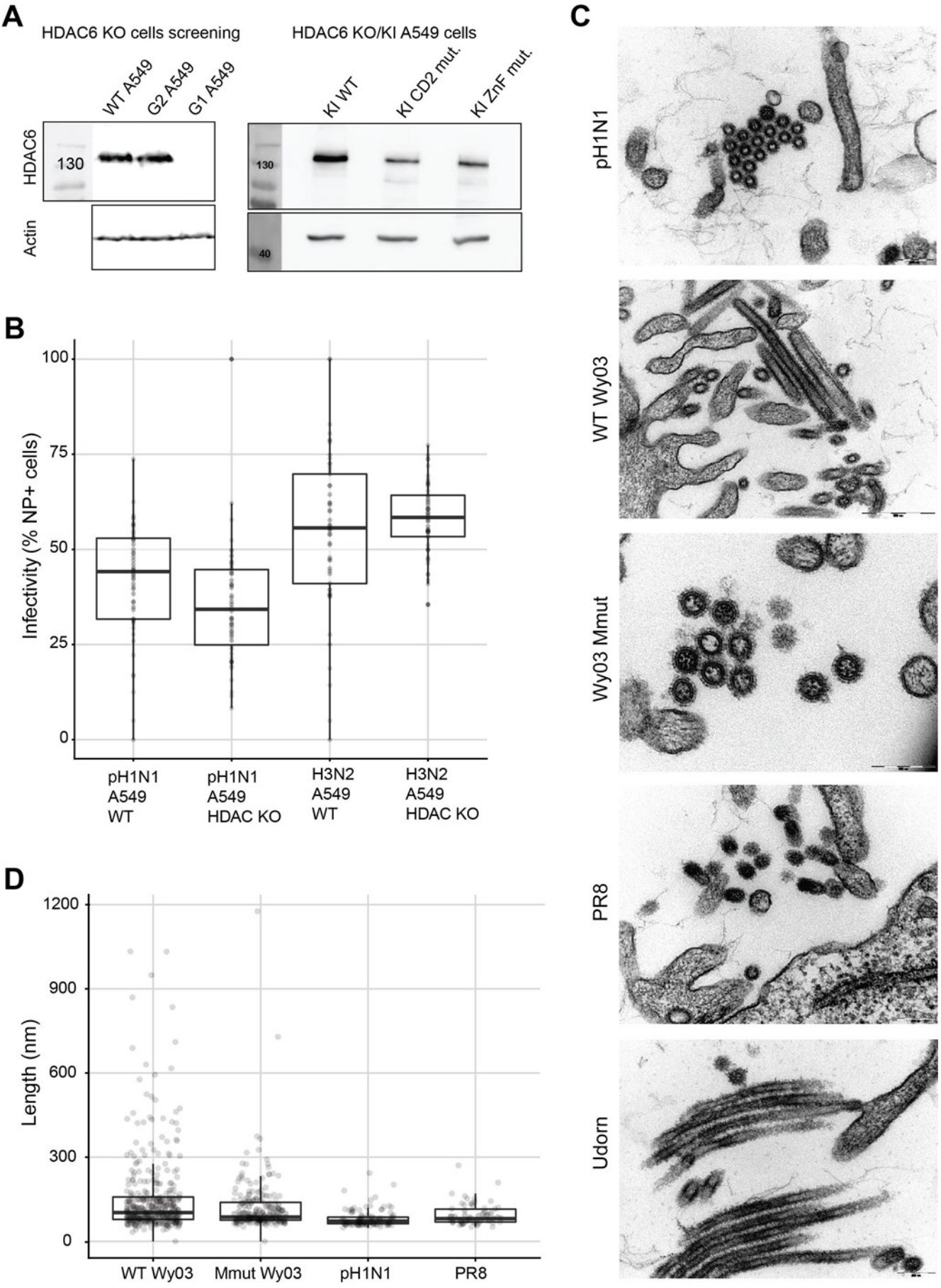
A
HDAC6 KO cells screening
HDAC6 KO/KI A549 cells
WT A549
G2 A549
G1 A549
KI WT
KI CD2 mut.
KI ZnF mut.
HDAC6
130
Actin
130
40
B
Infectivity (% NP+ cells)
100
75
50
25
0
pH1N1 A549 WT
pH1N1 A549 HDAC KO
H3N2 A549 WT
H3N2 A549 HDAC KO
C
pH1N1
WT Wy03
Wy03 Mmut
PR8
Udorn
D
Length (nm)
1200
900
600
300
0
WT Wy03
Mmut Wy03
pH1N1
PR8

Figure S4: Viral morphology.

(A) HDAC6 knockouts were generated by CRISPR Cas 9 (left panel gRNA1) and reconstituted with WT, CD2 mutant or Znf mutant HDAC6 (right panel) by lentiviral transduction.

(B) Multicycle growth curves of A/Wyoming/03/2003 WT or M1 A218T mutant in (left panel) A549 HDAC6wt reconstituted HDAC6 knockout cells or (right panel) A549 HDAC6 ZnF mutant reconstituted HDAC6 knockout cells.

(C) The A218T substitution affects virus morphology. MDCK infected at MOI 10 and fixed 10 hpi. Scale bar: 500 nm for WT WY03, otherwise 200 nm. Medians with interquartile ranges.

(D) Viral particles length. Boxes show median and interquartile ranges.

References

Anchisi, S., Goncalves, A.R., Mazel-Sanchez, B., Cordey, S., and Schmolke, M. (2018). Influenza A Virus Genetic Tools: From Clinical Sample to Molecular Clone. Methods Mol Biol 1836, 33-58.

Banerjee, I., Miyake, Y., Nobs, S.P., Schneider, C., Horvath, P., Kopf, M., Matthias, P., Helenius, A., and Yamauchi, Y. (2014). Influenza A virus uses the aggresome processing machinery for host cell entry. Science 346, 473-477.

Banerjee, I., Yamauchi, Y., Helenius, A., and Horvath, P. (2013). High-content analysis of sequential events during the early phase of influenza A virus infection. PloS one 8, e68450.

Brandariz-Nuñez, A., Liu, T., Du, T., and Evilevitch, A. (2019). Pressure-driven release of viral genome into a host nucleus is a mechanism leading to herpes infection. eLife 8, e47212.

Carnes, S.K., Zhou, J., and Aiken, C. (2018). HIV-1 Engages a Dynein-Dynactin-BICD2 Complex for Infection and Transport to the Nucleus. Journal of virology 92, e00358-00318.

Dadonaite, B., Vijayakrishnan, S., Fodor, E., Bhella, D., and Hutchinson, E.C. (2016). Filamentous influenza viruses. J Gen Virol 97, 1755-1764.

Elleman, C.J., and Barclay, W.S. (2004). The M1 matrix protein controls the filamentous phenotype of influenza A virus. Virology 321, 144-153.

Fernandez, J., Machado, A.K., Lyonnais, S., Chamontin, C., Gärtner, K., Léger, T., Henriquet, C., Garcia, C., Portilho, D.M., and Pugnière, M. (2019). Transportin-1 binds to the HIV-1 capsid via a nuclear localization signal and triggers uncoating. Nat Microbiol 4, 1840-1850.

Flatt, J.W., and Butcher, S.J. (2019). Adenovirus flow in host cell networks. Open Biology 9, 190012.

Francis, A.C., Marin, M., Shi, J., Aiken, C., and Melikyan, G.B. (2016). Time-resolved imaging of single HIV-1 uncoating in vitro and in living cells. PLoS pathogens 12, e1005709.

Gennerich, A., Carter, A.P., Reck-Peterson, S.L., and Vale, R.D. (2007). Force-induced bidirectional stepping of cytoplasmic dynein. Cell 131, 952-965.

Gonnet, P., Dimopoulos, S., Widmer, L., and Stelling, J. (2012). A specialized ODE integrator for the efficient computation of parameter sensitivities. BMC systems biology 6, 46.

Greber, U.F., and Flatt, J.W. (2019). Adenovirus Entry: From Infection to Immunity. Annual Review of Virology.

Gschweitl, M., Ulbricht, A., Barnes, C.A., Enchev, R.I., Stoffel-Studer, I., Meyer-Schaller, N., Huotari, J., Yamauchi, Y., Greber, U.F., and Helenius, A. (2016). A SPOPL/Cullin-3 ubiquitin ligase complex regulates endocytic trafficking by targeting EPS15 at endosomes. eLife 5, e13841.

Hai, Y., and Christianson, D.W. (2016). Histone deacetylase 6 structure and molecular basis of catalysis and inhibition. Nature Chemical Biology 12, 741.

Hancock, W.O. (2014). Bidirectional cargo transport: moving beyond tug of war. Nature Reviews Molecular Cell Biology 15, 615.

He, F., Wollscheid, H.-P., Nowicka, U., Biancospino, M., Valentini, E., Ehlinger, A., Acconcia, F., Magistrati, E., Polo, S., and Walters, K.J. (2016). Myosin VI contains a compact structural motif that binds to ubiquitin chains. Cell reports 14, 2683-2694.

Helenius, A. (2018). Virus Entry: Looking Back and Moving Forward. Journal of molecular biology 430, 1853-1862.

Hilsch, M., Goldenbogen, B., Sieben, C., Hofer, C.T., Rabe, J.P., Klipp, E., Herrmann, A., and

Chiantia, S. (2014). Influenza A matrix protein M1 multimerizes upon binding to lipid membranes. Biophysical journal 107, 912-923.

Hook, S.S., Orian, A., Cowley, S.M., and Eisenman, R.N. (2002). Histone deacetylase 6 binds polyubiquitin through its zinc finger (PAZ domain) and copurifies with deubiquitinating enzymes. Proceedings of the National Academy of Sciences 99, 13425-13430.

Hubbert, C., Guardiola, A., Shao, R., Kawaguchi, Y., Ito, A., Nixon, A., Yoshida, M., Wang, X.-F., and Yao, T.-P. (2002). HDAC6 is a microtubule-associated deacetylase. Nature 417, 455-458.

Huotari, J., Meyer-Schaller, N., Hubner, M., Stauffer, S., Katheder, N., Horvath, P., Mancini, R., Helenius, A., and Peter, M. (2012). Cullin-3 regulates late endosome maturation. Proceedings of the National Academy of Sciences of the United States of America 109, 823-828.

James, L.C., and Jacques, D.A. (2018). The Human Immunodeficiency Virus Capsid Is More Than Just a Genome Package. Annu Rev Virol 5, 209-225.

Johnston, J.A., Ward, C.L., and Kopito, R.R. (1998). Aggresomes: A Cellular Response to Misfolded Proteins. The Journal of Cell Biology 143, 1883-1898.

Kawaguchi, Y., Kovacs, J.J., McLaurin, A., Vance, J.M., Ito, A., and Yao, T.P. (2003). The deacetylase HDAC6 regulates aggresome formation and cell viability in response to misfolded protein stress. Cell 115, 727-738.

Kovacs, J.J., Murphy, P.J.M., Gaillard, S., Zhao, X., Wu, J.-T., Nicchitta, C.V., Yoshida, M., Toft, D.O., Pratt, W.B., and Yao, T.-P. (2005). HDAC6 Regulates Hsp90 Acetylation and Chaperone-Dependent Activation of Glucocorticoid Receptor. Molecular cell 18, 601-607.

Kural, C., Kim, H., Syed, S., Goshima, G., Gelfand, V.I., and Selvin, P.R. (2005). Kinesin and Dynein Move a Peroxisome in Vivo: A Tug-of-War or Coordinated Movement? Science 308, 1469-1472.

Kwon, S., Zhang, Y., and Matthias, P. (2007). The deacetylase HDAC6 is a novel critical component of stress granules involved in the stress response. Genes & development 21, 3381-3394.

Larson, G.P., Tran, V., Yú, S., Caì, Y., Higgins, C.A., Smith, D.M., Baker, S.F., Radoshitzky, S.R., Kuhn, J.H., and Mehle, A. (2019). EPS8 Facilitates Uncoating of Influenza A Virus. Cell Reports 29, 2175- 2183.e2174.

Lázaro-Diéguez, F., Aguado, C., Mato, E., Sánchez-Ruíz, Y., Esteban, I., Alberch, J., Knecht, E., and Egea, G. (2008). Dynamics of an F-actin aggresome generated by the actin-stabilizing toxin jasplakinolide. J Cell Sci 121, 1415-1425.

Lukic, Z., Dharan, A., Fricke, T., Diaz-Griffero, F., and Campbell, E.M. (2014). HIV-1 Uncoating Is Facilitated by Dynein and Kinesin 1. Journal of virology 88, 13613-13625.

Malikov, V., and Naghavi, M.H. (2017). Localized Phosphorylation of a Kinesin-1 Adaptor by a Capsid- Associated Kinase Regulates HIV-1 Motility and Uncoating. Cell Reports 20, 2792-2799.

Marquez, C.L., Lau, D., Walsh, J., Shah, V., McGuinness, C., Wong, A., Aggarwal, A., Parker, M.W., Jacques, D.A., and Turville, S. (2018). Kinetics of HIV-1 capsid uncoating revealed by single-molecule analysis. eLife 7, e34772.

Marsh, M., and Helenius, A. (2006). Virus Entry: Open Sesame. Cell 124, 729-740.

Miyake, Y., Keusch, J.J., Decamps, L., Ho-Xuan, H., Iketani, S., Gut, H., Kutay, U., Helenius, A., and Yamauchi, Y. (2019). Influenza virus uses transportin 1 for vRNP debundling during cell entry. Nature Microbiology 4, 578-586.

Muller, M.J., Klumpp, S., and Lipowsky, R. (2008). Tug-of-war as a cooperative mechanism for bidirectional cargo transport by molecular motors. Proceedings of the National Academy of Sciences of the United States of America 105, 4609-4614.

Müller, M.J., Klumpp, S., and Lipowsky, R. (2008). Tug-of-war as a cooperative mechanism for bidirectional cargo transport by molecular motors. Proceedings of the National Academy of Sciences 105, 4609-4614.

Naghavi, M.H., Walsh, D., and Glaunsinger, B.A. (2017). Microtubule Regulation and Function during Virus Infection. Journal of virology 91.

Norstrom, M.F., Smithback, P.A., and Rock, R.S. (2010). Unconventional processive mechanics of non- muscle myosin IIB. The Journal of biological chemistry 285, 26326-26334.

Ortega-Esteban, A., Bodensiek, K., San Martín, C., Suomalainen, M., Greber, U.F., de Pablo, P.J., and Schaap, I.A.T. (2015). Fluorescence Tracking of Genome Release during Mechanical Unpacking of Single Viruses. ACS Nano 9, 10571-10579.

Ortega-Esteban, A., Pérez-Berná, A.J., Menéndez-Conejero, R., Flint, S.J., Martín, C.S., and de Pablo, P.J. (2013). Monitoring dynamics of human adenovirus disassembly induced by mechanical fatigue. Scientific Reports 3, 1434.

Ouyang, H., Ali, Y.O., Ravichandran, M., Dong, A., Qiu, W., MacKenzie, F., Dhe-Paganon, S., Arrowsmith, C.H., and Zhai, R.G. (2012). Protein aggregates are recruited to aggresome by histone deacetylase 6 via unanchored ubiquitin C termini. The Journal of biological chemistry 287, 2317-2327.

Qin, C., Li, W., Li, Q., Yin, W., Zhang, X., Zhang, Z., Zhang, X.-E., and Cui, Z. (2019). Real-time dissection of dynamic uncoating of individual influenza viruses. Proceedings of the National Academy of Sciences 116, 2577-2582.

Radtke, K., Kieneke, D., Wolfstein, A., Michael, K., Steffen, W., Scholz, T., Karger, A., and Sodeik, B. (2010). Plus- and Minus-End Directed Microtubule Motors Bind Simultaneously to Herpes Simplex Virus Capsids Using Different Inner Tegument Structures. PLoS pathogens 6, e1000991.

Ran, F.A., Hsu, P.D., Wright, J., Agarwala, V., Scott, D.A., and Zhang, F. (2013). Genome engineering using the CRISPR-Cas9 system. Nat Protoc 8, 2281-2308.

Rankovic, S., Varadarajan, J., Ramalho, R., Aiken, C., and Rousso, I. (2017). Reverse Transcription Mechanically Initiates HIV-1 Capsid Disassembly. Journal of virology 91, e00289-00217.

Rawle, D.J., and Harrich, D. (2018). Toward the "unravelling" of HIV: Host cell factors involved in HIV-1 core uncoating. PLoS pathogens 14, e1007270.

Saito, M., Hess, D., Eglinger, J., Fritsch, A.W., Kreysing, M., Weinert, B.T., Choudhary, C., and Matthias, P. (2019). Acetylation of intrinsically disordered regions regulates phase separation. Nature Chemical Biology 15, 51-61.

Schliwa, M. (1982). Action of cytochalasin D on cytoskeletal networks. The Journal of cell biology 92, 79- 91.

Schmidt, T., Samaras, P., Frejno, M., Gessulat, S., Barnert, M., Kienegger, H., Krcmar, H., Schlegl, J., Ehrlich, H.-C., Aiche, S., et al. (2018). ProteomicsDB. Nucleic Acids Research 46, D1271-D1281.

Schneider, C.A., Rasband, W.S., and Eliceiri, K.W. (2012). NIH Image to ImageJ: 25 years of image analysis. Nature methods 9, 671-675.

Seigneurin-Berny, D., Verdel, A., Curtet, S., Lemercier, C., Garin, J., Rousseaux, S., and Khochbin, S. (2001). Identification of Components of the Murine Histone Deacetylase 6 Complex: Link between Acetylation and Ubiquitination Signaling Pathways. Molecular and cellular biology 21, 8035-8044.

Soderholm, J.F., Bird, S.L., Kalab, P., Sampathkumar, Y., Hasegawa, K., Uehara-Bingen, M., Weis, K., and Heald, R. (2011). Importazole, a small molecule inhibitor of the transport receptor importin-β. ACS chemical biology 6, 700-708.

Strunze, S., Engelke, Martin F., Wang, I.H., Puntener, D., Boucke, K., Schleich, S., Way, M., Schoenenberger, P., Burckhardt, Christoph J., and Greber, Urs F. (2011). Kinesin-1-Mediated Capsid Disassembly and Disruption of the Nuclear Pore Complex Promote Virus Infection. Cell host & microbe 10, 210-223.

Su, W.C., Chen, Y.C., Tseng, C.H., Hsu, P.W., Tung, K.F., Jeng, K.S., and Lai, M.M. (2013). Pooled RNAi screen identifies ubiquitin ligase Itch as crucial for influenza A virus release from the endosome during virus entry. Proceedings of the National Academy of Sciences of the United States of America 110, 17516- 17521.

Taylor, M.P., Koyuncu, O.O., and Enquist, L.W. (2011). Subversion of the actin cytoskeleton during viral infection. Nature Reviews Microbiology 9, 427.

Tyanova, S., Temu, T., and Cox, J. (2016). The MaxQuant computational platform for mass spectrometry- based shotgun proteomics. Nat Protoc 11, 2301-2319.

Walsh, D., and Naghavi, M.H. (2019). Exploitation of Cytoskeletal Networks during Early Viral Infection. Trends in microbiology 27, 39-50.

Yamauchi, Y. (2020). Influenza A virus uncoating. Advances in Virus Research 106, 1-38.

Yángüez, E., Hunziker, A., Dobay, M.P., Yildiz, S., Schading, S., Elshina, E., Karakus, U., Gehrig, P., Grossmann, J., and Dijkman, R. (2018). Phosphoproteomic-based kinase profiling early in influenza virus infection identifies GRK2 as antiviral drug target. Nature communications 9, 3679.

Zhang, K., Wang, Z., Liu, X., Yin, C., Basit, Z., Xia, B., and Liu, W. (2012). Dissection of influenza A virus M1 protein: pH-dependent oligomerization of N-terminal domain and dimerization of C-terminal domain. PloS one 7, e37786.

Zhang, X., Yuan, Z., Zhang, Y., Yong, S., Salas-Burgos, A., Koomen, J., Olashaw, N., Parsons, J.T., Yang, X.-J., Dent, S.R., et al. (2007). HDAC6 Modulates Cell Motility by Altering the Acetylation Level of Cortactin. Molecular cell 27, 197-213.

Zhang, Y., Li, N., Caron, C., Matthias, G., Hess, D., Khochbin, S., and Matthias, P. (2003). HDAC-6 interacts with and deacetylates tubulin and microtubules in vivo. The EMBO journal 22, 1168-1179.

Zhao, X., Zhang, G., Liu, S., Chen, X., Peng, R., Dai, L., Qu, X., Li, S., Song, H., Gao, Z., et al. (2019). Human Neonatal Fc Receptor Is the Cellular Uncoating Receptor for Enterovirus B. Cell 177, 1553-1565.e1516.

Part III

Targeting the HDAC6 zinc finger domain impacts virus infection and cellular stress pathways (submitted)

(I generated all the data and experiments in this section, except for the virus infection experiments presented in Figure 4, 5 and S7).

Targeting the HDAC6 zinc finger domain impacts virus infection and cellular stress pathways

Longlong Wang[a, b], Etori Aguiar Moreira[a], Georg Kempf[a], Yasuyuki Miyake[c, d], Blandina I. Oliveira Esteves[e, f], Marco P. Alves[e, f], Jonas V. Schaefer[g, $], Birgit Dreier[g], Yohei Yamauchi[c], Andreas Plückthun[g] & Patrick Matthias[a, b*]

Affiliations:

[a] Friedrich Miescher Institute for Biomedical Research, 4058 Basel, Switzerland

[b] Faculty of Sciences, University of Basel, 4031 Basel, Switzerland

[c] School of Cellular and Molecular Medicine, University of Bristol, Bristol BS8 1TD, UK

[d] Dept of Virology, Nagoya University Graduate School of Medicine, Nagoya, Aichi 464-8601, Japan

[e] Institute of Virology and Immunology, Bern, Switzerland

[f] Department of Infectious Diseases and Pathobiology, Vetsuisse Faculty, University of Bern, Bern, Switzerland

[g] Department of Biochemistry, University of Zürich, 8057 Zürich Switzerland

[$] Present address: Novartis Institutes for Biomedical Research, 4056 Basel Switzerland

***Correspondence:**

Patrick Matthias, Friedrich Miescher Institute for Biomedical Research, Maulbeerstrasse 66, 4058 Basel, Switzerland, Phone: 41-61-697-6661, FAX: 41-61-697-3976, E-mail: patrick.matthias@fmi.ch

Abstract

The deacetylase HDAC6 is important for the cellular stress response, by promoting the recruitment of misfolded proteins to the aggresome and the formation of stress granules (SGs), structures that have been linked to the pathogenic granules in neurodegenerative diseases. When infecting cells, influenza A virus subverts the aggresome/HDAC6 pathway to facilitate capsid uncoating. HDAC6 binding to unanchored ubiquitin via its zinc finger (ZnF) domain is essential for these processes. We have generated nanobodies and DARPins selectively binding to the ZnF domain *in vitro* and *in vivo*, and one of them prevents interaction with ubiquitin. Crystallographic analysis shows that this DARPin blocks

the ZnF domain pocket where ubiquitin engages. We show that expression of this DARPin in cells impairs infection by two RNA viruses, influenza A and also Zika. Moreover, SGs and aggresomes are also blocked. These results demonstrate that the HDAC6 ZnF domain is an attractive target for drug discovery.

Keywords

HDAC6; Influenza A virus; ZIKA virus; Aggresome; Stress Granules; DARPin; Ubiquitin

Introduction

The coronavirus disease 2019 (COVID-19) pandemic caused by the severe acute respiratory syndrome coronavirus 2 (SARS-CoV-2) which has taken the world by surprise exemplifies how viruses represent a continuous -but often underestimated- threat to human health. Beyond the new SARS-CoV-2 virus, RNA viruses such as influenza A virus (IAV) and coronaviruses come seasonally and affect every year millions of people worldwide. Viruses have evolved a multitude of highly specific and unique mechanisms that intersect with cellular pathways, often to favor the infection. One such pathway is ubiquitination, the process by which the small 76 amino acid cellular protein ubiquitin (Ub) is used to generate a variety of polymeric chains that can be post-translationally conjugated to proteins. Depending on which lysine residues (K48, K63 …) are used for branching, the Ub polymers are structurally different and have distinct functions. By modulating protein function (e.g. localization, trafficking ...) or fate (e.g. degradation), ubiquitination impinges on most aspects of cellular metabolism. Proteins ubiquitinated by K48-branched chains are targeted for degradation by the ubiquitin proteasome system (UPS) (reviewed in (Komander and Rape, 2012)). Viruses often depend on the UPS (Isaacson and Ploegh, 2009): proteasome inhibitors block productive IAV entry and impact the replication of various virus classes (reviewed in (Rudnicka and Yamauchi, 2016)). In addition, Ub plays an important role in innate immunity, for example by modulating the activity of the RNA helicase retinoic acid-inducible gene I (RIG-I), which acts as a major viral RNA sensor and elicits the production of interferons (Peisley et al., 2014).

Ub is also important for the cellular stress response. Under stress, cells form a variety of membraneless organelles as part of defense mechanisms. When misfolded proteins fail to be degraded -in case of proteasome overload which can also be associated to genetic conditions- they assemble together with Ub chains to form a temporary perinuclear structure called the aggresome (Johnston et al., 1998a). This process depends on protein transport along the microtubules, mediated by molecular motors such as dynein and also histone deacetylase 6 (HDAC6). In some cases, aggresomes have been associated with sites of viral replication (Wileman, 2006). Stress granules (SGs) are dynamic RNA-protein aggregates that build up following a wide range of stresses, such as oxidative stress, heat shock or even viral

infection (Nover et al., 1989). SGs contain RNAs and proteins including components of the translational machinery, proteins involved in RNA metabolism, Ub and others (reviewed in (Protter and Parker, 2016)). UPS inhibition can also induce SG formation (Mazroui et al., 2007), and unconjugated Ub co-localizes with SGs (Markmiller et al., 2019). Several proteins involved in neurodegenerative diseases such as FUS or TDP43 are components of SGs and disease-associated mutations have been found to correlate with altered SGs dynamics or modified *in vitro* biophysical properties (Wolozin and Ivanov, 2019; Zhang et al., 2018). Furthermore, SGs have also been associated with cancer and viral replication (Anderson et al., 2015; Montero and Trujillo-Alonso, 2011; Reineke and Lloyd, 2013). SGs and aggresomes are considered to be temporary protective mechanisms against a harmful cellular environment (Hao et al., 2013; Protter and Parker, 2016; Wheeler et al., 2016). Properly regulated dynamics of these membraneless granules forms an integral part of normal cellular physiology; these dynamics can be altered in pathological situations and this by itself can contribute to the pathologies (Ash et al., 2014; Olzmann et al., 2008).

For both IAV entry and cellular granules formation the Ub-interacting deacetylase HDAC6 is important. HDAC6 is a mostly cytoplasmic lysine deacetylase with unique properties: it has tandem catalytic domains (CD) which are organized in a pseudo-two-fold symmetric structure (Miyake et al., 2016) and also a conserved zinc finger domain (ZnF-UBP, hereafter ZnF) with homology to the Ub binding domain of deubiquitinases (Hook et al., 2002; Seigneurin-Berny et al., 2001). The main substrates of HDAC6 are tubulin (Hubbert et al., 2002; Zhang et al., 2003a), and also the chaperone HSP90 (Kovacs et al., 2005), cortactin (Zhang et al., 2007) or the RNA helicase DDX3X (Saito et al., 2019a). By regulating the level of tubulin and cortactin acetylation HDAC6 influences microtubule dynamics, cytoskeletal trafficking and cellular motility (Boyault et al., 2007). A variety of HDAC6-specific small molecule inhibitors have been developed which target its deacetylase activity and have shown efficacy in some cancer models (Brindisi et al., 2019; Cosenza and Pozzi, 2018; Mishima et al., 2015). In many cases the biological functions of HDAC6 depend, beyond the catalytic activity, on the ZnF domain which binds with high affinity to unanchored Ub chains via their C-terminal diglycine -GG motif (Boyault et al., 2006; Ouyang et al., 2012): formation of SGs and aggresomes requires an intact HDAC6 ZnF domain (Kawaguchi et al., 2003; Kwon et al., 2007). Likewise, infection by IAV only proceeds normally when the HDAC6 ZnF domain is functional; mutation of the HDAC6 ZnF domain so as to impair Ub chains recruitment strongly reduces the capacity of IAV to uncoat its capsid and release its nucleic acids (Banerjee et al., 2014a). Many viruses carry and need Ub for infectivity (Gustin et al., 2011); the IAV viral capsid recapitulates key aspects of the aggresome pathway by bringing along unanchored Ub chains (Artcibasova et al., 2020, submitted). Moreover, this pathway and its core components (HDAC6 and Ub) have been very recently shown to be an essential part of the inflammasome activation (Magupalli et al., 2020). Thus, infection by IAV (and possibly other viruses) as well as cellular processes that are part of the stress or inflammatory response need the interaction

between unanchored Ub chains and HDAC6; targeting this interaction may therefore be of great therapeutic interest.

Here we have generated nanobodies and Designed Ankyrin Repeat Proteins (DARPins) that selectively recognize the zinc finger of human HDAC6. We show by biochemical and crystallographic structural analysis that one DARPin binds with high affinity to the HDAC6 ZnF domain and effectively blocks the pocket in which Ub normally engages. Owing to its high affinity, it is able to displace Ub from the ZnF domain *in vitro* as well as in cells. Conditional expression of this DARPin in cells leads to reduced infection by IAV and also by Zika virus, thereby establishing that this pathway is used by RNA viruses beyond IAV. Moreover, in these cells the formation of aggresomes is impaired and the number of SGs is reduced. This demonstrates that manipulation of the ZnF domain-Ub interaction can be used to modulate the cellular response to stress and viral infection.

Results

Identification of nanobodies and DARPins selectively recognizing the HDAC6 ZnF doamin

We set out to identify small antibody-like molecules that selectively target the ZnF domain. The purified human HDAC6 ZnF domain was used as a bait for identification of nanobodies and DARPins binding specifically to the target protein (Figure 1A) (see Methods). We first examined the nanobodies obtained and established stably expressing human lung adenocarcinoma A549 cell lines. We used these to test whether intracellularly expressed nanobodies are capable to target the ZnF domain of HDAC6 *in vivo* and used a co-immunoprecipitation assay. As shown in Figure S1A, precipitation of the ZnF nanobodies from cell lysates via their GFP fusion moiety led to robust co-precipitation of endogenous HDAC6. The same cell lines were then used for an infection assay with IAV and a moderate reduction was observed with two of the nanobodies, when compared to the control nanobody (Figure S1B). We reasoned that, although interacting with the ZnF domain, the available nanobodies might not target regions that are important for the Ub – ZnF domain interaction and decided to focus our further work on DARPins (Binz et al., 2004; Binz et al., 2003; Plückthun, 2015).

DARPins were selected from a large library by *in vitro* ribosome display (Brauchle et al., 2014; Dreier and Plückthun, 2012). Following the initial high-throughput screen, we used a HTRF assay (Table S1) and identified 24 DARPins that bound to the ZnF domain. We then expressed these *in vitro* and used them for binding assays in the presence of purified ZnF domain and Ub, with all proteins added together at equimolar ratios. As shown in Figure S2A, all DARPins efficiently bound to the ZnF domain, thus confirming the screening result; in addition, one DARPin (F10) prevented interaction with Ub (Figure 1B). Changing the order of addition of the different proteins showed that maximal interference was obtained when F10 was first incubated with the ZnF domain, but that addition of F10 to a preformed ZnF – Ub complex was also able to partially displace Ub; as expected, another DARPin from this screen

(B10), while binding efficiently to the ZnF domain, did not interfere with Ub binding under any of the conditions (Figure S2B).

To test whether the DARPin F10 can also interfere with the Ub – ZnF domain interaction *in vivo*, we established a split-GFP assay (Cabantous et al., 2013) in 293T cells (Figure 1C). In this assay, fluorescence requires reconstitution of a functional GFP molecule, which is mediated by interaction between the HDAC6 ZnF domain and Ub; mutation of a single residue in the ZnF domain (W1182A) which is known to disrupt interaction with Ub (Hao et al., 2013) abolished the GFP signal, demonstrating the assay specificity. Using this assay, expression of DARPin F10 was found to suppress the fluorescence signal, while expression of DARPin A10, which binds the ZnF domain but does not block Ub, did not interfere (Figure 1B, 1C).

Furthermore, when transiently expressed in A549 cells, DARPin F10 -but not control DARPin E3_5 (a non-binder from the unselected library (Binz et al., 2003))- can be used to precipitate endogenous HDAC6, indicating that it also robustly interacts with intact HDAC6 (Figure 1D). Analysis of the immunoprecipitates by mass spectrometry showed that under these conditions only five proteins in addition to HDAC6 were precipitated by F10, none of which has a zinc finger domain (Figure 1E). In conclusion, DARPin F10 is able to interfere *in vivo* with high specificity with the HDAC6 zinc finger domain and thereby disrupt its interaction with Ub. We additionally performed RNA-seq transcriptome analysis of A549 cells transiently expressing DARPin F10 or the control DARPin E3_5 and observed no significant gene expression changes, confirming the lack of promiscuous effects (Figure S3).

DARPin F10 forms a stable complex with the ZnF domain

To understand how DARPin F10 inhibits HDAC6 ZnF-Ub binding, the stoichiometric complex was purified by size-exclusion chromatography (Figure S4A) and subjected to crystallization experiments. A 2.55 Å structure was determined (Figure 2A) by molecular replacement using a ZnF-Ub C-terminal complex (PDB: 3GV4) as search model (see Table S2 for data collection and refinement statistics). In addition, an unbiased map was obtained by experimental phasing using the anomalous signal from the Zn^{2+} ions.

The asymmetric unit contains one copy of the ZnF-DARPin F10 complex and the entire sequence of the complex, except for the first two N-terminal amino acids of F10, is defined by electron density. As expected, DARPin F10 adopts the traditional Ankyrin repeat fold, with one repeat consisting of a □-bulge turn followed by two antiparallel α-helices (Binz et al., 2003). The N-capping Ankyrin repeat of F10 consists of two α-helices and is followed by four complete repeats, together including α-helices 1 to 10 (α1 to α10) and the □-turns 1 to 4 (L1 to L4; Figure 2A).

The complex interface was analysed with QtPISA yielding a total buried interface surface area of 853.4 $Å^2$. The extensive binding interface of F10, including L1-L4 and parts of α3, α5, and α7, encloses the tip of the protruding ZnF motif III (loops aa 1133-1142 and aa 1153-1160) and the four □-turns of F10

insert like fingers into the canyon-like cleft between ZnF motif II (loops aa 1184-1187 and aa 1112-1116) and ZnF motif III of the ZnF domain (Figure 2B). The protruding ZnF motif III is contacted mainly by residues from the α-helical scaffold (α3, α5), while the cleft is occupied by one or two apical side chains of each □-turn (L1-L4). These interactions are governed by an intricate network of both hydrophobic contacts and polar interactions. Important hydrogen bonds are Tyr 1156 from ZnF to Arg 113 from F10 α-helix 7 (α7), Asn 1158 (ZnF) to Lys 47 (F10, α3), Arg 1155 (ZnF) to Asp 67 (Loop 2 from F10, or L2), Tyr 1156 (ZnF) to Asp 100 (F10, L3) (Figure 2C). Moreover, Arg 1155 (ZnF) forms a salt bridge with Asp 67 (F10, L2; Figure S4B). This shows that parts of the central Ankyrin repeats (L2, L3, α3 and α7) form the main structural platform for ZnF recognition. Considering that the characteristic shape of the ZnF motif III region, from Arg 1155 to Asn 1158, is complemented by the Ankyrin scaffold and tethered by multiple polar contacts, we speculate that this region is critical for F10-binding specificity.

Next, we examined the ZnF region 1155 to 1158 which is also defined as Ub-binding motif (Figure 1A); hence we aligned the DARPin F10-bound ZnF to the Ub-bound ZnF structure (3GV4) to evaluate the structural differences between the two conformations (Figure 2D). After removing the low electron density at both ends, an overall root-mean-square deviation (RMSD) of 1.062 Å was obtained. Limited shift is observed on the backbone; in contrast, the side chain of Arg1155 and Tyr1156, which are ”gatekeepers” for Ub binding (Ouyang et al., 2012), are bent outward from the cleft, with a shift (measured by the far-end nitrogen and oxygen atom) equal to 6 Å and 2.5 Å in distance respectively, due to DARPin F10 binding (Figure 2D right). Another key amino acid for interaction with Ub is W1182 in ZnF (Hao et al., 2013; Ouyang et al., 2012); although it makes hydrophobic contacts (distance > 4 Å) with DARPin F10 (Met69), its position was not affected (Figure S4C). Hence, rearrangement of Arg1155/Tyr1156 may close the gate for Ub entry and lead to its displacement.

DARPin F10 occupies the HDAC6 ZnF Ub-binding pocket with high affinity

In the ZnF-Ub structure (3GV4), the negatively charged C-terminus of Ub inserts into a positively charged pocket (denoted as ZnF binding pocket, ZBP; Figure S5B left), which is part of the characteristic cleft of the ZnF domain. Once Ub is bound, the ZBP is filled by the charged Ub C-terminal -L-R-G-G peptide. Superposition of F10 onto the ZnF-Ub structure revealed that the Ub binding site is completely occupied by F10 residues (Figure 3A, 3B). Especially backbone atoms from Histidine 101 to Glycine 103 (Figure 3A), and side chains of Lys 102 (L3) and Met 69 (L2) are directly clashing with Leu 73 and Arg 74 of Ub (Figure S5A). Analysis of the electrostatic surface potential showed that binding of F10 to the positively charged Ub-binding pocket of ZnF is not significantly facilitated by charge complementarity as observed for Ub binding (Figure S5B). Only a positively charged cavity of F10 (formed by residues from L2 and L3) is filled with the weakly negatively charged ZnF motif III loop (Figure S5B). Thus, complex formation and inhibition of Ub-binding appear to rely on substantial

shape complementarity and are driven by both non-polar and polar interactions. Using isothermal titration calorimetry (ITC), we determined the *in vitro* binding affinities between the HDAC6 ZnF domain and either mono Ub or DARPin F10 (Figure 3C). These experiments revealed that the ZnF domain has a 55-fold higher affinity for DARPin F10 (K_D 95.05 ± 12.3 nM) than for Ub (K_D 5.16 ± 0.47 μM), supporting a specific binding mode. In conclusion, by forming an interlocked interface encompassing large parts of the ZnF domain, F10 binds stronger than Ub and competitively blocks access to the Ub-binding pocket.

Targeting HDAC6 ZnF impairs influenza A virus infection during uncoating

We wished to examine whether expression of DARPin F10 in cells can impact cellular processes in which HDAC6 has been implicated, such as the formation of aggresomes (Kawaguchi et al., 2003) or SGs (Kwon et al., 2007; Legros et al., 2011; Saito et al., 2019a) and virus infection (Banerjee et al., 2014a). For this, we generated A549 cell lines stably expressing DARPin F10, C-terminally fused to an $FKBP^{F36V}$ degron tag (F10 cell line). In these cells, conditional degradation can be rapidly induced by addition of the chemical dTAG-13 (hereafter dTAG), which engages $FKBP^{F36V}$ and the E3 ligase Cereblon, leading to proteasomal degradation (Nabet et al., 2018) (Figure S6A). In F10 cells, addition of dTAG to the medium led to rapid degradation of the DARPin F10 fusion protein, which was complete in ca. 6 hrs (Figure S6B). Pre-treatment of the cells with proteasome inhibitors, including MG132, Carfilzomib and Bortezomib, completely prevented the dTAG-induced degradation (Figure S6C). However, when MG132 was added after the dTAG treatment, expression of DARPin F10 was not recovered for at least 18 hrs (Figure S6D). Notably, expression of the DARPin F10 fusion did not impact the enzymatic activity of HDAC6, as evidenced by the fully deacetylated tubulin in these cells, as in parental cells (Figure S6E).

Infection by influenza A virus (strain X31, H3N2) has been shown to depend on the HDAC6/aggresome pathway at the uncoating stage, with the HDAC6 ZnF domain and Ub playing an important role (Artcibasova et al., 2020, submitted; Banerjee et al., 2014a). We therefore tested virus infection in the different cell lines; parental A549, F10 and $FKBP^{F36V}$ control cell lines were infected by IAV X31 at a multiplicity of infection (MOI) of 0.05 plaque-forming unit (PFU) per cell and the virus titer in the culture supernatant was analyzed by plaque assay every 12 hrs post infection. Viral growth curve showed a ca. 10-fold reduction of virus titer in F10 cells compared to the cells lacking the DARPin (Figure 4A). Remarkably, this difference was maintained throughout multiple replication cycles for up to 72 hrs post-infection. Degradation of DARPin F10 by dTAG addition (indicated in Figure 4B upper scheme) prior to infection restored susceptibility to virus (Figure 4B lower). We also examined the virus titer within one replication cycle (up to 8 hrs). Consistent with the above results, a robustly reduced viral load was detected as early as 6 hrs post infection in F10 cells (Figure 4C).

To visualize the uncoating step, we monitored by confocal microscopy the release of matrix protein M1 from viral particles and its cellular distribution. M1 was stained by a specific monoclonal antibody and the signal intensity was quantified. As shown in Figure 4D (top left panel), 3.5 hrs after infection the M1 signal (green) was detected as a weak diffuse staining with dots in untreated WT A549 cells. In Bafilomycin-treated WT cells, in which endosomal acidification and transport are blocked, the M1 signal was strongly reduced, indicative of blocked uncoating. A similar pattern of M1 signal was observed in F10 cells, reflecting impaired uncoating. Addition of dTAG, which leads to degradation of the DARPin, restored the M1 signal. Quantification of M1 signal intensity in the cytoplasm confirmed that the presence of DARPin F10 inhibits the IAV uncoating process (Figure 4D, right panel).

Infection by Zika virus is inhibited by DARPin F10

Zika virus (ZIKV) is a mosquito-borne enveloped single-stranded RNA virus; it has spread to the Americas in 2015 (Campos et al., 2015) after an outbreak in Micronesia in 2009 (Duffy et al., 2009) and French Polynesia in 2013 (Cao-Lormeau et al., 2014), and is currently a major threat to public health. We set out to test if this virus is also sensitive to blockade of the HDAC6 ZnF domain. We used a low passage clinical isolate of Asian lineage (ZIKV PRVABC59) to infect A549 WT, F10 and dTAG-treated (2 μM, 3 to 6 hrs) F10 cells at MOI of 0.1 and the viral titer was determined at different time points across the virus life cycle. As shown in Figure 5A and Figure S7, at each time point the viral titer was reduced several-fold in DARPin F10 expressing cells, compared to the parental A549 cells; pre-treatment of the cells with dTAG to degrade DARPin F10 led to elevated virus titers, similar to those in A549 cells. To directly examine whether blockade of the HDAC6 ZnF leads to a reduced infection by ZIKV, we fixed cells at 72 hrs post-infection and stained for Zika envelope (E) protein, as well as for DAPI to visualize nuclei and monitor cell number (Figure 5B). By quantifying the number of cells positive for Zika E-protein signal, we calculated that the infectivity ratio was about 20% in WT A549 cells. In contrast, in the F10 cell line, this value dropped to roughly 3%, and it partially recovered to 10% in dTAG-treated F10 cells. Taken together, these results demonstrate that ZIKV, like IAV, also needs HDAC6 and Ub recruitment for infection and that impinging on this pathway via DARPin F10 leads to a strong reduction in infectivity.

Targeting the HDAC6 ZnF domain impairs cellular granules formation, including aggresome and SGs

Following dTAG treatment, re-expression of DARPin F10 takes more than 18 hrs (Figure S6D). Since an 18 hrs MG132 treatment has been widely used to induce aggresome formation in human cells (Kawaguchi et al., 2003), this experimental setup allowed us to test the effect of the DARPin F10 on this process. Following MG132 treatment, staining for HDAC6 was used to visualize the aggresome; as shown in Figure 6A, in parental A549 cells a strong perinuclear aggresomal staining was observed

(red staining), which was dramatically disrupted in DARPin F10-expressing cells. However, when these cells were first treated with dTAG to induce DARPin degradation (green signal, Figure 6A lower panels), aggresome formation was restored. Quantification of the number of aggresomes under the different conditions showed that aggresome formation was reduced by 60% in DARPin F10 cells compared to WT A549 cells, but was restored in dTAG-treated cells. This confirmed that F10, by blocking the ZnF domain of HDAC6, strongly impairs aggresome formation (Figure 6B).

We next examined oxidative stress (arsenite)-induced SGs and monitored their presence by staining for G3BP1, a widely used SG marker (Tourrière et al., 2003). F10-expressing cells had approximately 2-fold less SGs than the parental A549 cells, or dTAG-treated F10 cells (Figure 6C, 6D). However, the size and roundness of SGs, two parameters that are related to SG maturation, were not altered by F10 expression and blocking of the ZnF domain (Figure S8). This is in good agreement with our recent studies showing a role for HDAC6 catalytic activity in SG maturation (Saito et al., 2019a).

Discussion

Here we have generated nanobodies and DARPins that bind the ZnF domain of HDAC6 and characterized their effect on cellular responses. We identified one DARPin (F10) that interferes with Ub recruitment by HDAC6 and showed by crystallographic analysis that it blocks the pocket in which the Ub C-terminal tail normally engages. We found that DARPin F10 is able to interfere with Ub binding also in cells and that this leads to clear biological phenotypes. Over the past decade HDAC6 has become an established target for drug discovery. Inhibition of the catalytic domains by selective small molecules such as Tubastatin A, Nexturastat A or others has shown antitumor activity and synergy with chemotherapy (Brindisi et al., 2019; Li et al., 2018b). While the main interest of drug discovery has been focused on HDAC6 catalytic domains, our work highlights an alternative approach for interfering with some HDAC6-dependent pathways. Compared to the recently described small molecules binding the ZnF domain Ub-binding pocket (Ferreira de Freitas et al., 2018; Harding et al., 2017), we used the entire Ub protein, not only the C-terminal peptide, to show that its binding can be interfered with (in our case by DARPin F10). Furthermore, we showed that this can be achieved not only *in vitro* but also *in vivo* and that it leads to robust biological phenotypes. Indeed, displacing Ub from the HDAC6 ZnF domain has a strong impact on IAV infection and viral titers were reduced >10 fold. Remarkably, the same effect was observed with ZIKA, another RNA virus, demonstrating that this pathway is used by multiple RNA viruses that cause disease in humans. In addition, we observed a strong reduction of SGs and aggresomes formation in DARPin F10-expressing cells that had been subjected to oxidative stress or proteasomal inhibition, respectively.

For these experiments we made use of cell lines expressing F10 fused to the $FKBP^{F36V}$ degron, which allowed us to conditionally regulate the ZnF-Ub interaction; chemically-induced degradation of F10-$FKBP^{F36V}$ relieved the inhibition of virus uncoating or of granules formation. However, in the case of SGs induction but not that of aggresomes, we observed lower granule numbers in dTAG-treated A549 F10 cells compared to WT A549 cells. Considering the different time scales in the two experimental setups (30 min for SGs, 18 hrs for aggresomes), this suggests that at the timepoint at which SGs are monitored there may still be a small amount of DARPin F10 in cells which prevents quantitative binding of HDAC6 to Ub. The described affinity between Ub-binding proteins and Ub is ca. 5 to 500 μM (Hicke et al., 2005); e.g. IsoT binds to Ub with a K_D of 2.9 μM (Reyes-Turcu et al., 2006). The K_D of approximately 5 μM for HDAC6 ZnF-Ub binding described here fits well to this notion. We observed that in spite of this relatively high affinity, immunoprecipitation of endogenous HDAC6 from non-stressed cells fails to co-precipitate Ub appreciably (data not shown); it is possible that *in vivo* interaction between HDAC6 and Ub may be regulated. Together with the observations that unanchored Ub chain binding activates HDAC6 catalytic activity on some substrates such as cortactin (Hao et al., 2013), it is possible that under non-stressed conditions HDAC6 is in an inactive state that prevents/reduces interaction with Ub. In addition, we observed that blocking the ZnF domain led to a reduced number of SGs following oxidative stress, however their size or shape was unaltered. In contrast, we found previously that impairment of HDAC6 catalytic activity results in normal SG numbers, which, however, were small and failed to mature. We could show that lack of SG maturation is due to the lack of deacetylation and impaired liquid-liquid phase separation of the RNA helicase DDX3X, an important component of SGs under certain stress conditions (Saito et al., 2019a). Thus, it appears that both functional domains of HDAC6 can play a role at distinct steps of the SG formation process.

Aggresomes and SGs are widely considered to be cellular-protective inclusion bodies that shield cells from acute stress (Advani and Ivanov, 2020; Taylor et al., 2003). However, they have also been linked to neurodegenerative disease and cancers (Anderson et al., 2015; Mishima et al., 2015; Olzmann et al., 2008). Chronic stress associated with aging leads to the pathological accumulation of proteins like TDP-40, Tau, Htt in SGs (Sweeney et al., 2017), leading to their transformation from transient to persistent structures, accompanied by further damages to the neurons. Lewy bodies are aggresome-related structures prominently observed in the brains of Parkinson disease patients. They are enriched in misfolded proteins, Ub and also HDAC6 (Kawaguchi et al., 2003).Formation of SGs is thought to protect the tumor cells from a complex microenvironment marked by multiple stresses, and to enhance their resistance to chemotherapy (reviewed in (Gao et al., 2019)). It was recently shown that in mouse testis G3BP translation and SGs formation are inhibited, thereby enhancing the germ cells viability and fertility (Lee et al., 2020). Thus, the beneficial or detrimental effect of SGs and aggresomes is tightly linked to the specific situation. In some scenarios, downregulating SG and aggresome formation by

interfering with the HDAC6 - Ub interaction could synergize with therapies against diseases such as aging-related neurodegeneration, cancer and infertility.

In contrast, viruses are without doubt associated with disease and interfering with their infectivity is beneficial. Past and current antiviral treatments are based on targeting viral proteins like the M2 ion channel (to block uncoating) and neuraminidase (NA) (to block budding) of IAV (Du et al., 2012; Hussain et al., 2017). However, such antivirals can lead to the generation of viral escape mutants as many RNA viruses causing human disease are prone to mutations. We show here that targeting a cell-assisted viral uncoating mechanism by disrupting the interaction between Ub and HDAC6 may be an attractive alternative approach. Mice lacking HDAC6 are viable and do not show overt phenotypes under standard laboratory conditions other than dramatically elevated tubulin acetylation (Zhang et al., 2008). Similarly, mice in which the HDAC6 ZnF domain or the catalytic domains have been inactivated appear largely normal (unpublished data). It is therefore possible that transient impairment of the HDAC6 ZnF domain-Ub interaction through specific inhibitors might be tolerated. It is likely that additional viruses to IAV and ZIKV also hijack the HDAC6/aggresome pathway to their advantage. Thus, interfering selectively with the HDAC6 ZnF-Ub interaction may represent a universal therapeutic modality that could be combined with virus-specific approaches in the future.

Author Contributions

L. W. and P.M. designed the project; L.W. performed biochemical and microscopy experiments and interpreted the data under the supervision of P.M.; E.A.M. and L. W. performed IAV experiment and analysis; E.A.M., B. O., L. W. and M.A performed ZIKV experiments and analysis; L.W. and G.K performed X-Ray data processing and structure refinement; J.S., B.D., and A.P. performed experimental design and analysis for DARPin selection; Y.Y. and Y. M. performed nanobody-related experiments; L.W and P.M wrote the manuscript and all authors contributed to the final version.

Acknowledgements

We thank L. Gelman and S. Bourke (FMI) for help with microscopy analysis, D. Hess, J. Seebacher and V. Iesmantavicius (FMI) for mass spectrometry analysis and H. Gut (FMI) for help with X-ray data collection. We thank H. Rice and A. Herman of the FACS facility at the University of Bristol, and H. Kohler from the FMI FACS facility. We thank C. Cao and G. Matthias for excellent support, and T. Reinberg, S. Furler, J. Marinho for help with DARPin selection and screening, M. Saito for help with cloning, S. Iketani and J. Tormo for nanobody experiments and G. Langousis and J. Sanchez for comments on the manuscript. Financial support through the SystemsX.ch MRD project VirX 2014/264, evaluated by the Swiss National Science Foundation, is gratefully acknowledged. This work was supported by the Novartis Research Foundation.

Competing Financial Interests Statement

The authors declare no competing interests

Figure & legends

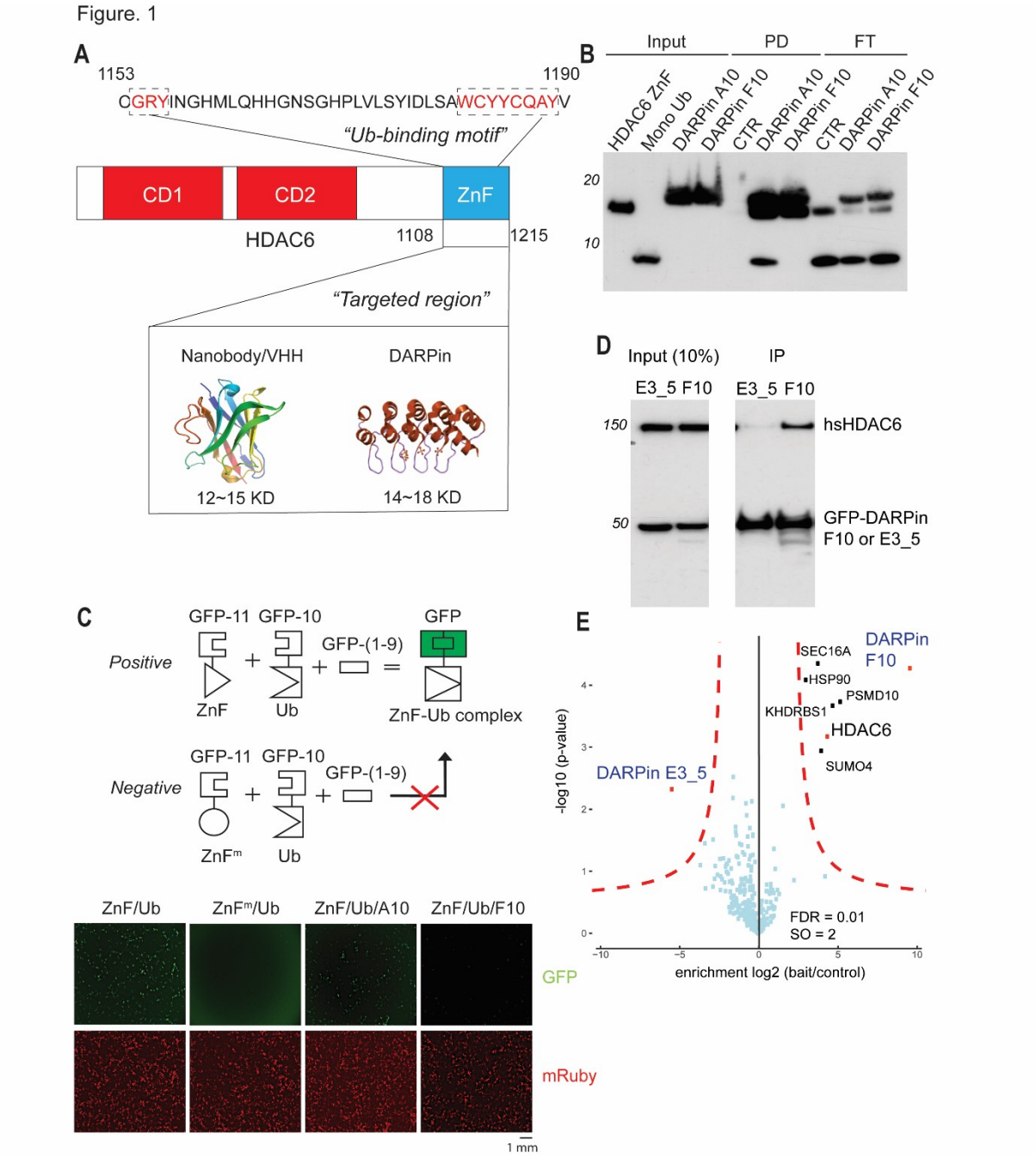

Figure 1. DARPin F10 inhibits with high specificity ZnF and Ub interaction *in vitro* and *in vivo*.

(A) Schematic of HDAC6, showing the catalytic domains (CD1, CD2) and the zinc finger domain (ZnF) region that was expressed (amino acids 1108 to 1215) and used to identify binders. Generic nanobody and DARPin structures (PDB:1I3V and PDB:2QJY, respectively) are shown below. Part of the HDAC6 sequence (1153 to 1190) is indicated at top to present the Ub binding motifs (Uniprot: Q9UBN7)(Ouyang et al., 2012), which are coloured in red and framed.

(B) DARPin F10 blocks Ub and ZnF domain interaction *in vitro*. Purified His-tagged ZnF domain (1108-1215), Flag-tagged DARPin A10 or F10 and mono-Ub were mixed together for a binding reaction; following incubation,

the ZnF domain was pulled down with anti-Flag agarose beads. The precipitated complex was eluted and analysed by immunoblotting, using anti-His, anti-Ub and anti-Flag antibodies. PD, pull-down; FT, flow-through.

(C) *In vivo* interaction between the ZnF domain and Ub is disrupted by DARPin F10, as monitored by a split-GFP assay. The ZnF domain (1108-1215) and Ub were fused to separate GFP fragments so that ZnF-Ub interaction is required to reconstitute a functional GFP molecule and fluorescence (see scheme at top). The GFP beta strands encoded in the different proteins are indicated: GFP-(1-9), GFP-10, GFP-11. A mutant ZnF domain (W1182A; ZnF^{m}) which cannot interact with Ub was also used as a control for specificity of the assay. A plasmid expressing mRuby was included in all transfections as a control for transfection efficiency (red signal). Scale bar presents 1 mm.

(D) Efficient immunoprecipitation of endogenous HDAC6 by DARPin F10. A GFP-DARPin F10 or control DARPin E3_5 fusion protein was transiently expressed in A549 cells, and the DARPins were immunoprecipitated with GFP-trap beads. The immunoprecipitated material (IP) was eluted and analysis was done by immunoblotting, using antibodies against GFP or HDAC6.

(E) Mass spectrometry analysis to determine the interactome of DARPin F10. Immunoprecipitated material (from D above) was analysed by mass spectrometry and enriched proteins are annotated.

Figure. 2

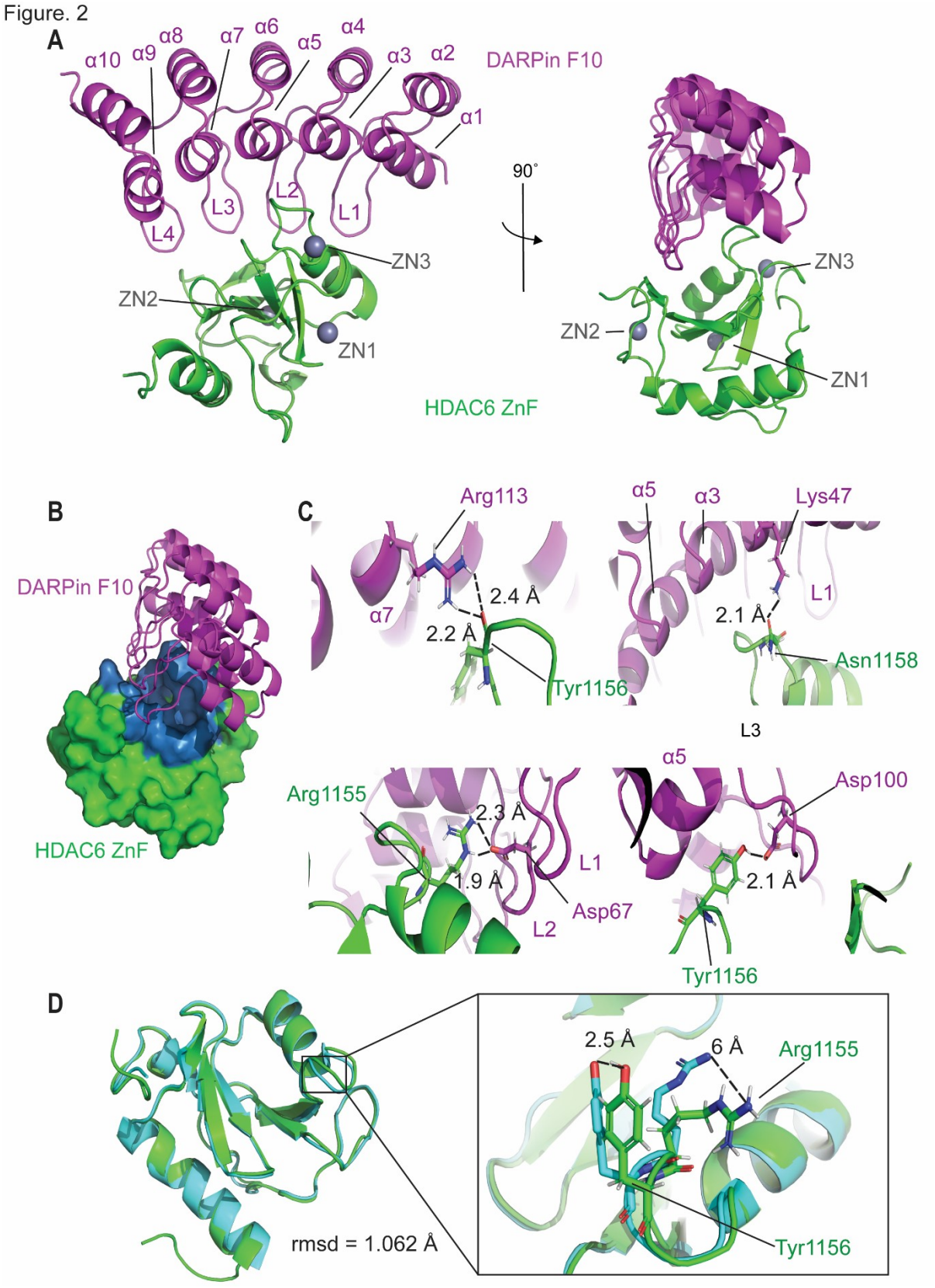

Figure 2. 2.55 Å crystal structure of HDAC6 ZnF-DARPin F10 complex.

(A) DARPin F10 bound to HDAC6 ZnF domain. DARPin F10, HDAC6 ZnF (aa 1108-1215) and Zn^{2+} ions are coloured purple, green and grey, respectively. DARPin F10 α-helices (α1 to α10) and β-turns (L1 to L4) are numbered starting from the N-terminus (PDB:7ATT).

(B) DARPin F10 β-turns/loops insert into ZnF (shown with surface representation, ZnF coloured in green, canyon-like cleft of ZnF coloured in blue).
(C) Key amino acids involved in ZnF-DARPin F10 polar interactions. The hydrogen bonds are shown by dashed lines with distances indicated.
(D) HDAC6 ZnF conformation alignment in two binding forms. Green presents the ZnF structure bound to DARPin F10, and cyan presents the ZnF bound to ubiquitin (from PDB: 3GV4). A zoomed-in view of "gatekeeper" amino acids, Arg1155 and Tyr1156, for Ub binding is shown on the right, with the shifting of side chains indicated by dashed lines. The distance is labelled.

Figure. 3

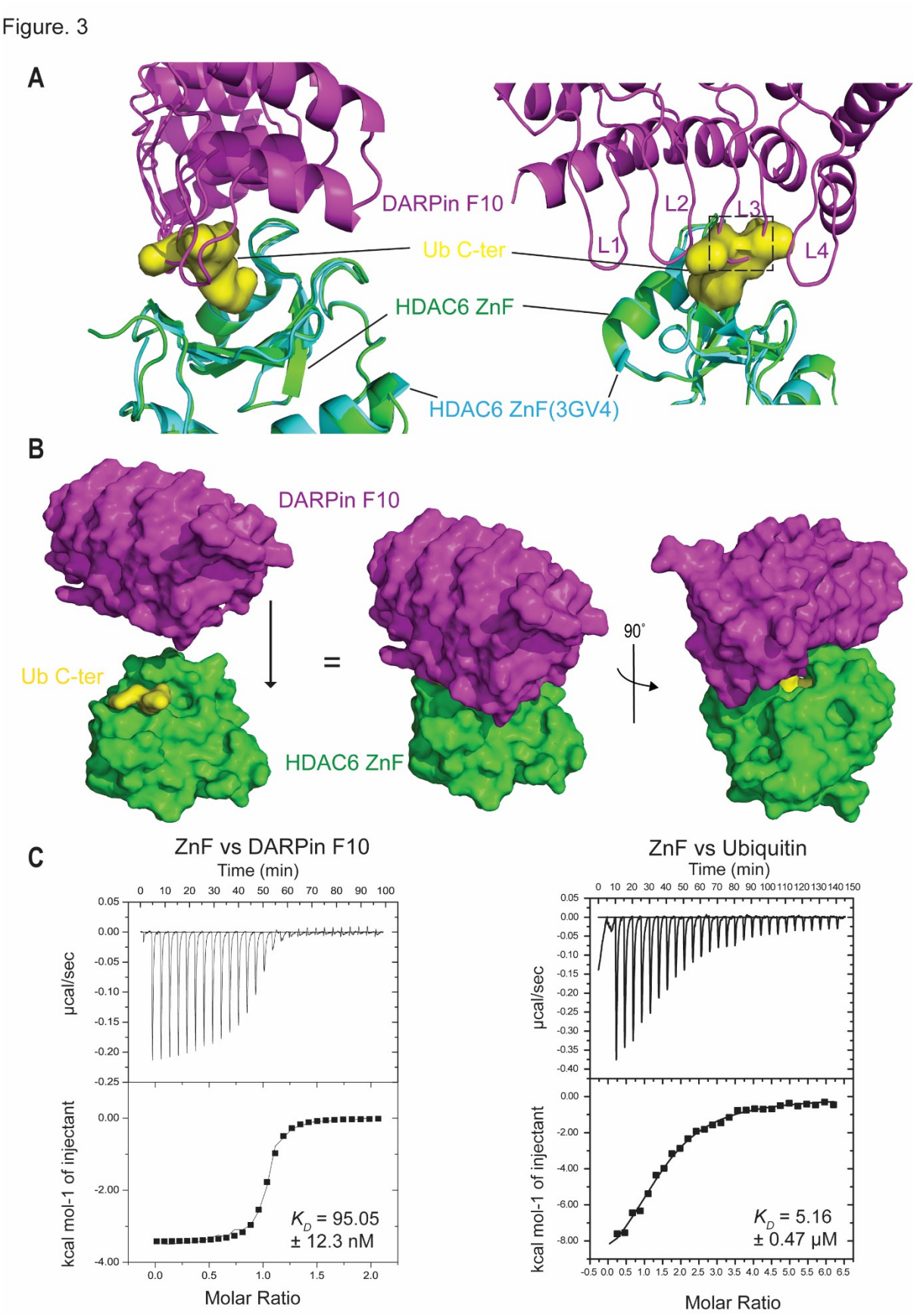

Figure 3. DARPin F10 blocks Ub binding through spatial occupation with high affinity.

(A) Zoomed-in views of the ZnF Ub-binding pocket. The ZnF-DARPin F10 structure is superimposed onto the ZnF-Ub C-terminal tail structure (PDB: 3GV4). The Ub C-terminal tail is shown in surface representation (yellow). DARPin F10 L3 backbone is clashing with the Ub tail. Region Histidine 101 to Glycine 103 is rectangle by dash line (right).

(B) Surface representation of the ZnF domain in complex with DARPin F10. Ub C-terminus is buried in the ZnF "canyon". In the left panel, DARPin F10 and ZnF are moved apart for clarity. In the middle and right panels, the bound complex is shown, illustrating the occlusion of the Ub binding site by DARPin F10.

(C) Affinities of HDAC6 ZnF for DARPin F10 or free Ub, determined by isothermal titration calorimetry experiments. In ZnF-DARPin F10 assay, ΔS = 20.6 cal/mol/deg, N = 1.01; in ZnF-Ub assay, ΔS = -12.8 cal/mol/deg, N = 1.46.

Figure. 4

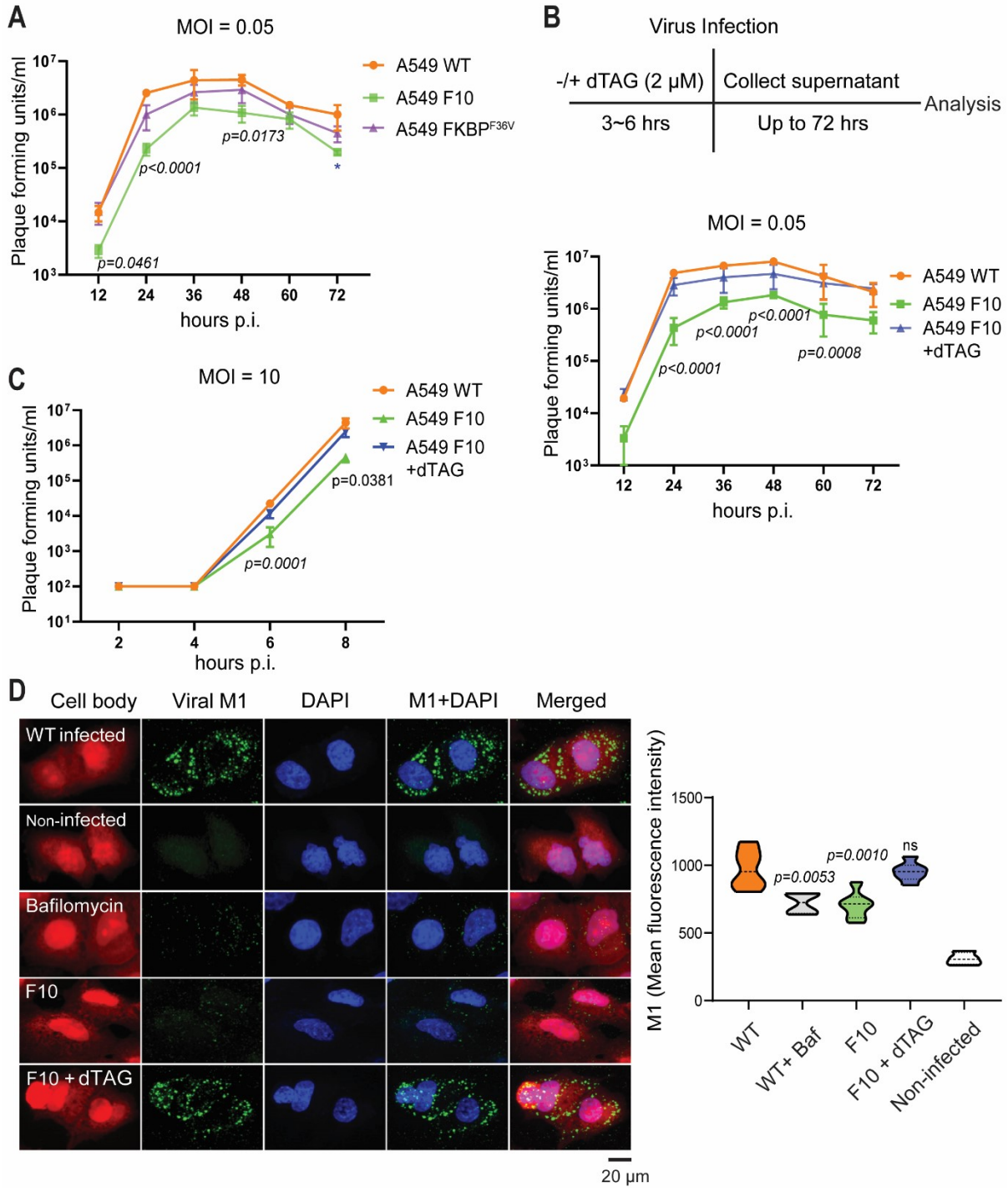

Figure 4. Blocking the HDAC6 ZnF-Ub interaction by DARPin F10 interferes with IAV infection.

(A) DARPin F10 impairs IAV infection. The indicated cell lines (A549 WT, F10 or FKBP^{F36V}) were infected with IAV at a MOI of 0.05 (n=3), and culture supernatants were collected every 12 hrs until 72 hrs. Viral titer in supernatant was quantified by plaque assay. Statistical analysis was done with ANOVA, and p-value is shown in the graph to illustrate the significant difference (FDR<0.05) between cell lines expressing or not DARPin F10.

(B) Treatment with dTAG restores IAV susceptibility. The indicated cell lines (A549 WT, DARPin F10 without or with dTAG pre-treatment) were infected with IAV at a MOI of 0.05 (n=3), and culture supernatants were collected every 12 hrs until 72 hrs. Viral titer in supernatant was quantified by plaque assay. Statistical analysis

was done with ANOVA, and p-value is shown in the graph to illustrate the significant difference (FDR<0.05) between A549 WT and F10 cell line.

(C) Effect of DARPin F10 on a single IAV life cycle. The indicated cell lines were infected with IAV at a MOI of 10 (n=3) and culture supernatants were collected every 2 hrs up to 8 hrs. Viral titer was determined by plaque assay. Statistical analysis was done with ANOVA test, and p-value is shown in the graph to illustrate the significant difference (FDR<0.05) between A549 WT and F10 cell line.

(D) IAV uncoating is impaired by DARPin F10. The left panels show confocal microscopy visualization of uncoating, by staining for the viral capsid M1 protein (green). Parental A549 cells or F10 cells (without or with dTAG pre-treatment) were used for IAV infection and M1 expression was analysed 3.5 hrs post infection. Bafilomycin A1 treatment was used as a control for blocked infection. Total protein was stained to visualize the cell body (red). The right panel presents a quantification of the M1 analysis in the different samples. Ca. 30 cells were selected per view (6 to 9 views for each condition) and M1 fluorescence intensity was analysed. The p-value, indicating the difference against A549 WT, was calculated by ANOVA test (with a FDR<0.05). The scale bar represents 20 μm.

Figure. 5

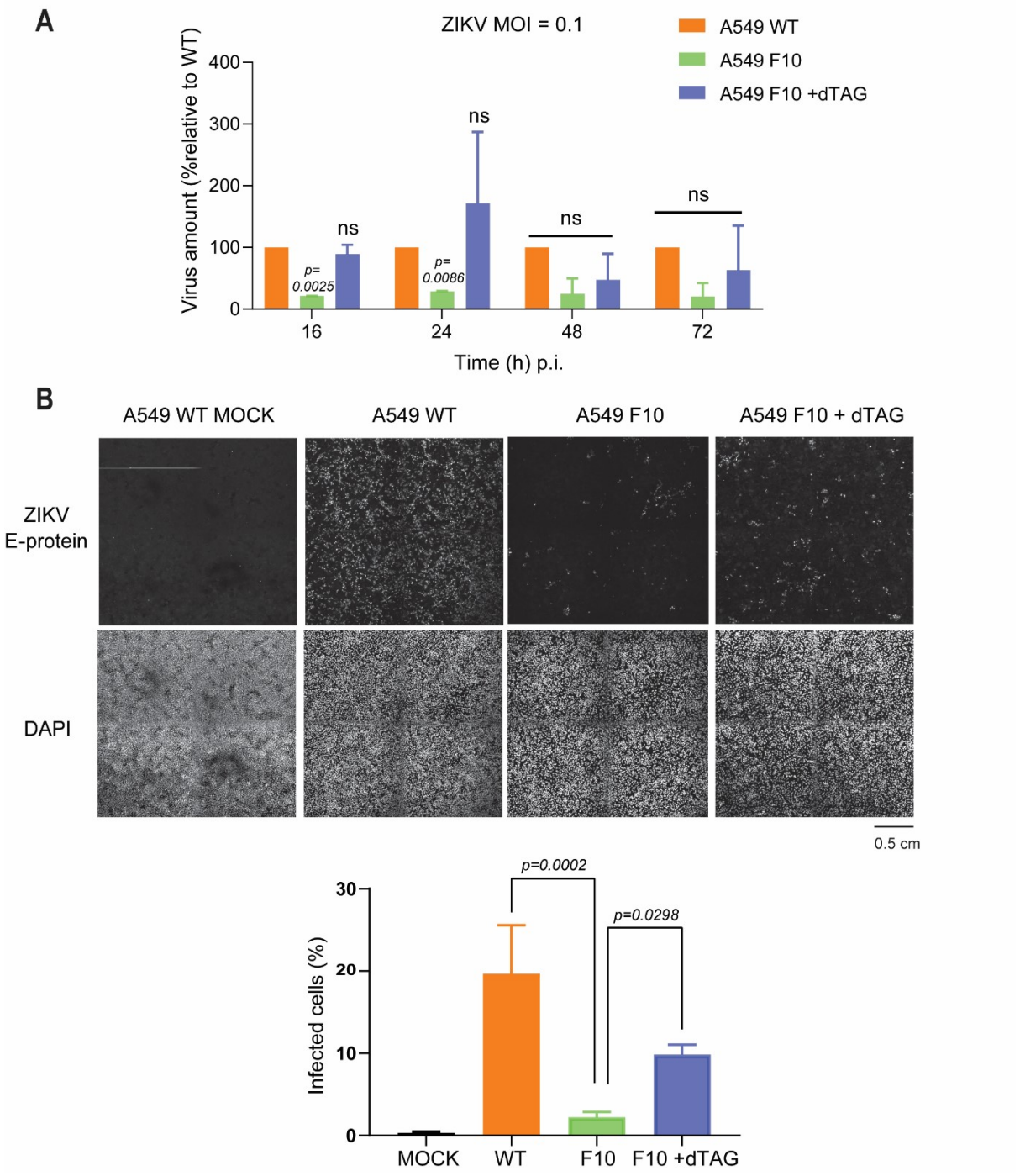

Figure 5. ZIKV replication is inhibited by DARPin F10.

(A) Reduction of ZIKV titer in DARPin F10-expressing cells. The indicated cell lines (WT, DARPin F10 without or with dTAG pre-treatment) were infected with ZIKV at a MOI of 0.1 $TCID_{50}$/cell and culture supernatants were collected at 16, 24, 48 and 72 hrs post-infection. Viral titers were determined with a $TCID_{50}$ assay; the baseline titer obtained with A549 WT cells at each time point was set to 100%. Statistical analysis was done with ANOVA, and p-value is shown in the graph to illustrate the significant difference (FDR<0.05) between A549 WT and each cell line; ns, non-significant.

(B) Reduced ZIKV infection in the F10 cell line. The upper panels show microscopy visualization of infection. Following ZIKV titer quantification in (A), the cells at 72 hrs post-infection were stained by DAPI and for ZIKV E protein. A combination of the neighbouring 4 views (10 x objective, containing 6500 to 7000 cells) showed a strong reduction in the number of cells positive for ZIKV E protein when F10 was expressed. The lower panels present a quantification (n=3) of the ZIKV E protein-positive cells. Statistical analysis was done with ANOVA; p-values refer to the significant difference (FDR<0.05) between samples, as indicated. The scale bar represents 0.5 cm.

Figure. 6

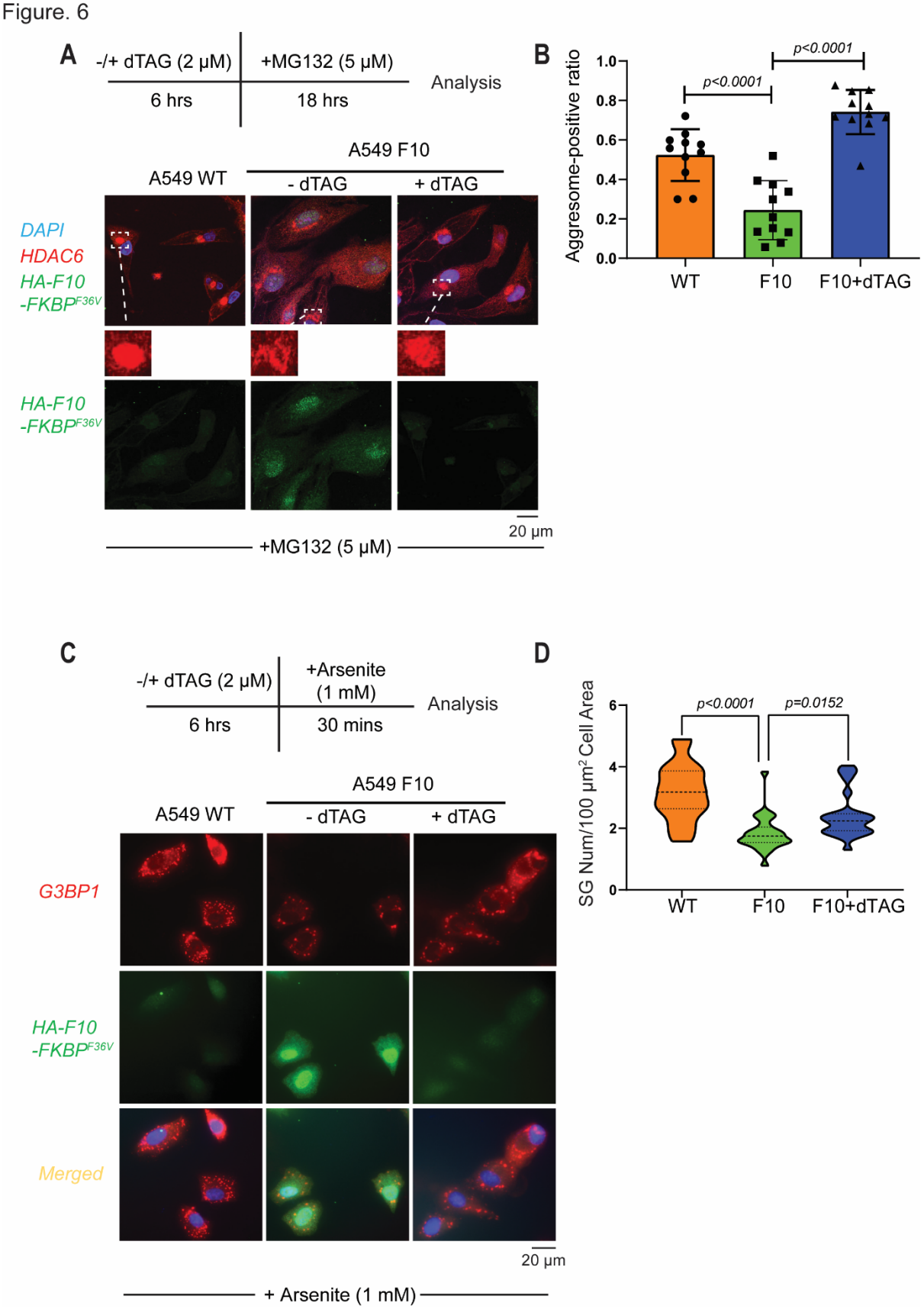

Figure 6. Disruption of HDAC6 ZnF-Ub interaction by DARPin F10 impairs cellular granules formation.

(A) Aggresome formation was induced with MG132 in parental A549 and F10 cells without or with dTAG pre-treatment to investigate the impact of the DARPin on aggresome formation. Aggresomes were detected by staining

with an anti-HDAC6 antibody and DARPin F10 expression was visualized with an anti-HA antibody. DAPI was used to stain the nucleus. The inset shows a magnified view of an aggresome; representative pictures are shown. The scale bar represents 20 μm.

(B) Quantification of aggresome formation in parental A549 cells, or F10 cells without or with dTAG pre-treatment. The top graph shows the percentage of aggresome positive cells; each data point represents the percentage obtained in randomly chosen micrograph containing 50 to 100 cells. Statistical analysis was done by ANOVA (upper graph) or unpaired t-test (lower graph), p-value is shown accordingly in the graph.

(C) SGs were induced with arsenite in parental A549 cells or in F10 cells without or with dTAG pre-treatment; SGs were visualized by staining for G3BP1. Representative pictures are shown. The scale bar represents 20 μm.

(D) Quantification of the number of SGs per cell area. Ca. 30 cells were used, with > 700 SGs in normal conditions. Statistical analysis was done by ANOVA, p-value is shown accordingly in the graph.

Supplementary Figures

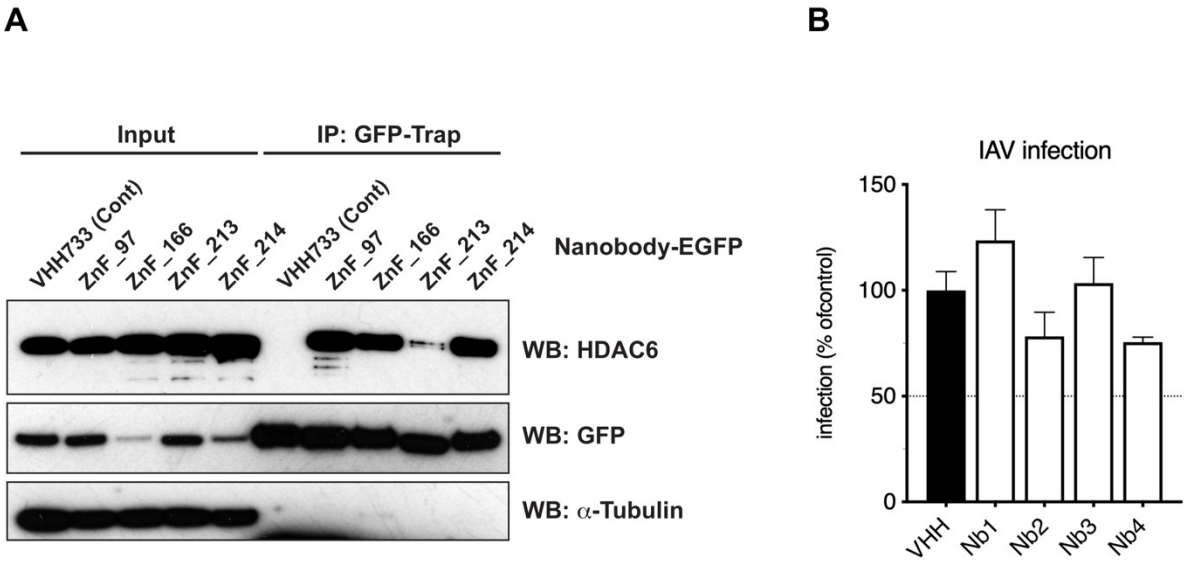

Supplementary Figure 1. ZnF domain nanobodies' interaction with HDAC6 ZnF and its effect on IAV infection.

(A) A549 cells stably expressing nanobodies against HDAC6 ZnF were used for lysate preparation followed by pull-down with anti-GFP beads. The precipitate was analysed by SDS-PAGE and immunoblotted for HDAC6, GFP, and Tubulin. The input lanes were loaded with five percent of the lysate.

(B) IAV infection was analysed in A549 cells stably expressing the HDAC6 ZnF nanobodies. Infectivity was normalised to the VHH control nanobody.

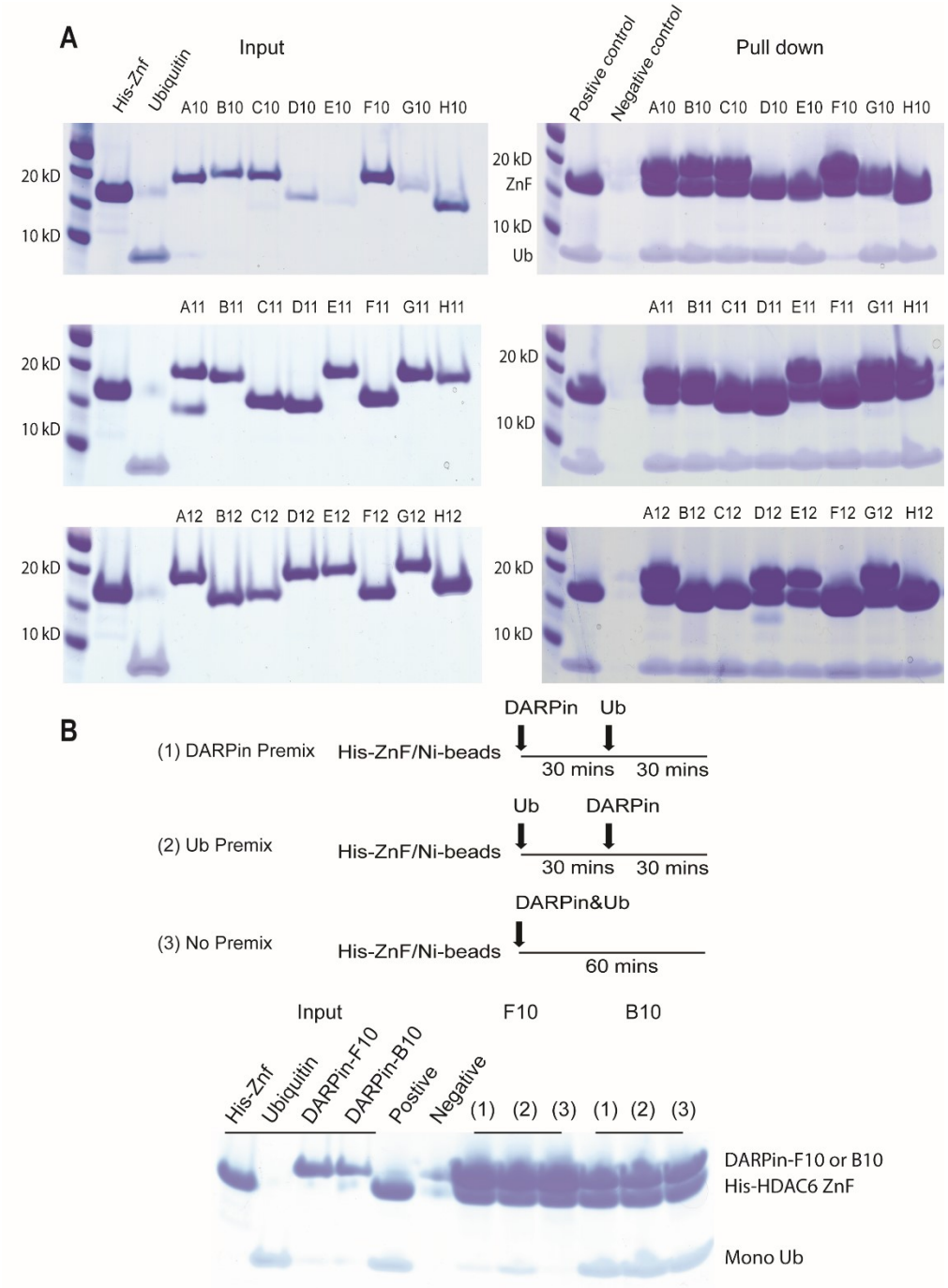

Supplementary Figure 2. Initial screen for DARPins blocking the HDAC6 ZnF-Ub interaction.

(A) Purified His-tagged HDAC6 ZnF (1108-1215), Flag-tagged DARPin candidates (A10-H10, A11-H11, A12-H12) and mono-ub were incubated together with Ni-NTA beads for 30 min, followed by precipitation and elution from the beads. Samples were analyzed by SDS-PAGE and visualized with Coomassie protein stain. As is visible on the input panel, the size of the different DARPins varies slightly, depending on whether they have four or five loops. If a DARPin interacts with the ZnF domain without disturbing the binding of Ub, pull-down of the ZnF domain via its His tag results in all three proteins being precipitated (pull down panel). In the case of DARPin F10, Ub is not precipitated, indicating that F10 binding interferes with Ub binding.

(B) DARPin F10, and B10 as a control, were used for order of addition experiments. (1) The DARPin was pre-mixed with His-ZnF, followed by Ub addition 30 min later; (2) Ub was pre-mixed with His-ZnF, followed by

DARPin addition 30 min later; (3) All three proteins were mixed together at the same time, followed by incubation for 60 min. Following the incubation, the ZnF domain was captured and analysis was done by SDS-PAGE and Coomassie staining. As shown, even when Ub is pre-mixed with the ZnF domain, its binding is displaced by addition of DARPin F10.

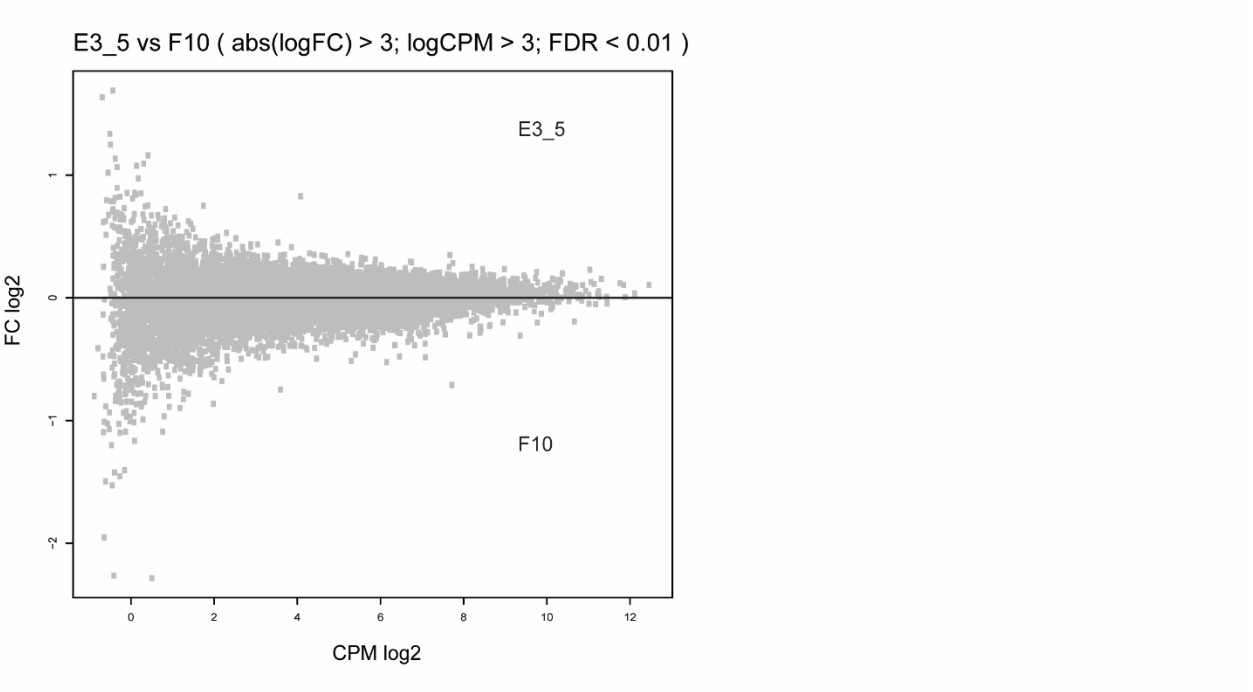

Supplementary Figure 3. DARPin F10 does not influence gene expression or HDAC6 activity.
Transcriptome analysis by RNA-seq. A549 cells were transiently transfected with GFP-tagged DARPin F10 or control DARpin, then GFP positive cells were sorted by FACS and total RNA was extracted 3 days after transfection. The $\log_2$ fold change under the two conditions is displayed on an MA plot.

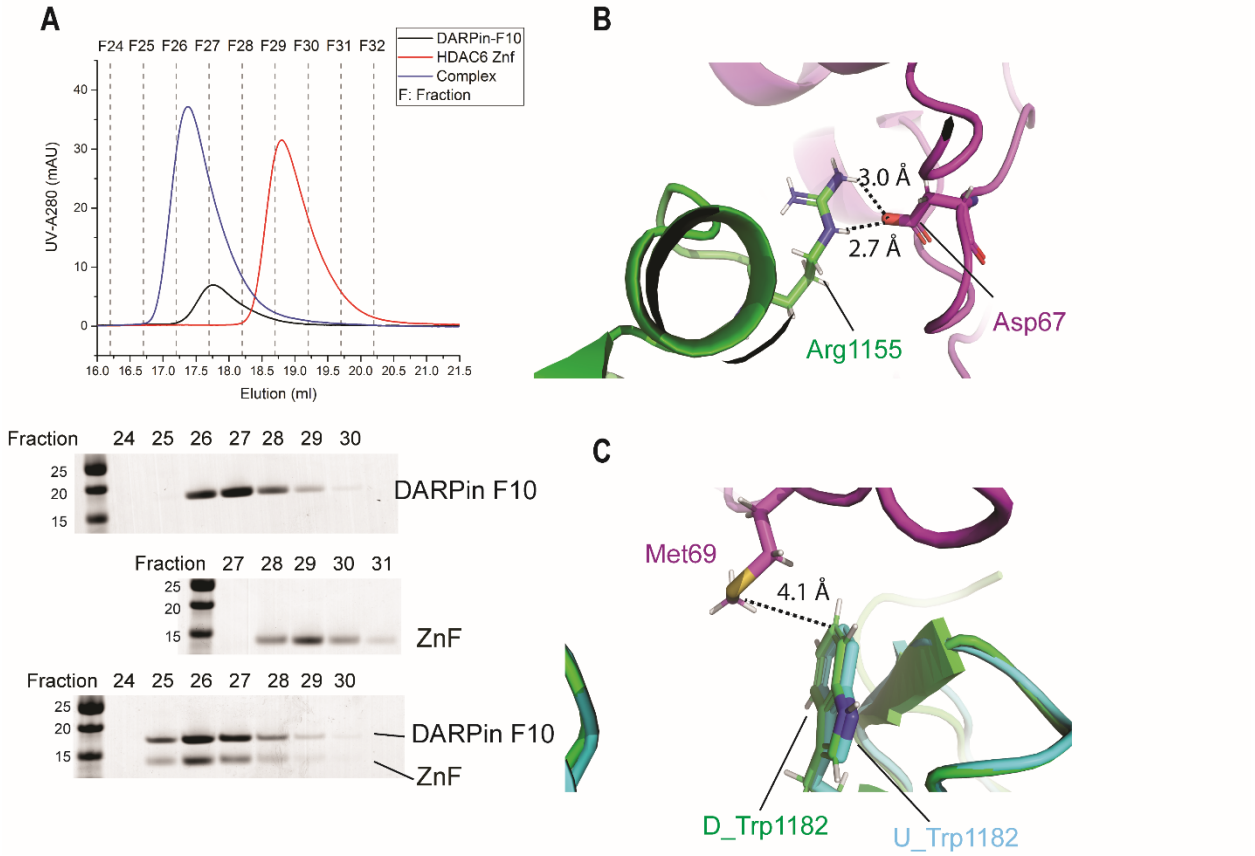

Supplementary Figure 4. DARPin F10 forms a stable complex with the HDAC6 ZnF domain.

(A) Size exclusion chromatography of purified DARPin F10 (black line), HDAC6 ZnF domain (red line) or the mixture of both (blue line). The upper graph shows the chromatographic profile. The lower panels show the analysis of indicated fractions by SDS-PAGE and Coomassie staining. The ZnF domain and DARPin F10 form a stable stoichiometric complex.

(B) Salt bridge between ZnF R1155 and DARPin F10 D67.

(C) Trp1182 is not affected by DARPin F10 binding. Met 69 from DARPin F10 is shown to measure the distance to Trp1182 of the ZnF domain. D_Trp1182: Trp1182 in DARPin binding conformation; U_Trp1182: Trp1182 in Ub binding conformation.

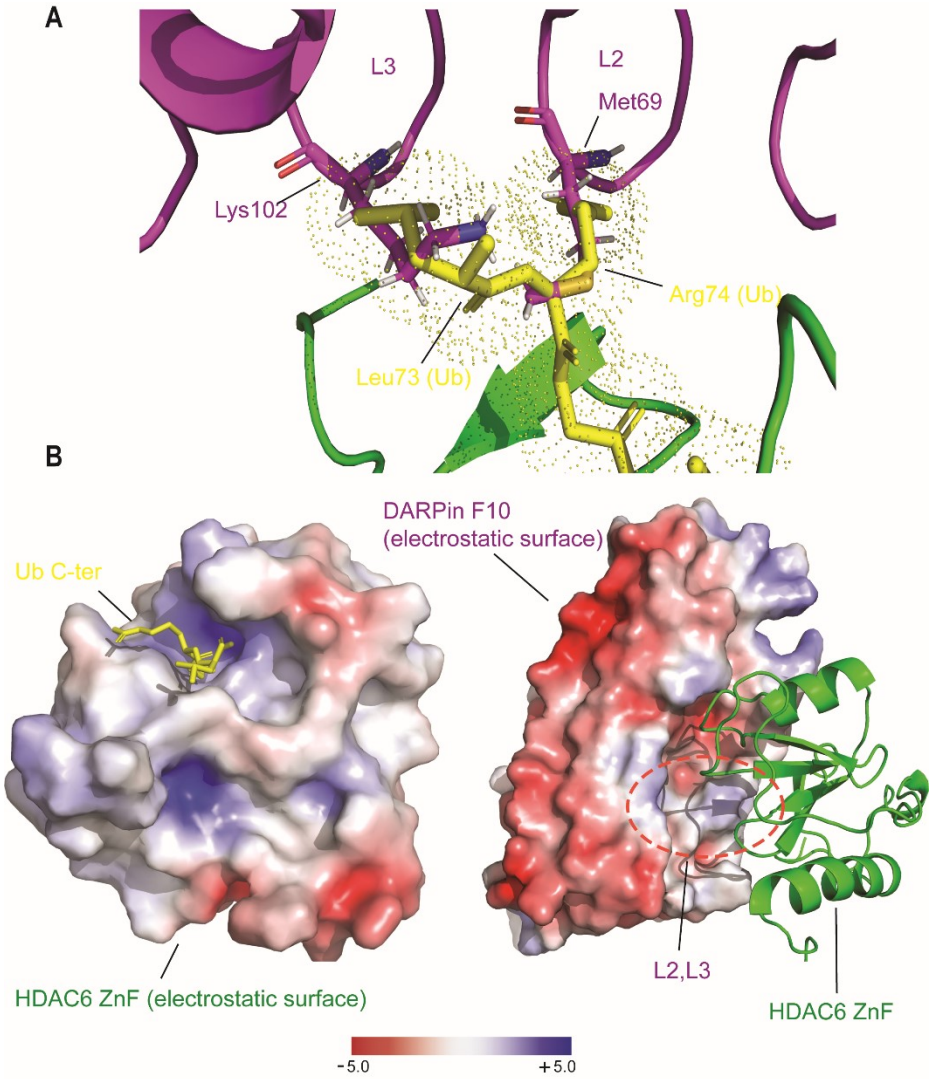

Supplementary Figure 5. DARPin F10 loop 3 zoom in & electrostatic map showing the ZnF domain Ub-binding pocket.

(A) DARPin F10 residue Lys 102 (in L3) and Met (69) (L2) occupy the space where the Ub C-terminus would engage. DARPin F10, purple; ZnF domain, green; Ub, yellow.

(B) Electrostatic surface potential map of the ZnF-Ub C-terminal complex structure (PDB: 3GV4). In the panel on the left, Ub is depicted as yellow sticks, showing that it fits into a positively charged pocket of the ZnF domain (only ZnF electrostatic surface potential map is indicated). In the right panel, the electrostatic surface potential map of DARPin F10 is shown. The region contacting the Ub-binding site (L2, L3, dashed circle) is neutral or slightly positively charged. Electrostatic surface potential maps were calculated with APBS (as PyMOL plugin) and range from -5 to +5 kT/e.

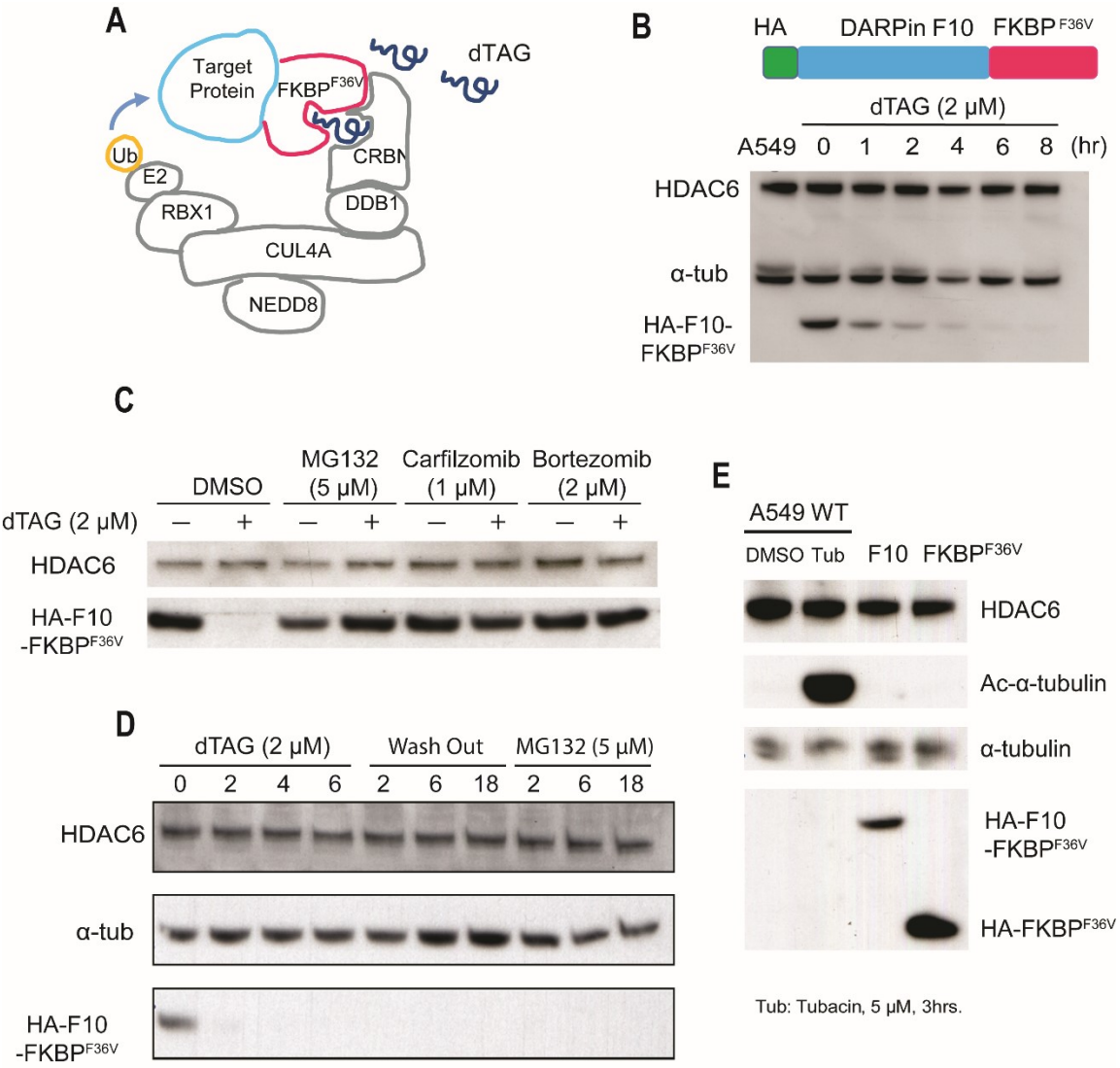

Supplementary Figure 6. Inducible degradation of DARPin F10 in A549 cells.

(A) Scheme illustrating the principle of the FKBP^{F36V}-dTAG system. The target protein is fused to a mutant version of the immunophilin FKBP, FKBP^{F36V}, which selectively binds to the small molecule dTAG-13. This allows recruitment of the cereblon (CRBN) Ub ligase complex, leading to ubiquitination and ensuing proteasomal degradation of the target protein.

(B) The top drawing shows a schematic of the lentiviral construct used to generate A549 cells stably expressing DARPin F10 fused to FKBP^{F36V} (cell line hereafter called F10 cell line). The middle panel shows an immunoblotting experiment with lysates of F10 cell line treated the indicated times with dTAG (2 μM). The leftmost lane shows the parental A549 cells. The membrane was probed with antibodies detecting HDAC6, alpha-tubulin and DARPin-F10 (detected with anti-HA).

(C) DARPin F10 degradation induced by dTAG is proteasome-dependent. When the F10 cell line was pre-incubated with proteasome inhibitors (MG132 5 μM, Carfilzomib 1 μM, Bortezomib 2 μM for 3 hrs, then followed by dTAG treatment for 3 hrs), degradation of DARPin F10 was blocked.

(D) Once degraded, DARPin F10 does not stably reappear for at least 18 hours, even in the presence of proteasomal inhibition. A549 F10 cells were treated with dTAG to induce the degradation of DARPin F10; after

6 hours the medium was changed and replaced by normal medium (wash out) or medium containing MG132. Samples were analysed at different time points to monitor the re-expression of DARPin F10.

(E) F10 does not affect the activity of HDAC6, as monitored by α-tubulin acetylation. The indicated cells (parental A549 cells, F10 cells and $FKBP^{F36V}$ control cells) were used to examine the level of tubulin acetylation by immunoblotting. As a reference, A549 cells were treated with Tubacin (Tub; 5 uM, 3 hrs) to inhibit HDAC6 and elevate α-tubulin acetylation (second lane). The bottom panel shows the expression level of the DARPin F10-$FKBP^{F36V}$ fusion protein, and of the $FKBP^{F36V}$ control.

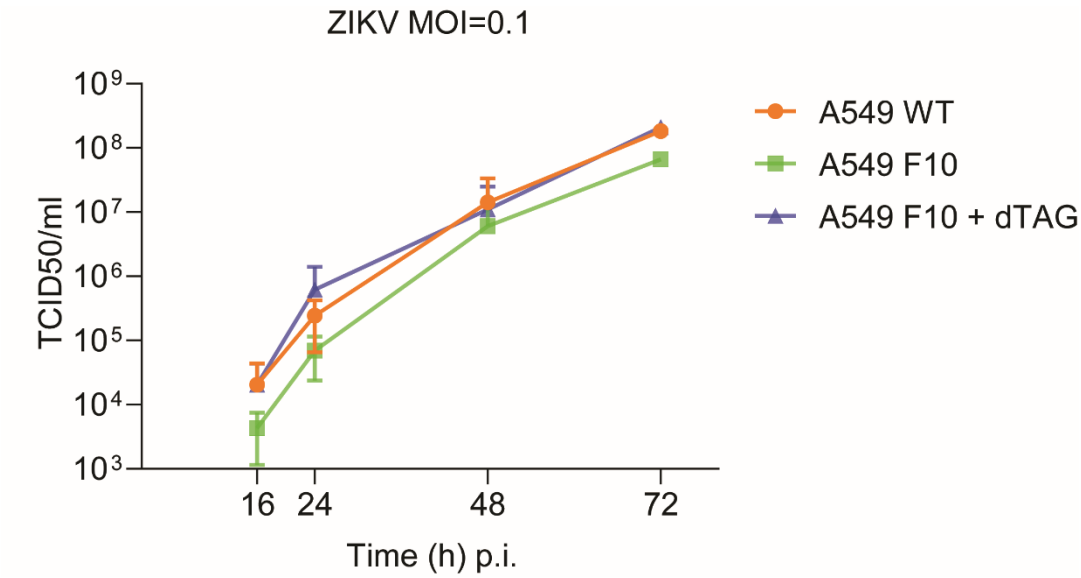

Supplementary Figure 7. ZIKV replication curve.

The indicated cells were infected with ZIKV at a MOI=0.1 $TCID_{50}$/cell and culture supernatants were collected at 16, 24, 48 and 72 hrs post-infection. Viral titers were quantified with a $TCID_{50}$ assay; the samples are originating from the Figure 7A experiment. A significant decrease of the ZIKV titers in A549 F10 cell line was observed here.

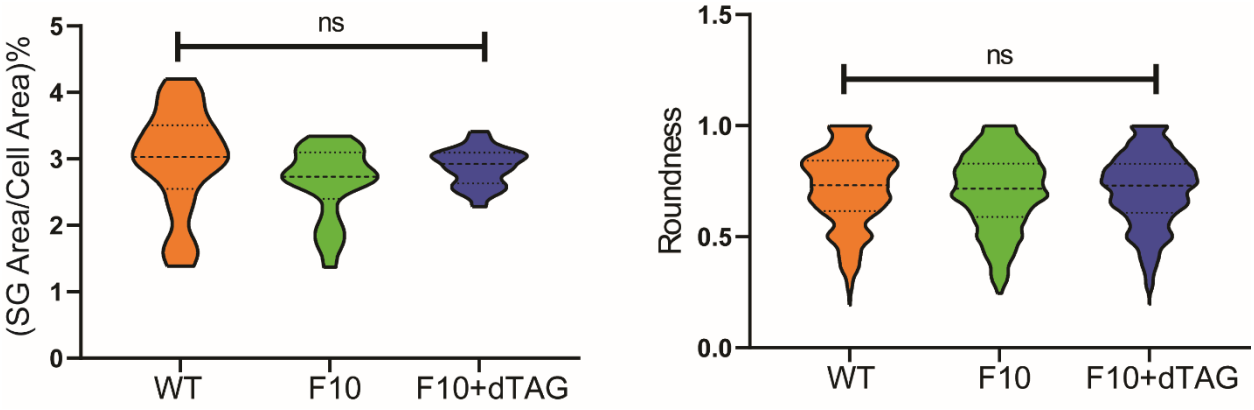

Supplementary Figure 8. Disruption of HDAC6 ZnF-Ub interaction by DARPin F10 does not affect SGs maturation.

SGs were induced with arsenite (1 mM, 30 min) in parental A549 cells or in F10 cells without or with dTAG pre-treatment (pre-incubation 2 μM for 6 hrs) and were visualized by staining for G3BP1. Representative pictures are shown in Figure 5. Left: quantification of the size of SGs per cell area. Ca. 30 cells were used, with a total of > 700 SGs in parental A549 cells. Right: shape of SGs, as analyzed by ImageJ SG counter. Statistical analysis was done by ANOVA test. ns, no significant difference.

References

Advani, V., and Ivanov, P. (2020). Stress granule subtypes: an emerging link to neurodegeneration. Cellular and Molecular Life Sciences.

Anderson, P., Kedersha, N., and Ivanov, P. (2015). Stress granules, P-bodies and cancer. Biochimica et biophysica acta 1849, 861-870.

Artcibasova, A., Wang, L., A., S., Yohei, Y., Mirco, S., Matthias, P., and Stelling, J. (2020, submitted). A quantitative model for HDAC6-mediated virus uncoating predicts Influenza A infectivity (Submitted). Cell Host Microbe Submitted.

Ash, P., Vanderweyde, T., Youmans, K., Apicco, D., and Wolozin, B. (2014). Pathological stress granules in Alzheimer's disease. Brain Res 1584, 52-58.

Banerjee, I., Miyake, Y., Nobs, S.P., Schneider, C., Horvath, P., Kopf, M., Matthias, P., Helenius, A., and Yamauchi, Y. (2014). Influenza A virus uses the aggresome processing machinery for host cell entry. Science 346.

Binz, H.K., Amstutz, P., Kohl, A., Stumpp, M.T., Briand, C., Forrer, P., Grutter, M.G., and Plückthun, A. (2004). High-affinity binders selected from designed ankyrin repeat protein libraries. Nat Biotechnol 22, 575-582.

Binz, H.K., Stumpp, M.T., Forrer, P., Amstutz, P., and Plückthun, A. (2003). Designing Repeat Proteins: Well-expressed, Soluble and Stable Proteins from Combinatorial Libraries of Consensus Ankyrin Repeat Proteins. Journal of Molecular Biology 332, 489-503.

Boyault, C., Gilquin, B., Zhang, Y., Rybin, V., Garman, E., Meyer-Klaucke, W., Matthias, P., Muller, C.W., and Khochbin, S. (2006). HDAC6-p97/VCP controlled polyubiquitin chain turnover. The EMBO journal 25, 3357-3366.

Boyault, C., Sadoul, K., Pabion, M., and Khochbin, S. (2007). HDAC6, at the crossroads between cytoskeleton and cell signaling by acetylation and ubiquitination. Oncogene 26, 5468-5476.

Brauchle, M., Hansen, S., Caussinus, E., Lenard, A., Ochoa-Espinosa, A., Scholz, O., Sprecher, S.G., Plückthun, A., and Affolter, M. (2014). Protein interference applications in cellular and developmental biology using DARPins that recognize GFP and mCherry. Biology open 3, 1252-1261.

Brindisi, M., Saraswati, A.P., Brogi, S., Gemma, S., Butini, S., and Campiani, G. (2019). Old but Gold: Tracking the New Guise of Histone Deacetylase 6 (HDAC6) Enzyme as a Biomarker and Therapeutic Target in Rare Diseases. Journal of medicinal chemistry.

Cabantous, S., Nguyen, H., Pedelacq, J., Koraïchi, F., Chaudhary, A., Ganguly, K., Lockard, M., Favre, G., Terwilliger, T., and Waldo, G. (2013). A New Protein-Protein Interaction Sensor Based on Tripartite Split-GFP Association. Scientific Reports 3, 2854.

Campos, G.S., Bandeira, A.C., and Sardi, S.I. (2015). Zika Virus Outbreak, Bahia, Brazil. Emerging infectious diseases 21, 1885-1886.

Cao-Lormeau, V.M., Roche, C., Teissier, A., Robin, E., Berry, A.L., Mallet, H.P., Sall, A.A., and Musso, D. (2014). Zika virus, French polynesia, South pacific, 2013. Emerging infectious diseases 20, 1085-1086.

Cosenza, M., and Pozzi, S. (2018). The Therapeutic Strategy of HDAC6 Inhibitors in Lymphoproliferative Disease. Int J Mol Sci 19.

Dreier, B., and Plückthun, A. (2012). Rapid selection of high-affinity binders using ribosome display. Methods in molecular biology (Clifton, NJ) 805, 261-286.

Du, J., Cross, T.A., and Zhou, H.X. (2012). Recent progress in structure-based anti-influenza drug design. Drug Discov Today 17, 1111-1120.

Duffy, M.R., Chen, T.H., Hancock, W.T., Powers, A.M., Kool, J.L., Lanciotti, R.S., Pretrick, M., Marfel, M., Holzbauer, S., Dubray, C., et al. (2009). Zika virus outbreak on Yap Island, Federated States of Micronesia. The New England journal of medicine 360, 2536-2543.

Ferreira de Freitas, R., Harding, R.J., Franzoni, I., Ravichandran, M., Mann, M.K., Ouyang, H., Lautens, M., Santhakumar, V., Arrowsmith, C.H., and Schapira, M. (2018). Identification and Structure-Activity Relationship of HDAC6 Zinc-Finger Ubiquitin Binding Domain Inhibitors. Journal of medicinal chemistry.

Gao, X., Jiang, L., Gong, Y., Chen, X., Ying, M., Zhu, H., He, Q., Yang, B., and Cao, J. (2019). Stress granule: A promising target for cancer treatment. British journal of pharmacology 176, 4421-4433.

Gustin, J.K., Moses, A.V., Fruh, K., and Douglas, J.L. (2011). Viral takeover of the host ubiquitin system. Front Microbiol 2, 161.

Hao, R., Nanduri, P., Rao, Y., Panichelli, R.S., Ito, A., Yoshida, M., and Yao, T.P. (2013). Proteasomes activate aggresome disassembly and clearance by producing unanchored ubiquitin chains. Molecular cell 51, 819-828.

Harding, R., Ferreira de Freitas, R., Collins, P., Franzoni, I., Ravichandran, M., Ouyang, H., Juarez-Ornelas, K., Lautens, M., Schapira, M., von Delft, F., et al. (2017). Small molecule antagonists of the interaction between the histone deacetylase 6 zinc-finger domain and ubiquitin. Journal of medicinal chemistry.

Hicke, L., Schubert, H.L., and Hill, C.P. (2005). Ubiquitin-binding domains. Nat Rev Mol Cell Biol 6, 610-621.

Hook, S.S., Orian, A., Cowley, S.M., and Eisenman, R.N. (2002). Histone deacetylase 6 binds polyubiquitin through its zinc finger (PAZ domain) and copurifies with deubiquitinating enzymes. Proc Natl Acad Sci U S A 99, 13425-13430.

Hubbert, C., Guardiola, A., Shao, R., Kawaguchi, Y., Ito, A., Nixon, A., Yoshida, M., Wang, X., and Yao, T. (2002). HDAC6 is a microtubule-associated deacetylase. Nature 417, 455-458.

Hussain, M., Galvin, H., Haw, T., Nutsford, A., and Husain, M. (2017). Drug resistance in influenza A virus: the epidemiology and management. Infect Drug Resist 10, 121-134.

Isaacson, M.K., and Ploegh, H.L. (2009). Ubiquitination, ubiquitin-like modifiers, and deubiquitination in viral infection. Cell Host Microbe 5, 559-570.

Johnston, J.A., Ward, C.L., and Kopito, R.R. (1998). Aggresomes: a cellular response to misfolded proteins. The Journal of cell biology 143, 1883-1898.

Kawaguchi, Y., Kovacs, J., McLauri, A., Vance, J., Ito, A., and Yao, T. (2003). The Deacetylase HDAC6 Regulates Aggresome Formation and Cell Viability in Response to Misfolded Protein Stress. Cell Vol. 115, 727–738.

Komander, D., and Rape, M. (2012). The ubiquitin code. Annu Rev Biochem 81, 203-229.

Kovacs, J.J., Murphy, P.J., Gaillard, S., Zhao, X., Wu, J.T., Nicchitta, C.V., Yoshida, M., Toft, D.O., Pratt, W.B., and Yao, T.P. (2005). HDAC6 regulates Hsp90 acetylation and chaperone-dependent activation of glucocorticoid receptor. Molecular cell 18, 601-607.

Kwon, S., Zhang, Y., and Matthias, P. (2007). The deacetylase HDAC6 is a novel critical component of stress granules involved in the stress response. Genes & development 21, 3381-3394.

Lee, A.K., Klein, J., Fon Tacer, K., Lord, T., Oatley, M.J., Oatley, J.M., Porter, S.N., Pruett-Miller, S.M., Tikhonova, E.B., Karamyshev, A.L., et al. (2020). Translational Repression of G3BP in Cancer and Germ Cells Suppresses Stress Granules and Enhances Stress Tolerance. Molecular cell 79, 645-659 e649.

Legros, S., Boxus, M., Gatot, J.S., Van Lint, C., Kruys, V., Kettmann, R., Twizere, J.C., and Dequiedt, F. (2011). The HTLV-1 Tax protein inhibits formation of stress granules by interacting with histone deacetylase 6. Oncogene 30, 4050-4062.

Li, T., Zhang, C., Hassan, S., Liu, X., Song, F., Chen, K., Zhang, W., and Yang, J. (2018). Histone deacetylase 6 in cancer. J Hematol Oncol 11, 111.

Magupalli, V., Negro, R., Tian, Y., Hauenstein, A., Di Caprio, G., Skillern, W., Deng, Q., Orning, P., Alam, H., Maliga, Z., et al. (2020). HDAC6 mediates an aggresome-like mechanism for NLRP3 and pyrin inflammasome activation. Science 369.

Markmiller, S., Fulzele, A., Higgins, R., Leonard, M., Yeo, G.W., and Bennett, E.J. (2019). Active Protein Neddylation or Ubiquitylation Is Dispensable for Stress Granule Dynamics. Cell reports 27, 1356-1363 e1353.

Mazroui, R., Di Marco, S., Kaufman, R.J., and Gallouzi, I.E. (2007). Inhibition of the ubiquitin-proteasome system induces stress granule formation. Molecular biology of the cell 18, 2603-2618.

Mishima, Y., Santo, L., Eda, H., Cirstea, D., Nemani, N., Yee, A.J., O'Donnell, E., Selig, M.K., Quayle, S.N., Arastu-Kapur, S., et al. (2015). Ricolinostat (ACY-1215) induced inhibition of aggresome formation accelerates carfilzomib-induced multiple myeloma cell death. Br J Haematol 169, 423-434.

Miyake, Y., Keusch, J.J., Wang, L., Saito, M., Hess, D., Wang, X., Melancon, B.J., Helquist, P., Gut, H., and Matthias, P. (2016). Structural insights into HDAC6 tubulin deacetylation and its selective inhibition. Nat Chem Biol 12, 748-754.

Montero, H., and Trujillo-Alonso, V. (2011). Stress granules in the viral replication cycle. Viruses 3, 2328-2338.

Nabet, B., Roberts, J.M., Buckley, D.L., Paulk, J., Dastjerdi, S., Yang, A., Leggett, A.L., Erb, M.A., Lawlor, M.A., Souza, A., et al. (2018). The dTAG system for immediate and target-specific protein degradation. Nat Chem Biol 14, 431-441.

Nover, L., Scharf, K.D., and Neumann, D. (1989). Cytoplasmic heat shock granules are formed from precursor particles and are associated with a specific set of mRNAs. Mol Cell Biol 9, 1298-1308.

Olzmann, J., Li, L., and Chin, L. (2008). Aggresome formation and neurodegenerative diseases: therapeutic implications. Curr Med Chem 15, 47-60.

Ouyang, H., Ali, Y.O., Ravichandran, M., Dong, A., Qiu, W., MacKenzie, F., Dhe-Paganon, S., Arrowsmith, C.H., and Zhai, R.G. (2012). Protein aggregates are recruited to aggresome by histone deacetylase 6 via unanchored ubiquitin C termini. The Journal of biological chemistry 287, 2317-2327.

Peisley, A., Wu, B., Xu, H., Chen, Z.J., and Hur, S. (2014). Structural basis for ubiquitin-mediated antiviral signal activation by RIG-I. Nature 509, 110-114.

Plückthun, A. (2015). Designed ankyrin repeat proteins (DARPins): binding proteins for research, diagnostics, and therapy. Annu Rev Pharmacol Toxicol 55, 489-511.

Protter, D.S.W., and Parker, R. (2016). Principles and Properties of Stress Granules. Trends Cell Biol 26, 668-679.

Reineke, L.C., and Lloyd, R.E. (2013). Diversion of stress granules and P-bodies during viral infection. Virology 436, 255-267.

Reyes-Turcu, F., Horton, J., Mullally, J., Heroux, A., Cheng, X., and Wilkinson, K. (2006). The Ubiquitin Binding Domain ZnF UBP Recognizes the C-Terminal Diglycine Motif of Unanchored Ubiquitin. Cell 124, 1197-1208.

Rudnicka, A., and Yamauchi, Y. (2016). Ubiquitin in Influenza Virus Entry and Innate Immunity. Viruses 8.

Saito, M., Hess, D., Eglinger, J., Fritsch, A.W., Kreysing, M., Weinert, B.T., Choudhary, C., and Matthias, P. (2019). Acetylation of intrinsically disordered regions regulates phase separation. Nat Chem Biol 15, 51-61.

Seigneurin-Berny, D., Verdel, A., Curtet, S., Lemercier, C., Garin, J., Rousseaux, S., and Khochbin, S. (2001). Identification of components of the murine histone deacetylase 6 complex: link between acetylation and ubiquitination signaling pathways. Molecular and cellular biology 21, 8035-8044.

Sweeney, P., Park, H., Baumann, M., Dunlop, J., Frydman, J., Kopito, R., McCampbell, A., Leblanc, G., Venkateswaran, A., Nurmi, A., et al. (2017). Protein misfolding in neurodegenerative diseases: implications and strategies. Transl Neurodegener 6, 6.

Taylor, P., Tanaka, F., Robitschek, J., Sandoval, C.M., Taye, A., Markovic-Plese, S., and Fischbeck, K. (2003). Aggresomes protect cells by enhancing the degradation of toxic polyglutamine-containing protein. Human Molecular Genetics 12, 749-757.

Tourrière, H., Chebli, K., Zekri, L., Courselaud, B., Blanchard, J.M., Bertrand, E., and Tazi, J. (2003). The RasGAP-associated endoribonuclease G3BP assembles stress granules. The Journal of cell biology 160, 823-831.

Wheeler, J.R., Matheny, T., Jain, S., Abrisch, R., and Parker, R. (2016). Distinct stages in stress granule assembly and disassembly. Elife 5.

Wileman, T. (2006). Aggresomes and Autophagy Generate Sites for Virus Replication. Science 312, 875-878.

Wolozin, B., and Ivanov, P. (2019). Stress granules and neurodegeneration. Nat Rev Neurosci 20, 649-666.

Zhang, K., Daigle, J.G., Cunningham, K.M., Coyne, A.N., Ruan, K., Grima, J.C., Bowen, K.E., Wadhwa, H., Yang, P., Rigo, F., et al. (2018). Stress Granule Assembly Disrupts Nucleocytoplasmic Transport. Cell 173, 958-971 e917.

Zhang, X., Yuan, Z., Zhang, Y., Yong, S., Salas-Burgos, A., Koomen, J., Olashaw, N., Parsons, J.T., Yang, X.J., Dent, S.R., et al. (2007). HDAC6 modulates cell motility by altering the acetylation level of cortactin. Molecular cell 27, 197-213.

Zhang, Y., Kwon, S., Yamaguchi, T., Cubizolles, F., Rousseaux, S., Kneissel, M., Cao, C., Li, N., Cheng, H.L., Chua, K., et al. (2008). Mice lacking histone deacetylase 6 have hyperacetylated tubulin but are viable and develop normally. Mol Cell Biol 28, 1688-1701.

Zhang, Y., Li, N., Caron, C., Matthias, G., Hess, D., Khochbin, S., and Matthias, P. (2003). HDAC-6 interacts with and deacetylates tubulin and microtubules in vivo. The EMBO journal 22, 1168-1179.

Appendix

1) HDAC6 CD1+2 (82-837) interacts with IAV H3N2 NP *in vitro*

In addition to the interaction between HDAC6 and IAV viral protein M1 (shown in "Result Part II"), we also tested the interaction between HDAC6 and IAV nucleoprotein (NP) *in vitro*. His-tagged HDAC6 CD1+2 (82~837), NP were purified separately, then both were incubated with Ni-NTA beads, which is able to bind to His-tag. If these two can interact with each other, NP should be precipitated together with HDAC6 CD1+2 by Ni-NTA. As shown in Figure 1, His-tagged HDAC6 CD1+2 (82~837) is able to pull down NP from solution, indicating a direct interaction. Next, we confirmed the interaction by size exclusion as well. In Figure 2, a complex peak is observed prior to HDAC6 CD1+2 and NP individually. Commassie stain shows the complex is composed of HDAC6 CD1+2 and NP.

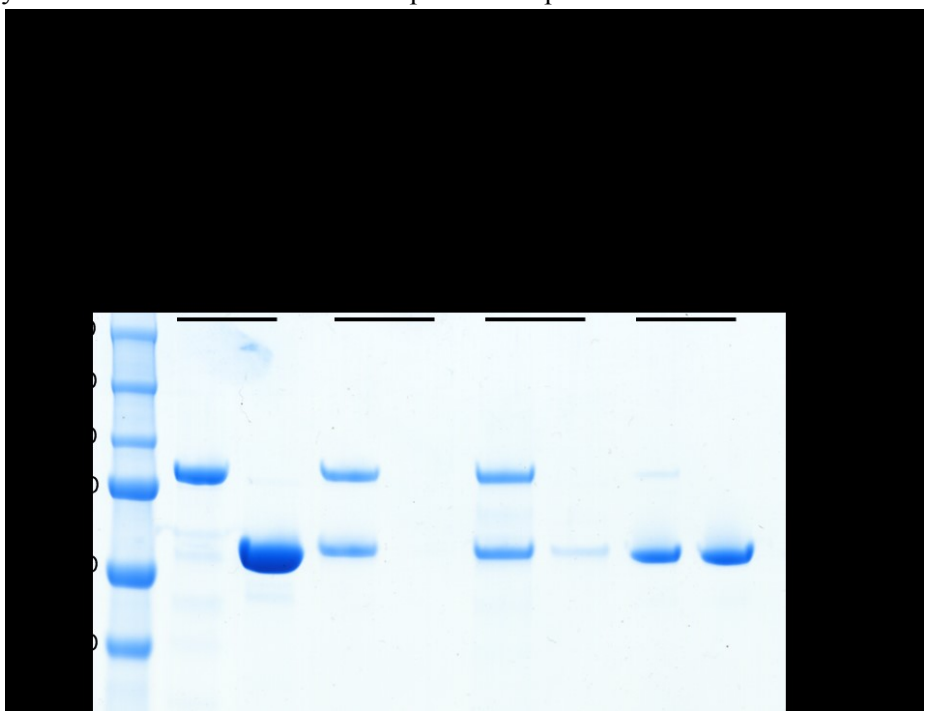

Figure 1, His-tagged HDAC6 CD1+2 interacts with NP

Purified His-tagged HDAC6 CD1+2 (10 µg) and H3N2 NP full length (FL) (20 µg) proteins were incubated together with Ni-NTA beads (7~10 µl slurry) at 4°C in 500 µl binding buffer (10 mM Tris pH=7.5, 100 mM NaCl, 10 mM imidazole) for 30 mins to 1 hr. The beads later were spun down at 4°C, 250 g, for 1 min. The supernatant was removed carefully and kept in new 1.5 ml eppendof (EP) tube, named flow through (FT). Beads were re-suspended with 500 µl binding buffer. By repeating the spin-down and re-suspension steps 3 times, wash step completes. Next, 50 µl elution buffer (10 mM Tris pH=7.5, 100 mM NaCl, 150 mM imidazole) was added to beads, incubated together for 10 mins on shaker, 1000 rpm. Finally, the beads were spun down again and the supernatant was transferred to new 1.5 ml EP tube, named Elution. The beads are boiled together with 20 µl LDS sample buffer (supplied with DTT freshly) for 10 mins, 80°C. The sample buffers with precipitated proteins were named as Beads. For analysis, we loaded 10% input, 40% (=20 µl) Elution, 100% Beads, and 4% (=20 µl) FT on

4-12% gradient NuPAGE Gel and stained with Instant Blue (Expedeon). P-D: pull-down, refers to the experimental group containing two proteins, NP and HDAC6 CD1+2; Control: control, containing only NP protein.

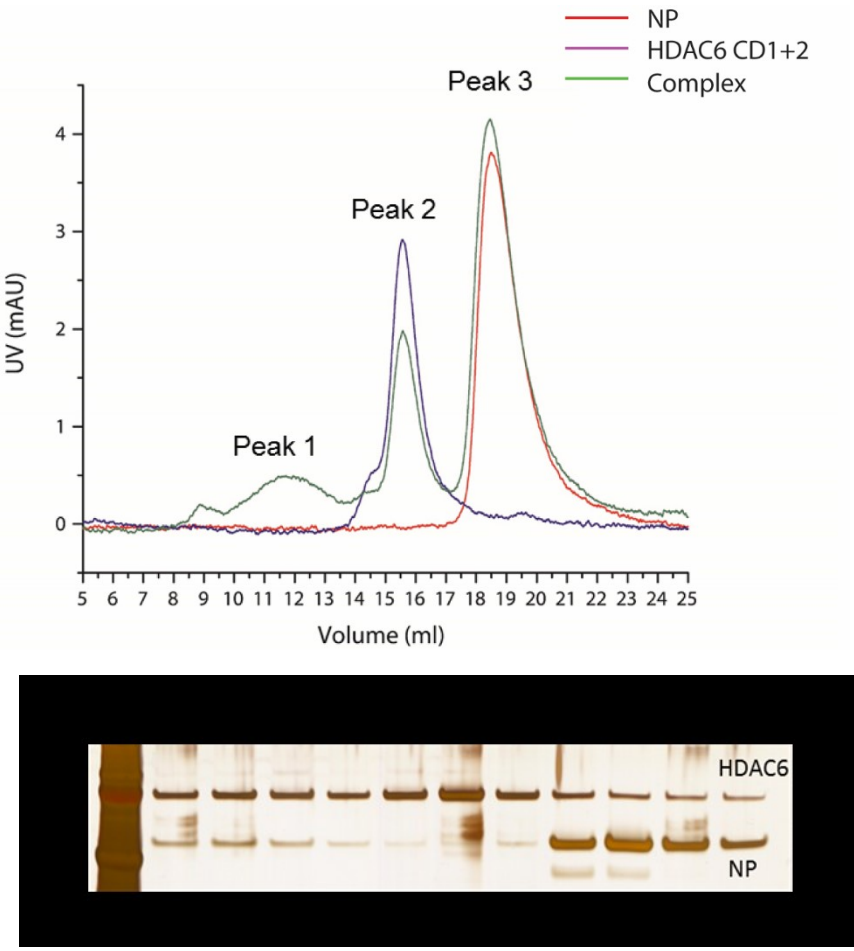

Figure 2, HDAC6 CD1+2 region forms a complex with NP in gel filtration.

20 μg NP and HDAC6 CD1+2 are incubated with 500 μl Gel filtration buffer (10 mM Tris pH=7.5, 100 mM NaCl) on ice for 30 mins, and the mixture is loaded to Superdex 200 10/300 GL. Each fraction from Akta system is detected by SDS-PAGE.

2) Cytochalasin D (CytoD) induces HDAC6-actomyosin interaction in a time-dependent manner

As shown in Results Part II, we found that CytoD treatment induces HDAC6-actomyosin interaction but Latrunculin A (Lat-A) not. The difference seems to be the different effect of these two inhibitors on actin filament: Lat-A keeps actin in globulular form, but CytoD promotes the formation of short actin filaments (Taylor et al., 2011). Therefore, we suggest that HDAC6 interacts with F-actin but not G-actin. If this is correct, we expect to see that HDAC6 will capture more actin by increasing CytoD incubation time as the number of F-actin is increased. Thus, we collected 1 μM CytoD-treated MEF cells at 3 time points, with incubation time from 2 to 6 hours, together with a recovering group (after 6 hrs CytoD treatment, the medium is changed and cells were further cultured for 0.5 hours, named 6 h(R)). Endogenous HDAC6 is immunoprecipitated by the same antibody as used in the "Results I" section.

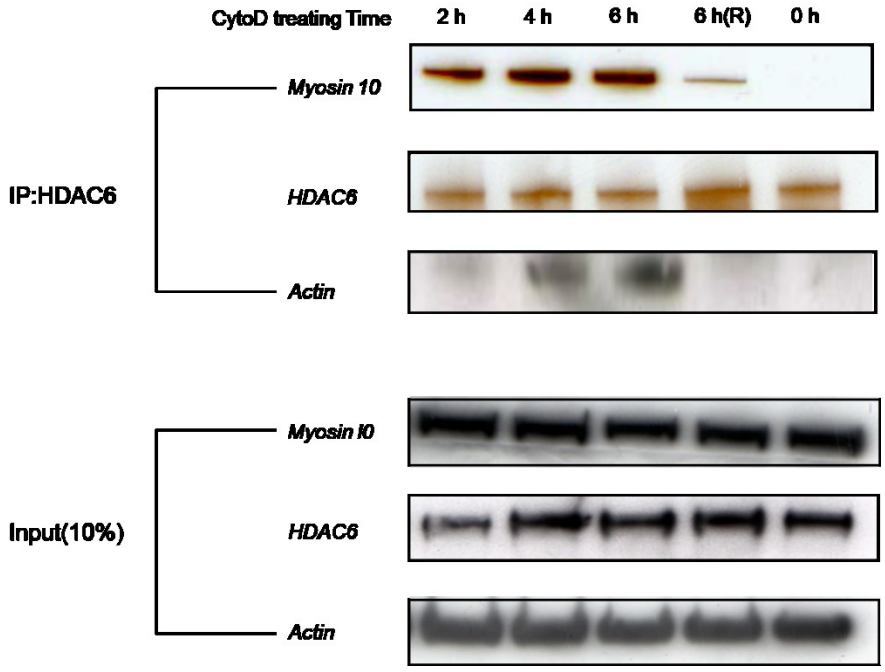

Figure 3, HDAC6 interacts with actomyosin under CytoD treatment

As shown, a longer CytoD treatment (more short-filament actins) leads to a stronger band of actin captured by HDAC6. Once the chemical is removed by changing the medium and washed away, actin is not recruited by HDAC6 immediately and Myosin 10 signal is reduced dramatically but still can be detected as compared to CTR (=Control, refers to non-treated cells). Moreover, since Myosin 10 but not actin, already binds to HDAC6 at 2 hr time point, and still can be detected at 6 h(R) condition, we suggest that Myosin 10 acts on the upstream of actin, meaning HDAC6 binds to Myosin 10 first and then is located to F-actin.

3) Inhibition on HDAC6 deacetylase activity does not affect actomyosin recruitment by HDAC6

We have shown that HDAC6 interacts with actin and myosin 10 under both proteasome inhibition (MG132 treatment) and actin stress (CytoD treatment). We wondered whether HDAC6 deacetylase activity is important for the interaction or not. Hence, we treated MEF WT cells with 5 μM Tubastatin A (TubA), a specific HDAC6 inhibitor, prior to previous two stresses. Immunoprecipitation of HDAC6 showed that addition of TubA to both MG132 and CytoD treated cells does not affect HDAC6 interaction with actomyosin system, indicating HDAC6 enzymatic activity is dispensible for the interactions. (Ac-α-tub, refers to acetylated α-tubulin)

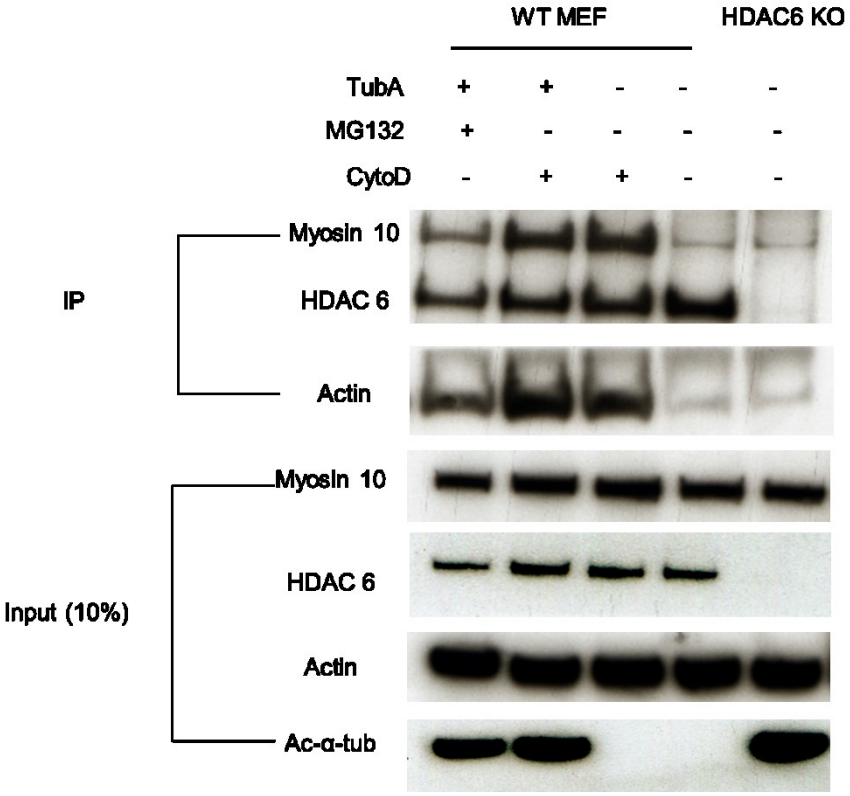

Figure 4, Tubastatin A (TubA) had no impact on HDAC6-actomyosin interaction

4) Over-expressed FKBP^{F36V}-mCherry-F10 is not degraded after dTAG addition

Before the generation of inducible F10 cell line by lentivirus, we tested constructs by expressing FKBP^{F36V}-mCherry-F10 and mCherry-F10-FKBP^{F36V} (in pcDNA3.1) in HEK 293T cells. Surprisingly, after an incubation with 1 μM dTAG-13 for 4 hours (see Figure 5 below), we did not see a significant signal reduction of mCherry. This may be due to 1) the over-expressed F10 overwhelms cellular proteasome capacity; 2) fluorescent tags, like GFP and mCherry, are too stable to be degraded by proteasome pathway (Chirico and Kraut, 2016). Moreover, it has been suggested that target expression and local concentration affect the degradability (Sievers et al., 2018).

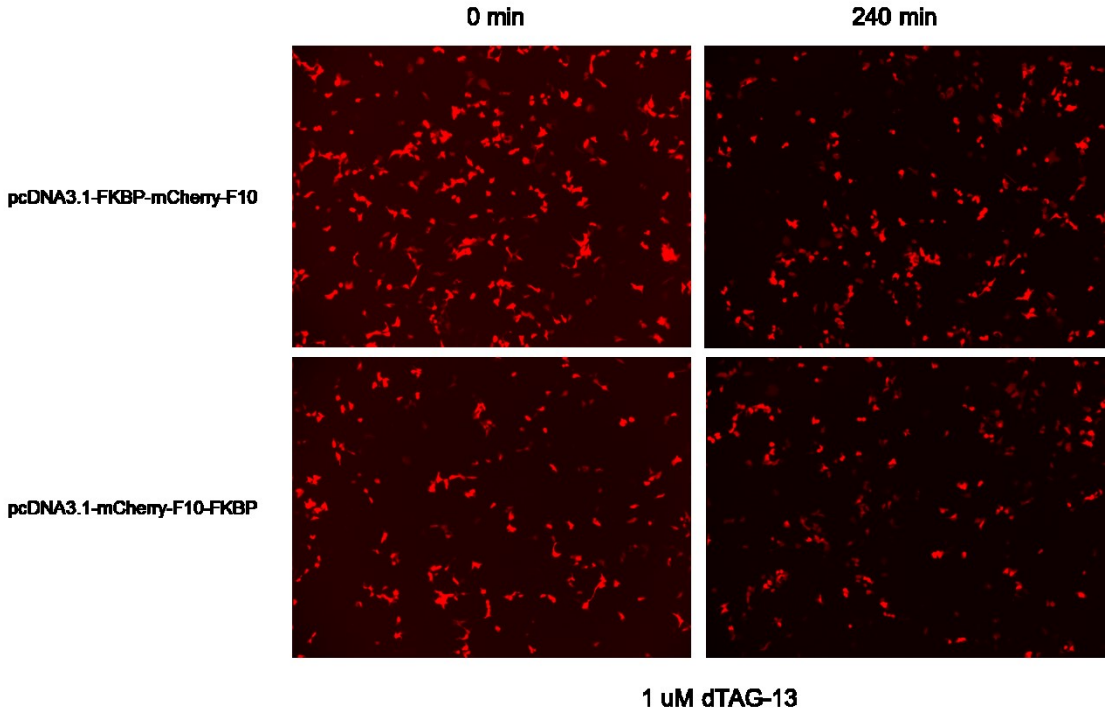

Figure 5, over-expressed FKBP^{F36V} fused mCherry-F10 cannot be degraded by dTAG treatment

Both constructs (2 μg) were transfected by FuGENE HD to 293T cells (in 6-well plate, each well was seeded with 0.1 million cells at 24 hours before transfection). mCherry signal was checked under wide-field microscope.

5) Inhibition of the proteasome after dTAG treatment does not restore HA-F10-FKBP^{F36V} expression rapidly

In Results Part III), we showed that pre-incubating F10-FKBP^{F36V} expressing A549 cells with proteasome inhibitors (MG132, Carfilzomib, and Bortezomib) blocks the dTAG-induced degradation. We wondered whether addition of the proteasome inhibitors after dTAG treatment would result in a rapid restoration of F10 expression. Therefore, after 4 hours incubation of dTAG (1 μM), 5 μM MG132, 1 μM Carfilzomib and 1 μM Bortezomib were added to cells individually after changing the medium, and incubated for 3 hours more. As shown below, we found that the F10 signal was not restored.

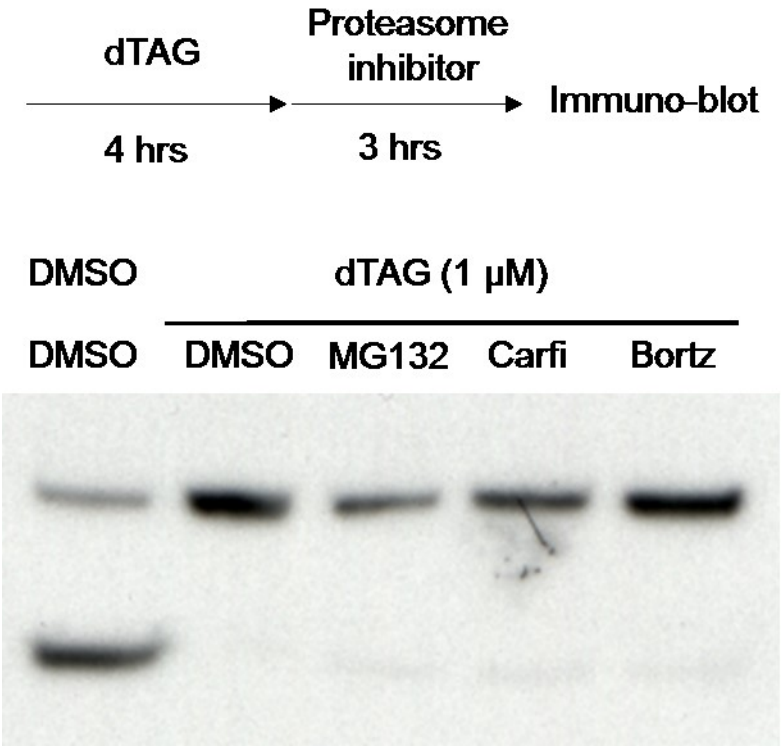

Figure 6, proteasome inhibitors did not rescue F10 expression in 3 hrs

In case that the result is due to the short incubating time (3 hrs), which may be not enough to completely block the degradation, we extended the treating time to 3 days. MG132 was chosen, as Carfilzomib and Bortezomib kill cells after 24 hrs treatment. To verify that MG132 functioned properly, we also examined the Ub signal for all conditions by immunoblotting. As we can see (Figure 7), even with after a 3-day MG132 treatment, expression of F10 was not restored.

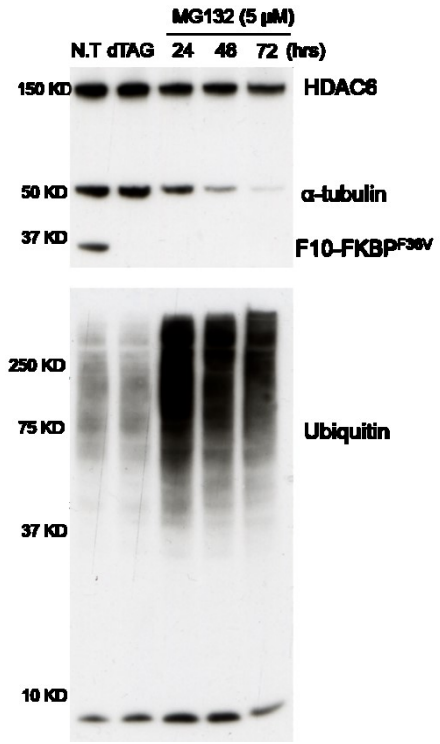

Figure 7, 3-day incubation of MG132 does not restore F10 expression

Next, as MG132 is not able to reverse F10 degradation, we focussed on the two second-generation proteasome inhibitors - Carfilzomib and Bortezomib. To reduce their cell toxicity, we only extended the incubation time up to 24 hours. Surprisingly, both Carfilzomib and Bortezomib partially restored F10 expression, while MG132 still did not (Figure 8). However, the recovery ratio was less than 50%. This result strongly indicates that in comparison to MG132, Carfilzomib and Bortezomib are much stronger proteasome inhibitors, and that the previous negative observations for recovery are likely the result of incomplete proteasome inhibition.

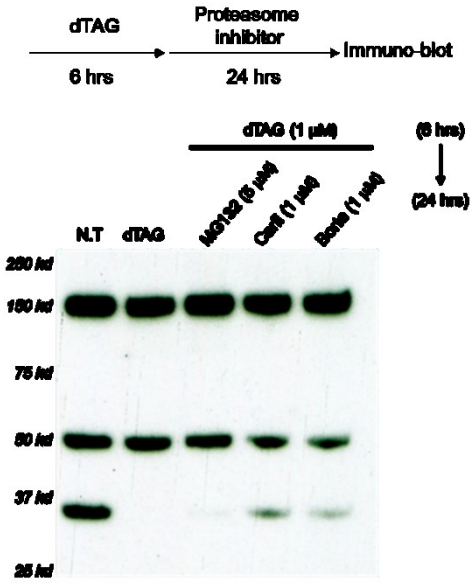

Figure 8, Carfilzomib and Bortezomib can restore F10 expression slightly

Finally, we investigated the effect of re-seeding cells on recovery of dTAG-induced degradation. Cells were divided into 3 groups after 6 hrs dTAG treatment. 1) cells were treated by Carfilzomib for 24 hrs; 2) cells are washed by PBS for 3 times, then the dTAG-containing medium is replaced by fresh DMEM followed by 24 hrs culturing; 3) cells are detached by Trypsin and half of them are re-seeded to a new plate, culturing for 24 hrs more. As expected, a recovery is observed in Carfilzomib-treated cells, and intriguingly, re-seeded cells also showed some recovery (Figure 9). We believe that the step of re-seeding (or passage) efficiently dilutes the dTAG cellular concentration with respond to cell division, while simply changing the medium couldn't.

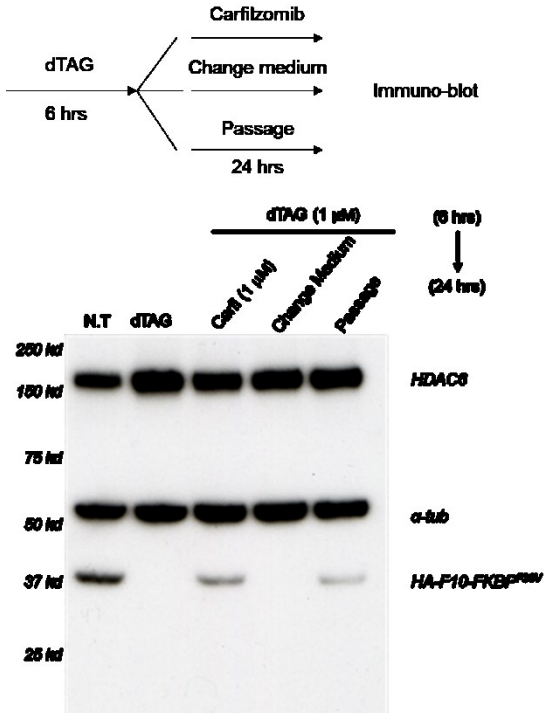

Figure 9, re-seeding (or passaging) could also restore F10 expression

6) Carfilzomib induces Aggresome formation as well

Considering that MG132 is less potent than Carfilzomib and affects many other pathways in addition to proteasome (Kadlcíková et al., 2004), although it has been widely used to induce aggresome formation, we tested Carfilzomib in aggresome formation experiment. WT A549 cells were treated with 2 μM Carfilzomib for 16 hours, and Aggresome is stained by HDAC6 and Ub antibody, and actin is visualized with 488nm-Phalloidin, which is specific against F-actin. As shown (Figure 10), Carfilzomib induced aggresome formation nicely as MG132 does.

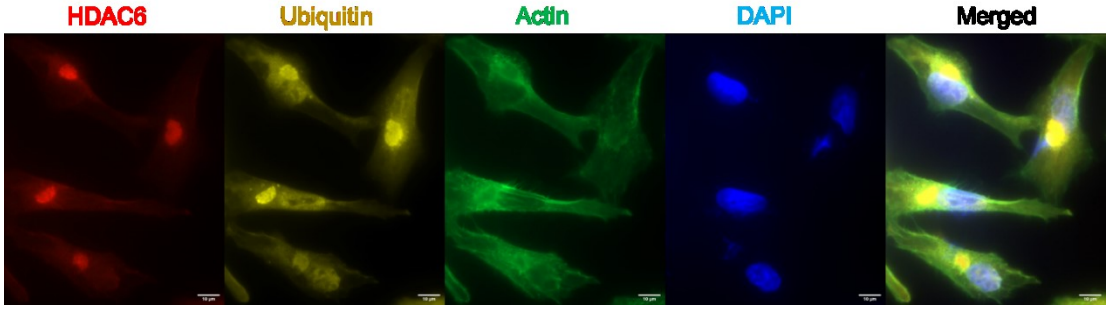

Figure 10, Aggresome induced by Carfilzomib, visualized by Wide-Field Microscopy

We noticed that the actin filament network (discussed in Results Section) is also present around the Carfilzomib-induced aggresome. To further confirm its existence, we used confocal microscopy to scan the actin network layer by layer. 39 cross-sectional views were obtained sequentially, and the mid one (view-19), which presents the maximal diameter of aggresome, was chosen for visualization (Figure 11). Actin, HDAC6 and DAPI signals are colored in Green, Red, Blue, respectively. As we can see, in the white arrow pointed sites, an actin circle is observed around the aggresome. Since Phalloidin only binds to filamentous actin, we confirm that an F-actin cage is organized around the aggresome. Furthermore, this data confirms Carfilzomib as a substitute for MG132. However, to minimize its toxicity, we still need to optimize the working concentration and incubation time.

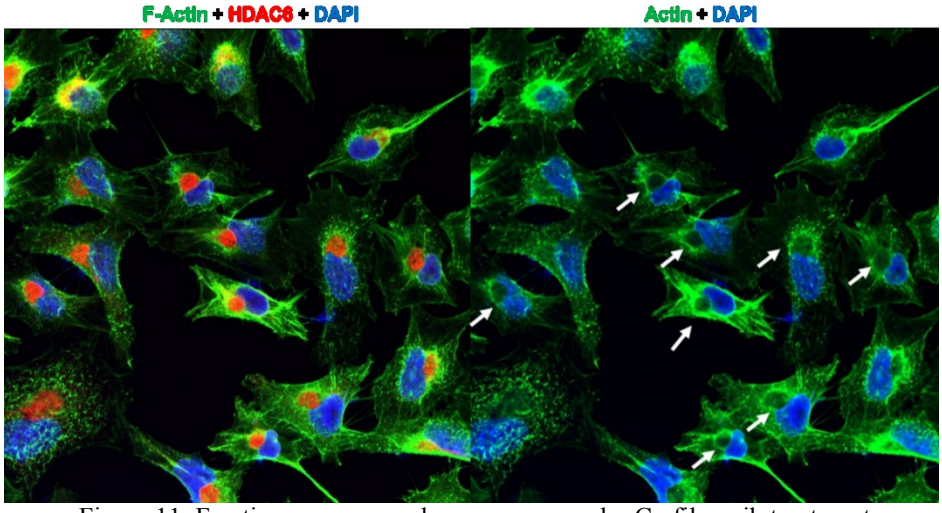

Figure 11, F-actin cage surrounds aggresome under Carfilzomib treatment

F-actin, HDAC6, and nucleus are colored with Green, Red, and Blue, respectively. White arrows indicate the F-actin cage surrounding Aggresome.

7) MG132 treatment does not enhance the interaction between Myosin 10 C-termini (1103-1961) and HDAC6 ZnF (1108-1215)

As shown in Results Part II, Ub chains bridge Myosin 10 and HDAC6, possibly together with additional proteins. Herein, we tested the interaction between over-expressed GST-HDAC6 ZnF (1108-1215) and GFP-Myosin 10 (1103-1961) in HEK 293T with an upregulation of Ub chains through MG132 treatment (5 μM, 6 hrs). In Figure 12, we see that Myosin 10 C-termini pulls down GST-ZnF as expected, however, the precipitated ZnF signal does not increase after MG132 treatment. We suggest that it is due to the effect of MG132, which actually leads to an increase of ubiquitinated proteins, but not Ub chains. The generation of Myosin 10-HDAC6 interaction favored Ub chains is dependent on DUBs, whose activity are not changed under MG132 treatment. Another remaining question is that Myosin 10 C-termini interacts with HDAC6 ZnF even without MG132 treatment, and this seems contradictory to our previous conclusion that interaction between HDAC6 and Myosin 10 only happens under stress. The explanation may be that over-expressing a protein is already a stress for cell. This activates the unfolded protein response (Raden et al., 2005), mimicking MG132 treatment to some extent, although without MG132 treatment, GFP-Myosin 10 C-termini was ubiquitinated as well (seen in Ub signal blot). Therefore, for future exepriments an alternative manner to upregulate the *in vivo* Ub chains amount should be considered.

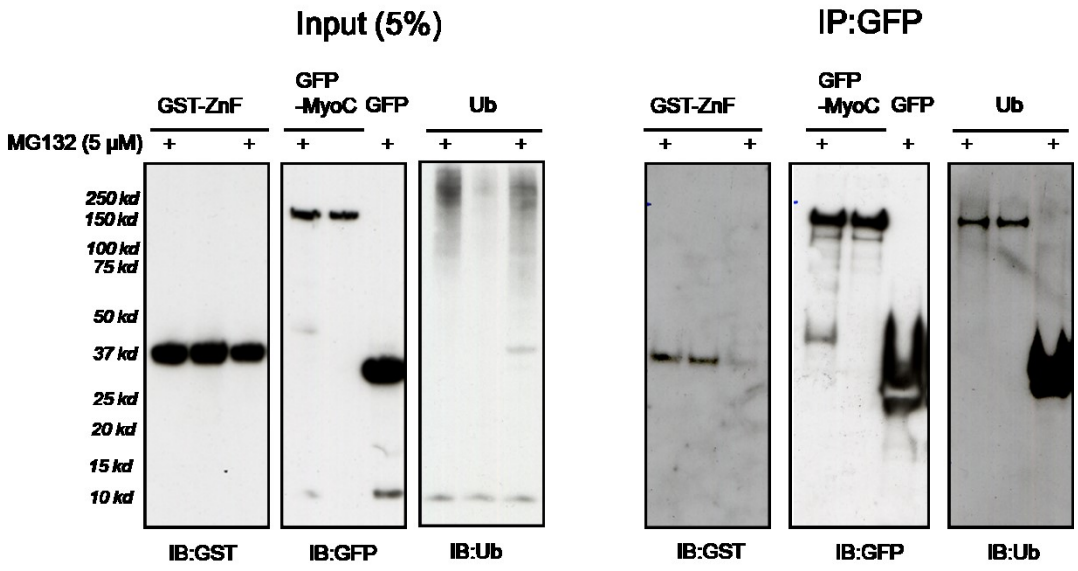

Figure 12, MG132 does not enhance the interaction between over-expressed Myosin 10 C-termini (1103-1961) (MyoC) and HDAC6 ZnF.

pOPINJ-GST-hsHDAC6 ZnF (1108-1215) (5 μg), pCDNA3.1-GFP and pCDNA3.1-GFP-Myoin 10 (1103-1961) (5 μg) were co-transfected to 293T cells (1 miliion cells were seeded 24 hours before transfection). At Day 2 after transfection, cells were treated with 5 μM MG132 as indicated. Cells were harvested and lysed by RIPA buffer.

Co-immunoprecipitation was done with GFP_Trap MA beads (20 µl). Proteins were identified by specific antibodies.

8) Investigation of HDAC6 ZnF containing complex by Native Gel

To investigate the different complexes formation *in vitro*, we incubated ZnF protein (20 µg) with mono Ub (10 µg), F10 (20 µg), His-HA-F10 (20 µg) and His-F10-Flag (20 µg) separately in binding buffer (10 mM Tris pH=7.5, 100 mM NaCl), and checked the complex conformation by Glycine Native Gel. The molar ratio of ZnF to Ub/F10/His-HA-F10/His-F10-Flag in mixture was 4:3, 4.3, 3:2 and 3:2, respectively. From the result (Figure 13, below), we saw an obvious band-shift after comparing the ZnF/F10, ZnF/His-HA-F10, ZnF/His-F10-Flag complex lanes to the corresponding individual proteins (initial position is indicated by dash lanes) lanes, confirming that a stable complex is formed between ZnF and F10 (tagged or not). We also observed that a new band appears at the top position, indicating a big complex is formed after incubation, and this happens only with tagged F10. The formation of this complex is not clear, but considering that the N- and C-termini cap are critical for DARPin properties (Plückthun, 2015), this observation suggests that a tag might change the binding affinity to the target. Another interesting finding is that after incubation, we did not see a stable complex band that represents for ZnF-Ub complex. Instead, the smear, which is observed in Ub alone lane, moves down a little bit in ZnF-Ub complex lane. This abnormal observation indicates that the ZnF-Ub complex is not stable. This has been observed previously; researcher argued that the complex of Ub-binding protein and Ub has a built-in "dynamic stability", meaning that it can undergo rapidly assembly and disassembly (Hicke et al., 2005). Since a similar smear appears at the top of the Ub lane, we consider that Ub could form an amyloid-like aggregate so that it is shifted to the top in Native Gel, even after the recruitment of ZnF. Docking of ZnF protein reduces the entropy, transferring the aggregate to a condensed confirmation, hence, the smear shifts down.

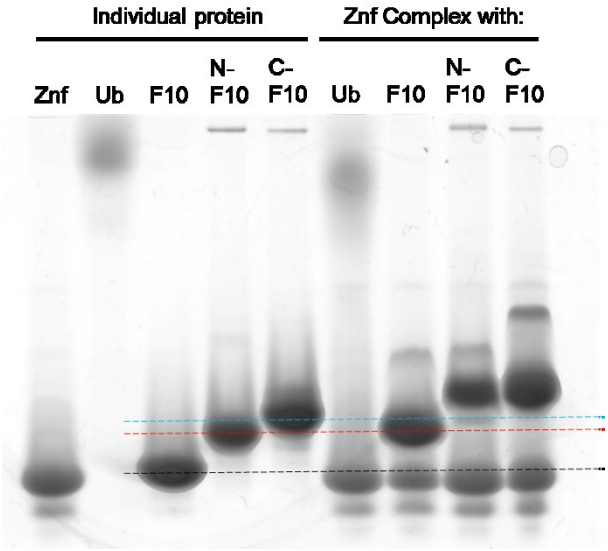

Figure 13, ZnF formed a stable complex together with F10 protein but no mono Ub.

The black, red and blue dashed lines indicate the initial position of F10, His-HA-F10 and His-F10-Flag. N-F10 refers to His-HA-F10; C-F10 refers to His-F10-Flag; Ub, mono-Ub. (Running buffer: 25 mM Tris pH=7.0, 192 mM Glycine. 1 hr 45 mins, constant 100 V; Native Gel recipe: for 5 ml stacking gel: 0.375 mM Tris =8.8, 4.275 ml; Acrylamide/Bis-acrylamide(30%), 0.67 ml; 10% (w/v) ammonium persulfate (AP), 0.05 ml; TEMED, 5 µl; 10 ml separating gel(10%): 0.375 mM Tris =8.8, 6.49 ml; Acrylamide/Bis-acrylamide(30%), 3.4 ml; 10% (w/v) ammonium persulfate (AP), 100 µl; TEMED, 10 µl)

Discussion

Summary

Mathematic modeling for IAV uncoating

In this thesis, we systematically examined the role of HDAC6 in the stress response, especially under the influenza A virus (IAV) infection. Firstly, our biochemical data, combined with the mathematical modeling results from our collaborators from D-BSSE ETH, allowed us to make a quantitative and mechanistic description of how HDAC6, via its interaction with two different cytoskeleton motor proteins -- myosin 10 and dynein, facilitates IAV to break its capsid in uncoating step. This model describes a scenario whereby the application of numerous copies of myosin 10, which dominated uncoating efficiency, and few dyneins (≥1) is the optimal strategy for the virus to achieve the highest rate of successful uncoating. The critical modulator is the interaction between HDAC6 ZnF domain and C-termini free Ub or Ub chains. Further, we simulated the outcome of multiple chemical treatments with our model, and the results agree well with experimental data. Last but not least, from this model we successfully predicate that H1N1 strain is more dependent on the HDAC6 pathway than H3N2, and this was verified in the experiments with corresponding clinical strains. Considering that IAV is not the only virus found to be HDAC6 dependent, this refined model stands a chance to be applied to other viruses and contributes to drug discovery.

Targeting HDAC6 ZnF via DARPin F10

Since the previous finding has shown that mHDAC6 ZnF point mutation (W1116A), which silences its interaction with Ub, leads to a great inhibition of IAV infection, we would like to block ZnF-Ub interaction with synthetic proteins (e.g. nanobody, DARPin…). In collaboration with the University of Zurich, we successfully identify an artificial small protein, DARPin F10 that targets ZnF domain and blocks its binding to Ub specifically. X-ray structure explicitly demonstrated that DARPin F10 occupies the Ub-binding pocket on ZnF motif. Due to its high affinity (K_D 95 nM), DARPin F10 can replace Ub from HDAC6 ZnF domain. After the blockage, we observe a significant down-regulation on not only the cellular granules (e.g. Aggresome and SGs) formation, but also IAV and ZIKA virus infection in A549 cells. Again, those findings emphasize the importance of the HDAC6-Ub interaction during cellular stress responses, including chemical stresses and virus infection. Currently, the antiviral effect of DARPin F10 is tested under SARS-Cov2 infection by collaborating with the University of Bristol (UK).

Remaining questions

HDAC6 interactome

To understand how HDAC6 works under stress conditions, identifying HDAC6 interacting proteins is

the prerequisite. Endogenous HDAC6 immunoprecipitation by polyclonal antibody followed by an LC-MS/MS analysis (Results Part II) illustrates dozens of candidates. Most of them are involved in the cytoskeleton system, especially the actin network. Since tubulin is a well-known HDAC6 substrate, we expected to see microtubules-related proteins initially. However, few were identified. Besides, *in vitro* interaction tests (not shown) between purified zebrafish HDAC6 catalytic domains (CD1, CD2 and CD1+2) and α-tubulin or microtubule were all negative. Therefore, we believe that the binding of HDAC6 to microtubule is not a stable protein-protein interaction, but an enzyme-substrate reaction, which happens very transiently. Similarly, the interaction with actin-related proteins seems "fragile" as well. We tested multiple lysis buffers to perform the immunoprecipitation assay, and only a very gentle and mild buffer (CSK buffer from CSH protocol, described in "Results Part II method"), which can preserve the entire cytoskeleton system, gave positive results. Any harsh conditions, for example, high salt concentration (>200 mM NaCl) or strong detergent (e.g. 0.1% NP-40), disassociate the "complex". Herein, we propose an amyloid-like aggregate, of which the formation is mediated by Ub chains, to explain HDAC6 interaction with other proteins during the stress response. Initially, free Ub-chains, either from proteasome inhibition (e.g. generated from ataxin-2's deubiquitination activity) or viral infection (e.g. the C-termini free Ub inside IAV particle), forms fibrillary aggregates due to their physicochemical properties (Morimoto et al., 2015), and thanks to this fiber structure which possess abundant free C-termini, multiple copies of HDAC6 and motor proteins (e.g. myosin 10) will be recruited to the aggregate through specific interactions (dynein can be loaded as well by interacting with HDAC6 loop region). As a result, an aggregate or a complex, composed of HDAC6/Motor proteins/Ub chains is formed. In contrast to a traditional protein complex which is formed by a fixed number of its components, this fibrillary aggregate has a varied number of HDAC6, Ub and myosin 10 (or others). For example, Ub chains, either K48 or K63 or any other linkage, may possess n (n>2) copies of mono-Ub. Considering that Ub chains can also have branches (Meyer and Rape, 2014; Ohtake et al., 2016), the aggregate has more than one free C-terminals exposed to HDAC6 ZnF, so does the site for myosin 10 binding (Figure 1, "Discussion"). Therefore, the formulation of the complex could be written as (n) HDAC6-(m) Ub-(x) Myosin 10 (m>>n & x), suggesting the complex does not maintain a stable 3D structure which can be determined by X-ray or CryoEM. Recently, many amyloid-like/fibrillary structures have been put forward, for instance, HDAC6 regulates DDX3X-amyloid aggregates formation via changing LLPS process (discussed in Introduction 2-4), and they are as important as the stable protein complex. Generally, they are sensitive to outside stimuli, e.g. temperature, and only exist under certain conditions.

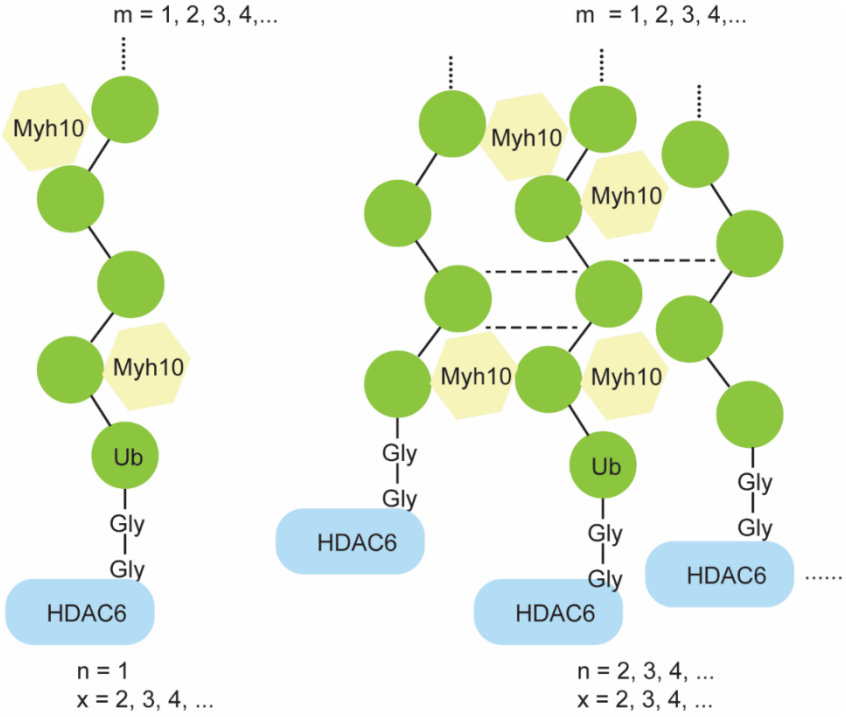

Figure 1, composition of (n) HDAC6-(m) Ub-(x) Myosin 10 aggregate

One Ub chain has one free C-terminal for HDAC6 binding (n = 1), but it can recruit several Myh10 (short for myosin 10) (x > 1), and the length of the Ub chain varies (m = 2, 3, 4 …). Considering multiple Ub chains can form a fibrillary aggregate which is maintained by weak interactions (indicated by dash lines), therefore it is capable of recruiting multiple HDAC6 (n > 1) to its numerous free C-terminals (represented by the C-terminal Gly-Gly motif).

HDAC6 binds to Ub selectively

Another question from Mass Spectrometry analysis is we did not identify the well-known HDAC6 interacting protein Ub as a binding candidate. Immunoprecipitation of endogenous HDAC6, in which the same antibody was used as for LC/MS, indeed significantly enriches Ub signal (detected by Western Blot) from WT MEF cells under proteasome inhibition as compared to HDAC6 KO cells. We reasoned that the difference between Mass Spectrometry analysis and Western blot detection is the specificity of the two techniques. Western blot, which greatly depends on the antibody, is more specific than MS in terms of visualizing one protein, because it will not be affected by the background/noise signal from other proteins. While for MS, considering that the endogenous HDAC6 protein level is low, the amount of pulled-down Ub might be very low as compared to the vast noise signal at Ub peak, so that the differential Ub signal will be ignored in later analysis. Taking the *in vitro* assays (e.g. the crystal structure of ZnF-Ub in Introduction Figure 5a) into account, we believe that Western blot data reflects the truth. Nevertheless, we found that endogenous HDAC6 only pulls down Ub chains that appear at site which equals to high molecular weight region (>50 kd) as a smear. Mono-Ub (<10 kd) is not

captured by HDAC6. Besides, the data from our collaborator shows that after incubating HDAC6 with IAV particles posterior to acidification, capturing HDAC6 merely pulls down high molecular weight Ub chains from the solution (data not shown). Those findings seem in contrast to the results from binding data between HDAC6 ZnF and mono-Ub either *in vitro* with ITC (Kd=5 µM) or *in vivo* with split-GFP assay. Meanwhile, we found that HDAC6 does not pull down any Ub under normal (non-stressed) conditions (Results II). Therefore, we assume that the interaction between HDAC6 and Ub needs an activation during the stress response. For instance, considering that there is a long unstructured region (~400 amino acids) between CD2 and ZnF, HDAC6 can adopt different conformations: With the closed state, Ub-binding pocket is inaccessible, while after exposed to some stimulus, HDAC6 is opened and exposes ZnF domain to Ub (Figure 2 below). Although the hypothesis above is very appealing, there is no direct evidence yet. The 3D structure of full length HDAC6-Ub chain complex will hopefully provide an insight to HDAC6's selective Ub binding mode.

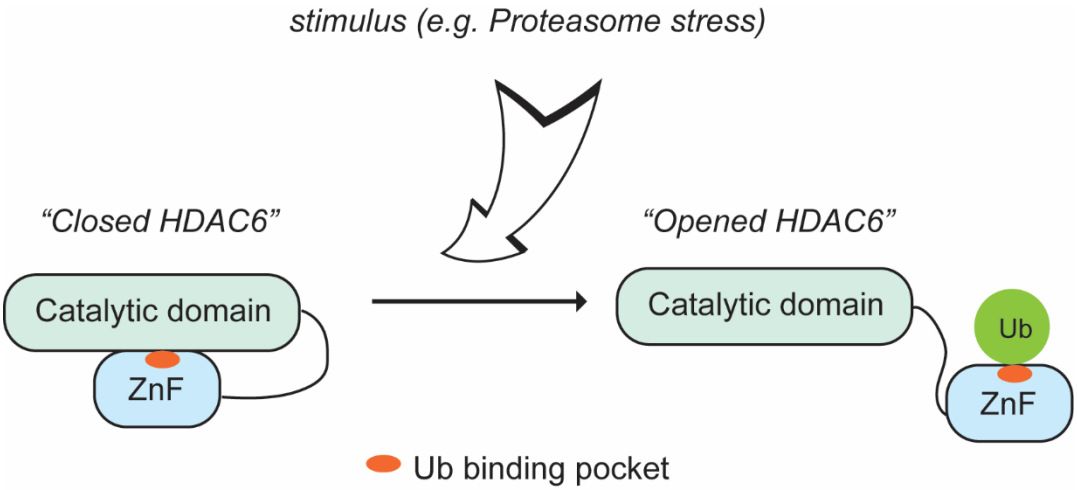

Figure 2, proposed conformation change of HDAC6

We propose that HDAC6 will experience a conformation transfer (from closed to opened state) to expose its ZnF domain for Ub recruitment after the stimulus, which perhaps induces post-modifications on HDAC6. However, the precise mechanism is largely unknown.

Ub binding activates the HDAC6/Myosin 10 pathway

Based on our data, we learned that the mutated hsHDAC6 ZnF domain (W1182A) impairs the binding between HDAC6 and myosin 10/actin, but inversely enhanced the affinity with dynein, suggesting that after binding to Ub, HDAC6 will participate in actomyosin pathway, rather than HDAC6-dynein/microtubule pathway. However, HDAC6-actomyosin and HDAC6-dynein/microtubule pathways are not mutually exclusive, but function complementarily to break viral capsid. Knock-down of myosin 10 and dynactin 2 (a subunit of the dynein complex) individually or simultaneously dramatically downregulate virus uncoating (Banerjee et al., 2014a). We argue that Ub is the switch to

decide the portion of HDAC6 in both pathways. Both biological data and mathematic modeling support that that myosin 10 dominates IAV uncoating step. The scenario from the computational simulation shows 1 dynein and 7~8 Myosin motor proteins could break viral capsid efficiently. The switch, Ub or Ub chains, are responsible for assigning more HDAC6 into the actomyosin pathway. The driving force of the sorting might be due to the affinity difference: the affinity between HDAC6 and Ub may be higher than that in HDAC6-dynein. Meanwhile, a higher in situ Ub concentration facilitates HDAC6-myosin 10 interaction as well. As shown, IAV particle is filled with C-terminal free Ub. Its release increases local Ub concentration around the viral capsid, recruiting HDAC6 and enhancing the interaction with myosin 10. Last but not the least, considering both dynein complex and Ub chains/Myosin 10 aggregate have a quite high molecular weight (>300 kd) and will occupy a large surface of HDAC6 once bound, it is possible that binding of either of them to HDAC6 will create spatial constraints for binding the other, and this may be the structural basis for our "asymmetric model".

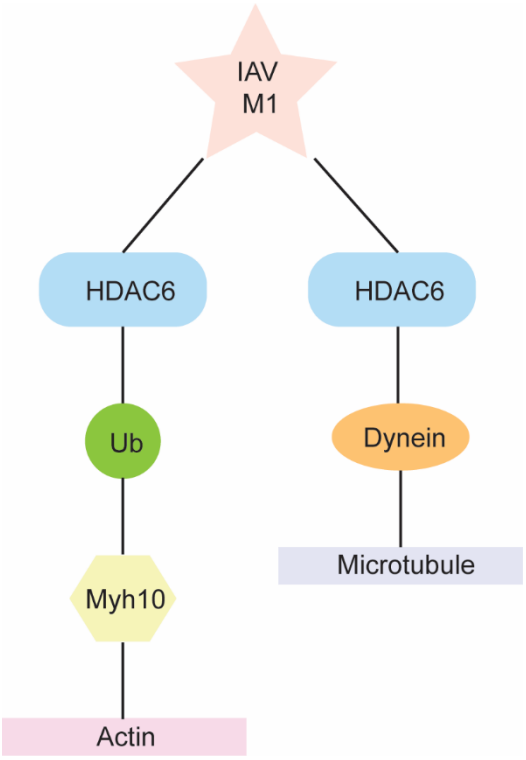

Figure 3, the asymmetric model for IAV uncoating

On one hand, HDAC6 binds to Ub/Myosin 10 or Dynein, further connected to Actin or Microtubule respectively. On the other hand, HDAC6 interacts with IAV capsid protein (e.g. M1) spontaneously. The movement of two complexes leads to the breakage of the virus capsid. The detail is in Results Part II.

An F-actin network is needed for virus uncoating

In actin stress, we showed that with Cytochalasin D (Cyto-D) treatment, HDAC6 binds to actin, while

with Latrunculin A (Lat-A) not (see in "Result Part II"). Considering that Cyto-D converts long actin filament (F-actin) to shorter filament while Lat-A depolymerizes F-actin to globular actin (G-actin, monomer) (Manfred, 1982; Taylor et al., 2011), we concluded that HDAC6 is recruited to F-actin via myosin 10. Immunofluorescent data with phalloidin, which is specific for F-actin, gave a direct visualization that an F-actin network is formed at the rim of HDAC6 indicated aggresome (Appendix 6). From published data, this filamentous network is believed to be linked to aggresome clearance, in which myosin 10 & HDAC6 are required to translocate the aggregates to autophagosome (Hao et al., 2013). Although HDAC6 interacts with actin during IAV uncoating (Banerjee et al., 2014a), we still don't know whether actin exists as G-actin or F-actin. Due to the small size of IAV particles (1~10 nm in diameter), it is difficult to test the presence of an F-actin network around viral particles directly by microscopy. However, the data from the treatment of Cyto-D which reduces viral uncoating efficiency by 70% emphasized the importance of an intact F-actin network. Meanwhile, after the endosome stage, the viral particle will be relocated to the perinuclear area, where a randomized but complex actin network is already constituted (Khatau et al., 2009; Pfisterer et al., 2017). Intriguingly, another key protein for IAV uncoating, myosin 10 (also known as NMMYH-IIb), is distributed around the nucleus as well. In contrast, myosin 9 (or NMMYH-IIa), which is highly conserved to myosin 10 in sequence, exists mainly underneath the plasma membrane (Vicente-Manzanares et al., 2009) (Figure 4, below) so that its deletion did not affect virus uncoating. Thus, similar to the F-actin around aggresome, although it is not visualized, a filamentous network of actin around the viral particle is indispensable. And this network is the path for numerous HDAC6/Ub/Myosin 10 complexes to walk on, all together providing the structural basis for our IAV uncoating model.

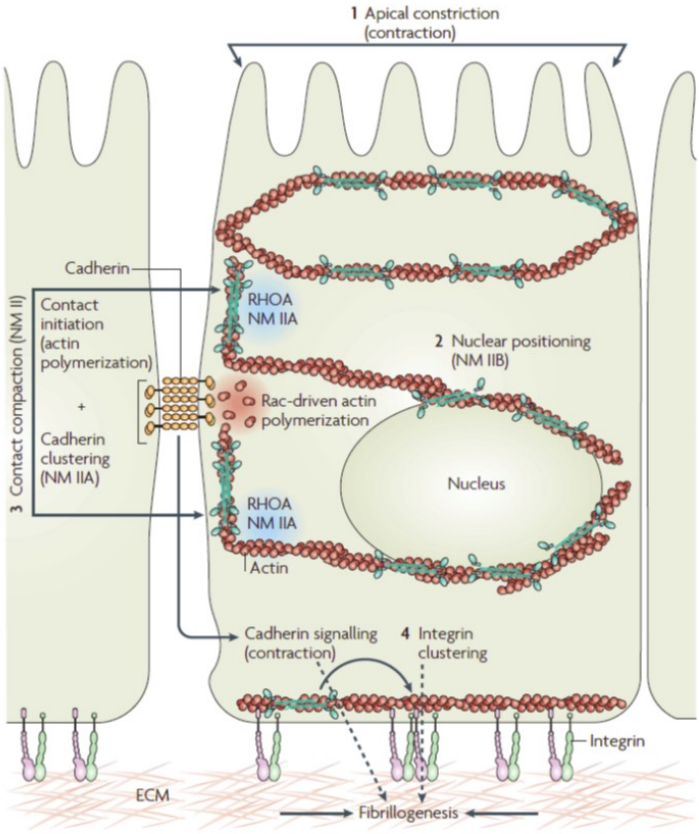

Figure 4, Myosin 9(NM IIA) and Myosin 10 (NM IIB) are located in plasma membrane and perinuclear area, respectively. Figure is taken from (Vicente-Manzanares et al., 2009)

Indirect interaction between HDAC6 and dynein

Although we know that the interaction between HDAC6 and myosin 10 is bridged by Ub, how does HDAC6 interact with dynein? The HDAC6 region responsible for dynein binding has been identified by genetic analysis, and from our structure (PDB: 5G0J), region (436-484) is exposed at the surface (Figure 5 in Discussion), meaning it is easily accessed. We thought initially the interaction between HDAC6 and dynein complex would be direct. Thus, by collaborating with Andrew Carter Group in MRC-LMB, we tested different HDAC6 clones with purified dynein C-terminal **t**ail/**d**ynactin/**BI**CD2 (TDB) complex (Urnavicius et al., 2015). Purified human HDAC6 (82-837), mouse HDAC6 CD1, mouse HDAC6 CD2, mouse HDAC6 CD1+2, zebrafish HDAC6 CD1+2 and the full-length zebrafish HDAC6 were individually incubated with DDB complex, then the mixture was loaded on the size exclusion column. Unfortunately, no HDAC6-Dynein complex peak could be observed from the solution. There are several hypotheses to explain the different results of Co-IP and Gel filtration: 1) the interaction between HDAC6 and Dynein is bridged by an intermediary connector. Unfortunately, from our previous LC/MS result, no such candidate was identified or indicated. 2) The DDB complex used does not possess the sub-component that HDAC6 interacts with. Dynein typically functions with dynactin and other proteins like BICD2 (activating adaptor) as a motor unit. Although the core

components are conserved, some components can be replaced by other proteins accordingly, for instance, BICD2 can be changed with BICDR1, suggesting the functional dynein complex has different "versions". The one we worked with was extracted from pig brain, and according to the HDAC6 proteome data from human, we know that in brain HDAC6 expression level is lower than average (Jiang et al., 2020) (Figure 5 below), therefore DDB maybe not the one which can interact with HDAC6. Taken together, to explore more on HDAC6-Dynein interaction, a systematic analysis by different approaches is urgent.

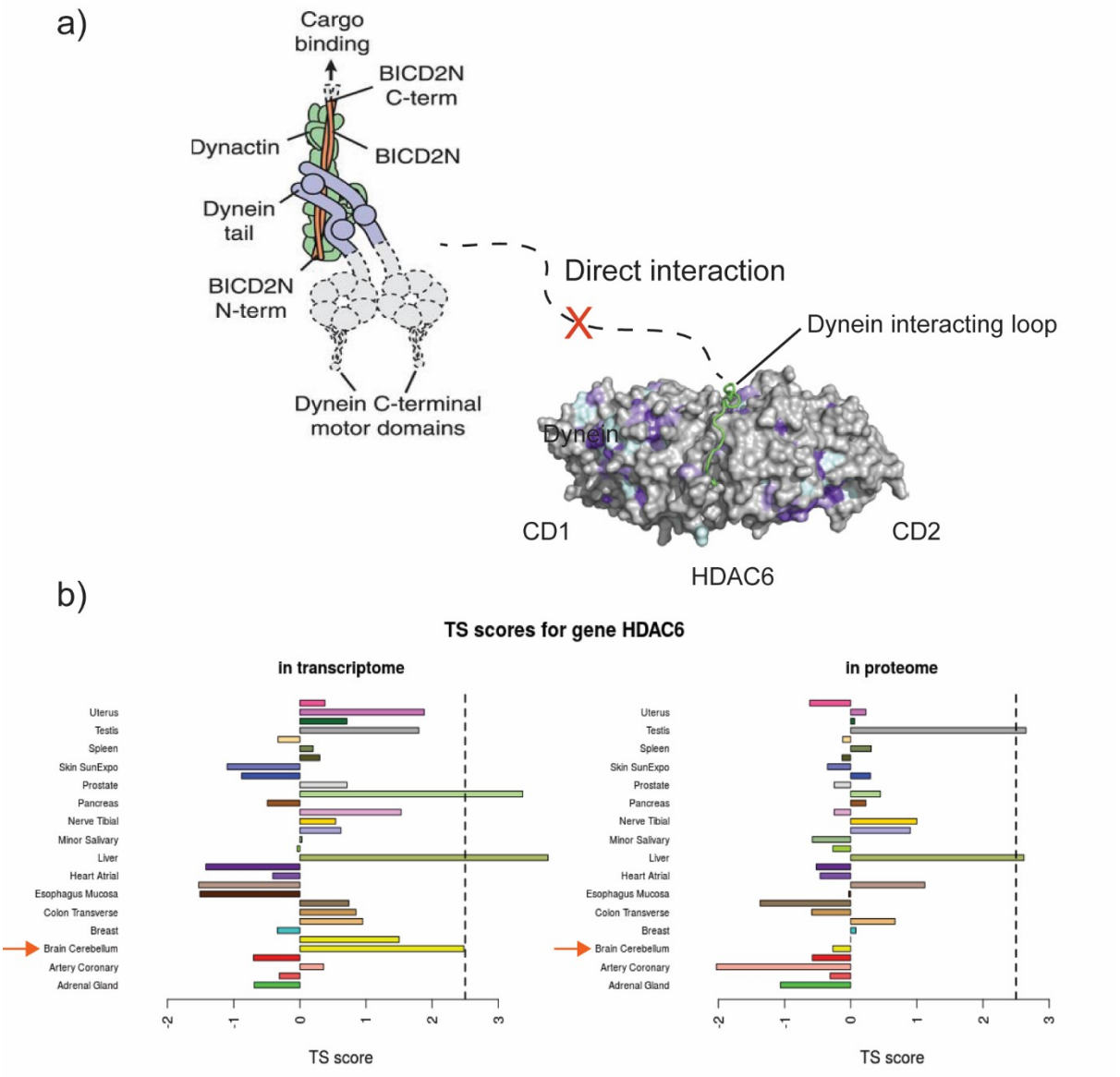

Figure 5, HDAC6 has no direct interaction with a purified Dynein C-terminal tail/Dynactin/BICD complex a) By testing purified HDAC6 proteins from different species (including Zebra fish, mouse, and human) with Dynein C-terminal tail/Dynactin/BICD complex, we could not detect a direct interaction. Dynein complex figure is taken from (Urnavicius et al., 2015). b) HDAC6 expression level is compared in different tissues (human). If HDAC6 has TS (tissue specificity) scores at least in one tissue >= 2.5 (indicated by a dashed line), it is called tissue-enriched (including tissue-enriched-but-not-specific and tissue-specific). In the plots, the vertical lines are at thresholds 2.5 and 4. As it shows, HDAC6 is enriched in testis, while in the brain (pointed by red arrows),

HDAC6 expression level is lower than average. Figure is taken from the published database in the reference (Jiang et al., 2020)

Distinct roles of HDAC6-dynein-microtubule & HDAC6-myosin 10-actin

In a previous study, researchers showed that the HDAC6-Dynein motor complex is the carrier for ubiquitinated protein, participating in aggresome formation, and further evidence that LRRK2-mediated phosphorylation of HDAC6 regulates HDAC6-dynein interaction and aggresome formation consolidates the idea (Lucas et al., 2019). Meanwhile, the actomyosin system is mainly responsible for aggresome clearance, which is stimulated by Poh I-derived free K63 linked Ub chains (Hao et al., 2013). It was shown that knockdown of cortactin and myosin 10 inhibit aggresome clearance. However, the authors showed by immunofluorescence that actin exists inside the aggresome, while from our data we describe an F-actin/myosin 10 cage structure that surrounds the aggresome, similar to vimentin cage, a hallmark structure formed during aggresome formation. Considering that vimentin function in the autophagy pathway (e.g. via relocation of the autophagosome) is to clean aggregates (Morrow et al., 2020), as well as that vimentin is a key regulator of actin organization (Serres et al., 2020), F-actin network may participate in autophagy-dependent aggresome clearance either. However, we cannot exclude the possibility that F-actin/Myosin 10 network is active during aggresome formation. As in our data we show that K48 linked Ub chains bridges HDAC6 and myosin 10, while in the publication (Hao et al., 2013) it is that K63 linked Ub chain activates HDAC6 to deacetylate cortactin and promote actin filament formation, further facilitating aggresome clearance. It is possible that K63 does not recruit myosin 10 to HDAC6, but K48 does, which may participate in aggresome formation. Additional studies are required on the detail of aggresome life cycle. Currently, it seems that during uncoating phase, IAV utilizes 1) HDAC6-dynein-microtubule mootor system for aggresome formation and 2) HDAC6-myosin 10-actin system for aggresome clearance and to disassemble its capsid.

Limitations of the current modeling

In the asymmetric model (Figure 3, and in Results Part II), although we know HDAC6 interacts with myosin 10 and dynein via different domains (ZnF and loop region$_{436\text{-}484}$ respectively), the two domains are not considered individually during the simulation. Therefore, the current model cannot exactly reflect the binding difference between HDAC6 CD-Dynein and HDAC6 ZnF-Ub-myosin 10. Lack of experiment data, for instance, the full length HDAC6 3D structure, detail of dynein components as well as its HDAC6 interacting region, etc, all lead to the ambiguity. To simplify, we considered HDAC6 as a single unit (not HDAC6 ZnF or HDAC6 CD). Another simplification was the viral capsid. We modeled the capsid (C) as a pure M1 protein shell, hence the other components and protein modifications were not taken into consideration. However, among those ignored factors, some may participate in the uncoating process by interfering with HDAC6. As reported, M1 can be ubiquitinated

(Su et al., 2013), and the various branches of those fixed Ub chains may have the chance to competitively recruit HDAC6 ZnF domain from HDAC6-myosin 10 pathway, either interfering or facilitating the uncoating. Another ignored HDAC6 interacting protein is IAV nucleoprotein (NP), which encapsidates the negative strand viral RNA, protecting it from nucleases. We found that it binds to HDAC6 CD domain, but not to the C-terminal region (839-1215, covering ZnF domain) *in vitro* (Appendix 1). Interestingly, NP has been shown to form a complex with M1. The ternary complex composed of HDAC6-NP-M1 describes a new route that may strengthen the association between M1 and HDAC6, helping the uncoating. However, it is difficult to imagine the function of an internal viral component (NP) in a process that mainly happens in the external area. Collectively, those simplifications ignore many details inevitably. With the increase of experimental data, the model will be optimized further to better mimic reality.

Off-target effects of DARPin F10

Even though DARPin F10 has a high specificity against HDAC6 ZnF domain, there are still five off-target proteins under the conditions we tested. Among them, some are involved in virus infection and their unexpected DARPin F10 binding property might contribute more or less in the virus inhibition tests. For example, SEC16A, a molecular scaffold that plays a key role in the organization of the endoplasmic reticulum exit sites (ERES), acts as a docking platform to help influenza A virus vRNP form liquid organelles (Alenquer et al., 2019). PSMD10, short for 26S proteasome non-ATPase regulatory subunit 10, has been reported to interact with IAV protein as a host component (Watanabe et al., 2014). And KHDRBS1, an SH domain containing RNA binding protein, was identified as a host protein which interacts with IAV polymerase acidic protein to promote viral ribogenesis and infectivity (Capitanio; and Wozniak., 2012). Last but not least, the ubiquitin-like protein SUMO4, is deeply involved in the viral life cycle. IAV matrix protein M1 can be sumoylated, which controls the maturation and assembly of the virus (Wu et al., 2011). Adding of DARPin F10 may lead to F10's accumulation on M1 sumoylation site, further prohibiting the capsid breakage. As for the Hsp90, it has been categorized as an HDAC6 interacting protein and is a substrate (Kovacs et al., 2005). Its recruitment may be a result of HDAC6 enrichment. To minimize the off-target effect, we can optimize DARPin F10 by DARPin affinity maturation. On one hand, it is possible to change several critical amino acids on the binding surface to increase spatial complementary (=specificity) and affinity against ZnF domain. On the other hand, fusion of F10 with other ZnF-binding DARPins will double the specificity by combining two independent epitopes. After identifying the binding motif of other DARPins (the remained 23 DARPins from the preliminary screen), we can model the structure of those ZnF-DARPin complex. The one with the least spatial conflicts to DARPin F10 should be chosen. The linker's length will be adjusted according to the spatial position of two DARPins. Considering that current F10 already possessed a high specificity, a reinforced heterogeneous DARPin dimer may eliminate the off-targets effect.

Limitations of the FKBP^{F36V}-dTAG system

To generate a conditionally degrading F10 cell line, we fused an FKBP^{F36V} fragment to the DARPin F10 C-terminus. After adding dTAG-13, the fusion is degraded by the proteasome in 3~6 hours. This protein-level knockdown has several advantages, like faster-response and reversibility, as compared to other conditional systems. Yet, some problems were detected. First of all, the transiently over-expressed F10-FKBP^{F36V} was not efficiently degraded. In our experiments, the fused protein is based on the pcDNA 3.1 vector with strong promotors, leading to a high expression level in both 293T and A549 cell line within 24~48 hrs. The following treatment with dTAG-13 in different concentrations, varying from 1 μM to 1 mM, had little effect on F10 amount (Appendix 4). Conversely, in lentivirus infected cells, the same fusion protein was degraded as expected. The difference is perhaps a result of the expression level. With pcDNA 3.1 vector, the fused protein is very highly expressed and overloads the proteasome's capacity. Some are successfully degraded, but the portion might be too small to be visualized by microscopy. The second problem is connected to reversibility. As expected, adding any of three proteasome inhibitors (MG132, Carfilzomib, and Bortezomib) 3 hrs before dTAG treatment blocked the degradation of DARPin F10, but when proteasome inhibitors were added after dTAG treatment, surprisingly, F10 expression did not reappear within 3 hrs. After extending the incubation time of the inhibitor to 24 hrs, weak bands of F10 were detected in samples treated with the two new generation inhibitors, Carfilzomib and Bortezomib, whereas, the expression of F10 was never restored even after 3 days MG132 incubation (Appendix 4). The difference in inhibitor behavior can be easily explained that in terms of blocking proteasome, the next generation inhibitors (Carfilzomib and Bortezomib) are much more potent than the old MG132. In summary, although dTAG and FKBP^{F36V} mediated degradation is a cutting-edge technique to conditionally knockdown target proteins, and exhibits a very promising future in medical field (e.g. targeting the traditionally untargetable transcription factors) (Nabet et al., 2018), restriction exists, which will become more apparent with additional studies.

Mechanism and future of DARPin F10 inhibition on aggresome and SG

To investigate DARPin F10's impact on cellular granules, we chose aggresome and SG as our targets. The formation of these two Ub positive inclusion bodies were both halted due to the blockage of HDAC6 ZnF. Nevertheless, the underlying mechanism is different. In aggresome, as discussed above, DARPin F10 replaces the cargo – ubiquitinated aggregates from the HDAC6-dynein complex, and the transport of aggregates is interrupted. However, for SG formation, the HDAC6-dynein function is unclear. Unlike aggresome, which is unique, there are multiple SGs in the cell, and their distribution is not limited in a restricted area, e.g. MTOC site, suggesting that the formation of SG may not need the long-distance and directed transport of ubiquitinated proteins by HDAC6-dynein like in the aggresome formation. Notwithstanding, dynein and microtubules contribute to SG formation, but in different ways. It has been reported that microtubule depolymerization does not influence SG number and size, but

significantly reduced the average velocity of SG movement, the frequency of quick movement events, and the apparent diffusion coefficient of SGs. Besides, actin disorder had no effects on SG motility (Nadezhdina et al., 2010). This data indicates that nucleation (responsible for SG number) and maturation (final size of SGs) are both independent of the microtubule system. In contrast, publications from Graciela L. Boccaccio Group and David Pastre Group confirmed that dynein-microtubule is a key participant in SG formation by presenting that 1) microtubules dynamics is related to the size of SGs and responsible for the sliding of mRNA particles (Chernov et al., 2009), and 2) knockdown of dynein by siRNA against its heavy chain (DHC) reduces SG positive cells ratio by 50% under oxidative stress (Loschi et al., 2009). Due to those paradoxes, it is precarious to conclude that F10 inhibits SG nucleation by disassociating ubiquitinated cargos from the HDAC6-dynein motor complex. Meanwhile, it is possible that Ub bridged HDAC6-myosin 10 interaction regulates SG nucleation as well. The precise mechanism will be understood after researchers throw additional light on the entire SG formation pathway. In any case, from our observations, we can conclude that for two studied cellular inclusion bodies, aggresome and SG, regardless of the precise mechanism, DARPin F10 inhibits both granules formation.

Since the normal aggresome and SG are considered to be protective inclusion bodies for cells (Tanaka et al., 2004; Thomas et al., 2011), inhibition of their formation couldn't value a lot in future clinical application. However, in aging-related neurodegenerative diseases, like Alzheimer's, Parkinson or Huntington, several pathological granules have been connected with the disease progress. For example, the pathological SGs in Alzheimer's (Ash et al., 2014); the α-synuclein aggregates – Lewy body, which is HDAC6 and Ub positive, in Parkinson's (Kawaguchi et al., 2003); Huntington inclusions, which are enriched in SG components as well, in Huntington's (Ramdzan et al., 2017); in spite of the neurodegenerative disease, inhibiting SG formation leads to an upregulation of cell viability and fertility against heat stress inside mouse testis (Lee et al., 2020). All of these aggregates are either aberrant SGs-related or abnormal aggresome mimics (Lewy body). Interestingly, it was shown that there can be a transition from the aberrant SGs to aggresome, suggesting a relationship between these two types of inclusion bodies (Mateju et al., 2017). Taken together, it is conceivable that interfering with the HDAC6-Ub interaction, as DARPin F10 does, would lead to a reduction of these toxic and aberrant granules in cells. Hence, we plan to deliver DARPin F10 to the brain of an established Parkinson's mouse model (Kim et al., 2019), to test whether this can relieve some of the neurodegenerative symptoms.

Less difference observed in ZIKA growth curve under DARPin F10 inhibition

Unlike the obvious inhibition in IAV growth curve, we did not see a large difference in virus amount between F10 expressing and wild type cells in supernatant during ZIKA infection. In contrast, inside the host cell, we observed a dramatic decrease of ZIKA signal in F10 cells, indicating that much fewer cells were infected as compared to WT. That fewer cells are infected but similar virus amounts are

released to supernatant might be result of the F10's inhibitory on SG formation. It has been shown that SG, as an antiviral inclusion body, is inhibited by ZIKA, since the virus hijacks SG proteins like G3BP1, TIAR and Carpin-1 for genome amplification (Bonenfant et al., 2019; Hou et al., 2017). Inhibiting SG formation consequently released these RNA-processing proteins, therefore enhancing viral replication and more virus was produced. In summary, F10 prohibits ZIKA entry at earlier stage, but once ZIKA bypasses the inhibition and infects the host cell successfully, F10 might facilitate ZIKA replication in turn. We believe such a dilemma of DARPin F10 perhaps is not only observed in ZIKA infection. The antiviral effect of blocking HDAC6-Ub interaction should be carefully verified in terms of viruses. Last but not the least, we don't know whether inhibition of F10 on IAV or ZIKA is dosage-dependent. In our F10 cell line, the stochiometry of F10 appears to be less than HDAC6 (Figure 6, below). The outcome after upregulating F10's cellular concentration would be interesting to explore.

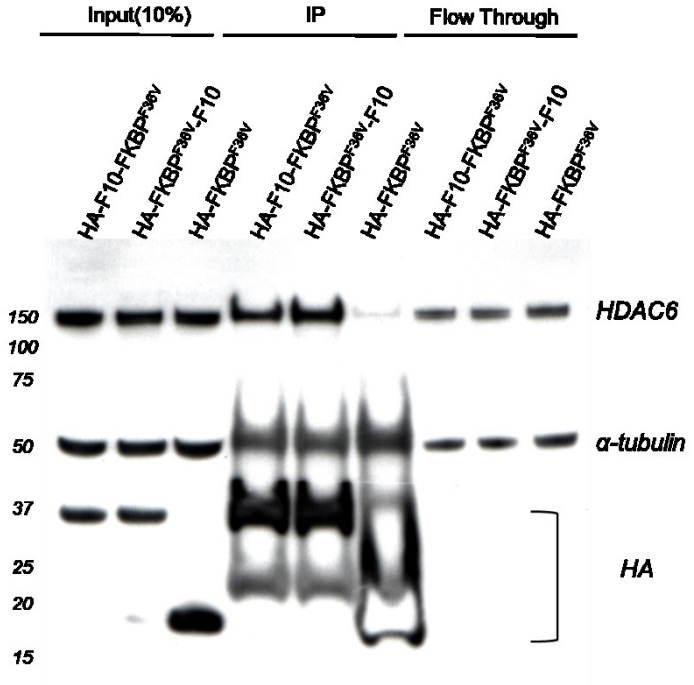

Figure 6, F10 cannot capture all the HDAC6 from cell lysate

HA-tagged DARPin F10 is trapped by anti-HA beads. From the lane of IP, we could see that in two DARPin F10 cell line (C-terminal FKBP^{F36V} or N-terminal FKBP^{F36V}), F10 pulled down HDAC6, but in the Flow-Through lanes, a big amount of HDAC6 was still observed.

HDAC6-Ub interaction may be essential in enveloped RNA virus

IAV and ZIKA are both enveloped, single-strand RNA viruses, and coincidently, depend on HDAC6-mediated entry. Furthermore, a postdoc in our lab, Etori Aguiar Moreira, further tested (data not shown) our HDAC6 mutant MEF cell lines with infectious Ebola VLP (**V**irus **L**ike **P**article), which consists of Ebola viral proteins but a defective viral genome. In ZnF (W1116A) mutated MEF, less Ebola VLP is

produced, while in CD2 dead mutants (W459A and D460A), the quantity of VLP was dramatically upregulated. This preliminary result not only re-confirms the dual (pro- and anti-viral) roles of HDAC6 in virus infection but also shows the HDAC6 dependence of the Ebola virus as well. Interestingly, the Ebola virus is categorized as an enveloped, single-strand RNA virus as well. Thus, we argue that HDAC6-mediated entry machinery may be conserved for most enveloped RNA virus infection. For instance, HIV, also an enveloped RNA virus, utilizes HDAC6 ZnF domain for its entry by eluding A3G antiviral activity (Valera et al., 2015). Such parallels nevertheless warrant more detailed experimental analysis *in vivo*. Finally, we noticed that the morphology of virus changes its HDAC6-dependence. In the tug-of-war model, we successfully predicted that H1N1 is more dependent on HDAC6 than H3N2, and this is due to M1 amino acid difference at site 218. It is a Threonine or Alanine in H1N1 or H3N2, respectively. In H1N1, the Thr218 assembles the virus as filamentous (Elleman and Barclay, 2004), and Ala218 in H3N2 turns it into an isolated virion. Filamentous H1N1 is capable of holding more viral Ub and recruiting more host HDAC6 than single virion (H3N2), then facilitates its uncoating. Considering that 1) Ebola is highly dependent on HDAC6, and 2) the typical morphology of Ebola is the filamentous virions (as named by "Filoviridae"), we suggest that other enveloped and filamentous RNA viruses need HDAC6-Ub interaction as well for the entry.

Closing Words

In summary, we describe an HDAC6 mediated IAV uncoating model in detail by combining biochemical data with computational simulation, and it not only answers the stoichiometry of myosin 10 and dynein during virus uncoating but also successfully predicts the H1N1 dependence on HDAC6. Results from dozens of chemicals inhibition on IAV uncoating highly agree with the predictions made by the mathematic model. Next, according to the model, an HDAC6 involved actomyosin pathway dominates the uncoating efficiency. And Ub bridges HDAC6-Ub interaction. Therefore, we develop a highly specific protein inhibitor-DARPin F10 to block this interaction, further downregulating the IAV and ZIKA infection as well as the cellular granules (aggresome & SG) formation. The potential applications of targeting the HDAC6 ZnF domain in clinical areas (e.g. antiviral and neurodegenerative field) motivate us to continuously work on it. Now, drugs against HDAC6 are mainly targeting its catalytic activity to upregulate cytosolic acetylation level, which leads to the inhibition of several tumors like myeloma and acute myeloid leukemia (Li et al., 2018a), while the clinical study on HDAC6 ZnF domain is blank. Our work, as a stepping brick, emphasizes the necessity of the future exploring of HDAC6 ZnF clinical value, which perhaps serves as a novel drug discovery target.

Methods details

Methods for "Results II: A quantitative model for HDAC6-mediated virus uncoating predicts Influenza A infectivity"

Mass-spring model for capsid breakage

The mass-spring mathematical model for capsid breakage represents a rectangular fragment of the capsid at the stage when it is exposed via the fusion pore and is interacting with host molecular motors, which pull it apart (**Figure 2A**).

Capsid M1 proteins (the masses) are arranged in a regular mesh approximately of the size of the fusion pore (see **Table S1** for all parameter values). Edge nodes of the mesh are bound to the lipid bilayer of the viral envelope/endosome and inner nodes are exposed to the cytoplasm. Here, we used a 6x6 mesh with 4x4 inner capsid proteins. Each inner mass is computed as the sum of protein masses bound to a particular node. For example, a free capsid node would simply correspond to the M1 protein mass, while a node attached to a myosin motor would have a total mass equal to the sum of masses of M1 protein, HDAC6, Ub, and myosin. Each edge node mass is the average mass of the endosome divided by the number of edge nodes.

The masses are connected to each other with elastic bonds, which we represent as a Morse potential that can explicitly include effects of bond breaking. Specifically, the Morse potential is

$$V_{Morse}(r) = D_e\left(1 - e^{-a(r-r_e)^2}\right), \text{ with } a = \sqrt{\frac{k_e^2}{D_e}},$$

which has two parameters: stiffness k_e and dissociation energy D_e. In this model we use two sets of Morse parameters for inner and outer nodes.

Each of the inner nodes of the capsid is acted on by the elastic forces of the 4 springs connecting it to other nodes. We calculate the change in spring length between two nodes as

$$\Delta l = \sqrt{(\Delta x)^2 + (\Delta y)^2} - l_{\text{eqilibrium}},$$

where $\Delta x = x_{\text{neighbor}} - x_{\text{current}}$ and $\Delta y = y_{\text{neighbor}} - y_{\text{current}}$ are the differences between the x and y coordinates of the neighbor node and the current node, and $l_{\text{eqilibrium}}$ is the equilibrium spring length. The

change in spring length Δl determines the force acting on the node, created by each particular spring. We compute the force as

$$f_{\text{Morse spring}} = -2a^{\text{type}} \cdot D_e^{\text{type}} \cdot \exp\left(-a^{\text{type}}\Delta l\right)\left[1-\exp\left(-a^{\text{type}}\Delta l\right)\right],$$

where a^{type} and D_e^{type} are the parameters of the Morse spring, depending on the spring's type (inner nodes corresponding to capsid parameters and edge nodes to capsid with lipid bilayer cover).

We then compute the projections on the x and the y axis of the acceleration created by each of the spring forces as follows:

$$a_z^{\text{spring}} = \frac{f_{\text{Morse spring}}}{m_{\text{node}}} \cdot \left(\frac{-\Delta z}{(\Delta x)^2 + (\Delta y)^2}\right),$$

where m_{node} is the node's mass and z stands for either x or y.

Finally, the ODE system for one node looks as follows

$$\frac{d}{dt}\begin{pmatrix} \text{position } x \\ \text{position } y \\ \text{velocity } x \\ \text{velocity } y \\ \text{time} \end{pmatrix} = \begin{pmatrix} \text{velocity } x \\ \text{velocity } y \\ a_x^{\text{top}} + a_x^{\text{right}} + a_x^{\text{bottom}} + a_x^{\text{left}} + f_x^{\text{motor}} \big/ m_{\text{node}} \\ a_y^{\text{top}} + a_y^{\text{right}} + a_y^{\text{bottom}} + a_y^{\text{left}} + f_y^{\text{motor}} \big/ m_{\text{node}} \\ 1 \end{pmatrix}.$$

We model the cytoskeleton near the fusion pore by a single, randomly directed microtubule, and by a denser network of actin filaments with a nucleation point on one of the edge nodes. Molecular motors are directly or indirectly (which we do not distinguish in this model) connected to the exposed capsid M1 proteins and to the cytoskeleton, allowing them to exert forces on the capsid. Specifically, dynein motors can walk in a single direction along the microtubule, while myosin motors can walk along actin filaments in random directions away from the nucleation point. Dyneins can connect to any of the inner nodes, but they can only exert forces on the capsid if they fall within the microtubular area of effect, determined by its width (**Figure 2A**).

We compute the resulting forces through a tug-of-war model with experimentally determined motor characteristics (Gennerich et al., 2007; Muller et al., 2008; Norstrom et al., 2010), which we modified to represent dyneins, kinesins, and positive- and negative-direction myosins. Importantly, the model considers that the force exerted by each individual motor depends on all the other motors bound to the same cargo.

First, let us examine the one-dimensional case, where all the motors walk along the microtubule. Analogously to the two-motor scenario (Gennerich et al., 2007; Muller et al., 2008; Norstrom et al., 2010), we write a force balance.

$$n_k f_k + n_{m+} f_{m+} = -n_d f_d - n_{m-} f_{m-} = f_C\left(n_k, n_d, n_{m+}, n_{m-}\right), \quad (0.1)$$

where n_k, n_d, n_{m+}, n_{m-} are motor numbers and f_k, f_d, f_{m+}, f_{m-} are forces of kinesin, dynein, plus- and minus-end myosin motors, respectively. The cargo force is determined by the condition that all motors move with the same velocity v_C, as given by

$$v_C\left(n_k, n_d, n_{m+}, n_{m-}\right) = v_k\left(f_k\right) = v_{m+}\left(f_{m+}\right) = -v_d\left(f_d\right) = -v_{m-}\left(f_{m-}\right).$$

With this definition follows for the left part of the force balance equation Eq. (0.1)

$$f_C\left(n_k, n_d, n_{m+}, n_{m-}\right) = n_k f_k + n_{m+} f_{m+} = n_k f_k \left(1 + \frac{n_{m+} f_{m+}}{n_k f_k}\right),$$

which gives us an expression for the kinesin force:

$$f_k = \frac{f_C\left(n_k, n_d, n_{m+}, n_{m-}\right)}{n_k\left(1 + \frac{n_{m+} f_{m+}}{n_k f_k}\right)}.$$

Analogously, for the right part and the dynein force, we obtain:

$$f_d = -\frac{f_C\left(n_k, n_d, n_{m+}, n_{m-}\right)}{n_d\left(1 + \frac{n_{m-} f_{m-}}{n_d f_d}\right)}.$$

For simplicity, we assume here that the ratio of motor forces moving in the same direction is proportionate to the ratio of their stall forces (indicated by subscript S):

$$\frac{f_{m+}}{f_k} \propto \frac{f_{Sm+}}{f_{Sk}}, \quad \frac{f_{m-}}{f_d} \propto \frac{f_{Sm-}}{f_{Sd}}.$$

This allows us to write the expressions for kinesin and dynein forces as follows

$$f_k = \frac{f_C\left(n_k, n_d, n_{m+}, n_{m-}\right)}{n_k C_k\left(n_{m+}, n_k\right)}, \quad f_d = -\frac{f_C\left(n_k, n_d, n_{m+}, n_{m-}\right)}{n_d C_d\left(n_{m-}, n_d\right)},$$

where

$$C_k\left(n_{m+}, n_k\right) = 1 + \frac{n_{m+} f_{Sm+}}{n_k f_{Sk}}, \quad C_d\left(n_{m-}, n_d\right) = 1 + \frac{n_{m-} f_{Sm-}}{n_d f_{Sd}}.$$

We know that the velocity of a motor can be expressed as a function of the load force (Müller et al., 2008):

$$v(f) = \begin{cases} v_{forward}\left(1 - \frac{|f|}{f_S}\right) & \text{for } 0 \le f \le f_S \\ v_{backward}\left(1 - \frac{f}{f_S}\right) & \text{for } f > f_S \end{cases}.$$

Now we can use the expression for the cargo velocity to derive:

$$v_C\left(n_k,n_d,n_{m+},n_{m-}\right)=v_k\left(f_k\right)=-v_d\left(f_d\right)$$

$$v_C\left(n_k,n_d,n_{m+},n_{m-}\right)=v_{0k}\left(1-\frac{f_k}{f_{Sk}}\right)=v_{0k}\left(1-\frac{1}{f_{Sk}}\frac{f_C\left(n_k,n_d,n_{m+},n_{m-}\right)}{n_kC_k\left(n_{m+},n_k\right)}\right)=v_{0k}-\frac{v_{0k}}{f_{Sk}}\frac{f_C\left(n_k,n_d,n_{m+},n_{m-}\right)}{n_kC_k\left(n_{m+},n_k\right)}$$

$$v_C\left(n_k,n_d,n_{m+},n_{m-}\right)==-v_{0d}\left(1-\frac{f_d}{f_{Sd}}\right)=-v_{0d}\left(1-\frac{1}{f_{Sd}}\frac{f_C\left(n_k,n_d,n_{m+},n_{m-}\right)}{n_dC_d\left(n_{m-},n_d\right)}\right)=-\left(v_{0d}-\frac{v_{0d}}{f_{Sd}}\frac{f_C\left(n_k,n_d,n_{m+},n_{m-}\right)}{n_dC_d\left(n_{m-},n_d\right)}\right)$$

$$v_C\left(n_k,n_d,n_{m+},n_{m-}\right)=v_{0k}-\frac{v_{0k}}{f_{Sk}}\frac{f_C\left(n_k,n_d,n_{m+},n_{m-}\right)}{n_kC_k\left(n_{m+},n_k\right)}=-v_{0d}+\frac{v_{0d}}{f_{Sd}}\frac{f_C\left(n_k,n_d,n_{m+},n_{m-}\right)}{n_dC_d\left(n_{m-},n_d\right)}.$$

By shuffling the second and third terms in this equation, we get the expression for the cargo force

$$v_{0k}+v_{0d}=\frac{v_{0k}}{f_{Sk}}\frac{f_C\left(n_k,n_d,n_{m+},n_{m-}\right)}{n_kC_k\left(n_{m+},n_k\right)}+\frac{v_{0d}}{f_{Sd}}\frac{f_C\left(n_k,n_d,n_{m+},n_{m-}\right)}{n_dC_d\left(n_{m-},n_d\right)},$$

$$v_{0k}+v_{0d}=f_C\left(n_k,n_d,n_{m+},n_{m-}\right)\frac{v_{0k}f_{Sd}n_dC_d\left(n_{m-},n_d\right)+v_{0d}f_{Sk}n_kC_k\left(n_{m+},n_k\right)}{f_{Sk}n_kC_k\left(n_{m+},n_k\right)f_{Sd}n_dC_d\left(n_{m-},n_d\right)},$$

$$f_C\left(n_k,n_d,n_{m+},n_{m-}\right)=\left(v_{0k}+v_{0d}\right)\frac{f_{Sk}n_kC_k\left(n_{m+},n_k\right)f_{Sd}n_dC_d\left(n_{m-},n_d\right)}{v_{0k}f_{Sd}n_dC_d\left(n_{m-},n_d\right)+v_{0d}f_{Sk}n_kC_k\left(n_{m+},n_k\right)}.$$

Now, for convenience we rewrite the equation:

$$f_C\left(n_k,n_d,n_{m+},n_{m-}\right)=\frac{v_{0k}f_{Sk}n_kC_k\left(n_{m+},n_k\right)f_{Sd}n_dC_d\left(n_{m-},n_d\right)+v_{0d}f_{Sk}n_kC_k\left(n_{m+},n_k\right)f_{Sd}n_dC_d\left(n_{m-},n_d\right)}{v_{0k}f_{Sd}n_dC_d\left(n_{m-},n_d\right)\left(1+\frac{v_{0d}f_{Sk}n_kC_k\left(n_{m+},n_k\right)}{v_{0k}f_{Sd}n_dC_d\left(n_{m-},n_d\right)}\right)},$$

$$f_C\left(n_k,n_d,n_{m+},n_{m-}\right)=\frac{f_{Sk}n_kC_k\left(n_{m+},n_k\right)+\frac{v_{0d}f_{Sk}n_kC_k\left(n_{m+},n_k\right)f_{Sd}n_dC_d\left(n_{m-},n_d\right)}{v_{0k}f_{Sd}n_dC_d\left(n_{m-},n_d\right)}}{\left(1+\frac{v_{0d}f_{Sk}n_kC_k\left(n_{m+},n_k\right)}{v_{0k}f_{Sd}n_dC_d\left(n_{m-},n_d\right)}\right)},$$

$$f_C\left(n_k,n_d,n_{m+},n_{m-}\right)=f_{Sk}n_kC_k\left(n_{m+},n_k\right)\frac{1}{\left(1+\frac{v_{0d}f_{Sk}n_kC_k\left(n_{m+},n_k\right)}{v_{0k}f_{Sd}n_dC_d\left(n_{m-},n_d\right)}\right)}+f_{Sd}n_dC_d\left(n_{m-},n_d\right)\frac{\frac{v_{0d}f_{Sk}n_kC_k\left(n_{m+},n_k\right)}{v_{0k}f_{Sd}n_dC_d\left(n_{m-},n_d\right)}}{\left(1+\frac{v_{0d}f_{Sk}n_kC_k\left(n_{m+},n_k\right)}{v_{0k}f_{Sd}n_dC_d\left(n_{m-},n_d\right)}\right)},$$

to get the following expression for cargo force as a function of motor abundances

$$f_C\left(n_k,n_d,n_{m+},n_{m-}\right)=f_{Sk}n_kC_k\left(n_{m+},n_k\right)\lambda\left(n_k,n_d,n_{m+},n_{m-}\right)+f_{Sd}n_dC_d\left(n_{m-},n_d\right)\left(1-\lambda\left(n_k,n_d,n_{m+},n_{m-}\right)\right),$$

where

$$\lambda\left(n_k, n_d, n_{m+}, n_{m-}\right) = \frac{1}{\left(1 + \frac{v_{0d} f_{Sk} n_k C_k\left(n_{m+}, n_k\right)}{v_{0k} f_{Sd} n_d C_d\left(n_{m-}, n_d\right)}\right)}.$$

After computing the cargo force, we can calculate the expressions for the kinesin and dynein forces:

$$f_k = \frac{f_C\left(n_k, n_d, n_{m+}, n_{m-}\right)}{n_k C_k\left(n_{m+}, n_k\right)},\ f_d = -\frac{f_C\left(n_k, n_d, n_{m+}, n_{m-}\right)}{n_d C_d\left(n_{m-}, n_d\right)},$$

and using those expressions, the expressions for myosin forces

$$f_{m+} = \frac{f_{Sm+} f_k}{f_{Sk}},\ f_{m-} = \frac{f_{Sm-} f_d}{f_{Sd}}.$$

In the two-dimensional case, dyneins and kinesins would still be walking along the microtubule, such that only the expressions for the myosins would change. Myosin forces are involved in the calculation of $C_k\left(n_{m+}, n_k\right)$ and $C_d\left(n_{m-}, n_d\right)$, but if we examine the formulas, we see that $n_{m\pm} f_{Sm\pm}$ are simply cumulative forces created by plus- and minus-end myosin motors. Thus, we can easily substitute these terms for $\sum_i f^i_{Sm\pm}$, where $f^i_{Sm\pm}$ is a projection of the stall force of a motor i on the direction of the microtubule. Similarly, expressions for myosin forces are computed individually for each motor with $f_{Sm\pm}$ being substituted by the projection $f^i_{Sm\pm}$.

To avoid division by zero, in simulations we assume that there are always one dynein and one kinesin bound to the endosome outside of the fusion pore because the endosome had to be transported inside the cell to initiate fusion pore formation. Due to the architecture of the Tug-of-War model and since all the microtubular motors can only generate forces along the microtubule, adding more endosomal motors would simply offset the optimal amount of dynein motors required for efficient breakage. All other motors are bound to the capsid from the very start of the simulation.

For simplicity, here we disregard tug-of-war between myosins in the direction perpendicular to the microtubule. However, this interaction can be computed and included into simulations similarly, by using the results of (Gennerich et al., 2007; Muller et al., 2008; Norstrom et al., 2010) for two motors:

$$f_C\left(n_{m+}, n_{m-}\right) = n_{m+} f_{Sm+} \lambda\left(n_{m+}, n_{m-}\right) + n_{m-} f_{Sm-} \lambda\left(n_{m+}, n_{m-}\right), \text{ where } \lambda\left(n_{m+}, n_{m-}\right) = \frac{1}{1 + \frac{n_{m+} f_{Sm+} v_{0m-}}{n_{m-} f_{Sm-} v_{0m+}}}.$$

Like before, we substitute $n_{m\pm} f_{Sm\pm}$ for $\sum_i f^i_{Sm\pm}$, where $f^i_{Sm\pm}$ are projections of the stall force of motor i in the direction perpendicular to the microtubule. Knowing $f_C\left(n_{m+}, n_{m-}\right)$, we can compute the motor forces as:

$f_{m+} = \frac{f_C(n_{m+}, n_{m-})}{n_{m+}}$, $f_{m-} = \frac{f_C(n_{m+}, n_{m-})}{n_{m-}}$.

During simulations of the mass-spring model, each motor configuration has a fixed number of each type of motor, but the placement and the directions of cytoskeletal filaments are randomized. The model is simulated for one microsecond of system time at least 100 times for each motor configuration using the MATLAB ODE solver ode15s (Mathworks, Natick / MA).

After a simulation, we examine the distance between all neighboring nodes in both x and y directions. If during the simulation the combined motor forces were sufficient to make any of the distances exceed the RNP complex diameter (a mock-up example for the one-dimensional case of break/no break scenarios showed in **Figure S1A**) for at least half the simulated system time (to avoid counting transient breaks), we classified the capsid as broken. Usually, however, if capsid breakage occurs, the initial break happens early in the simulation and persists through 80-90% of the simulation time (**Figure S1B**).

To analyze the robustness of the simulation results to changes in capsid parameters, we fixed a combination of motors (5 myosins and 1 dynein) that produced approximately 50% breakage, and varied the capsid bond parameters stiffness k_e and dissociation energy D_e. The values used in our simulations were $k_e \in$ [0.001, **0.002**, 0.003, 0.004, 0.005] N/m and $D_e \in$ [10, 12, **14**, 16, 18, 20] kJ, where boldface indicates the default values (**Figure S1C**).

To simplify computation of the capsid breakage probability, we interpolated it as a function of the total amount of molecular motors and the number of dynein motors using the R package akima on the basis of the values obtained from simulation of the mass-spring model (**Figure S1D**).

HDAC6 complex formation reaction model for motor complex formation

To develop the reaction model variants, we assumed mass-action kinetics for all biochemical interactions, leading to ordinary differential equation (ODE) models with 7 states and 12 (10 for the Viral Ub model variant) kinetic parameters. The reaction model schematics (**Figure 4A**) show all the possible bindings that can occur during motor complex formation. The model variant Viral Ub assumes competition between capsid-bound and cellular Ub chains (Ubs) for the zinc finger domain of HDAC6. In contrast, the Symmetric and Asymmetric model variants assume that cellular Ub chains assist with motor binding to HDAC6, both for myosin and dynein motors in the Symmetric, and only for myosin in the Asymmetric model variant.

To denote the biochemical species in the model variants, we use the following: U: Ub chain; H: HDAC6; C: capsid M1 protein; M: myosin; A: actin cytoskeleton; D: dynein; T: microtubule. Molecular complexes are denoted by concatenation of their constituents' abbreviations.

The Viral Ub variant has 16 reactions with two final products: CUHMA and CUHDT, corresponding to myosin and dynein motor complex respectively, according to the reaction network below:

1. $\mathrm{U} + \mathrm{H} \underset{k_{-UH}}{\overset{k_{UH}}{\rightleftharpoons}} \mathrm{UH}$
2. $\mathrm{M} + \mathrm{A} \underset{k_{-MA}}{\overset{k_{MA}}{\rightleftharpoons}} \mathrm{MA}$
3. $\mathrm{D} + \mathrm{T} \underset{k_{-DT}}{\overset{k_{DT}}{\rightleftharpoons}} \mathrm{DT}$
4. $\mathrm{CU} + \mathrm{H} \underset{k_{-UH}}{\overset{k_{UH}}{\rightleftharpoons}} \mathrm{CUH}$
5. $\mathrm{UH} + \mathrm{M} \underset{k_{-HM}}{\overset{k_{HM}}{\rightleftharpoons}} \mathrm{UHM}$
6. $\mathrm{UH} + \mathrm{D} \underset{k_{-HD}}{\overset{k_{HD}}{\rightleftharpoons}} \mathrm{UHD}$
7. $\mathrm{CUH} + \mathrm{M} \underset{k_{-HM}}{\overset{k_{HM}}{\rightleftharpoons}} \mathrm{CUHM}$
8. $\mathrm{UHM} + \mathrm{A} \underset{k_{-MA}}{\overset{k_{MA}}{\rightleftharpoons}} \mathrm{UHMA}$
9. $\mathrm{UH} + \mathrm{MA} \underset{k_{-HM}}{\overset{k_{HM}}{\rightleftharpoons}} \mathrm{UHMA}$
10. $\mathrm{CUH} + \mathrm{D} \underset{k_{-HD}}{\overset{k_{HD}}{\rightleftharpoons}} \mathrm{CUHD}$
11. $\mathrm{UHD} + \mathrm{T} \underset{k_{-DT}}{\overset{k_{DT}}{\rightleftharpoons}} \mathrm{UHDT}$
12. $\mathrm{UH} + \mathrm{DT} \underset{k_{-HD}}{\overset{k_{HD}}{\rightleftharpoons}} \mathrm{UHDT}$
13. $\mathrm{CUHM} + \mathrm{A} \underset{k_{-MA}}{\overset{k_{MA}}{\rightleftharpoons}} \mathrm{CUHMA}$
14. $\mathrm{CUH} + \mathrm{MA} \underset{k_{-HM}}{\overset{k_{HM}}{\rightleftharpoons}} \mathrm{CUHMA}$
15. $\mathrm{CUHD} + \mathrm{T} \underset{k_{-DT}}{\overset{k_{DT}}{\rightleftharpoons}} \mathrm{CUHDT}$
16. $\mathrm{CUH} + \mathrm{DT} \underset{k_{-HD}}{\overset{k_{HD}}{\rightleftharpoons}} \mathrm{CUHDT}$

The Symmetric variant has 22 reactions with two final products: CHUMA and CHUDT, corresponding to myosin and dynein motor complex, respectively. Here, a simplifying assumption is made, namely that the binding between HDAC6 and myosin requires that HDAC6 binds Ub first:

1. $\mathrm{C} + \mathrm{H} \underset{\mathrm{k_{-CH}}}{\overset{\mathrm{k_{CH}}}{\rightleftharpoons}} \mathrm{CH}$
2. $\mathrm{H} + \mathrm{U} \underset{\mathrm{k_{-HU}}}{\overset{\mathrm{k_{HU}}}{\rightleftharpoons}} \mathrm{HU}$
3. $\mathrm{D} + \mathrm{T} \underset{\mathrm{k_{-DT}}}{\overset{\mathrm{k_{DT}}}{\rightleftharpoons}} \mathrm{DT}$
4. $\mathrm{M} + \mathrm{A} \underset{\mathrm{k_{-MA}}}{\overset{\mathrm{k_{MA}}}{\rightleftharpoons}} \mathrm{MA}$
5. $\mathrm{C} + \mathrm{HU} \underset{\mathrm{k_{-CH}}}{\overset{\mathrm{k_{CH}}}{\rightleftharpoons}} \mathrm{CHU}$
6. $\mathrm{CH} + \mathrm{U} \underset{\mathrm{k_{-HU}}}{\overset{\mathrm{k_{HU}}}{\rightleftharpoons}} \mathrm{CHU}$
7. $\mathrm{HU} + \mathrm{D} \underset{\mathrm{k_{-HD}}}{\overset{\mathrm{k_{HD}}}{\rightleftharpoons}} \mathrm{HUD}$
8. $\mathrm{HU} + \mathrm{M} \underset{\mathrm{k_{-HM}}}{\overset{\mathrm{k_{HM}}}{\rightleftharpoons}} \mathrm{HUM}$
9. $\mathrm{C} + \mathrm{HUD} \underset{\mathrm{k_{-CH}}}{\overset{\mathrm{k_{CH}}}{\rightleftharpoons}} \mathrm{CHUD}$
10. $\mathrm{CHU} + \mathrm{D} \underset{\mathrm{k_{-HD}}}{\overset{\mathrm{k_{HD}}}{\rightleftharpoons}} \mathrm{CHUD}$
11. $\mathrm{HU} + \mathrm{DT} \underset{\mathrm{k_{-HD}}}{\overset{\mathrm{k_{HD}}}{\rightleftharpoons}} \mathrm{HUDT}$
12. $\mathrm{HUD} + \mathrm{T} \underset{\mathrm{k_{-DT}}}{\overset{\mathrm{k_{DT}}}{\rightleftharpoons}} \mathrm{HUDT}$
13. $\mathrm{C} + \mathrm{HUM} \underset{\mathrm{k_{-CH}}}{\overset{\mathrm{k_{CH}}}{\rightleftharpoons}} \mathrm{CHUM}$
14. $\mathrm{CHU} + \mathrm{M} \underset{\mathrm{k_{-HM}}}{\overset{\mathrm{k_{HM}}}{\rightleftharpoons}} \mathrm{CHUM}$
15. $\mathrm{HU} + \mathrm{MA} \underset{\mathrm{k_{-HM}}}{\overset{\mathrm{k_{HM}}}{\rightleftharpoons}} \mathrm{HUMA}$
16. $\mathrm{HUM} + \mathrm{A} \underset{\mathrm{k_{-MA}}}{\overset{\mathrm{k_{MA}}}{\rightleftharpoons}} \mathrm{HUMA}$
17. $\mathrm{C} + \mathrm{HUDT} \underset{\mathrm{k_{-CH}}}{\overset{\mathrm{k_{CH}}}{\rightleftharpoons}} \mathrm{CHUDT}$
18. $\mathrm{CHU} + \mathrm{DT} \underset{\mathrm{k_{-HD}}}{\overset{\mathrm{k_{HD}}}{\rightleftharpoons}} \mathrm{CHUDT}$
19. $\mathrm{CHUD} + \mathrm{T} \underset{\mathrm{k_{-DT}}}{\overset{\mathrm{k_{DT}}}{\rightleftharpoons}} \mathrm{CHUDT}$
20. $\mathrm{C} + \mathrm{HUMA} \underset{\mathrm{k_{-CH}}}{\overset{\mathrm{k_{CH}}}{\rightleftharpoons}} \mathrm{CHUMA}$
21. $\mathrm{CHU} + \mathrm{MA} \underset{\mathrm{k_{-HM}}}{\overset{\mathrm{k_{HM}}}{\rightleftharpoons}} \mathrm{CHUMA}$
22. $\mathrm{CHUM} + \mathrm{A} \underset{\mathrm{k_{-MA}}}{\overset{\mathrm{k_{MA}}}{\rightleftharpoons}} \mathrm{CHUMA}$

The Asymmetric variant has 29 reactions with two final products: CHUMA and CHDT, corresponding to myosin and dynein motor complex, respectively

1. $C + H \underset{k_{-CH}}{\overset{k_{CH}}{\rightleftharpoons}} CH$
2. $H + D \underset{k_{-HD}}{\overset{k_{HD}}{\rightleftharpoons}} HD$
3. $D + T \underset{k_{-DT}}{\overset{k_{DT}}{\rightleftharpoons}} DT$
4. $H + U \underset{k_{-HU}}{\overset{k_{HU}}{\rightleftharpoons}} HU$
5. $U + M \underset{k_{-UM}}{\overset{k_{UM}}{\rightleftharpoons}} UM$
6. $M + A \underset{k_{-MA}}{\overset{k_{MA}}{\rightleftharpoons}} MA$
7. $C + HD \underset{k_{-CH}}{\overset{k_{CH}}{\rightleftharpoons}} CHD$
8. $CH + D \underset{k_{-HD}}{\overset{k_{HD}}{\rightleftharpoons}} CHD$
9. $H + DT \underset{k_{-HD}}{\overset{k_{HD}}{\rightleftharpoons}} HDT$
10. $HD + T \underset{k_{-DT}}{\overset{k_{DT}}{\rightleftharpoons}} HDT$
11. $C + HU \underset{k_{-CH}}{\overset{k_{CH}}{\rightleftharpoons}} CHU$
12. $CH + U \underset{k_{-HU}}{\overset{k_{HU}}{\rightleftharpoons}} CHU$
13. $H + UM \underset{k_{-HU}}{\overset{k_{HU}}{\rightleftharpoons}} HUM$
14. $HU + M \underset{k_{-UM}}{\overset{k_{UM}}{\rightleftharpoons}} HUM$
15. $U + MA \underset{k_{-UM}}{\overset{k_{UM}}{\rightleftharpoons}} UMA$
16. $UM + A \underset{k_{-MA}}{\overset{k_{MA}}{\rightleftharpoons}} UMA$
17. $C + HDT \underset{k_{-CH}}{\overset{k_{CH}}{\rightleftharpoons}} CHDT$
18. $CH + DT \underset{k_{-HD}}{\overset{k_{HD}}{\rightleftharpoons}} CHDT$
19. $CHD + T \underset{k_{-DT}}{\overset{k_{DT}}{\rightleftharpoons}} CHDT$
20. $C + HUM \underset{k_{-CH}}{\overset{k_{CH}}{\rightleftharpoons}} CHUM$
21. $CH + UM \underset{k_{-HU}}{\overset{k_{HU}}{\rightleftharpoons}} CHUM$
22. $CHU + M \underset{k_{-UM}}{\overset{k_{UM}}{\rightleftharpoons}} CHUM$
23. $H + UMA \underset{k_{-HU}}{\overset{k_{HU}}{\rightleftharpoons}} HUMA$
24. $HU + MA \underset{k_{-UM}}{\overset{k_{UM}}{\rightleftharpoons}} HUMA$
25. $HUM + A \underset{k_{-MA}}{\overset{k_{MA}}{\rightleftharpoons}} HUMA$
26. $C + HUMA \underset{k_{-CH}}{\overset{k_{CH}}{\rightleftharpoons}} CHUMA$
27. $CH + UMA \underset{k_{-HU}}{\overset{k_{HU}}{\rightleftharpoons}} CHUMA$
28. $CHU + MA \underset{k_{-UM}}{\overset{k_{UM}}{\rightleftharpoons}} CHUMA$
29. $CHUM + A \underset{k_{-MA}}{\overset{k_{MA}}{\rightleftharpoons}} CHUMA$

For each set of parameters and initial conditions considered, we simulated the reaction model for 2 hours of system time using the MATLAB ODE solver odeSD (Gonnet et al., 2012), such that the protein interactions lead to a steady-state distribution of the molecular species. Then, we used the reaction model's myosin and dynein motor complex abundances (see definitions above) at the end of the simulation to predict average capsid breakage probabilities with an interpolated version of the corresponding simulation results for the mass-spring model (**Figure S1D**).

To optimize reaction rate parameters, we initially simulated each reaction model variant 100'000 times with fixed median values of initial concentrations and reaction rate constants sampled log normally in the range of ± 5 orders of magnitude around values reported in the literature (**Table S2**). These simulation results were then averaged for a single viral particle, and used to compute capsid breakage probabilities using our interpolated mass-spring model results (**Figure S1D**). The 'Viral Ub' variant failed to recruit enough motors to generate any capsid breakage for any combination of reaction rates. Therefore, we focused on the 'Symmetric' and 'Asymmetric' models.

For both variants, the distribution of capsid breakages showed four modes (**Figure S3A**). Many rate combinations led to zero breakage because the models failed to recruit any motors. The nextmode appeared at around 8% breakage, where the models recruited about 1 myosin motor and 1-2 dynein motors. The next mode capped out at about 50% breakage, with recruitment of 5-6 myosins, but very low numbers of dyneins, which corresponds to the 'no dyneins' case in the mass-spring model. The last mode yielded up to 80-90% breakage; while sparsely populated, it was able to recruit about 7 myosins

and 1-2 dyneins. Since we know that in the experiments capsid breakage depends on both myosins and dyneins, we chose this group for further analysis.

Next, we introduced a cost function to evaluate points in this group. It penalizes distance of reaction parameter values from literature values as well as low capsid breakage probability:

$$C = \sum_i \left| \log_{10} \left(\frac{k^i}{k^i_{\text{literature value}}} \right) \right| + \sum_i \left| \log_{10} \left(\frac{K^i}{K^i_{\text{literature value}}} \right) \right| + \left| \log_{10} \left(\frac{\%}{\%_{\max}} \right) \right|,$$

where k^i is an on rate, K^i is a dissociation constant, and $\%$ is a capsid breakage probability. Because literature parameter values were of the same order of magnitude (approximately 10^6 for on rates and 10^{-6} for dissociation constants), we did not introduce extra weight coefficients. We selected the parameter point with minimal value of the cost function as reference point.

To compare the performance of 'Symmetric' and 'Asymmetric' model variants (**Figure 4B, S3B, C, D**), we sampled the concentrations (20'000 times), reaction rates (20'000 times), and both together (40'000 times). Concentrations were sampled uniformly between 50% and 150%, and log-normally in ±1 orders of magnitude of the value reported in proteomics experiments (proteomicsDB; (Schmidt et al., 2018)). Reaction rates were sampled log-uniformly around the reference value in ±1 orders of magnitude, or log-normally around the reference value with a SD of 0.1.

To examine the influence of each individual parameter on the capsid breakage probability, we simulated the model variants with all but one parameter fixed. The free parameter was sampled log-uniformly 20'000 times for concentrations between 50% and 150% of the value reported in proteomics experiments (proteomicsDB; (Schmidt et al., 2018)), and log-uniformly 30'000 times for reaction rate constants around the reference value in ±5 orders of magnitude.

Experimental perturbations, when possible, were translated into model perturbations by changing either reaction rate constants or initial concentrations of reactants (**Table S2**). We simulated each perturbation 20'000 times similarly to the unperturbed system, with initial concentrations sampled as above and rate constants sampled log-normally around the reference value in ±1 order of magnitude, except for the experiment-specific perturbed parameters or initial conditions, which were sampled in the modified ranges as specified in **Table S3**.

siRNA for Dynactin2 prevented the binding of dynactin and reduced the amount of available dynein to $1/10$ of the norm. Ciliobrevin D, which inhibits the dynein motor activity, stopped the motors from walking, but not from binding; we simulated that case as control, but then assumed zero active dyneins for computing the breakage probability. siRNAs for myosin10 affected the amount of available myosin

by reducing it to $1/10$ of the norm. siRNAs for myosin9 were not modeled given that experiments showed little effect on the breakage probability. ML-9 and Blebbistatin cases were not simulated as they correspond to zero effective myosins, which, according to the mass-spring model, fails to generate breakage. For the HDAC6 ΔDMC MEF cell line, we assumed an increase of the dissociation constant for HDAC6-dynein binding by a factor of 1000. The HDAC6 KO MEF cell line and siRNA HDAC6 had initial concentrations of HDAC6 reduced to $1/100$ and $1/10$ of the norm, respectively. The HDAC6 ZnFm (W1116A) MEF cell line had the dissociation constant of HDAC6-Ub binding increased by a factor 1000. We assumed that Cytochalasin D and Nocodazole, which affect actin and tubulin polymerization, reduced the amount of available cytoskeletal scaffolding to $1/10$ and $1/100$ of the norm, respectively. Importazole is a selective inhibitor of the nuclear transport receptor importin-beta and prevents nuclear import of NLS-containing proteins (Soderholm et al., 2011). MG132 is a proteasome inhibitor, leading to misfolded proteins accumulation in the cell and to a depletion of free cellular Ub chains that are no longer recycled during proteasomal degradation of those proteins; therefore, we assumed a reduction in Ub concentration to $1/10$ of the norm.

An alternative and, perhaps, more biologically reasonable approach to model the domain deletion from HDAC6 would be to remove dynein motors and Ub from the simulation entirely. However, doing so in our ODE reaction model leads to the simulation becoming unstable, and ideally requires additional model modifications, making comparisons between the different reaction models difficult. Modifying reaction rates in contrast, allows us to account for random effects of unspecific binding while keeping the model simple and deterministic.

For the M1 binding signal perturbations, we used H1N1 M1 (and its 'restored' virus version H3N2 M1 A218T) as a control, and H2N2 M1 (and its 'restored' virus version H1N1 M1 T218A) as a perturbation that increases the HDAC6-capsid dissociation constant by a multiplication factor. We used the average M1 binding signal for the H1N1 M1 T218 mutant and H3N2 WT (**Figure 6E**), and fitted a corresponding value of binding to capsid breakage in our individual parameter perturbation experiments (**Figure 4C**, **D**). The final multiplication factor values were 14.6 for the 'Asymmetric' and 23.7 for the 'Symmetric' model variant.

For the virus infectivity perturbations, we considered pH1N1 ko/ki WT to be a control, H3N2 ko/ki WT, corresponding to M1-HDAC6 binding dissociation constant being increased by the multiplication factor above, pH1N1 ko/ki ZnF mutant to have an increased ofHDAC6-Ub dissociation constant by a factor of 1000, and H3N2 ko/ki ZnF mutant as both.

Clone Construction

GFP tagged human Myosin 10 C-terminal (1103-2007), Influenza virus strain H1N1 and H3N2's full length M1 wild type and mutants were constructed in modified pCDNA 3.1-HA-Flag-mEGFP-POI vector. GST tagged human HDAC6 CD (82-837) and C-terminal region (838-1215) were constructed in pOPINJ-His-GST-POI vector (Oxford Protein Production Facility). His tagged human Myosin 10 C-terminal (1103-2007) and HDAC6 ZnF (1108-1215) are constructed in pOPINF-His-POI vector (Oxford University).

Endogenous mouse HDAC6, Myosin 10, Actin Co-immunoprecipitation (CoIP)

Wild type, HDAC6 knock out, and HDAC6 ZnF mutant (W1116A) (Banerjee et al., 2014b) Mouse Embryonic Fibroblast (MEF) cells were cultured in 10 cm dishes in DMEM medium, and treated with MG132 (10 μM), Cytochalasin D (10 μM) or Latrunculin A (10 μM) for 6 hours, then lysed with Cytoskeletal (CSK) buffer (10 mM PIPES pH=6.8, NaCl 100 mM, Sucrose 300 mM, 0.1% Triton X-100, EGTA 1 mM, $MgCl_2$ 1mM, DTT 1mM, Protease Inhibitor Cocktail 1 tablet for 50 ml) on ice. To immunoprecipitate endogenous HDAC6, 1μg polyclonal antibody (#27260) was used to incubate with 500 μg protein-containing cell lysate and 10 μl Dyna-beads slurry (Invitrogen) at 4°C cold room, on rotator overnight. Beads were washed with Wash Buffer 1 (20 mM Tris pH=7.5, 100 mM NaCl, 0.1% Triton X-100) 2 times and Wash Buffer 2 (20 mM Tris pH=7.5, 150 mM NaCl) 3 times. After removing the supernatant, 4x LDS loading buffer was added to the pellet and the sample was heated at 80°C for 5 min. Samples were analyzed on NuPAGE 4-12% Bis-Tris Gel (Invitrogen). Protein was transferred by Semi-Dry Western Blot method (Bio-rad Turbo Trans Blot) onto PVDF membranes (Millipore#88518). To detect endogenous mouse HDAC6, Myosin 10 and Actin, a lab-made polyclonal anti-HDAC6 ZnF antibody (Saito et al., 2019b), commercial anti-Myosin 10 antibody (CST#3404) and pan-actin antibody (Sigma#SAB4502632) were used. HRP-conjugated anti-rabbit and anti-Mouse secondary antibody (Invitrogen # 31430 and # 65-6120), ECL western blot detect reagent (GE#RPN2209) were used to develop the signal on Fuji film (#FUJIF57164152).

Mass Spectrometry analysis of HDAC6 interacting proteins

To identify HDAC6 interacting proteins following viral infection or under Proteasome or Actin Stress, MEF cells (described above) were treated, lysed and co-immunoprecipitated as for the CoIP experiment, but without 4x LDS loading sample buffer elution. Samples on beads were treated with Lys-C and Trypsin to perform on-beads digestion (FMI Protein Analysis Facility). Digested samples were further acidified and analyzed by Liquid chromatography–mass spectrometry (LC-MS). Data was analyzed by MaxQuant Perseus Software Version 1.5.2.6 (Tyanova et al., 2016). Volcano Plots were generated by R-Studio software.

Endogenous mouse Dynein, HDAC6, HDAC6-ZnF mutant Co-immunoprecipitation

Cells, reagents and methods are the same as described above except for: To precipitate endogenous Dynein Complex, an anti-dynein antibody (#MAB1618) was incubated with 500 µg protein-containing MEF cell lysate together with 10 µl Dyna-beads slurry. Protein concentration was determined by Bradford Assay. Samples after loading buffer elution were analyzed by immunoblotting with specific antibodies. HDAC6 signal was firstly normalized by Dynein input bands, then quantified. All the analysis was done with ImageJ software.

Immunofluorescence of endogenous human HDAC6, Myosin 10 and Actin

To visualize HDAC6, Myosin 10 and Actin in vivo, 3 x 10^4 A549 cells were seeded and cultured overnight, then treated with MG132 (5 µM) for 18 hours before fixation. Cells were washed with cold PBS, fixed with methanol at -20°C for 15 mins and permeabilized with TBS solution containing 0.5% Triton X-100, then incubated with monoclonal anti-HDAC6 antibody (CST#D2E5), anti-Myosin 10 antibody (CST#3404), and anti-actin antibody (Sigma#SAB4502632). Goat anti-Rabbit IgG (H+L) Highly Cross-Adsorbed Secondary Antibody Alexa Fluor 568 or Goat anti-Mouse IgG (H+L) Highly Cross-Adsorbed Secondary Antibody, Alexa Fluor 488 were applied according to the source of primary antibody. Pictures were taken with a widefield microscope (ZEISS Z1, 60x objective) or confocal microscope (Yokogawa CSU W1, 63x objective) and analyzed by ImageJ.

Detecting the interaction between human Myosin 10 and Ub

For in vivo Co-IP experiments, a plasmid encoding GFP-tagged Myosin 10 C-terminal (1103-2007) region (MyoC) was transfected with Lipofectamine 3000 (Invitrogen# L3000008) and over-expressed in A549 cells. The cells were subsequently treated with MG132 (10 µM, 6 hours) to upregulate the Ub level before harvest. Cells were lysed with CoIP buffer (10 mM Tris pH=7.5, 100 mM NaCl, 0.5% NP-40, 0.5 mM EDTA, 0.09% Na-Azide, Protease Inhibitor). To precipitate GFP-MyoC, 13 µl GFP_Trap M beads slurry (ChromoteK #gtm-20) were incubated with 500 µg protein-containing cell lysate in 4°C cold room, on rotator overnight. Beads were washed with Wash buffer (20 mM Tris pH=7.5, 100 mM NaCl) 3 times and beads were captured with a magnet. The subsequent analysis was done as for the endogenous Co-IP above. GFP-tagged protein and Ub were detected with anti-GFP antibody (CST# 2037S) and anti-Ub antibody (Santa Cruz P4D1 clone).

For in vitro experiments, His-tagged human Myosin 10 (1103-2007) was expressed in SF9 cells and purified by His-Trap HP histidine-tagged protein purification column (5 ml, GE healthcare) followed

by size exclusion with a Superdex 200 10/300 GL column on AKTA system. Synthesized K48/K63 linked Poly-Ub chains were obtained from Boston BioChem (#UC-240 & UC-340). To detect the interaction, 20 µg purified His-MyoC was mixed with 5 µg K48 or K63 linked poly-Ub chains in Ub binding buffer (20 mM Tris pH=7.5, 100 mM NaCl, 0.1% Triton X-100, 20 mM imidazole, 2% Glycerol), together with Ni-NTA beads (Promega# 30210) at 4°C for 1 hour. Beads were then washed with Ub binding buffer twice. 4x LDS loading buffer was added and heated at 80°C to elute the samples which were analyzed on NuPAGE 4-12% Bis-Tris SDS Gels and visualized by immunoblotting. Ub signal was detected with specific anti-K48/K63 linked Ub chain antibody (CST# 4289S & 5621S). Input samples were visualized by staining the membrane with Instant Blue (Expedeon#ISB1L) stain.

Detecting human HDAC6 interaction with IAV H1N1 & H3N2 wild type or mutant M1

GST-tagged HDAC6 CD (82-837) and C-terminal region (838-1215), GFP-tagged H1N1 & H3N2 wild type or mutant (A213T or T213A, respectively) M1 were transiently overexpressed in HEK 293T cells by FuGENE HD (Promega#E2311**)** mediated transfection. After two days culturing at 37°C, cells were lysed with CoIP buffer as above. GST_Trap M beads were used to precipitate GFP tagged M1 protein from 500 µg protein extract. Pulled-down samples were eluted by 4x LDS Sample buffer and analyzed by immunoblotting. Protein was visualized by anti-GFP (CST#2037S) and anti-GST (CST#2624S) antibody. Endogenous actin signal served as loading amount control.

We processed raw immunoblotting image files for two replicates in ImageJ (Schneider et al., 2012). We selected the lanes containing the bands of interest "GST-HDAC6 CD" and "GFP-M1/GFP" using the rectangle tool. We chose the width and the height of the lane rectangle to get a sample of the local background surrounding the band of interest. We plotted lane profiles using the gel analysis tool, and subtracted the background intensity by individually connecting each profile peak's left and right background intensity by using the line tool. We used the magic-wand tool to calculate the integrated area within the band profile of interest and obtain the final raw density value. Lastly, we normalized the "GFP-M1/GFP" density by corresponding "GST-HDAC6 CD" values. The resulting intensities (**Figure 6E**) were plotted using R package ggplot2.

Influenza A virus amplification

All procedures involving infectious material were performed under strict BSL2 condition and approved by federal authorities (BLV, Switzerland). Clinical viral isolates pH1N1 and H3N2 were kindly provided by Dr. Samuel Cordey, HUG, Geneva, Switzerland. Viruses were grown on MDCKII cells as described previously (Anchisi et al., 2018). Briefly, sub-confluent (80%) MDCKII were infected with 0.001 to 0.01 MOI of virus in DMEM supplemented with 1% (v/v) penicillin/streptomycin and 0.2%

(w/v) BSA. Virus containing supernatants were collected after 48-72h, separated from cell debris by 10 min centrifugation at 2000 x g, aliquoted and stored at -70˚C. Virus titers were determined by standard plaque assay on MDCKII cells as described previously (Anchisi et al., 2018). Briefly, viruses were serially diluted in PBS+0.2% BSA and tittered on fully confluent MDCK cells. Cells were infected with virus dilutions and incubated at 37˚C for 45 minutes, shaking plates every 5-10 minutes. At the end of the incubation time, virus dilutions were removed from the wells and cells were overlaid by agar solution (infection media + low melting agar (Oxoid) + TPCK-trypsin) pre-heated to 52˚C. Plaques were counted after 48h. Titrations were repeated three times in technical duplicates for each virus.

Reverse genetics

The pDZ reverse genetics system for A/Wyoming/03/2003 was kindly provided by Adolfo García-Sastre, Icahn School of Medicine at Mount Sinai, New York, USA. M1 A218T substitutions were introduced by site directed mutagenesis. Viral cDNA sequences were confirmed by Sanger sequencing. Recombinant viruses were rescued by transfection of eight pDZ plasmids (one encoding each viral segment) in 293T cells. Cells were co-cultured 48h post transfection with MDCKII to propagate rescued virus particles. Virus stocks were grown as described above. The whole genome of recombinant viruses was controlled by Sanger sequencing, to confirm the introduction of a given sequence manipulation (Anchisi et al., 2018).

Measure of influenza A virus infectivity in A549 cells by automated fluorescence microscopy.

A549 cells were seeded in 96-well optical plates (10’000 cells per well) in culture medium (DMEM supplemented with 10% FBS and 1% penicillin-streptomycin) and incubated overnight in 37˚C, 5% CO2. Viruses were diluted in infection medium (DMEM supplemented with 0.2% BSA and 1% penicillin-streptomycin). Cells were washed with 100 µl/well PBS to remove FBS. Cells were infected or mock-infected with 50 µl/well of virus dilution or infection medium and incubated for 7h in 37˚C, 5% CO2. Cells were fixed with 4% formaldehyde (final concentration) for 30 min at RT, washed three times with PBS and stored overnight in PBS at 4°C. Cells were stained for immunofluorescence assay by being permeabilized with 0.1% Triton X100 in PBS for 15 min at RT, blocked with PBS+1% BSA 1h RT, incubated with primary antibody in 30 µl PBS+1% BSA 1h RT (anti-NP 1:500 (Thermo Scientific, 41071), washed three times with PBS + 1% BSA, incubated with secondary antibody + DAPI in 30 µl PBS+1% BSA 45 min-1h RT in darkness (anti-rabbit 1:2000 (Alexa 488, GFP) and DAPI 1:500) and washed five times with PBS. Cells were stored in PBS + 0.02% sodium azide and stored at 4˚C. The percentage of infected cells was measured by automated fluorescence microscope, objective 10x, 3x3 pictures per well. Data were analyzed using MetaXpress software.

Generation of A549 HDAC6 ko cells.

HDAC6 was knocked-out in A549 cells using CRISPR/Cas9 and two different guide RNA (G1: CTCTATCCCCAATCTAGCGGAGG and G2: GCTAGATTGGGGATAGAGCGGGG). Guide RNAs were cloned into SpCas9n(BB)-2A-GFP (PX461) (Addgene plasmid: 48140, a gift from Feng Zhang (Ran et al., 2013)). A549 were transfected with sequence confirmed PX461 plasmids expressing the respective gRNA or empty PX461. 48h post transfection GFP positive cells were sorted and 10e2 cells were seeded into a 100mm dish. 14d post seeding single cell clone based colonies were isolated and expanded. HDAC knockout was confirmed by specific western blot. Cells knocked-out for HDAC6 using G1 were used for assays described in this work and used as background cell-line to build HDAC6 ko/ki A549 cells. The corresponding WT and mutant cDNAs of HDAC6 were cloned into pLVX-IRES-puro vectors (Clontech). HDAC6 reconstitution was achieved by lentiviral transduction of HDAC6 knockout cells. Reconstitution was confirmed by specific western blot against HDAC6.

Virus morphology determined by electron microscopy

MDCK cells were infected at MOI 10 in PBS/BSA. Cells were fixed at 16 hpi in 2% glutaraldehyde in buffer NaPO4 0.1M pH 7.4 for 1h. Cells were scraped off the plate and spun down for 5 min at 600g. Cell pellet was washed gently three times in buffer NaPO4 0.1M pH 7.4. Samples were then treated and resin mounted by our microscopy facility (Bioimaging center, Université de Genève). Samples were observed by electron microscope (FEI Tecnai™ G2 Sphera) and the maximum virus particle length of a given section (n = 66-378/virus) was determined on pictures using iTEM software version 5.2 (Olympus Soft Imaging Solutions GmbH).

Methods for "Results III: Targeting the HDAC6 zinc finger domain impacts virus infection and cellular stress pathways"

Nanobody screens & preparation

The target protein was a 6xHis- and HALO-tagged human HDAC6 ZnF domain (aa 1106-1215, expressed from plasmid pHis6HaloTag-hHDAC6ZnF) which was prepared by expression in E. coli

BL21(DE3)RIL+. As a control, 6xHis-HALO protein (expressed from plasmid pH6HTN His6HaloTag) was prepared in a similar manner. Cells were induced with 0.5 mM IPTG at 20 °C for 20 h. E. coli BL21 (DE3) cells expressing 6xHis-HALO-tagged ZnF-UBP were pelleted, rapidly frozen in liquid nitrogen and stored at −80 °C. The frozen cells were resuspended in ice-cold lysis buffer (20 mM Tris, pH7.5, 200 mM NaCl, 20 mM imidazole, 2 mM TCEP, 0.2% Tween-20) supplemented with Complete EDTA-free protease inhibitors (Roche) and 3 U/ml Benzonase (Sigma). After 30 min on ice the lysate was centrifuged at 30,000g for 30 min at 4 °C. The clarified soluble lysate was incubated for 30 min at 4 °C in batch mode with Ni-NTA IMAC agarose (Qiagen), and then transferred into a 10 ml Econo-Pac column (Bio-Rad) for washing with nickel wash buffer (20 mM Tris, pH 7.5, 200 mM NaCl, 20 mM imidazole, 2 mM TCEP). The target protein was eluted in nickel wash buffer containing 250 mM imidazole. The eluted protein was concentrated with Amicon ultra concentration device (30,000MWCO)(Millipore) and separated using a DUO FLOW system (Bio-Rad) with a Sephacryl S-300 16/60 gel filtration column (GE Healthcare) equilibrated in 20 mM Tris, pH 7.5, 200 mM NaCl, 2 mM TCEP, 5% Glycerol and 0.02% NaN3. Protein fractions were analyzed on a 4–12% Bis-Tris NuPAGE (Invitrogen) gels and pure fractions were pooled and concentrated to 15 mM for Nanobody production. Gels were stained with InstantBlue (Expedeon). Identification of nanobodies against the HDAC6 ZnF domain was done by Hybrigenics Services SAS. In brief, HALO-ZnF (or HALO as control) protein was biotinylated in vitro using HaloTag® PEG-Biotin Ligand (Promega: G8591 or G8592) following the manufacturer's instruction and then used for three rounds of phage display with a naïve synthetic library based on a proprietary Lama scaffold. The Phage library was first incubated with the biotinylated His-HALO; the supernatant was then incubated with the biotinylated HALO-ZnF. Following selection, the positive hits were used to generate a yeast two-hybrid library, which was then screened against the human HDAC ZnF domain as bait (aa 1106-1215). Positive hits were isolated and validated by an intrabody assay. Following this, four different positive clones (Nb1 to 4) as well as a control clone were selected for further analysis.

GFP-Trap pull-down assay

C-terminally eGFP-tagged nanobodies were cloned into pLVX-puro lentiviral expression vectors. The lentiviral vector was co-transfected with Pol-Gag and VSV-G plasmids into HEK293T cells to produce lentivirus. Each eGFP-tagged nanobody was stably expressed in A549 cells after lentivirus infection, then eGFP-positive cells were sorted by FACS. A549 cells expressing each nanobody were harvested with ice-cold PBS from a 10 cm dish, spun down at 1,000*g* for 5 min. The pelleted samples were rapidly frozen at -80 °C. The frozen pellet was treated with CSK (cytoskeleton) buffer (10 mM PIPES pH6.8, 300 mM sucrose, 100 mM NaCl, 3 mM $MgCl_2$, 1 mM EGTA, 0.1%(v/v) Triton X-100) with 1x Complete EDTA free protease inhibitor cocktail (Roche#CO-RO) for 30 min on ice. The lysed cell extracts were subjected to low-speed centrifugation (3,000 rpm for 5 min) to separate the soluble cytoplasmic fraction. eGFP-tagged nanobodies were pulled-down with GFP-Trap agarose beads

(Chromotek#gtm-20) equilibrated with CSK buffer containing 1% BSA. The soluble fractions were incubated with GFP-Trap beads for 30 min at 4°C, then spun down 1,000*g* for 2 min. The beads were washed with GFP-Trap Wash buffer (10 mM Tris, pH7.5, 200 mM NaCl, 0.5 mM EDTA, 5% Glycerol) twice, and finally washed with 10 mM Tris, pH7.5, 100 mM NaCl, 5% Glycerol buffer once. The bead samples were dissolved in Laemmli sample buffer supplemented with 10 mM DTT and boiled for 5 min at 95°C before loading on a 4-12% Bis-Tris NuPAGE gels. Proteins were transferred onto polyvinylidene fluoride (PVDF) membranes (Millipore#05317) by using the iBlot2 Dry Blot system (Thermo Fisher Scientific) following to instruction manual, and detected with specific antibodies (anti-HDAC6 (D2E5, Cell Signaling Technology), 1:1,000, GFP (JL-8, Takara), 1:1,000, and a-Tubulin (Abcam ab4074) 1:1,000).

IAV infection assay (in nanobody expressing cells)

A549 cells stable expressing the HDAC6 ZnF nanobodies were infected with IAV X-31 (H3N2) strain. The cells were trypsinised and fixed in 4% FA at 5.5 hours post infection. The cells were stained for FACS analysis in FACS buffer (PBS, 0.1% BSA) containing 0.1% Saponin. The primary antibody used was mAb HB-65 (anti-nucleoprotein, ATCC), 1:200, and secondary was goat anti-mouse IgG Alexa Fluor 647 (Invitrogen), 1:2500. Antibodies were incubated for 30 min at room temperature. The cells were washed by centrifugation at 2,500 rpm for 5 min, resuspended in 100 µL of FACS buffer and analysed using Novocyte Flow Cytometer (Aceabio). The fcs files were analysed using Flow Jo version 10.3.0.

Selection and screening of DARPins

To generate DARPin binders against HDAC6-ZnF, the biotinylated target protein (see below) was immobilized on MyOne T1 streptavidin-coated beads (Pierce). Ribosome display selections were performed essentially as described (Dreier and Plückthun, 2012). Selections were performed over four rounds with decreasing target concentration and increasing washing steps to enrich for binders with high affinities. After four rounds of selection, the enriched pool was cloned into a bacterial pQIq-based expression vector as fusion with an N-terminal $MRGSH_8$-and C-terminal FLAG tag. After transformation into *E.coli* XL1-blue 380 single DARPin clones were expressed in 96 well format and lysed by addition of Cell lytic B reagent (Sigma), Lysozyme and Pierce nuclease. These bacterial crude extracts of single DARPin clones were subsequently used in a Homogeneous Time Resolved Fluorescence (HTRF)-based screen to identify potential binders. Binding of the FLAG-tagged DARPins to streptavidin-immobilized biotinylated HDAC6-ZnF was measured using FRET (donor: streptavidin-Tb cryptate, 610SATLB; acceptor: anti-FLAG-d2, 61FG2DLB; both Cisbio). Experiments were performed at room temperature in white 384-well Optiplate plates (PerkinElmer) using the Taglite assay buffer (Cisbio) at a final volume of 20 µL per well. FRET signals were recorded after an incubation time of 30 minutes using a Varioskan LUX Multimode Microplate (Thermo Scientific) with the

following settings: Delay time: 60 µs, integration time: 200 µs, measurement time: 1'000 ms, dynamic range: automatic. HTRF ratios were obtained by dividing the acceptor signal (665 nm) by the donor signal (620 nm) and multiplying this value by 10'000 to derive the 665/620 ratio. The background signal was determined by using reagents in the absence of DARPins. From this result, potential binders were identified (Table S1)

Expression and purification of Biotinylated His-Avi-HDAC6 ZnF (1108-1215), HDAC6 ZnF (1108-1215) and DARPin F10

E.coli BL21 (DE3), transfected by pOPINF-His-Avi-HDAC6 ZnF (in this case, bacteria was co-transfected with pet21a-BirA expressing plasmid, pOPINF-His-HDAC6 ZNF or DARPin F10 plasmid (pQiq_K_MRGS_His10-HA-3C-1766_F10), was cultured first in 50 ml LB medium overnight at 37°C, then 10 ml medium was transferred to 1 L 2xYT medium for continuous culturing in 2.5 L flask. When OD = 0.6 was reached, IPTG was added into the 1 L medium (final concentration 1 mM) and the temperature was reduced to 17°C (to induce ZnF protein biotinylation, D-biotin was added to 2xYT medium to a final concentration of 20 µM). Cultures were grown further for 18 hrs and bacteria were collected by centrifugation (4000 rpm, 15 mins, 4°C). The pellet was frozen at -80°C. All constructs were purified as follows.

The bacterial pellet was lysed with an ultrasonic sonicator (15 cycles, one cycle = 20 secs ON, 40 secs OFF) to completely break the bacteria. The cell lysate was dissolved in Ni column loading buffer (buffer 1, containing 20 mM Tris pH=7.5, 500 mM NaCl, 10 mM imidazole, supplied with protease inhibitor 1mM PMSF). The cell debris were separated from the protein by High-speed-centrifugation (17000rpm, 1 hr, 4°C). After filtering (0.45 µM filter, Merck#SLHVM33RS) the supernatant, the protein solution was loaded onto a HisTrap column (#GE17-5248-01) using a peristaltic pump at a flow rate of 5 ml/min. The column was washed with 4 to 5 column volume (CV) of buffer 1. To elute the target protein, we used a gradient elution by the AKTA system. The elution buffer (buffer 2, containing 20 mM Tris pH=7.5, 500 mM NaCl, 250 mN imidazole) was used together with the buffer 1 to generate the gradient. Eluted protein was digested by 3C protease (obtained from FMI protein facility) in dialysis buffer (20 mM Tris pH=7.5, 500 mM NaCl) at 4°C. Digested protein was re-loaded onto a HisTrap column to remove the His tag. His-Avi-ZnF protein was not treated with 3C protease, but loaded directly to the gel filtration step. The flow-through was collected and protein purity was determined by SDS-PAGE. Different fractions (with a purity >50%) from gradient elution were combined and applied onto an ion exchange column. Here, the protein solution was diluted 5 times with 20 mM Tris pH=7.5 buffer and loaded onto a 5 ml pre-pack HiTrap Q HP(#GE29-0513-25) column. Protein was eluted over a 25 min period with a gradient generated by the AKTA system, by mixing buffer A (20 mM Tris pH=7.5, 100 mM NaCl, 2 mM Tcep) and buffer B (20 mM Tris pH=7.5, 1 M NacL, 2 mM Tcep). Eluted target protein was concentrated and loaded onto Gel filtration system, using either a Superdex® 200 Increase 10/300 GL (#GE28-9909-44) or HiLoad 16/600 Superdex 200pg (#GE28-9893-35) column. After Gel

filtration, the separated target protein was flash-frozen with liquid nitrogen in Gel filtration buffer (20 mM Tris pH=7.5, 100 mM NaCl, 1 mM TCEP). Protein concentration was determined by its absorbance at 280 nm.

Pull-down Assay to identify inhibitory DARPin

10 µg Purified His-HDAC6 ZnF (1108-1215) was immobilized with 20 µL Ni-NTA agarose (Promega#30210) slurry at 4°C for 30 mins. Subsequently, 20 µg DARPin protein and 10 µg Ub were added to the Ni-NTA-ZnF solution at same time (in Figure S1b, they were mixed as described in the figure legend). All proteins were diluted in Ni-NTA loading buffer (20 mM Tris pH=7.5, 100 mM NaCl, 10 mM imidazole). The reaction volume was 500 µL, incubation was at 4°C on rotator for 30 mins. After incubation, the beads were washed 3 times with washing buffer (20 mM Tris pH=7.5, 150 mM NaCl). The supernatant was removed after spinning down the beads (500 g, 2 mins), and 20 µL 1x LDS sample buffer (Invitrogen# NP0007) was added to each reaction. Following heating at 80°C for 10 mins, all the samples were loaded onto NuPAGE 4-12% gradient gels. The proteins were visualized with Instant Blue reagent (expedeon#ISB1L).

Isothermal titration calorimetry (ITC) for determining affinity

The experiment was performed on a MicroCal VP-ITC machine. Protein HDAC6 ZnF (1108-1215) and DARPin F10 were purified as described, and Ub was purchased from BostonBiochem(Cat# U-100H). All the proteins were dialyzed in ITC buffer (10 mM Tris pH=7.5, 100 mM NaCl) for 3 hrs at 4°C before the experiment. We titrated 0.2 mM DARPin F10 protein (in the syringe) to 0.02 mM HDAC6 ZnF (1108-1215) protein in the cell (for determination of Ub and ZnF, 0.25 mM Ub was titrated to the 0.01 mM ZnF). The curve and statistics were done with the MicroCal ITC Origin Analysis software.

LC-MS analysis for DARPin F10 interacting protein

5 µg pcDNA3.1-GFP-DARPin F10 and pcDNA3.1-GFP-DARPin E3_5 were transfected into A549 cells; for each construct 3x 10 cm dishes were used, each containing 2 x 10^6 cells in 10 cm dishes. For each sample 15 µL Lipofectamine 3000 were used and the cells were cultured for 2 days to allow for sufficient expression. After collecting the cells, each dish was lysed with 500 µL CoIP buffer (10 mM Tris pH=7.5, 150 mM NaCl, 0.5 mM EDTA, 0.5%NP-40). The lysate was centrifuged at 14,000 rpm and 10 mins, 4°C. Supernatant was transferred to a new tube, and the protein concentration was determined by Bradford Assay (Biorad#5000006). Same amount of protein lysate (1.0 to 1.5 µg) was incubated with 10 µL GFP_Trap M beads (Chromotek#gtm-20) on rotator at 4°C, overnight. In the following morning, the beads were washed with washing buffer (20 mM Tris pH=7.5, 150 mM NaCl) 3 times.

To digest the protein on the beads, we used 10 µL Lys-C (0.2µg/µL in 50 mM Hepes pH 8.5) and 50 µL digestion buffer (3M GuaHCl, 20 mM EPPS pH 8.5, 10 mM CAA, 5 mM TCEP) to make master

mix, and added 6 µL of this mixture to the beads from each 10 cm dish. After short spin down (<1000 g) and 4 hours incubation at 37°C, we added 17 µL 50mM HEPES pH 8.5 as well as 1 µL 0.2 µg/µL trypsin to further digest the protein at 37°C overnight. Next morning, 1 more µL trypsin was added to the solution for 6 additional hours digestion. Then the sample was processed at the FMI Protein Analysis facility for mass spectrometry. The data was analyzed by software Perseus (version 1.5.2.6). And protein was annotated with human (v2017-04) database.

RNA Seq analysis for DARPin F10 impact on cellular gene expression

The A549 cells were transfected as described in above (same as in section "LC-MS analysis"). Each plasmid was transfected into 3x 10 cm dish cells. After 2 days in culture, 1.5 million GFP positive cells were isolated from each dish by FACS (that is, 3 x 1.5 million cells for one transfected DARPin), and total RNA was extracted with the RNA extracting Kit (QIAGEN#74004). The samples were further processed at the FMI genomics Facility and sequenced on a Hi-Seq instrument; the results were analysed with R-Studio.

Generation of A549 cells expressing a conditionally degradabale DARPin F10

Plasmid Plenti-Puro-Flag-HA-DARPin F10-FKBP^{F36V} and Plenti-Puro-Flag-HA-FKBP^{K36V} (each 20 µg) were co-transfected with packaging plasmids (expressing tat, rev, gag, vsv-g, each at 1 µg) together with 75 µL FuGENE HD reagent (Promega#E2311) in 0.5 ml Opti-MEM medium (Sigma#31985062). After 25 mins incubation at room temperature, the mix was added to 293T cells in 10 cm dish, seeded one day before with 1.6 million cells per dish. Cells were cultured at 37°C for 3 days; the medium was collected and filtered with 0.45 µm filter (Merck#SEIM003M00), and 1x LentiX concentrator (Takara#631231) was added (1/3 of the supernatant volume). The mixture was incubated at 4°C for 30 mins and the lentivirus was precipitated by centrifugation at 1500 g, 45 mins, 4°C. The pellet was re-suspended in 500 µL Opti-MEM (Gibco#31985062).

The re-suspended lentivirus pellet was added to the culture medium of A549 cells (10 cm dish, 0.6 million WT A549 cells seeded per dish one day before). Two days later the medium was changed to DMEM supplied with puromycin (final concentration 2 µg/ml). Puro-resistant cells were selected for 2 days and then single-cell sorted into 96 wells plates. After 1 month culturing, clones were expanded and analyzed by western blot with HA antibody (Abcam#18181) to identify the cell lines expressing HA-DARPin F10-FKBP^{F36V} or HA-FKBP^{F36V}.

Imaging and quantification of aggresome and SGs

For immunofluorescence, cells were seeded in 4 wells chamber slides (Millipore# C7182) to culture the cells. WT A549, DARPin F10-FKBP^{F36V} and dTAG treated (2 µM, 6 hrs) F10 expressing cells were treated by 5 µM MG132 for 18 hrs to induce the aggresome formation. HDAC6 was used as a marker for aggresome and stained by anti-HDAC6 antibody (CST#7558). The nucleus (DNA) was stained by

DAPI (Sigma#D1306). Pictures were taken by spinning disk confocal microscopy with the same parameters (e.g. exposure time, binning, etc.) for all the conditions. Pictures were analysed by ImageJ software. The aggresome was identified by its signal intensity and shape, quantitated by Particle analysis in ImageJ.

For SGs, we used the same set-up as for the aggresome experiments, but used 1 mM Sodium Arsenite (30 mins treatment) instead of MG132 to induce SGs. G3BP1 was used as the marker for SGs and visualized by anti-G3BP1 antibody (Aviva Systems Biology#ARP37713_T100). The quantification and analysis were done with ImageJ, installed with SG Counter Plugin (developed by Ann Sablina, Lomonosov Moscow State University, Russia). Plot and statistics were all done in software Graphpad Prism 8.

Split-GFP assay

Plasmid pcDNA3.1-GFP(1-9), pcDNA3.1-GFP(10)-Ub, pcDNA3.1-GFP(11)-HDAC6 ZnF (1108-1215)/1182 mutant and pcDNA3.1-mRuby were co-transfected with FuGENE reagent (using the manufacturer's protocol) (Promega#E2311) together to 0.5 million 293T cells in 6 well plate, with a molarity ratio of 1:1:1:1 (1 μg for pcDNA3.1-GFP(1-9), other plasmids were adjusted accordingly). After 2 days culturing at 37°C, the GFP signal was visualized under wide field microscopy (Zeiss Z1). mRuby expression served as a transfection control.

To investigate DARPin interference, non-fluorescent tagged DARPin F10 and DARPin A10 plasmid (1 μg for both) were transfected together with the plasmids mentioned above. Visualization procedures were the same.

IAV uncoating assay

A549 cells were seeded on glass slides and, after reaching ca. 70% confluence, incubated at 4 °C with IAV X31 (H3N2, MOI = 30 PFU/cell) for 1 h to synchronize infection. After that, the cells were incubated at 37 °C for 3 h and fixed with paraformaldehyde 4% for 15min. For immunofluorescence, cells were permeabilized with 0.5% Triton X-100 in PBS for 5 min and incubated overnight in 1% BSA with M1-specific murine monoclonal antibody (ATCC#HB64, 1:4000). Cells were washed with PBS and incubated for 1 h with Alexa Fluor 488 goat anti-mouse (IgG) (H+L) (Thermo Fischer; 1:2000, 1% BSA) for 1 h at room temperature. Nuclei were stained for 5 min with DAPI (1:1000 in PBS). Glass slides were examined using spinning disk confocal scanning unit. Alex Fluor 647 NHS ester Tris was used to stain the total protein to visualize the cell body.

The mean fluorescence green intensity (MFI) was quantified using ImageJ. One representative out of three independent experiments is shown. For all panels, error bars represent standard deviation of the pictures analyzed (approximately 40 cells per picture and more than 200 cells in total) and statistical significance was determined by one-way ANOVA (ns (non-significant) = $P > 0.05$; *$P \leq 0.05$; **$P \leq 0.01$; ***$P \leq 0.001$).

Virus growth curve

A549 cells were infected in 6 well/plates with Influenza virus (Virapur, H3N2, purified Influenza A/X31, #B1707C) at 37°C in infection medium (DMEM 0.2% BSA, 2 mM L-glutamine and 1 µg/ml of TPCK-treated trypsin). For single cycle infection assays, cells and viruses were pre-incubated at 4°C for 1 h and the cells were washed with PBS before incubation at 37 °C for the indicated time points. Viruses from the harvested supernatants were quantified using plaque assay in MDCKII cells with 2% agar overlay.

A Zika virus stock from a low passage clinical isolate of Asian lineage (ZIKV PRVABC59) passaged on Vero cells and purified by ultracentrifugation was used to infect A549 cells in 24 well/plates at 37°C with in DMEM 10% FCS. Virus titers collected from the culture supernatant were determined on Vero cells (ATCC#CCL-81) and expressed as 50% tissue culture infective dose per ml (TCID50/ml) using the Reed and Muench method.

Immunofluorescence for Zika virus

For detection of Zika virus protein on infected cells 72hpi, the A549 cells were washed with PBS, fixed with 4% PFA and incubated with anti-E protein Flavivirus group antibody 4G2 in PBS supplemented with 1% BSA for 1h at 37 °C. Cells were washed with PBS and incubated for 1 h with Alexa Fluor 488 goat anti-mouse (IgG) (H+L) (Thermo Fischer; 1:2000, 1% BSA) for 1 h at room temperature. Nuclei were stained for 5 min with DAPI (Thermo Fischer, 1:1000 in PBS).

Quantification and Statistical Analysis

Peptides of raw DARPin F10 data from the mass spectrometers were identified and quantified by MQ version 1.5.3.8. For data searches the search engine Andromeda was used. A costume DB with the DARPin_F10 and E3_5 sequence combined with the human sub-set of the UNIPROT DB and the contaminant library from MaxQuant was searched. Results were filtered with a FDR of 1%.

Details of specific statistical tests and experimental design for immunofluorescent experiments are given in the relevant figure legends. All Virus growth curve experiments were performed in triplicate (n=3) for technical reolication. Each experiment was independently repeated 2 to 3 times to consolidate the conclusion. To analyze the data, two-way ANOVA test (using the Geisser-Greenhouse Correction) was performed with GraphPad Prism 8; Abbreviations for p values are as follows: $p < 0.05 = *$, $p < 0.01 = **$, $p < 0.001 = ***$, $p < 0.0001 = ****$; significant P values were shown.

Acknowledgements

With my highest respect and deepest gratitude, I would like to thank my mentor - Patrick Matthias for giving this precious opportunity to enable me to perform my Ph. D. study in this highly disciplined and organized lab, together with the warm-hearted talents from all over the world. Thanks to his guidance, my Ph. D. career is always on the right track. Although I encountered numerous difficulties in these years, yet your invaluable suggestions, as well as continuous supports, are the sunlight passing through the dark clouds, always showing me the right direction at the crossroad. It is an invaluable experience for my future scientific career that I could get this systematic training at the start-line.

Without the assistance and guidance from my thesis committee members – Dr. Nicolas Thöma and Prof. Anne Spang, I will hardly finish my Ph.D. Your golden words always remind me that a rigorous attitude is the key to success. Although we did not exchange the opinion frequently, your mottos keep pushing me to pursue the perfect rather than settle for the mediocre, and this, I am deeply convinced, will benefit me a lot in the future career.

I would show my appreciation to all the collaborators who support my Ph. D research. I want to thank Daniel Hess for his generous help in Mass Spectrometry analysis, and Laurent Gelman for the introduction to Microscopy imaging. I also want to thank Heinz Gut for helping to collect X-ray diffraction data, and Georg Kempf for instructing me about crystallography. I cannot forget my 2 weeks' experience in Cambridge with Prof. Andrew Carter, working on the dynein complex. Although it did not work as we expected, your kindness in sharing the material and technique is unforgettable. I will offer my special thanks to Alina Artcibasova, Prof. Jörg Stelling and Yohei Yamauchi. Working together with you, Alina and Jörg on the same project is a great honor for me, and our collaboration is quite a pleasure. Meanwhile, as a specialist in virology, Yohei's comments always deepen our understanding of the project.

I am very glad to work with all current and former lab members. Special thanks to Yasuyuki Miyake, who offers great help at the beginning of my Ph.D. I would like to thank Shuang Song and Makoto Saito for their friendship. Thanks to Etori Aguiar Moreira for the experiment with the virus. I would like to thank Jacint Sanchez and Gerasimos Langousis for discussing the issues from daily experiments, Chun Cao and Gabriele Matthias for their support for organizing the lab and providing a comfortable working environment. I also would like to thank all the former members: Amin M Choukrallah, Richard Heideman, Patricia Nigg, Vincent Pilonel and Jasmin Ostermayer.

I wish to extend my special thanks to all the FMI communities including the facilities for Microscopy imaging, protein analysis, protein purification, cell sorting, computational biology and the media kitchen. Without their support, I cannot finish my projects. I want to thank Elida Keller and Piera

Cicchetti for their kind help and advice on my daily life. I would thank all my friends who met at the University of Basel, the time spent with you will be precious for my whole life.

And last, I would like to thank my family for their understanding, support, and encouragement in these years.

Reference

Advani, V., and Ivanov, P. (2020). Stress granule subtypes: an emerging link to neurodegeneration. Cellular and Molecular Life Sciences.

Akella, J.S., Wloga, D., Kim, J., Starostina, N.G., Lyons-Abbott, S., Morrissette, N.S., Dougan, S.T., Kipreos, E.T., and Gaertig, J. (2010). MEC-17 is an alpha-tubulin acetyltransferase. Nature *467*, 218-222.

Alenquer, M., Vale-Costa, S., Etibor, T.A., Ferreira, F., Sousa, A.L., and Amorim, M.J. (2019). Influenza A virus ribonucleoproteins form liquid organelles at endoplasmic reticulum exit sites. Nature communications *10*, 1629.

Anchisi, S., Goncalves, A.R., Mazel-Sanchez, B., Cordey, S., and Schmolke, M. (2018). Influenza A Virus Genetic Tools: From Clinical Sample to Molecular Clone. Methods Mol Biol *1836*, 33-58.

Anderson, P., and Kedersha, N. (2009). RNA granules: post-transcriptional and epigenetic modulators of gene expression. Nat Rev Mol Cell Biol *10*, 430-436.

Anderson, P., Kedersha, N., and Ivanov, P. (2015). Stress granules, P-bodies and cancer. Biochimica et biophysica acta *1849*, 861-870.

Araujo, F.D., Stracker, T.H., Carson, C.T., Lee, D.V., and Weitzman, M.D. (2005). Adenovirus type 5 E4orf3 protein targets the Mre11 complex to cytoplasmic aggresomes. Journal of virology *79*, 11382-11391.

Ariumi, Y., Kuroki, M., Kushima, Y., Osugi, K., Hijikata, M., Maki, M., Ikeda, M., and Kato, N. (2011). Hepatitis C virus hijacks P-body and stress granule components around lipid droplets. Journal of virology *85*, 6882-6892.

Arnaud, F., Murcia, P.R., and Palmarini, M. (2007). Mechanisms of late restriction induced by an endogenous retrovirus. Journal of virology *81*, 11441-11451.

Artcibasova, A., Wang, L., A., S., Yohei, Y., Mirco, S., Matthias, P., and Stelling, J. (2020, submitted). A quantitative model for HDAC6-mediated virus uncoating predicts Influenza A infectivity (Submitted). Cell Host Microbe *Submitted*.

Ash, P., Vanderweyde, T., Youmans, K., Apicco, D., and Wolozin, B. (2014). Pathological stress granules in Alzheimer's disease. Brain Res *1584*, 52-58.

Aulas, A., Fay, M.M., Lyons, S.M., Achorn, C.A., Kedersha, N., Anderson, P., and Ivanov, P. (2017). Stress-specific differences in assembly and composition of stress granules and related foci. Journal of cell science *130*, 927-937.

Azzarito, V., Long, K., Murphy, N.S., and Wilson, A.J. (2013). Inhibition of alpha-helix-mediated protein-protein interactions using designed molecules. Nat Chem *5*, 161-173.

Badham, M.D., and Rossman, J.S. (2016). Filamentous Influenza Viruses. Current Clinical Microbiology Reports *3*, 155-161.

Bali, P., Pranpat, M., Bradner, J., Balasis, M., Fiskus, W., Guo, F., Rocha, K., Kumaraswamy, S., Boyapalle, S., Atadja, P.*, et al.* (2005). Inhibition of histone deacetylase 6 acetylates and disrupts the chaperone function of heat shock protein 90: a novel basis for antileukemia activity of histone deacetylase inhibitors. The Journal of biological chemistry *280*, 26729-26734.

Balmik, A.A., Sonawane, S.K., and Chinnathambi, S. (2019). Modulation of Actin network and Tau phosphorylation by HDAC6 ZnF UBP domain. bioRxiv, 702571.

Banaszynski, L.A., Chen, L.C., Maynard-Smith, L.A., Ooi, A.G., and Wandless, T.J. (2006). A rapid, reversible, and tunable method to regulate protein function in living cells using synthetic small molecules. Cell *126*, 995-1004.

Banerjee, I., Miyake, Y., Nobs, S.P., Schneider, C., Horvath, P., Kopf, M., Matthias, P., Helenius, A., and Yamauchi, Y. (2014a). Influenza A virus uses the aggresome processing machinery for host cell entry. Science *346*.

Banerjee, I., Miyake, Y., Nobs, S.P., Schneider, C., Horvath, P., Kopf, M., Matthias, P., Helenius, A., and Yamauchi, Y. (2014b). Influenza A virus uses the aggresome processing machinery for host cell entry. Science *346*, 473-477.

Behrends, C., and Harper, J.W. (2011). Constructing and decoding unconventional ubiquitin chains. Nat Struct Mol Biol *18*, 520-528.

Bertos, N.R., Gilquin, B., Chan, G.K., Yen, T.J., Khochbin, S., and Yang, X.J. (2004). Role of the tetradecapeptide repeat domain of human histone deacetylase 6 in cytoplasmic retention. The Journal of biological chemistry *279*, 48246-48254.

Binz, H.K., Amstutz, P., Kohl, A., Stumpp, M.T., Briand, C., Forrer, P., Grutter, M.G., and Pluckthun, A. (2004). High-affinity binders selected from designed ankyrin repeat protein libraries. Nat Biotechnol *22*, 575-582.

Binz, H.K., Stumpp, M.T., Forrer, P., Amstutz, P., and Plückthun, A. (2003). Designing Repeat Proteins: Well-expressed, Soluble and Stable Proteins from Combinatorial Libraries of Consensus Ankyrin Repeat Proteins. Journal of Molecular Biology *332*, 489-503.

Bondeson, D.P., Mares, A., Smith, I.E., Ko, E., Campos, S., Miah, A.H., Mulholland, K.E., Routly, N., Buckley, D.L., Gustafson, J.L.*, et al.* (2015). Catalytic in vivo protein knockdown by small-molecule PROTACs. Nat Chem Biol *11*, 611-617.

Bonenfant, G., Williams, N., Netzband, R., Schwarz, M.C., Evans, M.J., and Pager, C.T. (2019). Zika Virus Subverts Stress Granules To Promote and Restrict Viral Gene Expression. Journal of virology *93*.

Bouvier., N.M., and Palese., P. (2008). THE BIOLOGY OF INFLUENZA VIRUSES. Vaccine *12*, 49-54.

Boyault, C., Gilquin, B., Zhang, Y., Rybin, V., Garman, E., Meyer-Klaucke, W., Matthias, P., Muller, C.W., and Khochbin, S. (2006). HDAC6-p97/VCP controlled polyubiquitin chain turnover. The EMBO journal *25*, 3357-3366.

Boyault, C., Sadoul, K., Pabion, M., and Khochbin, S. (2007). HDAC6, at the crossroads between cytoskeleton and cell signaling by acetylation and ubiquitination. Oncogene *26*, 5468-5476.

Brauchle, M., Hansen, S., Caussinus, E., Lenard, A., Ochoa-Espinosa, A., Scholz, O., Sprecher, S.G., Plückthun, A., and Affolter, M. (2014). Protein interference applications in cellular and developmental biology using DARPins that recognize GFP and mCherry. Biology open *3*, 1252-1261.

Brindisi, M., Saraswati, A.P., Brogi, S., Gemma, S., Butini, S., and Campiani, G. (2019). Old but Gold: Tracking the New Guise of Histone Deacetylase 6 (HDAC6) Enzyme as a Biomarker and Therapeutic Target in Rare Diseases. Journal of medicinal chemistry.

Brooks, C.L., and Gu, W. (2011). The impact of acetylation and deacetylation on the p53 pathway. Protein Cell *2*, 456-462.

Buchan, J.R., Muhlrad, D., and Parker, R. (2008). P bodies promote stress granule assembly in Saccharomyces cerevisiae. The Journal of cell biology *183*, 441-455.

Cabantous, S., Nguyen, H., Pedelacq, J., Koraïchi, F., Chaudhary, A., Ganguly, K., Lockard, M., Favre, G., Terwilliger, T., and Waldo, G. (2013). A New Protein-Protein Interaction Sensor Based on Tripartite Split-GFP Association. Scientific Reports *3*, 2854.

Cai, J., Culley, M.K., Zhao, Y., and Zhao, J. (2018). The role of ubiquitination and deubiquitination in the regulation of cell junctions. Protein Cell *9*, 754-769.

Campochiaro, P.A., Channa, R., Berger, B.B., Heier, J.S., Brown, D.M., Fiedler, U., Hepp, J., and Stumpp, M.T. (2013). Treatment of diabetic macular edema with a designed ankyrin repeat protein that binds vascular endothelial growth factor: a phase I/II study. Am J Ophthalmol *155*, 697-704, 704 e691-692.

Campos, G.S., Bandeira, A.C., and Sardi, S.I. (2015). Zika Virus Outbreak, Bahia, Brazil. Emerging infectious diseases *21*, 1885-1886.

Cao-Lormeau, V.M., Roche, C., Teissier, A., Robin, E., Berry, A.L., Mallet, H.P., Sall, A.A., and Musso, D. (2014). Zika virus, French polynesia, South pacific, 2013. Emerging infectious diseases *20*, 1085-1086.

Capitanio;, J.S., and Wozniak., R.W. (2012). Host Cell Factors Necessary for Influenza A Infection: Meta-Analysis of Genome Wide Studies. arXiv.

Chen, B., Retzlaff, M., Roos, T., and Frydman, J. (2011). Cellular strategies of protein quality control. Cold Spring Harb Perspect Biol *3*, a004374.

Chen, H., Qian, Y., Chen, X., Ruan, Z., Ye, Y., Chen, H., Babiuk, L., Jung, Y., and Dai, J. (2019). HDAC6 Restricts Influenza A Virus by Deacetylation of the RNA Polymerase PA Subunit. Journal of virology *93*.

Chernov, K.G., Barbet, A., Hamon, L., Ovchinnikov, L.P., Curmi, P.A., and Pastre, D. (2009). Role of microtubules in stress granule assembly: microtubule dynamical instability favors the formation of micrometric stress granules in cells. The Journal of biological chemistry *284*, 36569-36580.

Ching, W., Koyuncu, E., Singh, S., Arbelo-Roman, C., Hartl, B., Kremmer, E., Speiseder, T., Meier, C., and Dobner, T. (2013). A Ubiquitin-specific Protease Possesses a Decisive Role for Adenovirus Replication and Oncogene-mediated Transformation. PLOS Pathogens *9*, e1003273.

Chirico, G.G., and Kraut, D.A. (2016). Mode of Ubiquitination Determines Complete or Partial Degradation of GFP Substrates by the 26S Proteasome. The FASEB Journal *30*, 597.593-597.593.

Choi, S.J., Lee, H.C., Kim, J.H., Park, S.Y., Kim, T.H., Lee, W.K., Jang, D.J., Yoon, J.E., Choi, Y.I., Kim, S.*, et al.* (2016). HDAC6 regulates cellular viral RNA sensing by deacetylation of RIG-I. The EMBO journal *35*, 429-442.

Cosenza, M., and Pozzi, S. (2018). The Therapeutic Strategy of HDAC6 Inhibitors in Lymphoproliferative Disease. Int J Mol Sci *19*.

Crick, F. (1970). Central Dogma of Molecular Biology. Nature *227*, 561-563

Dehay, B., Bourdenx, M., Gorry, P., Przedborski, S., Vila, M., Hunot, S., Singleton, A., Olanow, C.W., Merchant, K.M., Bezard, E.*, et al.* (2015). Targeting α-synuclein for treatment of Parkinson's disease: mechanistic and therapeutic considerations. The Lancet Neurology *14*, 855-866.

Donnelly, N., Gorman, A.M., Gupta, S., and Samali, A. (2013). The eIF2alpha kinases: their structures and functions. Cell Mol Life Sci *70*, 3493-3511.

Dreier, B., and Plückthun, A. (2012). Rapid selection of high-affinity binders using ribosome display. Methods in molecular biology (Clifton, NJ) *805*, 261-286.

Du, J., Cross, T.A., and Zhou, H.X. (2012). Recent progress in structure-based anti-influenza drug design. Drug Discov Today *17*, 1111-1120.

Duffy, M.R., Chen, T.H., Hancock, W.T., Powers, A.M., Kool, J.L., Lanciotti, R.S., Pretrick, M., Marfel, M., Holzbauer, S., Dubray, C.*, et al.* (2009). Zika virus outbreak on Yap Island, Federated States of Micronesia. The New England journal of medicine *360*, 2536-2543.

Elleman, C.J., and Barclay, W.S. (2004). The M1 matrix protein controls the filamentous phenotype of influenza A virus. Virology *321*, 144-153.

Elton, D., Bruce, E.A., Bryant, N., Wise, H.M., MacRae, S., Rash, A., Smith, N., Turnbull, M.L., Medcalf, L., Daly, J.M.*, et al.* (2013). The genetics of virus particle shape in equine influenza A virus. Influenza Other Respir Viruses *7 Suppl 4*, 81-89.

Ferreira de Freitas, R., Harding, R.J., Franzoni, I., Ravichandran, M., Mann, M.K., Ouyang, H., Lautens, M., Santhakumar, V., Arrowsmith, C.H., and Schapira, M. (2018). Identification and Structure-Activity Relationship of HDAC6 Zinc-Finger Ubiquitin Binding Domain Inhibitors. Journal of medicinal chemistry.

Fischer, E.S., Bohm, K., Lydeard, J.R., Yang, H., Stadler, M.B., Cavadini, S., Nagel, J., Serluca, F., Acker, V., Lingaraju, G.M.*, et al.* (2014). Structure of the DDB1-CRBN E3 ubiquitin ligase in complex with thalidomide. Nature *512*, 49-53.

Fournier, M.J., Gareau, C., and Mazroui, R. (2010). The chemotherapeutic agent bortezomib induces the formation of stress granules. Cancer cell international *10*, 12.

G.Katze, M., Yao-TsengChen, and M.Krug, R. (1984). Nuclear-cytoplasmic transport and VAI RNA-independent translation of influenza viral messenger RNAs in late adenovirus-infected cells. Cell *37*, 483-490.

Gao, X., Jiang, L., Gong, Y., Chen, X., Ying, M., Zhu, H., He, Q., Yang, B., and Cao, J. (2019). Stress granule: A promising target for cancer treatment. British journal of pharmacology *176*, 4421-4433.

Gao, Y.S., Hubbert, C.C., and Yao, T.P. (2010). The microtubule-associated histone deacetylase 6 (HDAC6) regulates epidermal growth factor receptor (EGFR) endocytic trafficking and degradation. The Journal of biological chemistry *285*, 11219-11226.

Gennerich, A., Carter, A.P., Reck-Peterson, S.L., and Vale, R.D. (2007). Force-induced bidirectional stepping of cytoplasmic dynein. Cell *131*, 952-965.

Gonnet, P., Dimopoulos, S., Widmer, L., and Stelling, J. (2012). A specialized ODE integrator for the efficient computation of parameter sensitivities. BMC systems biology *6*, 46.

Gray Pearson, F.R., Tara Beers Gibson, Bing-e Xu, Mahesh Karandikar, Kevin Berman, Melanie H. Cobb (2001). Mitogen-Activated Protein (MAP) Kinase Pathways: Regulation and Physiological Functions. Endocrine Reviews *22*, 153–183.

Guo, Z.J., Tao, L.X., Dong, X.Y., Yu, M.H., Tian, T., and Tang, X.D. (2015). Characterization of aggregate/aggresome structures formed by polyhedrin of Bombyx mori nucleopolyhedrovirus. Sci Rep *5*, 14601.

Gupta, N., Badeaux, M., Liu, Y., Naxerova, K., Sgroi, D., Munn, L.L., Jain, R.K., and Garkavtsev, I. (2017). Stress granule-associated protein G3BP2 regulates breast tumor initiation. Proc Natl Acad Sci U S A *114*, 1033-1038.

Gustin, J.K., Moses, A.V., Fruh, K., and Douglas, J.L. (2011). Viral takeover of the host ubiquitin system. Front Microbiol *2*, 161.

Guthrie, C.R., and Kraemer, B.C. (2011). Proteasome inhibition drives HDAC6-dependent recruitment of tau to aggresomes. J Mol Neurosci *45*, 32-41.

Hai, Y., and Christianson, D.W. (2016). Histone deacetylase 6 structure and molecular basis of catalysis and inhibition. Nat Chem Biol *12*, 741-747.

Hampe, C., Ardila-Osorio, H., Fournier, M., Brice, A., and Corti, O. (2006). Biochemical analysis of Parkinson's disease-causing variants of Parkin, an E3 ubiquitin–protein ligase with monoubiquitylation capacity. Human Molecular Genetics *15*, 2059-2075.

Hao, R., Nanduri, P., Rao, Y., Panichelli, R.S., Ito, A., Yoshida, M., and Yao, T.P. (2013). Proteasomes activate aggresome disassembly and clearance by producing unanchored ubiquitin chains. Molecular cell *51*, 819-828.

Harding, R., Ferreira de Freitas, R., Collins, P., Franzoni, I., Ravichandran, M., Ouyang, H., Juarez-Ornelas, K., Lautens, M., Schapira, M., von Delft, F.*, et al.* (2017). Small molecule antagonists of the interaction between the histone deacetylase 6 zinc-finger domain and ubiquitin. Journal of medicinal chemistry.

Heath, C.M., Windsor, M., and Wileman, T. (2001). Aggresomes Resemble Sites Specialized for Virus Assembly. JCB.

Hebron, M.L., Lonskaya, I., Sharpe, K., Weerasinghe, P.P., Algarzae, N.K., Shekoyan, A.R., and Moussa, C.E. (2013). Parkin ubiquitinates Tar-DNA binding protein-43 (TDP-43) and promotes its cytosolic accumulation via interaction with histone deacetylase 6 (HDAC6). The Journal of biological chemistry *288*, 4103-4115.

Hicke, L., Schubert, H.L., and Hill, C.P. (2005). Ubiquitin-binding domains. Nat Rev Mol Cell Biol *6*, 610-621.

Hilsch, M., Goldenbogen, B., Sieben, C., Hofer, C.T., Rabe, J.P., Klipp, E., Herrmann, A., and Chiantia, S. (2014). Influenza A matrix protein M1 multimerizes upon binding to lipid membranes. Biophys J *107*, 912-923.

Hook, S.S., Orian, A., Cowley, S.M., and Eisenman, R.N. (2002). Histone deacetylase 6 binds polyubiquitin through its zinc finger (PAZ domain) and copurifies with deubiquitinating enzymes. Proc Natl Acad Sci U S A *99*, 13425-13430.

Hou, S., Kumar, A., Xu, Z., Airo, A.M., Stryapunina, I., Wong, C.P., Branton, W., Tchesnokov, E., Gotte, M., Power, C.*, et al.* (2017). Zika Virus Hijacks Stress Granule Proteins and Modulates the Host Stress Response. Journal of virology *91*.

Houzelstein, D., Bullock, S.L., Lynch, D.E., Grigorieva, E.F., Wilson, V.A., and Beddington, R.S. (2002). Growth and early postimplantation defects in mice deficient for the bromodomain-containing protein Brd4. Mol Cell Biol *22*, 3794-3802.

Hu, Y.B., Dammer, E.B., Ren, R.J., and Wang, G. (2015). The endosomal-lysosomal system: from acidification and cargo sorting to neurodegeneration. Transl Neurodegener *4*, 18.

Hubbert, C., Guardiola, A., Shao, R., Kawaguchi, Y., Ito, A., Nixon, A., Yoshida, M., Wang, X., and Yao, T. (2002). HDAC6 is a microtubule-associated deacetylase. Nature *417*, 455-458.

Huo, L., Li, D., Sun, X., Shi, X., Karna, P., Yang, W., Liu, M., Qiao, W., Aneja, R., and Zhou, J. (2011). Regulation of Tat acetylation and transactivation activity by the microtubule-associated deacetylase HDAC6. The Journal of biological chemistry *286*, 9280-9286.

Husain, M., and Cheung, C.Y. (2014). Histone deacetylase 6 inhibits influenza A virus release by downregulating the trafficking of viral components to the plasma membrane via its substrate, acetylated microtubules. Journal of virology *88*, 11229-11239.

Husain, M., and Harrod, K.S. (2011). Enhanced acetylation of alpha-tubulin in influenza A virus infected epithelial cells. FEBS Lett *585*, 128-132.

Hussain, M., Galvin, H., Haw, T., Nutsford, A., and Husain, M. (2017). Drug resistance in influenza A virus: the epidemiology and management. Infect Drug Resist *10*, 121-134.

Isaacson, M.K., and Ploegh, H.L. (2009). Ubiquitination, ubiquitin-like modifiers, and deubiquitination in viral infection. Cell Host Microbe *5*, 559-570.

Ivanov, A.A., Khuri, F.R., and Fu, H. (2013). Targeting protein-protein interactions as an anticancer strategy. Trends Pharmacol Sci *34*, 393-400.

Jain, S., Wheeler, J.R., Walters, R.W., Agrawal, A., Barsic, A., and Parker, R. (2016). ATPase-Modulated Stress Granules Contain a Diverse Proteome and Substructure. Cell *164*, 487-498.

Jiang, L., Wang, M., Lin, S., Jian, R., Li, X., Chan, J., Dong, G., Fang, H., Robinson, A.E., Aguet, F.*, et al.* (2020). A Quantitative Proteome Map of the Human Body. Cell *183*, 269-283.e219.

Jiang, Y.W., Veschambre, P., Erdjument-Bromage, H., Tempst, P., Conaway, J.W., Conaway, R.C., and Kornberg, R.D. (1998). Mammalian mediator of transcriptional regulation and its possible role as an end-point of signal transduction pathways. Proc Natl Acad Sci U S A *95*, 8538-8543.

Jiang, Z., Li, W., Hu, X., Zhang, Q., Sun, T., Cui, S., Wang, S., Ouyang, Q., Yin, Y., Geng, C.*, et al.* (2019). Tucidinostat plus exemestane for postmenopausal patients with advanced, hormone receptor-positive breast cancer (ACE): a randomised, double-blind, placebo-controlled, phase 3 trial. The Lancet Oncology *20*, 806-815.

Johnston, J.A., Ward, C.L., and Kopito, R.R. (1998a). Aggresomes: a cellular response to misfolded proteins. The Journal of cell biology *143*, 1883-1898.

Johnston, J.A., Ward, C.L., and Kopito, R.R. (1998b). Aggresomes: A Cellular Response to Misfolded Proteins. The Journal of cell biology *143*, 1883-1898.

Kadlcíková, J., Holecek, M., Safránek, R., Tilser, I., and Kessler, B.M. (2004). Effects of proteasome inhibitors MG132, ZL3VS and AdaAhx3L3VS on protein metabolism in septic rats. Int J Exp Pathol *85*, 365-371.

Kajitani, N., Satsuka, A., Yoshida, S., and Sakai, H. (2013). HPV18 E1^E4 is assembled into aggresome-like compartment and involved in sequestration of viral oncoproteins. Front Microbiol *4*, 251.

Kawaguchi, Y., Kovacs, J., McLauri, A., Vance, J., Ito, A., and Yao, T. (2003). The Deacetylase HDAC6 Regulates Aggresome Formation and Cell Viability in Response to Misfolded Protein Stress. Cell *Vol. 115, 727–738*.

Khaperskyy, D.A., Hatchette, T.F., and McCormick, C. (2012). Influenza A virus inhibits cytoplasmic stress granule formation. FASEB journal : official publication of the Federation of American Societies for Experimental Biology *26*, 1629-1639.

Khatau, S.B., Hale, C.M., Stewart-Hutchinson, P.J., Patel, M.S., Stewart, C.L., Searson, P.C., Hodzic, D., and Wirtz, D. (2009). A perinuclear actin cap regulates nuclear shape. Proceedings of the National Academy of Sciences *106*, 19017-19022.

Khoury, G.A., Baliban, R.C., and Floudas, C.A. (2011). Proteome-wide post-translational modification statistics: frequency analysis and curation of the swiss-prot database. Sci Rep *1*.

Kim, S., Kwon, S.H., Kam, T.I., Panicker, N., Karuppagounder, S.S., Lee, S., Lee, J.H., Kim, W.R., Kook, M., Foss, C.A.*, et al.* (2019). Transneuronal Propagation of Pathologic alpha-Synuclein from the Gut to the Brain Models Parkinson's Disease. Neuron *103*, 627-641.e627.

Kimball., S.R. (1999). Eukaryotic initiation factor eIF2. The International Journal of Biochemistry & Cell Biology *31*, 25-29.

Komander, D., and Rape, M. (2012). The ubiquitin code. Annu Rev Biochem *81*, 203-229.

Kovacs, J.J., Murphy, P.J., Gaillard, S., Zhao, X., Wu, J.T., Nicchitta, C.V., Yoshida, M., Toft, D.O., Pratt, W.B., and Yao, T.P. (2005). HDAC6 regulates Hsp90 acetylation and chaperone-dependent activation of glucocorticoid receptor. Molecular cell *18*, 601-607.

Kozlov, M.V., Kleymenova, A.A., Konduktorov, K.A., Malikova, A.Z., and Kochetkov, S.N. (2014). Selective inhibitor of histone deacetylase 6 (tubastatin A) suppresses proliferation of hepatitis C virus replicon in culture of human hepatocytes. Biochemistry (Mosc) *79*, 637-642.

Kummer, L., Hsu, C.W., Dagliyan, O., MacNevin, C., Kaufholz, M., Zimmermann, B., Dokholyan, N.V., Hahn, K.M., and Pluckthun, A. (2013). Knowledge-based design of a biosensor to quantify localized ERK activation in living cells. Chem Biol *20*, 847-856.

Kummer, L., Parizek, P., Rube, P., Millgramm, B., Prinz, A., Mittl, P.R., Kaufholz, M., Zimmermann, B., Herberg, F.W., and Pluckthun, A. (2012). Structural and functional analysis of phosphorylation-specific binders of the kinase ERK from designed ankyrin repeat protein libraries. Proc Natl Acad Sci U S A *109*, E2248-2257.

Kwon, S., Zhang, Y., and Matthias, P. (2007). The deacetylase HDAC6 is a novel critical component of stress granules involved in the stress response. Genes & development *21*, 3381-3394.

Lafarga, V., Aymerich, I., Tapia, O., Mayor, F., Jr., and Penela, P. (2012). A novel GRK2/HDAC6 interaction modulates cell spreading and motility. The EMBO journal *31*, 856-869.

Lee, A.K., Klein, J., Fon Tacer, K., Lord, T., Oatley, M.J., Oatley, J.M., Porter, S.N., Pruett-Miller, S.M., Tikhonova, E.B., Karamyshev, A.L.*, et al.* (2020). Translational Repression of G3BP in Cancer and Germ Cells Suppresses Stress Granules and Enhances Stress Tolerance. Molecular cell *79*, 645-659 e649.

Lee, Y.S., Lim, K.H., Guo, X., Kawaguchi, Y., Gao, Y., Barrientos, T., Ordentlich, P., Wang, X.F., Counter, C.M., and Yao, T.P. (2008). The cytoplasmic deacetylase HDAC6 is required for efficient oncogenic tumorigenesis. Cancer Res *68*, 7561-7569.

Legros, S., Boxus, M., Gatot, J.S., Van Lint, C., Kruys, V., Kettmann, R., Twizere, J.C., and Dequiedt, F. (2011). The HTLV-1 Tax protein inhibits formation of stress granules by interacting with histone deacetylase 6. Oncogene *30*, 4050-4062.

Li, T., Zhang, C., Hassan, S., Liu, X., Song, F., Chen, K., Zhang, W., and Yang, J. (2018a). Histone deacetylase 6 in cancer. Journal of hematology & oncology *11*, 111-111.

Li, T., Zhang, C., Hassan, S., Liu, X., Song, F., Chen, K., Zhang, W., and Yang, J. (2018b). Histone deacetylase 6 in cancer. J Hematol Oncol *11*, 111.

Li, Y., Shin, D., and Kwon, S.H. (2013). Histone deacetylase 6 plays a role as a distinct regulator of diverse cellular processes. FEBS J *280*, 775-793.

Lim, K.-L., Dawson, V.L., and Dawson, T.M. (2006). Parkin-mediated lysine 63-linked polyubiquitination: A link to protein inclusions formation in Parkinson's and other conformational diseases? Neurobiology of Aging *27*, 524-529.

Lin, Y., Protter, D.S., Rosen, M.K., and Parker, R. (2015). Formation and Maturation of Phase-Separated Liquid Droplets by RNA-Binding Proteins. Molecular cell *60*, 208-219.

Lindquist, M.E., Lifland, A.W., Utley, T.J., Santangelo, P.J., and Crowe, J.E., Jr. (2010). Respiratory syncytial virus induces host RNA stress granules to facilitate viral replication. Journal of virology *84*, 12274-12284.

Liu, H.M., Jiang, F., Loo, Y.M., Hsu, S., Hsiang, T.Y., Marcotrigiano, J., and Gale, M., Jr. (2016). Regulation of Retinoic Acid Inducible Gene-I (RIG-I) Activation by the Histone Deacetylase 6. EBioMedicine *9*, 195-206.

Loschi, M., Leishman, C.C., Berardone, N., and Boccaccio, G.L. (2009). Dynein and kinesin regulate stress-granule and P-body dynamics. Journal of cell science *122*, 3973-3982.

Lucas, R.M., Bauer, C.S., Chinnaiya, K., Schwartzentruber, A., MacDonald, R., Collins, M.O., Aasly, J.O., Brønstad, G., Ferraiuolo, L., Mortiboys, H.*, et al.* (2019). LRRK2-mediated phosphorylation of HDAC6 regulates HDAC6-cytoplasmic dynein interaction and aggresome formation. bioRxiv, 554881.

Lucera, M.B., Tilton, C.A., Mao, H., Dobrowolski, C., Tabler, C.O., Haqqani, A.A., Karn, J., and Tilton, J.C. (2014). The histone deacetylase inhibitor vorinostat (SAHA) increases the susceptibility of uninfected CD4+ T cells to HIV by increasing the kinetics and efficiency of postentry viral events. Journal of virology *88*, 10803-10812.

Lyubomir T. Vassilev, B.T.V., Bradford Graves, Daisy Carvajal, Frank Podlaski, Zoran Filipovic, Norman Kong, Ursula Kammlott, Christine Lukacs, Christian Klein, Nader Fotouhi, Emily A. Liu (2004). In Vivo Activation of the p53 Pathway by Small-Molecule Antagonists of MDM2. Science *303*, 844-848.

Magupalli, V., Negro, R., Tian, Y., Hauenstein, A., Di Caprio, G., Skillern, W., Deng, Q., Orning, P., Alam, H., Maliga, Z.*, et al.* (2020). HDAC6 mediates an aggresome-like mechanism for NLRP3 and pyrin inflammasome activation. Science *369*.

Manfred, S. (1982). Action of Cytochalasin D on Cytoskeletal Networks. The Journal of cell biology *92*.

Markmiller, S., Fulzele, A., Higgins, R., Leonard, M., Yeo, G.W., and Bennett, E.J. (2019). Active Protein Neddylation or Ubiquitylation Is Dispensable for Stress Granule Dynamics. Cell reports *27*, 1356-1363 e1353.

Markmiller, S., Soltanieh, S., Server, K.L., Mak, R., Jin, W., Fang, M.Y., Luo, E.C., Krach, F., Yang, D., Sen, A.*, et al.* (2018). Context-Dependent and Disease-Specific Diversity in Protein Interactions within Stress Granules. Cell *172*, 590-604 e513.

Mateju, D., Franzmann, T.M., Patel, A., Kopach, A., Boczek, E.E., Maharana, S., Lee, H.O., Carra, S., Hyman, A.A., and Alberti, S. (2017). An aberrant phase transition of stress granules triggered by misfolded protein and prevented by chaperone function. The EMBO journal *36*, 1669-1687.

Matrosovich., A., T., N., B., A., G., A., K., MR., C., I., D., and Y., K. (2000). Early alterations of the receptor-binding properties of H1, H2, and H3 avian influenza virus hemagglutinins after their introduction into mammals. Journal of virology *74*, 8502-8512.

Matsuoka, Y., Matsumae, H., Katoh, M., Eisfeld, A.J., Neumann, G., Hase, T., Ghosh, S., Shoemaker, J.E., Lopes, T.J., Watanabe, T.*, et al.* (2013). A comprehensive map of the influenza A virus replication cycle. BMC Syst Biol *7*.

Maxwell, M.M., Tomkinson, E.M., Nobles, J., Wizeman, J.W., Amore, A.M., Quinti, L., Chopra, V., Hersch, S.M., and Kazantsev, A.G. (2011). The Sirtuin 2 microtubule deacetylase is an abundant neuronal protein that accumulates in the aging CNS. Hum Mol Genet *20*, 3986-3996.

Mazroui, R., Di Marco, S., Kaufman, R.J., and Gallouzi, I.E. (2007). Inhibition of the ubiquitin-proteasome system induces stress granule formation. Molecular biology of the cell *18*, 2603-2618.

Meyer, H.-J., and Rape, M. (2014). Enhanced protein degradation by branched ubiquitin chains. Cell *157*, 910-921.

Mishima, Y., Santo, L., Eda, H., Cirstea, D., Nemani, N., Yee, A.J., O'Donnell, E., Selig, M.K., Quayle, S.N., Arastu-Kapur, S.*, et al.* (2015). Ricolinostat (ACY-1215) induced inhibition of aggresome formation accelerates carfilzomib-induced multiple myeloma cell death. Br J Haematol *169*, 423-434.

Miyake, Y., Keusch, J.J., Wang, L., Saito, M., Hess, D., Wang, X., Melancon, B.J., Helquist, P., Gut, H., and Matthias, P. (2016). Structural insights into HDAC6 tubulin deacetylation and its selective inhibition. Nat Chem Biol *12*, 748-754.

Modell, A.E., Blosser, S.L., and Arora, P.S. (2016). Systematic Targeting of Protein-Protein Interactions. Trends Pharmacol Sci *37*, 702-713.

Montero, H., and Trujillo-Alonso, V. (2011). Stress granules in the viral replication cycle. Viruses *3*, 2328-2338.

Morimoto, D., Walinda, E., Fukada, H., Sou, Y.S., Kageyama, S., Hoshino, M., Fujii, T., Tsuchiya, H., Saeki, Y., Arita, K.*, et al.* (2015). The unexpected role of polyubiquitin chains in the formation of fibrillar aggregates. Nature communications *6*, 6116.

Morrow, C., Porter, T., Xu, N., Arndt, Z., Ako-Asare, K., Heo, H., Thompson, E., and Moore, D. (2020). Vimentin Coordinates Protein Turnover at the Aggresome during Neural Stem Cell Quiescence Exit. Cell Stem Cell *26*, 558-568.e559.

Muller, M.J., Klumpp, S., and Lipowsky, R. (2008). Tug-of-war as a cooperative mechanism for bidirectional cargo transport by molecular motors. Proceedings of the National Academy of Sciences of the United States of America *105*, 4609-4614.

Müller, M.J., Klumpp, S., and Lipowsky, R. (2008). Tug-of-war as a cooperative mechanism for bidirectional cargo transport by molecular motors. Proceedings of the National Academy of Sciences *105*, 4609-4614.

Munoz-Moreno, R., Barrado-Gil, L., Galindo, I., and Alonso, C. (2015). Analysis of HDAC6 and BAG3-aggresome pathways in African swine fever viral factory formation. Viruses *7*, 1823-1831.

Nabet, B., Roberts, J.M., Buckley, D.L., Paulk, J., Dastjerdi, S., Yang, A., Leggett, A.L., Erb, M.A., Lawlor, M.A., Souza, A.*, et al.* (2018). The dTAG system for immediate and target-specific protein degradation. Nat Chem Biol *14*, 431-441.

Nadezhdina, E.S., Lomakin, A.J., Shpilman, A.A., Chudinova, E.M., and Ivanov, P.A. (2010). Microtubules govern stress granule mobility and dynamics. Biochimica et biophysica acta *1803*, 361-371.

Nakagawa, T., and Guarente, L. (2011). Sirtuins at a glance. Journal of cell science *124*, 833-838.

Nakashima, H., Kaufmann, J.K., Wang, P.Y., Nguyen, T., Speranza, M.C., Kasai, K., Okemoto, K., Otsuki, A., Nakano, I., Fernandez, S.*, et al.* (2015). Histone deacetylase 6 inhibition enhances oncolytic viral replication in glioma. J Clin Invest *125*, 4269-4280.

Nanduri, P., Hao, R., Fitzpatrick, T., and Yao, T.P. (2015). Chaperone-mediated 26S proteasome remodeling facilitates free K63 ubiquitin chain production and aggresome clearance. The Journal of biological chemistry *290*, 9455-9464.

Narita, T., Weinert, B.T., and Choudhary, C. (2019). Functions and mechanisms of non-histone protein acetylation. Nat Rev Mol Cell Biol *20*, 156-174.

Natsume, T., and Kanemaki, M.T. (2017). Conditional Degrons for Controlling Protein Expression at the Protein Level. Annu Rev Genet *51*, 83-102.

Neklesa, T.K., Tae, H.S., Schneekloth, A.R., Stulberg, M.J., Corson, T.W., Sundberg, T.B., Raina, K., Holley, S.A., and Crews, C.M. (2011). Small-molecule hydrophobic tagging-induced degradation of HaloTag fusion proteins. Nat Chem Biol *7*, 538-543.

Norstrom, M.F., Smithback, P.A., and Rock, R.S. (2010). Unconventional processive mechanics of non-muscle myosin IIB. The Journal of biological chemistry *285*, 26326-26334.

North., B.J., Marshall., B.L., Borra., M.T., Denu., J.M., and Verdin., E. (2003). The Human Sir2 Ortholog, SIRT2,Is an NAD-Dependent Tubulin Deacetylase. Molecular cell *11*, 437-444.

Nover, L., Scharf, K.D., and Neumann, D. (1989). Cytoplasmic heat shock granules are formed from precursor particles and are associated with a specific set of mRNAs. Mol Cell Biol *9*, 1298-1308.

Nozawa, N., Yamauchi, Y., Ohtsuka, K., Kawaguchi, Y., and Nishiyama, Y. (2004). Formation of aggresome-like structures in herpes simplex virus type 2-infected cells and a potential role in virus assembly. Exp Cell Res *299*, 486-497.

Ohtake, F., Saeki, Y., Ishido, S., Kanno, J., and Tanaka, K. (2016). The K48-K63 Branched Ubiquitin Chain Regulates NF-kappaB Signaling. Molecular cell *64*, 251-266.

Ohtake, F., Tsuchiya, H., Saeki, Y., and Tanaka, K. (2018). K63 ubiquitylation triggers proteasomal degradation by seeding branched ubiquitin chains. Proc Natl Acad Sci U S A *115*, E1401-E1408.

Olzmann, J., Li, L., and Chin, L. (2008). Aggresome formation and neurodegenerative diseases: therapeutic implications. Curr Med Chem *15*, 47-60.

Olzmann, J.A., Li, L., Chudaev, M.V., Chen, J., Perez, F.A., Palmiter, R.D., and Chin, L.S. (2007). Parkin-mediated K63-linked polyubiquitination targets misfolded DJ-1 to aggresomes via binding to HDAC6. The Journal of cell biology *178*, 1025-1038.

Ouyang, H., Ali, Y.O., Ravichandran, M., Dong, A., Qiu, W., MacKenzie, F., Dhe-Paganon, S., Arrowsmith, C.H., and Zhai, R.G. (2012). Protein aggregates are recruited to aggresome by histone deacetylase 6 via unanchored ubiquitin C termini. The Journal of biological chemistry *287*, 2317-2327.

Parmigiani, R., WS, X., G, V.-P., H, E.-B., M, Y., P, T., and PA, M. (2008). HDAC6 is a specific deacetylase of peroxiredoxins and is involved in redox regulation. Proc Natl Acad Sci U S A *105*, 9633-9638.

Peisley, A., Wu, B., Xu, H., Chen, Z.J., and Hur, S. (2014). Structural basis for ubiquitin-mediated antiviral signal activation by RIG-I. Nature *509*, 110-114.

Pfisterer, K., Jayo, A., and Parsons, M. (2017). Control of nuclear organization by F-actin binding proteins. Nucleus (Austin, Tex) *8*, 126-133.

Plückthun, A. (2015). Designed ankyrin repeat proteins (DARPins): binding proteins for research, diagnostics, and therapy. Annu Rev Pharmacol Toxicol *55*, 489-511.

Protter, D.S.W., and Parker, R. (2016). Principles and Properties of Stress Granules. Trends Cell Biol *26*, 668-679.

Putcha, P., Yu, J., Rodriguez-Barrueco, R., Saucedo-Cuevas, L., Villagrasa, P., Murga-Penas, E., Quayle, S.N., Yang, M., Castro, V., Llobet-Navas, D*., et al.* (2015). HDAC6 activity is a non-oncogene addiction hub for inflammatory breast cancers. Breast Cancer Res *17*, 149.

Raden, D., Hildebrandt, S., Xu, P., Bell, E., Doyle, F.J., 3rd, and Robinson, A.S. (2005). Analysis of cellular response to protein overexpression. Systems biology *152*, 285-289.

Ramdzan, Y.M., Trubetskov, M.M., Ormsby, A.R., Newcombe, E.A., Sui, X., Tobin, M.J., Bongiovanni, M.N., Gras, S.L., Dewson, G., Miller, J.M.L*., et al.* (2017). Huntingtin Inclusions Trigger Cellular Quiescence, Deactivate Apoptosis, and Lead to Delayed Necrosis. Cell reports *19*, 919-927.

Ran, F.A., Hsu, P.D., Wright, J., Agarwala, V., Scott, D.A., and Zhang, F. (2013). Genome engineering using the CRISPR-Cas9 system. Nat Protoc *8*, 2281-2308.

Ran, J., Yang, Y., Li, D., Liu, M., and Zhou, J. (2015). Deacetylation of alpha-tubulin and cortactin is required for HDAC6 to trigger ciliary disassembly. Sci Rep *5*, 12917.

Rao, Y., Hao, R., Wang, B., and Yao, T.P. (2014). A Mec17-Myosin II Effector Axis Coordinates Microtubule Acetylation and Actin Dynamics to Control Primary Cilium Biogenesis. PloS one *9*, e114087.

Rathje, L.S., Nordgren, N., Pettersson, T., Ronnlund, D., Widengren, J., Aspenstrom, P., and Gad, A.K. (2014). Oncogenes induce a vimentin filament collapse mediated by HDAC6 that is linked to cell stiffness. Proc Natl Acad Sci U S A *111*, 1515-1520.

Reed, N.A., Cai, D., Blasius, T.L., Jih, G.T., Meyhofer, E., Gaertig, J., and Verhey, K.J. (2006). Microtubule acetylation promotes kinesin-1 binding and transport. Curr Biol *16*, 2166-2172.

Reineke, L.C., and Lloyd, R.E. (2013). Diversion of stress granules and P-bodies during viral infection. Virology *436*, 255-267.

Remillard, D., Buckley, D.L., Paulk, J., Brien, G.L., Sonnett, M., Seo, H.S., Dastjerdi, S., Wuhr, M., Dhe-Paganon, S., Armstrong, S.A.*, et al.* (2017). Degradation of the BAF Complex Factor BRD9 by Heterobifunctional Ligands. Angew Chem Int Ed Engl *56*, 5738-5743.

Reyes-Turcu, F., Horton, J., Mullally, J., Heroux, A., Cheng, X., and Wilkinson, K. (2006). The Ubiquitin Binding Domain ZnF UBP Recognizes the C-Terminal Diglycine Motif of Unanchored Ubiquitin. Cell *124*, 1197-1208.

Riolo, M.T., Cooper, Z.A., Holloway, M.P., Cheng, Y., Bianchi, C., Yakirevich, E., Ma, L., Chin, Y.E., and Altura, R.A. (2012). Histone deacetylase 6 (HDAC6) deacetylates survivin for its nuclear export in breast cancer. The Journal of biological chemistry *287*, 10885-10893.

RT, A., Z, Y., and DP, N. (1997). Association of Influenza Virus NP and M1 Proteins with Cellular Cytoskeletal Elements in Influenza Virus-Infected Cells. Journal of virology *74*, 2947-2958.

Rudnicka, A., and Yamauchi, Y. (2016). Ubiquitin in Influenza Virus Entry and Innate Immunity. Viruses *8*.

Saito, M., Hess, D., Eglinger, J., Fritsch, A.W., Kreysing, M., Weinert, B.T., Choudhary, C., and Matthias, P. (2019a). Acetylation of intrinsically disordered regions regulates phase separation. Nat Chem Biol *15*, 51-61.

Saito, M., Hess, D., Eglinger, J., Fritsch, A.W., Kreysing, M., Weinert, B.T., Choudhary, C., and Matthias, P. (2019b). Acetylation of intrinsically disordered regions regulates phase separation. Nature Chemical Biology *15*, 51-61.

Schmidt, T., Samaras, P., Frejno, M., Gessulat, S., Barnert, M., Kienegger, H., Krcmar, H., Schlegl, J., Ehrlich, H.-C., Aiche, S.*, et al.* (2018). ProteomicsDB. Nucleic Acids Research *46*, D1271-D1281.

Schneider, C.A., Rasband, W.S., and Eliceiri, K.W. (2012). NIH Image to ImageJ: 25 years of image analysis. Nature methods *9*, 671-675.

Schnoor, M., Stradal, T.E., and Rottner, K. (2018). Cortactin: Cell Functions of A Multifaceted Actin-Binding Protein. Trends Cell Biol *28*, 79-98.

Seeger, M.A., Mittal, A., Velamakanni, S., Hohl, M., Schauer, S., Salaa, I., Grutter, M.G., and van Veen, H.W. (2012). Tuning the drug efflux activity of an ABC transporter in vivo by in vitro selected DARPin binders. PloS one *7*, e37845.

Seidel, C., M., S., M., D., and M., D. (2015). Histone deacetylase 6 in health and disease. Epigenomics *7*, 103-118.

Seigneurin-Berny, D., Verdel, A., Curtet, S., Lemercier, C., Garin, J., Rousseaux, S., and Khochbin, S. (2001). Identification of components of the murine histone deacetylase 6 complex: link between acetylation and ubiquitination signaling pathways. Molecular and cellular biology *21*, 8035-8044.

Serres, M., Samwer, M., Truong Quang, B., Lavoie, G., Perera, U., Görlich, D., Charras, G., Petronczki, M., Roux, P., and Paluch, E. (2020). F-Actin Interactome Reveals Vimentin as a Key Regulator of Actin Organization and Cell Mechanics in Mitosis. Developmental Cell *52*, 210-222.e217.

Seto, E., and Yoshida, M. (2014). Erasers of histone acetylation: the histone deacetylase enzymes. Cold Spring Harb Perspect Biol *6*, a018713.

Shahbazian, M.D., and Grunstein, M. (2007). Functions of site-specific histone acetylation and deacetylation. Annu Rev Biochem *76*, 75-100.

Sievers, Q.L., Petzold, G., Bunker, R.D., Renneville, A., Slabicki, M., Liddicoat, B.J., Abdulrahman, W., Mikkelsen, T., Ebert, B.L., and Thoma, N.H. (2018). Defining the human C2H2 zinc finger degrome targeted by thalidomide analogs through CRBN. Science *362*.

Simoes-Pires, C., Zwick, V., Nurisso, A., Schenker, E., Carrupt, P.A., and Cuendet, M. (2013). HDAC6 as a target for neurodegenerative diseases: what makes it different from the other HDACs? Mol Neurodegener *8*, 7.

Siva, A.C., Kirkland, R.E., Lin, B., Maruyama, T., McWhirter, J., Yantiri-Wernimont, F., Bowdish, K.S., and Xin, H. (2008). Selection of anti-cancer antibodies from combinatorial libraries by whole-cell panning and stringent subtraction with human blood cells. J Immunol Methods *330*, 109-119.

Skultetyova, L., Ustinova, K., Kutil, Z., Novakova, Z., Pavlicek, J., Mikesova, J., Trapl, D., Baranova, P., Havlinova, B., Hubalek, M.*, et al.* (2017). Human histone deacetylase 6 shows strong preference for tubulin dimers over assembled microtubules. Sci Rep *7*, 11547.

Soderholm, J.F., Bird, S.L., Kalab, P., Sampathkumar, Y., Hasegawa, K., Uehara-Bingen, M., Weis, K., and Heald, R. (2011). Importazole, a small molecule inhibitor of the transport receptor importin-β. ACS chemical biology *6*, 700-708.

Solomon, S., Xu, Y., Wang, B., David, M.D., Schubert, P., Kennedy, D., and Schrader, J.W. (2007). Distinct structural features of caprin-1 mediate its interaction with G3BP-1 and its induction of phosphorylation of eukaryotic translation initiation factor 2alpha, entry to cytoplasmic stress granules, and selective interaction with a subset of mRNAs. Mol Cell Biol *27*, 2324-2342.

Souquere, S., Mollet, S., Kress, M., Dautry, F., Pierron, G., and Weil, D. (2009). Unravelling the ultrastructure of stress granules and associated P-bodies in human cells. Journal of cell science *122*, 3619-3626.

Su, M., Shi, J.J., Yang, Y.P., Li, J., Zhang, Y.L., Chen, J., Hu, L.F., and Liu, C.F. (2011). HDAC6 regulates aggresome-autophagy degradation pathway of α-synuclein in response to MPP+-induced stress. Journal of neurochemistry *117*, 112-120.

Su, W.C., Chen, Y.C., Tseng, C.H., Hsu, P.W., Tung, K.F., Jeng, K.S., and Lai, M.M. (2013). Pooled RNAi screen identifies ubiquitin ligase Itch as crucial for influenza A virus release from the endosome during virus entry. Proc Natl Acad Sci U S A *110*, 17516-17521.

Subramanian, C., Jarzembowski, J.A., Opipari, A.W., Jr., Castle, V.P., and Kwok, R.P. (2011). HDAC6 deacetylates Ku70 and regulates Ku70-Bax binding in neuroblastoma. Neoplasia *13*, 726-734.

Sweeney, P., Park, H., Baumann, M., Dunlop, J., Frydman, J., Kopito, R., McCampbell, A., Leblanc, G., Venkateswaran, A., Nurmi, A.*, et al.* (2017). Protein misfolding in neurodegenerative diseases: implications and strategies. Transl Neurodegener *6*, 6.

Tanaka, M., Kim, Y.M., Lee, G., Junn, E., Iwatsubo, T., and Mouradian, M.M. (2004). Aggresomes formed by alpha-synuclein and synphilin-1 are cytoprotective. The Journal of biological chemistry *279*, 4625-4631.

Taylor, M.P., Koyuncu, O.O., and Enquist, L.W. (2011). Subversion of the actin cytoskeleton during viral infection. Nat Rev Microbiol *9*, 427-439.

Taylor, P., Tanaka, F., Robitschek, J., Sandoval, C.M., Taye, A., Markovic-Plese, S., and Fischbeck, K. (2003). Aggresomes protect cells by enhancing the degradation of toxic polyglutamine-containing protein. Human Molecular Genetics *12*, 749-757.

Thomas, M.G., Loschi, M., Desbats, M.A., and Boccaccio, G.L. (2011). RNA granules: the good, the bad and the ugly. Cellular signalling *23*, 324-334.

Tong, S., Zhu, X., Li, Y., Shi, M., Zhang, J., Bourgeois, M., Yang, H., Chen, X., Recuenco, S., Gomez, J.*, et al.* (2013). New world bats harbor diverse influenza A viruses. PLoS Pathog *9*, e1003657.

Tourrière, H., Chebli, K., Zekri, L., Courselaud, B., Blanchard, J.M., Bertrand, E., and Tazi, J. (2003). The RasGAP-associated endoribonuclease G3BP assembles stress granules. The Journal of cell biology *160*, 823-831.

Tyanova, S., Temu, T., and Cox, J. (2016). The MaxQuant computational platform for mass spectrometry-based shotgun proteomics. Nat Protoc *11*, 2301-2319.

Urnavicius, L., Zhang, K., Diamant, A., Motz, C., Schlager, M., Yu, M., Patel, N., Robinson, C., and Carter, A.P. (2015). The structure of the dynactin complex and its interaction with dynein. Science *347*, 1441-1446.

Vale-Costa, S., and Amorim, M.J. (2016). Recycling Endosomes and Viral Infection. Viruses *8*, 64.

Valentin-Vega, Y.A., Wang, Y.D., Parker, M., Patmore, D.M., Kanagaraj, A., Moore, J., Rusch, M., Finkelstein, D., Ellison, D.W., Gilbertson, R.J.*, et al.* (2016). Cancer-associated DDX3X mutations drive stress granule assembly and impair global translation. Sci Rep *6*, 25996.

Valenzuela-Fernandez, A., Alvarez, S., Gordon-Alonso, M., Barrero, M., Ursa, A., Cabrero, J.R., Fernandez, G., Naranjo-Suarez, S., Yanez-Mo, M., Serrador, J.M.*, et al.* (2005). Histone deacetylase 6 regulates human immunodeficiency virus type 1 infection. Molecular biology of the cell *16*, 5445-5454.

Valera, M.-S., de Armas-Rillo, L., Barroso-González, J., Ziglio, S., Batisse, J., Dubois, N., Marrero-Hernández, S., Borel, S., García-Expósito, L., Biard-Piechaczyk, M.*, et al.* (2015). The

HDAC6/APOBEC3G complex regulates HIV-1 infectiveness by inducing Vif autophagic degradation. Retrovirology *12*, 53.

Valiente-Echeverría, F., Melnychuk, L., and Mouland, A.J. (2012). Viral modulation of stress granules. Virus research *169*, 430-437.

Vann, B., and Anthony, B. (2001). Spectrin and Ankyrin-Based Pathways: Metazoan Inventions for Integrating Cells Into Tissues. Physiological Reviews *81*, 1353-1392.

Vicente-Manzanares, M., Ma, X., Adelstein, R.S., and Horwitz, A.R. (2009). Non-muscle myosin II takes centre stage in cell adhesion and migration. Nat Rev Mol Cell Biol *10*, 778-790.

Virnekäs, B., L, G., A, P., KC, S., G, W., and SE., M. (1994). Trinucleotide phosphoramidites: ideal reagents for the synthesis of mixed oligonucleotides for random mutagenesis. Nucleic Acids Research, *22*, 5600-5607.

Vogel, F., Hofius, D., and Sonnewald, U. (2007). Intracellular trafficking of Potato leafroll virus movement protein in transgenic Arabidopsis. Traffic *8*, 1205-1214.

Waelter, S., Boeddrich, A., Lurz, R., Scherzinger, E., Lueder, G., Lehrach, H., and Wanker, E. (2001). Accumulation of Mutant Huntingtin Fragments in Aggresome-like Inclusion Bodies as a Result of Insufficient Protein Degradation. Molecular biology of the cell *12*, 1393-1407.

Watanabe, T., Kawakami, E., Shoemaker, J.E., Lopes, T.J., Matsuoka, Y., Tomita, Y., Kozuka-Hata, H., Gorai, T., Kuwahara, T., Takeda, E.*, et al.* (2014). Influenza virus-host interactome screen as a platform for antiviral drug development. Cell Host Microbe *16*, 795-805.

Watanabe, T., Watanabe, S., and Kawaoka, Y. (2010). Cellular networks involved in the influenza virus life cycle. Cell Host Microbe *7*, 427-439.

Wheeler, J.R., Matheny, T., Jain, S., Abrisch, R., and Parker, R. (2016). Distinct stages in stress granule assembly and disassembly. Elife *5*.

White, J.P., Cardenas, A.M., Marissen, W.E., and Lloyd, R.E. (2007). Inhibition of cytoplasmic mRNA stress granule formation by a viral proteinase. Cell Host Microbe *2*, 295-305.

Wileman, T. (2006). Aggresomes and Autophagy Generate Sites for Virus Replication. Science *312*, 875-878.

Wileman, T. (2007). Aggresomes and pericentriolar sites of virus assembly: cellular defense or viral design? Annu Rev Microbiol *61*, 149-167.

Winter, G.E., Buckley, D.L., Paulk, J., Roberts, J.M., Souza, A., Dhe-Paganon, S., and Bradner, J.E. (2015). Phthalimide conjugation as a strategy for in vivo target protein degradation. Science *348*, 1376-1381.

Wolozin, B., and Ivanov, P. (2019). Stress granules and neurodegeneration. Nat Rev Neurosci *20*, 649-666.

Wu, C.-Y., Jeng, K.-S., and Lai, M.M.C. (2011). The SUMOylation of matrix protein M1 modulates the assembly and morphogenesis of influenza A virus. Journal of virology *85*, 6618-6628.

Xu, Z., Schaedel, L., Portran, D., Aguilar, A., Gaillard, J., Marinkovich, M.P., Thery, M., and Nachury, M.V. (2017). Microtubules acquire resistance from mechanical breakage through intralumenal acetylation. Science *356*, 328-332.

Yan, J., Seibenhener, M.L., Calderilla-Barbosa, L., Diaz-Meco, M.T., Moscat, J., Jiang, J., Wooten, M.W., and Wooten, M.C. (2013). SQSTM1/p62 interacts with HDAC6 and regulates deacetylase activity. PloS one *8*, e76016.

Yang, X., Shen, Y., Garre, E., Hao, X., Krumlinde, D., Cvijovic, M., Arens, C., Nystrom, T., Liu, B., and Sunnerhagen, P. (2014). Stress granule-defective mutants deregulate stress responsive transcripts. PLoS Genet *10*, e1004763.

Zhang, K., Daigle, J.G., Cunningham, K.M., Coyne, A.N., Ruan, K., Grima, J.C., Bowen, K.E., Wadhwa, H., Yang, P., Rigo, F.*, et al.* (2018). Stress Granule Assembly Disrupts Nucleocytoplasmic Transport. Cell *173*, 958-971 e917.

Zhang, X., Yuan, Z., Zhang, Y., Yong, S., Salas-Burgos, A., Koomen, J., Olashaw, N., Parsons, J.T., Yang, X.J., Dent, S.R.*, et al.* (2007). HDAC6 modulates cell motility by altering the acetylation level of cortactin. Molecular cell *27*, 197-213.

Zhang, Y., Kwon, S., Yamaguchi, T., Cubizolles, F., Rousseaux, S., Kneissel, M., Cao, C., Li, N., Cheng, H.L., Chua, K.*, et al.* (2008). Mice lacking histone deacetylase 6 have hyperacetylated tubulin but are viable and develop normally. Mol Cell Biol *28*, 1688-1701.

Zhang, Y., Li, N., Caron, C., Matthias, G., Hess, D., Khochbin, S., and Matthias, P. (2003a). HDAC-6 interacts with and deacetylates tubulin and microtubules in vivo. The EMBO journal *22*, 1168-1179.

Zhang, Y., Li, N., Caron, C., Matthias, G., Hess, D., Khochbin, S., and Matthias, P. (2003b). HDAC-6 interacts with and deacetylates tubulin and microtubules in vivo. The EMBO journal *22*, 1168-1179.

Zhao, Z., Cao, L., and Reece, E.A. (2017). Formation of neurodegenerative aggresome and death-inducing signaling complex in maternal diabetes-induced neural tube defects. Proc Natl Acad Sci U S A *114*, 4489-4494.

Curriculum Vitae

Personal Information

Name: Longlong Wang

Nationality: Chinese

Current Address: Friedrich Miescher Institute for Biomedical Research, affiliated institute of University of Basel. Maulbeerstrasse 66, CH-4058 Basel, Switzerland

E-mail: longlong.wang@fmi.ch

ORCID: 0000-0001-5279-1885

Education & Employment

2015,1 - Present **University of Basel/ Friedrich Miescher Institute (FMI) for Biomedical Research, Novartis.**

Topic: *Investigation of HDAC6 – Ubiquitin interaction in stress response and virus infection*

PhD student

Supervisor: Prof. Patrick Matthias

2011.9 - 2014.9 **Shanghai Institute of Biochemistry and Cell Biology (SIBCB), University of Chinese Academy of Science.**

Master of Biochemistry

Topic: *Structure analysis of PRC complex in Arabidopsis*

Supervisor: Dr. Ying Huang.

2007.9 - 2011.9 **Wuhan University, Wuhan, China**

Bachelor of Science (Molecular Biology)

Supervisor: Prof. Zhixiong Xie

Honors and Awards

2007 to 2011	The scholarship of Wuhan University * for students with the highest GPA
2011	The Outstanding Graduate
2010	National Motivational Scholarship * for the best students in University
2008	The Outstanding Person in Social Practice of Wuhan University

Publication

Alina Artcibasova*, **Longlong Wang***, Stephanie Anchisi, Yohei Yamauchi, Mirco Schmolke, Patrick Matthias, Jörg Stelling. A quantitative model for HDAC6-mediated virus uncoating predicts Influenza A infectivity. (2020) (Ready for submission)

Longlong Wang*, Etori Aguiar Moreira, Georg Kempf, Yasuyuki Miyake, Blandina I. Oliveira Estevese, Marco P. Alvese, Jonas V. Schaeferg, Birgit Dreier, Yohei Yamauchi, Andreas Plückthun & Patrick Matthias. Targeting the HDAC6 zinc finger domain impacts virus infection and cellular stress pathways. Cell Reports (2020) (Under review)

Ling Peng*, **Longlong Wang***, Yingpei Zhang*, Aiwu Dong, Wen-Hui Shen and Ying Huang. Structural Analysis of the Arabidopsis AL2-PAL and PRC1 Complex Provides Mechanistic Insight into Active-to-Repressive Chromatin State Switch. J Mol Biol 430, 4245-4259, doi:10.1016/j.jmb.2018.08.021 (2018).

Yasuyuki Miyake*, Jeremy J Keusch*, **Longlong Wang**, Makoto Saito, Daniel Hess, Xiaoning Wang, Bruce J Melancon, Paul Helquist, Heinz Gut & Patrick Matthias. Structural insights into HDAC6 tubulin deacetylation and its selective inhibition. Nat Chem Biol 12, 748-754, doi:10.1038/nchembio.2140 (2016).

*: equal contribution.

Conference

2017. 9 **Swiss Initiative in System Biology Conference**

Bern, Switzerland

Poster presentation

2016. 9 **Swiss Initiative in System Biology Conference**

Bern, Switzerland

Poster presentation

2013.12 **Shanghai Structural Annual Conference**

Shanghai, China.

Invited Speaker: “Structure of new PRC1 complex – AL2 in *Arabidopsis*”

2012. 9 **Cold Spring Harbour Asia Conference**

Suzhou, China.

Poster presentation